https://researchcommons.waikato.ac.nz/

Research Commons at the University of Waikato

Copyright Statement:

The digital copy of this thesis is protected by the Copyright Act 1994 (New Zealand).

The thesis may be consulted by you, provided you comply with the provisions of the Act and the following conditions of use:

- Any use you make of these documents or images must be for research or private study purposes only, and you may not make them available to any other person.
- Authors control the copyright of their thesis. You will recognise the author's right to be identified as the author of the thesis, and due acknowledgement will be made to the author where appropriate.
- You will obtain the author's permission before publishing any material from the thesis.

How Life Uses Sound to Reorganise Matter:

The Role of Anharmonic Phonon Exchange in Enzyme Catalysis

A thesis submitted

for the degree of

Doctor of Philosophy

in Physics

by

Christopher Gerald Batterton

THE UNIVERSITY OF
WAIKATO
Te Whare Wānanga o Waikato

August 2024

The University of Waikato

Abstract

Biological enzyme catalysis is the name for life's ability to rapidly invoke coordinated rearrangements of molecular structures using highly specialised, relatively-large functional proteins called enzymes. It is well established that enzymes reduce the activation energy barrier, which vastly accelerates the rate of reaction, however the specific dynamics and quantum mechanics are largely uncharted. Recent experimentation and modelling hints that there is a phase transition dynamic that is fundamental to enzymatic catalysis. The hypothesis that I explore in this thesis is that a mathematical model of a substrate molecule based upon anharmonic quantum vibrational modes (molecular phonons) will predict phase transition dynamics due to the presence of the appropriate enzyme. A molecular phonon is one particular individualised wave pattern in the locations of atomic nuclei from the total molecular dance that spans the low-frequency bulk swaying motions, mid-frequency bond stretches, to the high-frequency oscillations of the hydrogen bond network.

In this thesis, I derive a generalised set of equations of motion for the anharmonic response behaviour of molecular phonons to enzyme stimulus via a dissipative quantum master equation, and I explore the phase transition dynamics by determining the stability bifurcation of the steady states. I then determine the critical minimum stimulus required for a molecular vibrational mode to exhibit a phase transition. The primary catalytic reaction of focus for this thesis is the cleavage of the glycosidic carbon–oxygen bond of the complex sugar isomaltose into two individual glucose molecules via the action of the enzyme MalL. Prior to this thesis, the atomic structure of MalL was obtained experimentally via X-ray diffraction crystallography of prepared MalL crystals, then digitised into the Gromacs software package and energy minimised in a simulated water bath to approximate the vibrational modes of the *in vivo* configuration. I obtain the substrate molecule's harmonic frequencies and anharmonic shifts via molecular dynamics performed using the Gaussian 09 normal mode analysis and simulated anharmonic infrared spectroscopy packages, respectively. I construct a generalised coding package in Matlab to extract the molecule and enzyme data, perform a quantum anharmonic analysis of the molecule–enzyme complex and their interactions, and then simulate the response of the molecule to stimulus from the enzyme.

I determine that the vibrational modes of isomaltose that significantly contribute to stretching the glycosidic carbon–oxygen bond occur within the 21 to 35 THz (700 to 1,170 cm^{-1}) frequency bandwidth, and the dominant stretching modes are contained within 28 to 33 THz (930 to 1,100 cm^{-1}), which is in agreement with the experimental literature of polysaccharides. In the final chapter, I perform numerical simulations of the equations of motion to compute the

energy response spectrogram for a proxy substrate (benzene) under conditions that are informed by literature and the theoretical findings of this thesis. In lieu of anharmonic isomaltose data, I selected benzene as it is a small molecule with a high degree of symmetry which has several bond stretching modes within the aforementioned bandwidth. The results show that while the stimulus from water is insufficient, there are vibrational modes pertaining to glycosidic bond stretching that can be selectively excited to phase transition behaviour due to a reasonable stimulus from the supply of phonons from the MalL enzyme.

Preface

A Brief History

I wish to provide a brief history on the origins of this mathematical quantum biophysics work which I am reporting on for this thesis.

In 2017, Prof. Vic Arcus and his colleagues were having success in probing the temperature dependence of enzyme catalysis by applying an extension of the Eyring chemical reaction rate equation that incorporated heat capacity, giving rise to the Macromolecular Rate Theory (MMRT). The energy barrier that a molecule must overcome in order for a reaction to occur is given by the Gibbs free energy of activation, and depends on the difference in enthalpy and entropy between an initial state and the transition state midway through the reaction. In the traditional Eyring equations, the enthalpy and entropy of activation are taken to be constant with temperature, whereas in MMRT, these quantities are temperature dependent. The inclusion of an activation heat capacity predicted a temperature optima for enzyme catalysis without invoking protein denaturation. The MMRT equation was applied to a range enzymes and their mutants with great success. This led to V. Arcus to collaborate with colleagues of different fields of study, including soil scientists, microbiologists, climate scientists, and physicists.

A series of conversations began between V. Arcus and Assoc. Prof. Alistair & Prof. Moira Steyn-Ross, which led to the question: is there a phase-transition dynamic inherent in enzyme catalysis? A. & M. Steyn-Ross have experience in developing a theoretical thermodynamics phase transition analogy from their research on the effect of anaesthetics on the human cortex [1]. The transition of mental states from conscious-awareness to anaesthetic-induced unconsciousness does not occur smoothly with increased anaesthetic, but instead exhibits a disjointed, sudden change. In the course of developing a statistical mechanics formalism, it was discovered that a cortical entropy and "heat capacity" analogue could be extracted from the model, if there was a non-thermal cortical "temperature" specified, which was termed excitability.

A result of A. & M. Steyn-Ross' work at the turn of the millennium was to show that there could be three steady states for cortical firing rates, depending on the extent of anaesthetic; a high-firing state, an unstable mid-branch, and a low-firing state. The steady states were distributed in a cubic S-bend, which is a signature of a classical first-order phase transition. Hence the inspiration for investigating such a behaviour in enzyme catalysis. From their discussions, M. Steyn-Ross crafted a set of equations of motion for the exchange of energy throughout the molecule–enzyme complex based upon her previous work on nonlinear quantum optics, especially her Masters Thesis: "*Laser Excitation of Vibrational Modes of Molecules*" [2].

The opportunity of a Ph.D. project arose, and was offered to me which I accepted with gratitude and appreciation. The work presented for this thesis was an ambitious and exciting challenge: apply the mathematics of nonlinear quantum sound waves (anharmonic phonons) to the interaction of an enzyme with its target substrate molecule. The focus of study was on the hydrolysis of isomaltose into two molecules of glucose via the catalytic action of the enzyme MalL, which V. Arcus' research group had been investigating for some time.

I feel privileged to be part of such a multi-disciplinary research team, as it was a collaborative effort that created this research. It has been a core intention and hope of mine to assist in the building of a bridge that links the scientific comprehension of biological processes with the mathematical rigour of quantum mechanics, a bridge which necessitated a significant body of knowledge of computational science. I have drawn upon a large body of work from many areas of study in order to assemble this thesis, and due credit must be given to all of those that have made discoveries within their respective fields.

Acknowledgements

I wish to express my sincere appreciation for the series of events that led to the creation of this work, in particular the preliminary discussions of my supervisors: Vic Arcus, Alistair & Moira Steyn-Ross. No progress occurs in isolation; it is when people of different expertise collaborate that the world becomes more connected and new ideas can become manifest. I wish to acknowledge the contributions and help of:

Prof. Vic Arcus for his enthusiasm of scientific understanding and excited open-mindedness to engage in multi-disciplinary discussion, as well as providing a friendly, social atmosphere in the student research room. Through Vic, all things seem possible;

Prof. Moira Steyn-Ross for her mathematical insight of nonlinear quantum optics that led to the foundational theoretical framework of catalysis that began this work. It was her undergraduate course on modern physics, which I elected extraneously to my Engineering degree, that solidified my intention for mathematical physics research;

Assoc. Prof. Alistair Steyn-Ross for his sage advice on the arcane intricacies of coding in MATLAB and LATEX, and for being a whetstone that has sharpened my tools necessary for effective research and communication;

The Marsden Grant for the funding of this research;

Daniel Schipper for his preparation of the MalL enzyme data and for assistance in establishing molecular dynamics simulations, as well as his curiosity and engagement in my work and its future projections;

The IT support at Waikato University for providing me with my specific computational needs, which I then probed the upper limits of.

Mathematical quantum biophysics encapsulates the superposition of my love of exploring the mysteries of life, the universe and everything.

Dedication

I dedicate this thesis —

To my parents for their love and support throughout this long journey,
To the memory of my grandfather, Noel Newling, for the passion of exploration,
To all my family,

To my friends for their fascination, encouragement, and willingness to expand their minds,
To the immortal vibration that is Mem for the place to discuss quantum imaginary spacetime,
To Whangaparaoa and Raglan for the inspiration on the wave processes of Nature,
And to all of the trees that have now become books full of equations,

You have all been inseparably connected.

If a picture paints a thousand words,
and an equation draws a thousand pictures,
then to save writing a million words
I will be speaking in the language of mathematics.

Waves of Creation and Annihilation — Relaxation dynamics of the creation and annihilation operators in imaginary spacetime from the quantum anharmonic enzyme catalysis model. Time progresses to the right, the imaginary axis is vertical, and the real axis points towards the page. The evolution of sampled stimulus frequencies of the creation operator evolution are coloured such that higher frequencies are towards the blue, and the symmetric annihilation operator trajectories have inverted colours. The prominent blue trajectory has a highly turbulent initial excitation, **then after time, a consistent surf break peels on to the beach at sunset.**

Contents

List of Figures

Acronyms and Abbreviations

1D, 3D	One-dimensional, three-dimensional
CB	Combination band
CHO	Classical harmonic oscillator
DFT	Density functional theory
DNA	Deoxyribonucleic acid
DoS	Density of states
EoM	Equation of motion
EoMs	Equations of motion
FB	Fundamental band
IR	Infrared
LHS	Left-hand side
MalL	Oligo-1,6-glucosidase 1 (MalL; EC 3.2.1.10)
MD	Molecular dynamics
MMRT	Macromolecular rate theory
ND1P	Non-dimesionalised, one-parameter
NMA	Normal mode analysis
ODE	Ordinary differential equation
OT	Overtone
PDB	Protein database
QAO	Quantum anharmonic oscillator
QHO	Quantum harmonic oscillator
QME	Quantum master equation
RHS	Right-hand side
RS	Reaction state
SDI	Spectral density integral
SI	Système international
SMRT	Single mode relaxation time
SS	Steady state
TS	Transition state
TST	Transition state theory
VDR	Vibrational dissipation rate
ZPE	Zero point energy

Chapter 1

Introduction

1.1 Enzyme Catalysis

Molecules are collections of atoms that are bound together in a stable manner. When there is an addition or removal of one or more atoms, or even a change in the molecular structure, the process is called a chemical reaction and the resultant matter structures are different molecules. In this way, a chemical reaction is fundamentally a reorganisation of matter. There is a threshold of energy required for a reaction to occur, known as the activation barrier, the 'height' of which is related to the stability of the molecule. In order for a molecule to undergo a reaction with a large activation barrier, then there must be a large supply of energy to the molecule.

Life, as we know it, uses deoxyribonucleic acid (DNA) to store the construction blueprints and molecular recipes necessary for continuing itself. The resultant molecular structures are called proteins, and functional proteins that facilitate a chemical reaction in a target molecule (substrate) are called enzymes. The process of an enzyme performing a chemical reaction on a substrate is called *catalysis* — life's way of reorganising matter. The action of enzyme catalysis is to reduce the activation barrier for the chemical reaction to be performed, which can make a significant increase in the rate at which reactions occur. As an example, there can be a rate acceleration of 10^{18} for the division of a molecular carbon–oxygen bond in the presence of the appropriate enzyme, compared with immersion only in water. Enzyme catalysis allows for the reactions required to support complex life to be performed in a rapid, controlled, and selective manner. The specific details of the mechanism by which the massive rate increase is achieved is the subject of much current research.

There is a stark difference in the size of an enzyme to their target molecule. In most cases, the substrate is composed of several atoms, whereas the enzyme has thousands. Furthermore, enzymes demonstrate incredible specificity for the molecules that it catalyses. It is also known, there is an *active site* of the enzyme which houses the molecule during the reaction, and behaves in a 'lock-and-key' type mechanism. Transition State Theory (TST), established in 1935, posits that there is a transition state during the course of the reaction associated with the highest energy, and it is this state that determines the rate of a reaction [3]. The transition state of the molecule is extremely short lived, typically a few picoseconds which is the duration of a few bond vibrations. While the theory has been qualitatively and quantitatively useful, in order for a complete description for the rate of a reaction, the precise knowledge of the potential energy landscape must be obtained [4].

Recently, there has been a growing attention on the *vibratory* nature of enzymes in the context of catalysis [5–7]. There exists evidence from nuclear magnetic resonance studies for a network of enzyme vibrations that promote catalysis by enhancing the stability of the active site close the transition state [8], which is consistent with TST. In particular, the slower fluctuations in the vibrational network promote a higher rate of reaction. It has also been observed that the loops on the surface of various enzymes have shown a correlated motion with the active site environment, with some vibrations being on the time-scale of the reaction [9].

1.2 Catalytic Hydrolysis of Isomaltose by the MalL Enzyme

The enzyme-catalysed reaction of focus in this thesis is the cleavage of the glycosidic bond of an isomaltose sugar molecule into two glucose molecules (Fig. 1.1) by the enzyme oligo-1,6-glucosidase 1 (MalL; EC 3.2.1.10), which from now will be referred to as *MalL* (Fig. 1.2 and Fig. 1.3). One motivation for the choice of studying the enzyme MalL is that the break down of wood products into cellulose and then into glucose involves a lot of glycosidic bond breaking. However, the theory and coding work that I have developed could be extended to treat other catalytic reactions.

Isomaltose is a disaccharide sugar composed of two glucose molecules joined by a glycosidic link, shown in bold in Fig. 1.1. The action of MalL is to sever this connection via a hydrolysis reaction. The MalL enzyme features a "TIM barrel" domain where there are eight beta-strands forming a cylindrical structure that is surrounded by eight alpha-helices; the active site sits above the TIM barrel as can be seen in Fig. 1.2 and Fig. 1.3. The structuring of the active site and the surrounding protein in MalL is specialised to have a high degree of specificity for isomaltose.

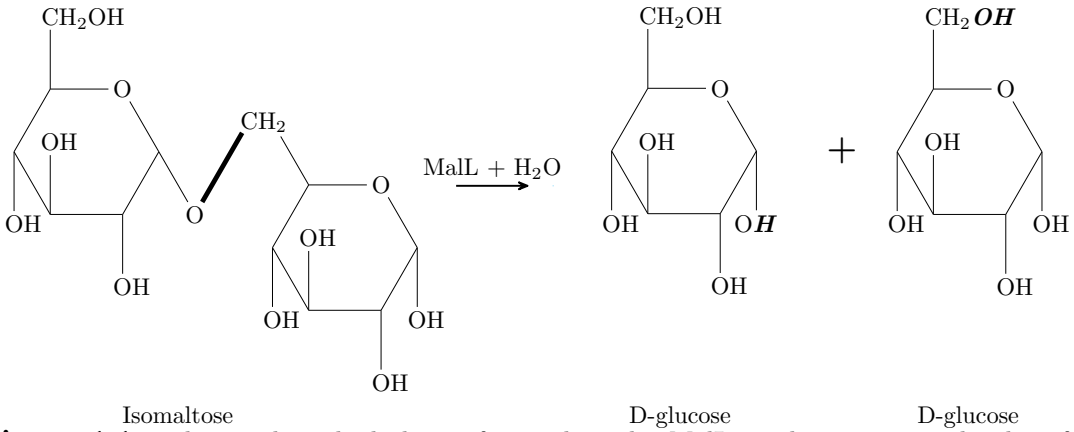

Figure 1.1: The catalytic hydrolysis of isomaltose by MalL producing two molecules of D-glucose. The thick line in isomaltose indicates the glycosidic bond that is broken during catalysis, and the bold italicised atoms in the D-glucose products indicates the atoms that have been added via hydrolysis

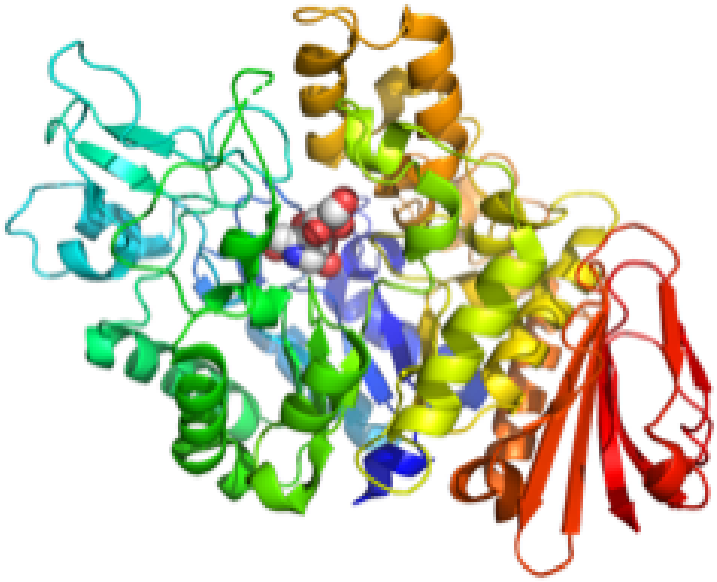

Figure 1.2: MalL cartoon representing the alpha-helices (coils) and beta-strands (arrows), where the colour varies from blue for the nitrogen terminus, to red for the oxygen terminus of the protein sequence. The isomaltose substrate is shown as a ball model in the active site.

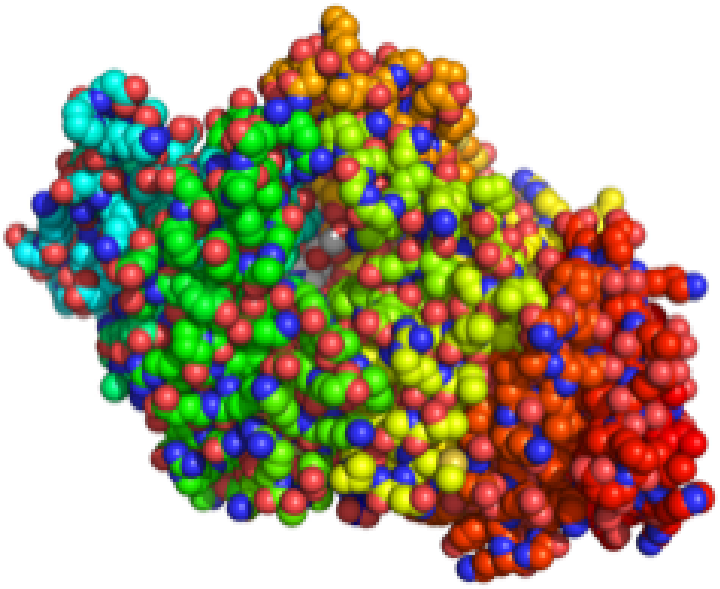

Figure 1.3: MalL showing the atoms as spheres: the carbon atoms are coloured sequentially the same as in Fig. 1.2, and the embedded red and blue spheres represent the oxygen and nitrogen atoms, respectively; hydrogen atoms are not shown. The isomaltose substrate can be seen embedded within the MalL active site.

1.3 Macromolecular Rate Theory

The core aspect of TST is that the rate of a chemical reaction, k, is dependent on temperature, T, and the energy of activation, E_a, which describes the height of the energy barrier that must be overcome for the reaction to progress. The theory was first formalised by Svante Arrhenius in 1889 [10] by the equation that is now named for him

$$k \;=\; A\;\exp\left(\frac{E_a}{RT}\right) \tag{1.1}$$

where $R = N_A\,k_B$ is the universal gas constant (the product of the Avogadro number, N_A, and the Boltzmann constant, k_B), exp is the exponential function, and A is a pre-exponential factor that carries dimensions of linear temporal frequency, $[\text{time}]^{-1}$. Further developments of chemical kinetics by Herny Eyring and others in 1935 [11] led to the more detailed description, named the Eyring equation

$$k \;=\; \kappa\,\frac{k_B T}{h}\;\exp\left(-\frac{\Delta G^{\ddagger}}{RT}\right) \tag{1.2}$$

where h is the Planck constant. Here, the activation energy is recognised to be the Gibbs free energy of activation, $\Delta G^{\ddagger}$, which is the difference between the free energy of the separate reactant molecules and the transition state complex (as introduced by René Marcelin in 1910). The pre-factor frequency has been determined to be a combination of universal constants and temperature, as well as a transmission coefficient, κ. The transmission coefficient is the ratio of molecules that pass over the barrier once the transition state is reached compared with those that relax back to reactants, and has a value of unity (one) if it is assumed that all molecules that reach the barrier cross over it. The Gibbs activation energy is a thermodynamic potential energy, which for a closed system at constant pressure and temperature, is

$$\Delta G^{\ddagger} \;=\; \Delta H^{\ddagger} \;-\; T\,\Delta S^{\ddagger} \tag{1.3}$$

showing a linear proportionality with temperature, with a value determined by the activation enthalpy ($\Delta H^{\ddagger}$) and entropy ($\Delta S^{\ddagger}$). Therefore, substitution of (1.3) into (1.2) shows that the TST rate equation can be expressed in terms of the activation enthalpy and entropy, as well as demonstrating a clear temperature dependence. While the Eyring rate equation has been extensively used to explore chemical reaction behaviour, it becomes inaccurate when applied to enzyme catalysis. Since it is assumed that the activation enthalpy and entropy are constant with temperature, the Gibbs free energy is linear with temperature. Because of this underlying assumption, any reduction of enzymatic rate that is observed by high temperature experiments is taken to be due to protein denaturation wherein the bulk tertiary structure of the enzyme is compromised and unravels.

A novel theory proposed by Vic Arcus and colleagues is the Macromolecular Rate Theory (MMRT) for enzyme catalysis [12, 13]. By allowing the activation enthalpy and entropy to be temperature dependent, then taking a first-order Taylor power expansion of the enthalpy and entropy in temperature about an arbitrary reference temperature, T_0, and using the results of

statistical mechanics, there is an extension to the Gibbs energy of activation given by

$$\Delta G^{\ddagger}_{T_0} \;=\; \left[\Delta H^{\ddagger}_{T_0} \;+\; (T \;-\; T_0)\;\Delta C^{\ddagger}_p\right] \;-\; T\;\left[\Delta S^{\ddagger}_{T_0} \;+\; \ln(T\,/\,T_0)\;\Delta C^{\ddagger}_p\right] \tag{1.4}$$

The square braces show the additional temperature-dependent terms for the activation enthalpy and entropy, respectively; these additional terms are due to an activation *heat capacity*, $\Delta C^{\ddagger}_p$. Equations of the form (1.4) are well-known and are routinely applied in the study of protein folding; the novel aspect is the application to enzyme catalysis. The difference in states is taken to be the difference in the enzyme–substrate complex and the transition state. Formally, heat capacity is the change in internal energy with temperature, and is a measure of the ability for a system to absorb energy, and it can be shown from thermodynamical arguments that it is due to fluctuations in enthalpy. Typical enzymes have a heat capacity, C_p, in the range of $25,000$ J.mol^{-1}.K^{-1}, with each amino acid contributing around 45 J.mol^{-1}.K^{-1}, whereas water under standard conditions has a heat capacity of 75 J.mol^{-1}.K^{-1}. Molecular dynamics simulations over long time-scales show that the low-frequency motions contribute an estimated 82% of C_p for globular proteins, with around 15% being due to the interactions with the solvent [14, 15].

Upon substitution of the extended expression of the Gibbs free energy of activation into the Eyring equation (1.2) leads to the MMRT equation

$$k \;=\; \frac{k_B T}{h}\;\exp\!\left(\;-\;\frac{1}{RT}\left[\Delta H^{\ddagger}_{T_0} \;+\; (T \;-\; T_0)\;\Delta C^{\ddagger}_p\right] \;+\; \frac{1}{R}\left[\Delta S^{\ddagger}_{T_0} \;+\; \ln\left(T\,/\,T_0\right)\;\Delta C^{\ddagger}_p\right]\right) \tag{1.5}$$

which has been shown to be a better fit for experimental enzymatic rates across a range of temperatures. Note that the transmission coefficient has been set to unity by assuming that the transition state always proceeds directly to products without reverting. The importance of $\Delta C^{\ddagger}_p$ for enzyme kinetics was first described by Hobbs et al. in 2013 [16], and since has been used to describe biological systems ranging from microorganism growth to entire ecosystems [17]. The significance of a variable heat capacity, C_p, in the context of protein stability has been known for over 40 years [18, 19], and $\Delta C^{\ddagger}_p$ has been well described for protein folding [20] where the value is typically negative due to the unfolded state having more flexibility compared to the compact transition state. Therefore a negative $\Delta C^{\ddagger}_p$ for catalysis implies that the transition state behaves in a more crystalline manner, wherein the fluctuations of enthalpy are reduced at the transition state. The significance of $\Delta C^{\ddagger}_p$ in MMRT is that the temperature dependence of catalysis is better described. MMRT exhibits an optimal temperature corresponding to the maximum rate, above which the rate drops, in the absence of denaturation. The optimal temperature is found by taking the derivative of (1.5) with temperature and then equating to zero, yielding

$$T_{\text{opt}} \;=\; \frac{T_0\;\Delta C^{\ddagger}_p \;-\; \Delta H^{\ddagger}_{T_0}}{\Delta C^{\ddagger}_p \;+\; R} \;\approx\; T_0 \;-\; \frac{\Delta H^{\ddagger}_{T_0}}{\Delta C^{\ddagger}_p} \tag{1.6}$$

The approximation is made by taking the absolute value of the activation heat capacity to be much larger the universal gas constant, $|\Delta C^{\ddagger}_p| \gg R$, and has been demonstrated for a range of enzymes and their mutants [21]. The concept of an optimal temperature for enzyme catalytic

rates is significant for biological adaptations in different climates, especially for extremophilic organisms [22, 23]. The experimental values for the activation heat capacity, $\Delta C_p^{\ddagger}$, from several sampled enzymes ranges between -12 and -1 kJ.mol^{-1}.K^{-1} [12, 13].

1.4 Molecular Bond Potential Energy and Dissociation Curve

Turning attention from the enzyme to the substrate molecule, I will introduce the mathematical descriptions that have been applied in the study of the breaking of a molecular bond. As an example, take isomaltose which is composed of two glucose molecules bridged via a carbon–oxygen bond called a glycosidic linkage. An isomaltose substrate in the presence of MalL undergoes enzymatic catalysis from which the products are two glucose molecules, meaning that the activation energy pertaining to the forces binding the two glucose molecules has been overcome, and they behave as individuals. Thus there is a connection with binding energy and the separation of the atoms. The plot of molecular energy as a function of inter–atomic distance is known as a *dissociation curve*, and is computed using molecular dynamics software. An initial mathematical description for the dissociation curve is the Lennard–Jones potential, first defined in 1924, and models soft attractive–repulsive molecular behaviour (van der Waals forces), hence describes only electronically neutral molecules [24]. Due to its long history, and simple analytic expression, the Lennard–Jones potential has been well researched despite its limitations [25].

A Density Functional Theory (DFT) is the mathematical computational engine used in molecular dynamics software to explore chemical phenomena, and the selection of which to use is non-trivial and an important aspect of simulating molecular behaviour. A DFT is a model approximation of molecular potential energy, and is used to calculate the force fields acting on a molecule. The first approximate DFT molecular model to include electronic structure theory is known as the Born–Oppenheimer model. The general procedure is to treat the nuclei as fixed point charges, and then to model the electron distribution via the Schrödinger equation. The Born–Oppenheimer approximation is valid in modelling many chemical processes due to the large difference in the mass- and time-scales of the behaviour of electrons and nuclei, but fails in non-adiabatic processes, and does not include zero-point energies.

A recent full-quantum formulation of constrained nuclear–electronic orbital density functional theory (cNEO-DFT) has been developed and implemented, which takes nucleon dynamics into account [26]. The NEO framework treats both electrons and nuclei simultaneously with molecular orbital theory, and in the last two decades, the quantum effects of both ground and excited molecular states have been studied [27]. In the cNEO-DFT model [28], the nuclear quantum effects can be incorporated at the cost of applying a constraint to the expectation value of the positions of key quantum nuclei. Molecular dynamics simulations using cNEO-DFT were performed on a range of diatomic molecules, involving hydrogen and deuterium, and the transition states of two hydrogen transfer reactions [26]. The dissociation curves were in good agreement with the Lennard–Jones potential, showing that the inclusion of nuclear quantum effects increases the equilibrium inter-atomic bond distance, and raises the minimum of molecular energy.

A direction for work outside the scope of this thesis would be to compute the dissociation curve for the carbon–oxygen glycosidic bond of isomaltose. Then the results of a QAO simulation can be converted into an animation of molecular behaviour from which the interatomic distance can be tracked with time and compared to the dissociation curve as a test of bond cleavage.

1.5 Vibrations in Matter — Sound, Molecular Normal Modes, Resonance, and Relaxation Oscillations

A cornerstone of physical models is the Classical Harmonic Oscillator (CHO), whose potential energy is parabolic and imparts a linear restoring force towards some equilibrium, resulting in a symmetric, sinusoidal oscillation. This dynamic has been equipped to model many systems, and most significantly for physical biochemistry, it has been applied to the vibratory behaviour of molecules. A stable molecule is taken to have an equilibrium geometry from which there are a set of oscillations that perturb the locations of the atomic nuclei in cyclic wave patterns. These oscillations are known as the molecular vibrational modes, whose frequencies and patterns of motion can be determined by a procedure known as Normal Mode Analysis (NMA). The method of NMA has become a commonly used tool for the investigations of molecular vibrations in the field of biochemical spectroscopy for small biomolecules, as well as large proteins and enzymes [29]. The methodology of obtaining the molecular vibrational modes will be a central theme of **Chapter 2**. In essence, NMA is a mathematical toolset derived from purely classical mechanics to calculate the frequencies of the available modes of the sinusoidal wave oscillations that the molecular structure supports; in a musical analogy, these are the notes that an instrument is able to play.

The underlying mathematics of NMA is the Christoffel equation, which was derived for describing the elastic waves in crystals via an elastic stress tensor [30]. Explicitly stated, NMA is the eigendecomposition of a system's Christoffel dynamical matrix, which is the mass-weighted curvature of potential energy of a molecule at its equilibrium geometry. The resultant eigenvalues are the (squares of) harmonic vibrational mode frequencies, and the associated eigenvector elements are (proportional to) the maximum atomic displacements during the oscillation. This provides sufficient information, along with the molecule's equilibrium geometry, to produce an animation of each vibrational mode available to a molecule. The Christoffel equation not only applies to molecular NMA, but is often used in materials science and engineering. The Christoffel equation in material science is a relation between the material stiffness tensor and the sound velocities in a solid [31], whose solutions are the dispersion relations of *sound waves*. There exists a rich depth of study with applications spanning a large variety of circumstances including, but not limited to, crystallography [32, 33], metallurgy and geology [34], seismology [35, 36], composites [37], ultrasonics [38], structural analysis [39], stress and elasticity [40], aerospace [41], anisotropy of the Earth [42], visualising acoustic waves in solids [31, 43], music [44], acoustic meta-materials [45], biomolecules and enzymes [46], essentially any vibrational system [47] — which, quantum mechanics shows is indeed *every* system.

A significant feature of classical molecular models is the oscillatory response of a molecule's energy to an oscillatory stimulus. A molecule in the presence of a solvent, enzyme or light will be perturbed into an excited state at a higher energy, while also dissipating its energy into the surrounding environment. This combined behaviour is known as a molecule's *relaxation oscillations*, and in many cases can be measured experimentally in order to determine the physical parameters of a system. A significant example is the spin–lattice (longitudinal) and spin–spin (transverse) relaxation oscillations of magnetically excited matter that are measured during nuclear magnetic resonance spectroscopy to determine atomic structures, and magnetic resonance imaging where the differences in the measured relaxation rates of the two dissipative processes enable 3D imagining within objects, including for medical diagnosis [48]. New Zealander, Sir Paul Callaghan, and his research group specialised in developing NMR methodologies for the study of molecular dynamics and molecular organisation in complex fluids, soft matter and porous materials [49] based upon experimentally determined relaxation oscillations.

1.6 Anharmonicity and Nonlinear Dynamics

The vibrations so far discussed are known as harmonic oscillations, which are characterised by a sinusoidal waveform and are treated as independent of each other; the vibrational model can be extended by the inclusion of nonlinear *anharmonics*. A useful musical metaphor for the difference between harmonic and *anharmonic* oscillators is to compare a digital keyboard and a grand piano. When a note (vibrational mode) is played on a keyboard it rings out in pure isolation; when a key is pressed on a piano, the vibration on its string causes all of the other strings to also vibrate to a varying amount. This is why a grand piano is said to bring a deep, resonant texture to the music — each note played is actually a synergistic harmony of *all* of the notes acting together in a dynamic resonance. It is this dynamism that necessitates the extension of the harmonic models into the nonlinear *anharmonics*.

A dynamical system is said to be linear if the change in the system's output is proportional to its input, as is the case with harmonic oscillators due to the linear restoring force. A dynamical system is nonlinear if the output is not directly proportional to its input, which indeed is almost all physical systems. In this thesis, I will model molecular response as governed by nonlinear differential equations which in general only have exact analytic solutions in very restrictive circumstances. However, the anharmonic molecular vibrational mode steady states and their stability can be obtained exactly.

An important nonlinear oscillator equation of motion is known as the Duffing equation, which was originally developed for modelling the self-oscillations of speed regulators in combustion engines [50], and have since been applied to model many different oscillatory physical systems with nonlinear stiffness and damping. Some applications include softening/hardening springs, large-amplitude beam deflections, electrical circuits, and the motion of a pendulum [51]. The Duffing equation can be transformed in to the form of a van der Pol oscillator, which was developed by van der Pol in 1920 to model the relaxation oscillations in electrical circuits using vacuum tubes. When the circuits are driven near the limit cycle, the driving signal pulls the current with it, resulting in a process called *entrainment* [52]. Recently, a quantum analogue

of the van der Pol equation (using the Lindbladian formalism [53, 54]), has been employed to study quantum *synchronisation*, [55]: the frequency entrainment of relaxation oscillations due to nonlinearity.

1.7 Phonons — The Quantum Treatment for Vibrations in Matter

The foundation of deriving a system's Equation of Motion (EoM) in both classical and quantum mechanical frameworks is by specifying the geometry of the potential energy landscape that the system experiences. In classical mechanics, the EoM is derived via the principal of least action applied to the difference in kinetic and potential energies, resulting in the Euler–Lagrange equation; the state of the classical system is expressed by its position, velocity, and total energy. Simple harmonic oscillating motion describes a *wave*, and so the dynamics would be better understood by using a wave-based approach; which is the speciality of the quantum approach. In quantum mechanics, the summation of the kinetic and potential energies is called the Hamiltonian, whose expectation value is the total energy of the system. The Quantum Master Equation (QME) is used to derive the EoM for the system, and the position and velocity coordinates are transformed into annihilation and creation operators, with their product being the number operator. At the heart of the quantum mathematical toolset is a pure wave oscillation, with the term 'quantum' denoting that we are observing an isolated individual excitation of a collective field; an analogy is to consider the surface of the ocean as being composed as the summation (superposition) of all wave-processes of the water. A quantum of vibration of the electromagnetic field (light) is called a photon, and a quantum of lattice vibration within matter (sound) is called a phonon [56–58]. How light and matter interact, in the language of quantum mechanics, is the exchange of photons and phonons.

The evolution of a quantum state in time is governed by the Schrödinger equation [59], which is a linear partial differential equation stating that a quantum state, $|\psi\rangle$, evolves in time due to the Hamiltonian, $\mathcal{H}$, according to

$$i\hbar \frac{\partial}{\partial t} |\psi\rangle \;=\; \mathcal{H} \, |\psi\rangle \tag{1.7}$$

where $\hbar = h/2\pi$ is the reduced Planck constant, $i = \sqrt{-1}$, is the imaginary unit, and $\frac{\partial}{\partial t}$ is the partial derivative with respect to time. If the Hamiltonian is explicitly independent on time, then the evolution of an initial state, $|\psi(0)\rangle$, to a state translated further in time, $|\psi(t)\rangle$, can be expressed as

$$|\psi(t)\rangle \;=\; \exp\left(\frac{\mathcal{H}\, t}{i\hbar}\right) \, |\psi(0)\rangle \;=\; U(t) \, |\psi(0)\rangle \tag{1.8}$$

where U is called the unitary time translation operator [60]. Therefore, by specifying the Hamiltonian, in particular the potential energy, the evolution of state for a given system is tracked by the Schrödinger equation. For the purposes of catalysis, the total enzymatic system can be split into a description of a molecular system (substrate and enzyme) embedded within a thermal environment from which the evolution of the reduced system is tracked by a QME (**Appendix A**). The free EoM for a system's quantum state is derived by the von Neumann QME, and the extension to accommodate interactions and dissipative dynamics lead to the Lindbladian QME,

which is also known as the quantum Liouvillian, or Gorini–Kossakowski–Sudarshan–Lindblad equation [53, 54].

In particle physics, there are two classes of subatomic particles: bosons and fermions [61]. Photons and phonons are both bosons, while fermions include quarks, baryons, and many atoms and nuclei [62]. A fermion obeys the Pauli exclusion principal meaning that it is either present (occupied state) or absent (unoccupied state), whereas a boson can have repeated excitations in a single state, with the lowest being called the ground state [63]. The phonon creation operator acts to add one phonon to the vibrational state, the annihilation operator removes one phonon; the number operator gives the number of phonons in that state. The EoM is derived from the Hamiltonian that has been transformed to be in terms of the number operator, which shows that the phonon number operator gives the energy *level* for the vibration. Therefore, the creation operator raises the energy level by one, and the annihilation operator lowers the energy level by one. The vibrational energy is given by the expectation value of the Hamiltonian, and is a linear function of the expectation value of the phonon number in the harmonic case.

Classical mechanics involves the precise tracking of the position and velocity of an object, while quantum mechanics tracks the probabilistic *expectation value* of where it is likely to be and how fast it could be moving. While this may seem to severely increase the complexity, all processes in reality occur with uncertainty and with a range of possibilities. If you are standing on the beach and ask 'Where is the wave?', there are uncountably infinite many viable answers with some being considered more accurate than others — pointing towards the ocean is a good start, but pointing upwards seems to be a wrong answer. Furthermore, the answers that are considered accurate at one instance will become inaccurate over time unless they are updated.

The concept of a probabilistic distribution is central to quantum mechanics, whose foundational operator formalisms are collectively known as the uncertainty relations. The most famous relation is the Heisenberg uncertainty relation first introduced in 1927 [64], which states that the more precisely the position of some state that is observed, the less accurately its momentum can be predicted from an initial condition, and there is a fundamental lower limit to the product of their accuracies as given by the Planck constant. Another uncertainty relation is between time and frequency (or energy), and poses a limit to the precision on which a signal (for example, a radio broadcast) can be analysed.

1.8 Quantum Thermodynamics

The quantum thermodynamics of a single phonon shows that its heat capacity is the temperature derivative of the total energy (expectation value of the Hamiltonian), and the heat capacity for the entire molecule is the summation of all phonons in each vibrational mode available to the molecule [56, 65]. From the statistical mechanics considerations used in the derivation of MMRT (1.5), the heat capacity is the temperature derivative of the internal energy and can be expressed by the fluctuations of enthalpy. In quantum mechanics the internal energy is due to the phonons, and the heat capacity is a measure of the ability for each phonon to absorb thermal energy [66].

The heat capacity of a phonon is the derivative of expectation energy with temperature

$$C_{\mathrm{p}} \equiv \frac{\partial}{\partial T} \langle \mathcal{H} \rangle \tag{1.9}$$

where $\mathcal{H}$ is the Hamiltonian (1.7), the angle braces denote the expectation value, and the energy of a phonon is the expectation value of the Hamiltonian, $E = \langle \mathcal{H} \rangle$. The expressions for phonon heat capacity are well defined for a purely harmonic model at thermal equilibrium. Common models used to calculate the heat capacity of solids are the Debye model (1912) [67] and Einstein photoelectric (1907) model [56], wherein a crystalline solid is assumed to contain many independent 3D quantum harmonic oscillators of the same frequency [34,57]. These models were improvements to Dulong–Petit law of the early 1800s which take the heat capacity of one mole of a solid crystalline substance to have a value of $3R$, where R is the universal gas constant, or in terms of the number of atoms, N, as

$$C_{\mathrm{DP}} = 3\,N\,k_B \tag{1.10}$$

A major limitation is that the result is not temperature-dependent [68]. One isolated oscillator of an Einstein solid has heat capacity

$$C_{\mathrm{ein}} = k_B \left(\frac{\hbar\omega}{2\,k_B T} \right)^2 \operatorname{csch}^2 \left(\frac{\hbar\omega}{2\,k_B T} \right) \tag{1.11}$$

where, $\operatorname{csch}(x) = 1/\sinh(x)$, is the hyperbolic cosecant function, and ω is the oscillation frequency of the phonon. This result is also obtained in the quantum harmonic model (**Chapter 4**), which will be used to compute the heat capacity of the substrate and enzyme. The Debye model is a solid-state equivalence to Planck's law of black body radiation, wherein a boson is confined within a volume of space producing a resonance cavity [47, 65]. The heat capacity of a Debye solid is expressed as an integral equation

$$C_{\mathrm{D}} = 9\,N\,k_B \left(\frac{T}{T_D} \right)^3 \int_0^{T_D/T} dx\, \frac{e^x\, x^4}{(e^x - 1)^2} \tag{1.12}$$

where T_D is called the Debye temperature defined by $T_D \equiv \hbar\omega/k_B$, and represents the temperature of a crystal's highest frequency normal mode vibration (equivalently, the highest temperature of single phonon). The Debye heat capacity can be solved approximately at different temperature regimes: for low temperatures, $T \ll T_D$, the integral can be solved via the Γ-function by taking $T_D/T \to \infty$, to give the Debye T^3 law; and for high temperatures the Dulong–Petit heat capacity (1.10) is recovered. The Debye model is the most accurate of the three and is in agreement with low-temperature experiments where the Einstein model fails. While the Debye model is well-understood and used in the study of solids, gasses, and more recently liquids [69], the concept of a fixed volume for an individual molecule immersed in a solvent is poorly defined since it is a vibratory structure of bound atoms. Moreover, these models do not include contributions from the electrons (non-negligible in conductors and semiconductors), and does not account for *anharmonicity*.

1.9 Anharmonic Phonon Exchange

In this thesis, the molecule–enzyme interaction is modelled in the quantum mechanical treatment by adding an interaction term into the total Hamiltonian. For the harmonic case, the molecule and enzyme exchange one phonon at a time, and each must be at exactly the same frequency to satisfy the resonance conditions. The inclusion of first-order anharmonics allows for a two-for-one exchange of phonons and hence an array of interesting phenomena related to chaos, nonlinearity, and stochastic behaviour [70]. Higher-order anharmonic processes have more phonons participating in each interaction, and are outside the scope of this thesis. There is a rich history on exploring the interaction behaviour of quantum systems [53, 56, 71, 72]. In modern parlance, a harmonic state experiences a parabolic potential energy, and the inclusion of a driving force acts to coherently *squeeze* and *displace* the harmonic state by altering the potential steepness and displacing the geometry corresponding to its energy minima, respectively. The EoM solutions therefore track the evolution of a *coherent* quantum state from an out-of-equilibrium excited state into a steady state due to a thermal equilibrium and an offset due to external stimulus (for example, an enzyme, solvent or light).

There exists a myriad of approaches for modelling anharmonic phonon exchange. The simplest model is that of an infinite linear chain of the same atom, and a common approximation made for modern semiconductors components is to assume there is a unit lattice cell that tiles space infinitely to produce an infinite crystal [73], in a similar way to the infinite elastic material assumed in the initial sound wave models. Since I am modelling individual biomolecules, I cannot make the infinite crystal assumption; however, there may be an experimental method for analysing sufficiently large crystals of biomolecules in order to connect the continuum approximation with experimentally determined dispersion relations [43].

One of the main physical parameters for the molecular vibrational modes is the Vibrational Dissipation Rate (VDR), whose inverse is the vibrational lifetime. For a harmonic free molecule, there is no exchange of energy with any other system and as such its dynamics persist indefinitely. The inclusion of anharmonics in the free molecule model allows for a dissipation pathway from one mode to all of the others with distinct values that I call the intramolecular VDR. This is analogous to playing one sustained note on a grand piano, which then transmits energy to all other strings, including itself, to varying amounts. By immersing the molecule into an environment, the molecule is able to exchange energy with its surroundings up to a thermal equilibrium, producing another dissipation pathway that I call the environmental VDR, and represents the dissipative interaction of the molecule into the solvent or enzyme. The total VDR for a molecular vibrational mode is summation of the intramolecular and environmental VDRs.

Since the VDR is a core parameter of quantum molecular modelling, there has been extensive work performed to determine these values experimentally for various molecular systems including proteins [72,74,75]. In general, the transition rate for a quantum state transforming into another is described by Fermi's Golden Rule [76, 77]. The Golden Rule was derived for describing the dispersions of atomic energy via emission and absorption of radiation (photons), and has since been adapted to account for the emission, absorption and scattering of phonons, including large

biological molecules [74, 78]. The intramolecular VDR for a molecule at thermal equilibrium is given by the Maradudin–Fein formula [71, 79], which is dependent only on atomic properties, NMA, and the third spatial derivative of potential energy [66], and has been used in the study of glass and proteins [75].

1.10 SI Unit Prefixes

I will be using the modern form of the metric system, *Systèm International* (SI) unit basis, throughout this thesis. The SI units are defined for human-scaled dynamics, and so the values for the various physical parameters in molecular dynamics are minuscule or enormous, thus I will be making use of the prefix notation. I list the SI prefixes below as a reference guide.

SI prefix values

Prefix	Symbol	Value
yotta	Y	10^{+24}
zetta	Z	10^{+21}
exa	E	10^{+18}
peta	P	10^{+15}
tera	T	10^{+12}
giga	G	10^{+9}
mega	M	10^{+6}
kilo	k	10^{+3}
hecto	h	100
deca	da	10
unity		1
deci	d	0.1
centi	c	0.01
milli	m	10^{-3}
micro	μ	10^{-6}
nano	n	10^{-9}
pico	p	10^{-12}
femto	f	10^{-15}
atto	a	10^{-18}
zepto	z	10^{-21}
yocto	y	10^{-24}

1.11 Implemented Software

All of my original coding work was constructed in MATLAB [80] including the automated scripts to extract data from other software. The Molecular Dynamics (MD) data is computed by the GAUSSIAN 09 [81] NMA and simulated anharmonic infrared (IR) spectroscopy packages, and the enzyme NMA was performed in GROMACS [82]. The choice of GAUSSIAN 09 is that it is able to compute the anharmonic frequencies for small molecule, whereas GROMACS is suited for the harmonic treatment of large molecules. Glucose and isomaltose are described with the quantum harmonic molecular models, and benzene is used in the quantum anharmonic model as a proxy substrate in the subsequent chapters. In order to make a meaningful discussion of the catalytic action of MalL, the anharmonic frequencies of isomaltose must be computed, and would be a vital aspect of continuing the work presented in this thesis. If the enzyme catalysed

reaction of study were to be for smaller substrate molecules, for which the anharmonic data could be obtained, then the work in this thesis can be utilised. I built the digital molecules in GaussView [83] and Avogadro [84], and then I performed harmonic NMA for benzene, glucose and isomaltose in Gaussian 09, as well as anharmonic MD for benzene. I have built scripts in Matlab that use open-source packages to read-in data from Gaussian 09 and Gromacs where possible (described in **Chapter 2**).

1.12 Mathematical Model Building Procedure

The extension of the Classical Harmonic Oscillator (CHO) molecule model into the quantum operator algebra will in this work be called the Quantum Harmonic Oscillator (QHO) model. The extension of the QHO model to include anharmonics is called the Quantum Anharmonic Oscillator (QAO), and is the main theoretical model that will be described. The free behaviour of the molecule is the oscillatory motion in the absence of any other system, and is described by the free QME. The molecule immersed in a dissipative environment is modelled by extending the QME to include Lindbladian dissipation terms which facilitate an exchange of phonons between a system and a thermal reservoir [53]. The interaction between the molecule and its environment is assumed to be a Markovian process, meaning that the reservoir retains no memory of an interaction, and continually supplies the molecule with the same stimulus. The solutions to the EoMs of this model are then able to capture the response of a molecule due to stimulus from either the enzyme or solvent. The stimuli are treated as distinct cases since the substrate is surrounded by the enzyme during catalysis, and it is assumed that there is no direct influence of the solvent to the substrate in the enzyme-stimulated case. The environmental interactions are derived within the framework of quantum mechanics, then a semi-classical approximation is imposed to allow the EoM to be numerically solvable.

The general procedure for the preparation and analysis of a quantum mathematical model is informed by [53, 56, 58] and follows

- Define the Hamiltonian operator of the system
- Define the QME which describes how the quantum state evolves with time
- Insert the Hamiltonian into the QME to obtain the EoMs for the evolutions of the substrate's quantum state
- Perform steady state and stability analysis on the EoMs
- Specify the material parameters of the substrate, enzyme and solvent
- Simulate the EoMs

These resultant EoMs are first-order ordinary differential equations, and so the tools required for the exploration of the model dynamics are well established. The analytic derivation of exact expressions for the system steady states and their (linearised) stability are determined for the QHO and QAO molecular models. The solutions to the EoMs are the evolutions of the expectation values for the annihilation, creation, and number operators; the evolution of the energy is found by substitution of the number operator EoM solution into the expectation value of the Hamiltonian. Of most interest for catalysis is how the molecular vibrational modes respond to

the presence of an enzyme, and how the superposed molecular energy spectrum changes with time. Heat capacity can be calculated from the expectation value of energy, and the thermodynamics of phonons will be essential in connecting quantum theory with experiment and MMRT.

The behaviour for the catalytic models can be categorised under four distinct cases:

- **Free**: an isolated molecule in a void that does not interact with anything and therefore retains a constant value of energy
- **Relaxing**: a molecule is immersed in a dissipative environment, and after some time it will relax to a static equilibrium
- **Stimulated**: a molecule that interacts with an external stimulus, but does not dissipate energy, and hence does not relax
- **Actual**: a molecule that is stimulated *and* is immersed in a dissipative environment.

I will describe these cases for the QHO and QAO models in **Chapter 3** and **Chapter 4**, respectively.

1.13 Aims and Thesis Structure

The overarching aim of this thesis is to explore the hypothesis that there exists a phase transition dynamic inherent to enzyme catalysis. This work is motivated by the experiments conducted by Vic Arcus and his collaborators that led to the MMRT equation which features an activation heat capacity, $\Delta C_{\mathrm{p}}^{\ddagger} \neq 0$, to account for non-Arrhenius enzyme rates . In a recent paper [85], it is proposed that enzymes exhibit something akin to a finite-size phase transition due to cooperative conformational transitions that restricts the conformational space of the enzyme along the reaction coordinate. The resultant description for $\Delta C_{\mathrm{p}}^{\ddagger}$ has sigmoidal shape with temperature, which suggests an analogy to a 2^{nd} order phase transition.

To explore the claim for the existence of an enzymatic phase transition, I construct a theoretical description and computational simulation of a substrate molecule's response to an enzyme in terms of phonon energy and phonon heat capacity, as well as deriving an analytic expression for the minimum stimulus requirement for a phase transition. The mathematical theory is based upon molecular vibrational modes which follows on from the work of Narducci [79] on the response of an anharmonic molecule to a laser, anharmonic molecular dissipation [53], as well as the modern treatment of the intramolecular vibrational relaxation in proteins [86]. I obtain data from computational MD NMA and anharmonic IR spectroscopy experiments. The resultant model describes the dissipative response of a substrate model to an enzyme that behaves as a 'phonon laser'.

The description of a conformational change via enzyme catalysis is an important yet not satisfactorily solved problem. The description of NMA and anharmonic vibrations have only relatively recently been equipped to assist in answering the many questions arising from the biophysics of enzymes, and its future appears bright [87].

The chapters are structured by the progression of mathematical complexity used for modelling molecular vibrations. The insights and intuition gained by progressing through the previous chapters serve as a foundation for understanding the results obtained from the full QAO model for the interaction of a molecule and enzyme during catalysis. Firstly in **Chapter 2**, the well-known classical harmonic oscillator (CHO) model is detailed in the context of molecular motion, leading to what is known as normal mode analysis (NMA). I then demonstrate the functionality of my coding work to extract the simulated molecular dynamics data from Gaussian 09 and Gromacs, which I use to construct animations of the molecular vibrational modes, and determine the vibrational modes that significantly stretch the glycosidic carbon–oxygen bond of isomaltose. In **Chapter 3**, I introduce the relevant mathematical tools of quantum mechanics, before I describe the quantum harmonic oscillator (QHO) molecular model. I derive the EoMs, their steady states, and exact solution. I then use the solutions to the EoMs for isomaltose in the presence of MalL to construct the response spectrograms for molecular energy and heat capacity. **Chapter 4** encapsulates the bulk of my original theoretical work, wherein I derive and explore the quantum anharmonic oscillator (QAO) catalytic model. I derive the QAO steady states, and perform a linear stability analysis from which I elucidate the saddle-node bifurcation points that are a signature of a first-order phase transition. I derive an expression for the minimum stimulus required for each vibrational mode to exhibit a phase transition, and an approximation for the phase transition boundary at higher stimulus. In **Chapter 5**, I will simulate the response of a proxy substrate (benzene) via the Matlab software package that I have built to numerically solve the QAO model EoMs. I then draw comparisons between the behaviour of the proxy substrate in a water bath, compared to in the presence of MalL. I summarise the core results in **Chapter 6**, and I will explain the potential future developments, model limitations, topics outside the scope of this work, and pose ideas for experimental means to determine the various parameters required for the QAO model.

1.14 Original Contributions

My original contributions are as follows:

- In general, unless otherwise stated, all computational coding work and their resultant images are my own work
- I applied the quantum mechanical framework of anharmonic phonon exchange to enzyme catalysis
- Construction of an automated MATLAB package to extract harmonic (normal mode) and anharmonic simulated molecular dynamics data from GAUSSIAN 09 and GROMACS
- Construction of an automated MATLAB package to produce animations of molecular harmonic normal modes
- Construction of an automated MATLAB package for the simulation of the harmonic and anharmonic equations of motion of the quantum state for any molecule in the presence of any stimulus
- A methodology for determining the dominant vibrational modes participating in a chemical reaction
- A map for the viable anharmonic interactions of a molecule and enzyme
- Analytic expressions for the minimum stimulus and critical bifurcation point for a vibrational mode to experience a phase transition dynamic
- The derivation of a non-dimensionalised expression with one parameter for the quantum anharmonic model
- An expression for the excitation heat capacity for the QHO molecules
- A simplified expression and codified implementation for the stimulus from an enzyme or solvent to a molecule
- A comparative simulation of a proxy substrate in water and bound to an enzyme, which shows that phase transition behaviour is only present in the enzyme-stimulated case

Chapter 2

Classical Harmonic Molecular Vibrations

In this chapter, I introduce the conventional vibrational analysis of molecules. I then demonstrate the coding work that I have built in Matlab to read–in and visualise the raw data calculated by running an MD simulation using the GAUSSIAN 09 software, and are performed by the MATLAB script: `Molecular_Harmonic_Vibrations_Pack`.

2.1 Vibrational Analysis of Biological Molecules

Vibrational Normal Mode Analysis (NMA) is one of the major simulation techniques used to probe the motions of biological molecules [88–92]. The molecule is modelled in the free classical harmonic oscillator (CHO) framework, wherein the potential energy of a molecule is treated as parabolic, and there is no dissipation or interaction with an environment. For the free CHO molecule, the deviations of the atomic nuclei from equilibrium, $\Delta x(t) = x(t) - x_{\text{eqm}}$, at a time, t, are restricted to sinusoidal oscillations of the general form

$$\Delta x(t) \;=\; A\;\cos(\omega\, t \;-\; \phi) \tag{2.1}$$

for amplitude envelope, A, oscillation frequency ω (period, $2\pi/\omega$), and an initial phase shift angle, ϕ. Thus the NMA model accounts for the dynamically independent (geometrically orthogonal) patterns of nuclei undulations known as vibrational modes. This allows for the separation of the high-frequency motions of the outer hydrogen atoms and the low-frequency swaying or bending motions of the entire molecule, and all those in between. This powerful technique allows for the correspondence of an experimentally determined absorbance peak to an actual vibratory motion of the molecule.

The motion of each atom in each spatial coordinate is *independent* of all others, thus a molecule consisting of N many atoms has a total of $3N$ degrees of freedom. The NMA method is performed by making a change of coordinate bases from a description of the the motions of atoms in 3D space into a basis set of *vibrational modes*. Because each coordinate of a basis set is linearly independent (orthogonal), they are described in algebraic terminology as being *normal to* each other, hence the 'normal' in NMA. Furthermore, since a basis is a linearly independent spanning set of coordinate vectors covering a vector space, whose number of elements gives the dimension of the space; an equivalent basis set for a given space will have the same dimensionality. For the molecule model, the vector space has $3N$ dimensions which can be described either by the positions of atomic nuclei, or by the molecular vibrational modes. The convention of NMA is to remove the (up to six) modes that are associated with translational and rotational

behaviours [93] (a further discussion is provided in **§ 2.4.2**). Thus the set of normal modes do not produce a spanning set for the molecule; hence I use the terminology 'vibrational mode', a subset of which are the 'normal modes'. A molecule of glucose has 24 atoms and so has 72 degrees of freedom; after the change of coordinate basis, there will be 72 vibrational modes, each with a distinct oscillation frequency and undulation pattern, 66 of which are the normal modes. Isomaltose is composed of 42 atoms, and therefore supports 126 vibrational modes, 120 of which are the normal modes. The highest frequency modes have an oscillation rate up to 1.2×10^{14} Hz (120 terahertz), or approximately 4,000 cm^{-1} in the spectroscopy wavenumber unit, $\omega/(2\pi c)$, where c is the speed of light in a vacuum.

The lowest frequency modes are the undulations of the entire molecule, the middle range includes the bond stretches of a few atoms such as the glycosidic link, and the highest frequency modes pertain to the rapid oscillations of hydrogen. Since each vibrational mode has a different natural oscillation frequency, these can be thought of as notes on a keyboard. A typical piano has 88 keys spanning seven octaves from A0 (27.5 Hz) to C8 (4,186 Hz). The note that is one octave above A0 is A1 and has double the frequency (55 Hz), the note ten octaves above A0 is A10 and has frequency found by ten successive doublings of the fundamental, $2^{10} \times (27.5 \text{ Hz}) = 28,160$ Hz. Whereas the highest 'note' available to glucose is the motion of the hydrogen at the end of the methanol group and has a natural fundamental frequency of 1.18×10^{14} Hz. The natural frequency of this hydrogen atom oscillation is 42 *octaves* above the musical note A0. Phonons in solids include acoustic sound waves, and so the reference to music is perhaps more of an equivalence than analogous. The natural frequencies of the hydrogen oscillations are on the order of *visible light*, which is contained within the bandwidth of 4.0×10^{14} Hz (infrared) to 8.0×10^{14} Hz (ultraviolet) for oscillations of the electromagnetic field. The frequency of the higher octave (overtone) for the hydrogen oscillations is around 2.3×10^{14} Hz, which is half of the frequency of red light (4.6×10^{14} Hz), and higher octaves of the vibrational modes will occupy the same bandwidth as visible light. In the quantum theory of phonons, these higher octaves are due to multi-phonon self-interactions [56], and if they pertain to optical phonons, they do couple to the electromagnetic field [53, 58].

The computational results of NMA do have a connection to the experimental techniques of infrared (IR) and Raman spectroscopy, providing predictions for the functional motions of proteins and other biological molecules [94]. In NMA studies, it is assumed that the vibrational modes with the lowest oscillation frequency that involve the entire molecule are the ones that are functionally relevant to catalysis [90, 94]. This assumption arises from the comparisons of NMA and experimental data with transitions derived from multiple X-ray conformations that do suggest that the low-frequency modes are often functionally relevant [46].

The harmonic approximation underlying the NMA method assumes a single minimum of potential energy. There exists abundant evidence, both experimental [95] and computational [96, 97], that the harmonic approximation breaks down spectacularly for proteins at biological temperatures, where the molecular state visits multiple energy minima, crossing energy barriers of various heights; these are the *anharmonic* contributions. The harmonic model however is sufficient to produce rudimentary dynamical animations of molecular motion, and determine

which vibrational modes stretch the glycosidic carbon–oxygen bond. This will be the direction and end goal of this chapter. The broader intention is to develop the full quantum anharmonic oscillator model of catalysis, which will mark the culmination of this thesis. The next step down the development corridor is to demonstrate the molecular vibrational modes that I have obtained by MD experiments performed in Gaussian 09, as well as to discuss the material parameters that characterise and inform the study of molecular behaviour.

2.2 Molecular Vibrational Normal Mode Analysis

In this section, I will demonstrate the underlying mathematics for the vibrational NMA that is performed within the Gaussian 09 software package [98] and detailed in their documentation [99]. The NMA for enzymes is performed by the Gromacs software as it is better suited for large atomic structures [82,100]. At the conclusion of this chapter, the functionality of the codes that I have built in Matlab, as well as the underlying mathematical machinery and physical insight will be developed sufficiently to create animations of *any* atomic structure's fundamental vibrations (up to several thousand atoms with current computational limitations on size).

2.2.1 Building a Digital Molecule

It is the potential energy of the molecule that determines the vibrational modes; however, obtaining the true potential energy is not possible using current experimental and computational techniques. An harmonic approximation takes the potential energy to be a parabolic polynomial given by a second-order Taylor power series expansion, $V_{\mathrm{CHO}} = V_0 + V_1 + V_2$. The constant term, V_0, represents the minimum of energy, the linear term, V_1, describes the forces (potential energy gradients) which are taken to be zero at equilibrium, and the quadratic term, V_2, describes the curvature. Since the constant term does not affect the dynamics, the harmonic assumption takes the potential energy to be entirely captured by the parabolic contributions, $V_{\mathrm{CHO}} = V_2$.

The quadratic potential coefficients are computed by specifying an appropriate molecular potential energy functional (also known as the force field or density functional theory) and then running the NMA. The selection of the potential energy is a non-trivial aspect of computational MD [101].

The Gaussian 09 package can perform computational MD experiments using various theoretical treatments of the molecule, each with their own specialisations and limitations [99]. There are two central options when specifying the level of theory for MD: the treatment of the molecular forces and the basis set for the atomic orbitals. Some of choices for the molecular forces include classical molecular mechanics (for example AMBER [102] and CHARMM [103]), self-consistent fields to approximate the stationary Schrödinger wavefunction equation (Hartree-Fock [104]), and density functional theory (notably the B3LYP hybrid functional which serves as a default option). The description of the orbitals are of the Slater-type [105], or the eponymous Gaussian orbitals which accelerates the calculation of the molecular electronic wavefunction structure [106].

I have chosen the WB97X-D hybrid functional [107] for the harmonic MD simulation of glucose and isomaltose since it has a better ability to handle weak interactions and dispersion effects

when compared to B3LYP. I used the Pople 6-31G split-valence basis set [108] for all MD simulations, which utilises six primitive Gaussian distributions to compose each core atomic orbital basis function, and the valence orbitals are composed of two basis functions each. Performing NMA is possible using most theories, however when including anharmonics, the viable options are more restricted as it is common to experience convergence errors which will prematurely terminate the simulation. The anharmonic MD data for benzene in **Chapters 4 & 5** used the restricted Hartree-Fock method that makes use the Born-Oppenheimer approximation which separates the treatment of atomic nuclei and electrons [109].

The GAUSSIAN 09 software package takes a molecular geometry as an input, for which I have used GAUSSVIEW due to its compatibility with GAUSSIAN 09, however other digital molecular builders are also valid. Before an MD experiment is performed on the molecule, its equilibrium geometry is found via energy minimalisation by iteratively perturbing the atomic nuclei positions until the sum of forces is under a specified threshold.

2.2.2 Molecular Potential Energy

In this section, I will demonstrate the computations performed by GAUSSIAN 09 to obtain the vibrational modes [99], in a notation that is consistent with this thesis. The CHO model has a potential energy given only by the quadratic coefficient. The curvatures of the CHO potential energy landscape are taken to be constant, and there exists a well defined fixed equilibrium of minimum energy for which the forces are minimised. The CHO potential energy in 3D space for a molecule with N atoms is

$$V_{\text{mol}} \;=\; \frac{1}{2}\sum_{i,j=1}^{3N} V_{ij}\; u_i\; u_j \tag{2.2}$$

where V_{ij} are the quadratic coefficients that are defined below (2.4), and u_i are the 3D atomic displacements from equilibrium, whose elements are of the set

$$\mathbf{u} \;=\; \left[\Delta x_1\;,\; \Delta y_1\;,\; \Delta z_1\;,\;\; \Delta x_2\;,\; \Delta y_2\;,\;\; \ldots\;,\; \Delta z_N\right] \tag{2.3}$$

For example, $u_1 = \Delta x_1$, is the displacement from equilibrium of the atom labeled 1 in the x-coordinate, and, $u_5 = \Delta y_2$, is the y-displacement of atom 2; thus there are $3N$ elements in the full set, $\mathbf{u}$ (2.3). The index running over one to $3N$ in the potential energy sum (2.2), with associated elements given by $\mathbf{u}$, will hence forth be called the 'atomic xyz index', and the naming of each atom with an integer from one to N will be called the 'atomic labels'. Note that the potential energy (2.2) is taken at its datum, and that the potential forces vanish when the molecule is at its equilibrium geometry, by its definition. The quadratic potential coefficients are the second spatial derivatives in Cartesian coordinates, V_{ij}, defined by a matrix of size, $3N \times 3N$, with elements

$$V_{ij} \;=\; \left(\frac{\partial^2\, V}{\partial u_i\;\partial u_j}\right)\Bigg|_{\text{eqm}} \tag{2.4}$$

where the subscript denotes that these quantities are evaluated at the equilibrium geometry of the molecule. The matrix of second spatial derivatives is called the Hessian matrix, and since the Hessian matrix evaluated at equilibrium coincides with the torsion-free local curvature, a more intuitive interpretation of V_{ij} is the *curvature* of potential energy [63], and can be positive or negative. The Christoffel dynamical matrix, $\mathbf{D}$, is a mass-weighted Hessian matrix in Cartesian coordinates with elements

$$D_{ij} \;=\; \frac{1}{\sqrt{m_i\; m_j}} \;\left(\frac{\partial^2\; V}{\partial u_i\; \partial u_j}\right)\Bigg|_{\text{eqm}} \tag{2.5}$$

where m_i is the mass of the atom associated with entry i of the atomic xyz labels, D_{ij} carries dimensions of $[\text{time}]^{-2}$. As an example, the $(1,1)$ element, $D_{11} = m_1^{-1}\big(\frac{\partial^2}{\partial x_1^2}V\big)\big|_{\text{eqm}}$, pertains to the curvature of the potential energy field due to the perturbation of the atom labelled 1 in the x-coordinate.

2.2.3 Molecular Vibrational Modes

The eigendecomposition of the dynamical matrix, $\mathbf{D}$, reveals the molecular vibrational modes. For the 1D CHO potential, $V_{\text{CHO}} = \frac{1}{2}\, m\, \omega^2\, x^2$, the 1D CHO dynamical matrix is

$$D \;=\; \frac{1}{m}\;\frac{d^2V}{dx^2} \;=\; \omega^2 \tag{2.6}$$

therefore, a 1D system's dynamical matrix is simply a scalar equal to the square of the natural oscillation frequency. The vibrational modes of any system are given by the eigendecomposition of the system's dynamical matrix, $\mathbf{D}$, [30]

$$\mathbf{D} \;=\; \mathbf{L}\;\mathbf{\Lambda}\;\mathbf{L}^{-1} \tag{2.7}$$

where $\mathbf{D}$ has elements (2.11), the diagonal eigenvalue matrix $\mathbf{\Lambda}$ has dimensions of $[\text{time}]^{-2}$, and the column-wise eigenvector matrix $\mathbf{L}$ has elements that are dimensionless (but proportional to a deviation in position from equilibrium). The atomic deviation pattern is contained within the eigenvector matrix, $\mathbf{L}$, and the eigenfrequencies are the squareroot of eigenvalues, $\mathbf{\Lambda}$, their combinations are collectively called the *eigenfunctions* of the matrix. A molecular vibrational mode is an undulating pattern of atomic motion with a specific oscillation frequency. Throughout this thesis, the term *vibrational mode* will refer to the eigenfunctions of the molecular Christoffel dynamical matrix (2.11). The eigendecomposition (2.7) is equivalent to solving the Christoffel equation [30, 31, 56],

$$\sum_{ij=1}^{3N}\Big[D_{ij} \;-\; \omega_i^2\;\delta_{ij}\Big]\;L_{ij} \;=\; 0 \tag{2.8}$$

where the elements L_{ij} are the eigenvectors and ω_i is the eigenfrequency which is the square root of the diagonal eigenvalue matrix elements, $\Lambda_{ij} = \omega_i^2\,\delta_{ij}$. The eigenvector matrix is diagonal due

to the Kronecker–δ defined

$$\delta_{ij} \;=\; \begin{cases} 1, & \text{if } \; i = j \\ 0, & \text{if } \; i \neq j \end{cases} \tag{2.9}$$

and acts as a switch such that it is 'on' only for equal indicies; a matrix with elements given by the Kronecker–δ composes the identity matrix. Using $\mathbf{D}$ (2.7) as the molecular dynamical matrix, then its eigendecomposition *immediately* gives the complete set of molecular vibrational modes. The quantities ω_i and $\mathbf{L}$, along with the equilibrium geometry, provide *all* of the information needed to visualise all of the molecule's vibrational modes, as will be detailed in **§ 2.8**. Thus the vibrational mode labelled i is an eigenmode with eigenfrequency ω_i, whose atomic polarisations are (proportional to) the associated eigenvector column L_{ij}.

The eigenvector matrix can be transformed into a rank-3 tensor, $L(rb|k)$, whose elements pertain to the atomic polarisation of atom b in the r^{th} Cartesian coordinate due to vibrational mode k. The k^{th} vibrational mode eigenfrequency in terms of the dynamical tensors is then computed by

$$\omega_k^2 \;=\; \sum_{r,r'}^{xyz} \sum_{b,b'=1}^{N_{\text{atom}}} L^{-1}(rb|k)\; D(rb|r'b')\; L(r'b'|k) \tag{2.10}$$

where $D(rb|r'b')$ is an element of the Christoffel dynamical tensor

$$D(rb|r'b') \;=\; \frac{1}{\sqrt{m_b\; m_{b'}}} \; \left(\frac{\partial^2 \, V}{\partial u_{rb} \; \partial u_{r'b'}} \right) \Bigg|_{\text{eqm}} \tag{2.11}$$

for atomic deviation u_{rb}. The dynamical eigenvector tensor element, $L(rb|k)$, acts as a coordinate transformation between atomic positions in 3D and vibrational modes; I use this notation for the mathematical derivations and coding work throughout this thesis.

2.3 The Molecular Harmonic Vibrations Package

In this section, I demonstrate the functionality of the MATLAB coding package that I have built to in order to extract and visualise the output data from GAUSSIAN 09. The raw data contains the atomic structure at equilibrium, as well as the matrix potential energy curvature coefficients, V_{ij}, which allow for the harmonic vibrational analysis via (2.8) in MATLAB and are in agreement with the GAUSSIAN 09 NMA data. The output figures of executing the `Molecular_Harmonic_Vibrations_Package` script are shown for both glucose and isomaltose in order to discuss the differences in the substrate and products of the catalytic action of MalL. The molecular behaviour in this section represent a free molecule in a vacuum in the absence of interactions and dissipation.

The top-level script can be run from the MATLAB terminal directly by

```
>> P = Molecular_Harmonic_Vibrations_Pack
```

where a pop-up window allows for the selection of the desired molecule by choosing the relevant GAUSSIAN 09 MD `log` file, then the data collection, computation, and visualisation are automated, and the output data structure, `P`, is stored as a `mat` file. In the script, the general definitions (atomic properties, universal constants and unit conversions) are packaged into a cell, and then all molecular dynamics data are collected and packaged by `Get_Molecule_Data`. Next, the dynamical eigenstates are calculated and packaged by calling `Solve_Dynamical_Matrix`, then the density of states is calculated and packaged by calling `Solve_Density_of_States`. The parameter cell is then passed into the drawing scripts `Draw_Molecule_Data`.

2.3.1 Code Hierarchy Tree

The full code hierarchy tree for the MATLAB scripts of `Molecular_Harmonic_Vibrations_Package` is given below. The list of the script is organised into their order of execution, and the indent depth represents nested functions.

```
>> Molecular_Harmonic_Vibrations_Pack
    · Get_All_Data
        · Get_General_Properties
            · Get_Atom_Properties
            · Get_Universal_Constants
            · Get_Unit_Conversions
        · Get_Molecule_Data
        · Solve_Dynamical_Matrix
        · Solve_Density_of_States
        · Save_Molecule_Data
        · Draw_Molecule_Eqm
        · Draw_Molecule_Eqm_w_Labels
        · Draw_Harmonic_Potentials
        · Draw_Harmonic_Energy_Levels
        · Draw_Vib_Eigenstates
        · Draw_Normal_Mode_Analysis
        · Draw_Density_of_States
        · Get_Enzyme_Data
        · Solve_Enzyme_Density_of_States
        · Save_Enzyme_Data
    · Draw_Molecule_Data
    · Save_all_plots
        · Plot_save_function
```

2.3.2 Equilibrium Structure

The molecule's equilibrium geometry is drawn by the script `Draw_Molecule_Eqm`, in 3D cubic (Cartesian) coordinates in a spatial unit basis of picometres (1 pm = 10^{-12} m), with an origin $(0, 0, 0)$ set internally by GAUSSIAN 09, from which the nuclei positions are measured from the origin.

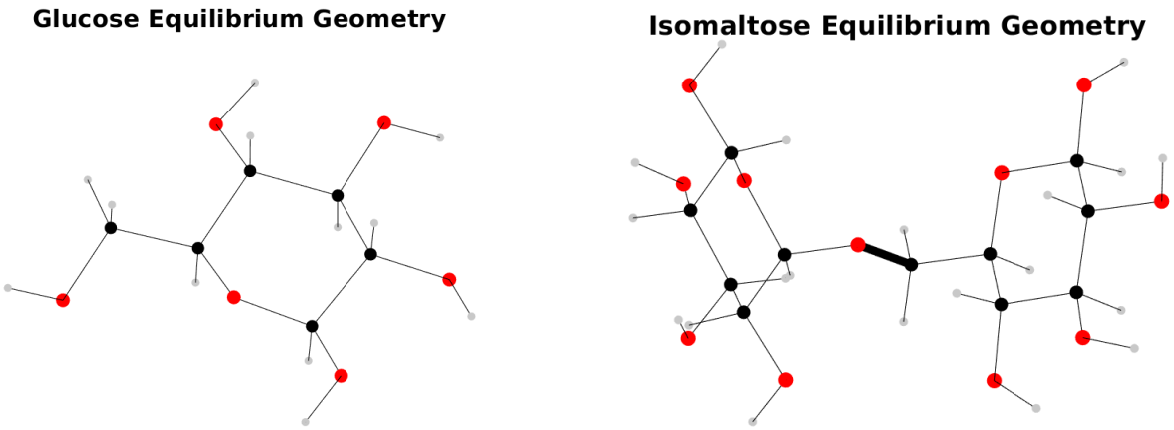

(a) Glucose **(b)** Isomaltose

Figure 2.1: Equilibrium structures of glucose (a) and isomaltose (b). The placements of the atom nuclei are defined by the output data of the GAUSSIAN 09 equilibrium geometry calculations. Both molecules are composed entirely of hydrogen (grey), carbon (black), and oxygen (red) atoms; the glycosidic carbon–oxygen bond that is cleaved by MalL is shown in bold.

MATLAB renders the atoms in a 3D rotational viewing window with the following aesthetic options: the locations of the atomic nuclei are shown as balls with sizes that are linearly scaled by the atomic number; the colours are defined explicitly in the script, `Get_Atom_Properties`, for each atom based upon a convention with the GAUSSIAN 09 molecule viewer. Fig. 2.1 shows the configuration of nuclei positions which correspond to the lowest potential energy state of glucose and isomaltose in a void.

2.3.3 Atomic Labelling

The script, `Draw_Molecule_Eqm_w_Labels`, is the same as, `Draw_Molecule_Eqm`, but with the inclusion of atomic labels with an arrow indicating the associated atom. The labelling of the molecule's atoms with numbers is defined by the GAUSSIAN 09 software. Where there are atoms drawn overlaying each other, their labels overlap as well; if it is desired to determine the labelling of all atoms, it is necessary to use the 3D figure within the MATLAB environment where the molecule can be rotated. Fig. 2.2 is used as a reference for the atomic labelling presented throughout this thesis.

Of particular interest are the atoms of isomaltose that are associated with the glycosidic bond: the glycosidic oxygen, 14; linking carbon, 11; and the two hydrogen atoms bound to the linking carbon, 12 and 13. The carbon–oxygen bond that is broken during catalysis is between the atoms labelled 11 and 14, which can be been in the dashed line in Fig. 2.3. A more detailed inspection of the glycosidic bond is presented in **§ 2.6**.

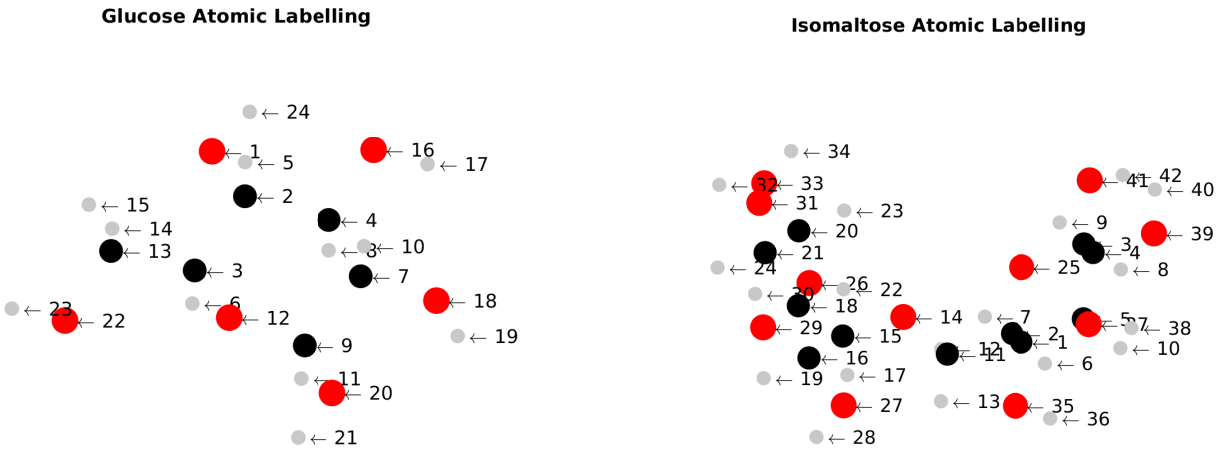

(a) Glucose (b) Isomaltose

Figure 2.2: Glucose (left) and isomaltose (right) drawn the same as the equilibrium geometry in fig. [2.1], with atom index labels and without atomic connections.

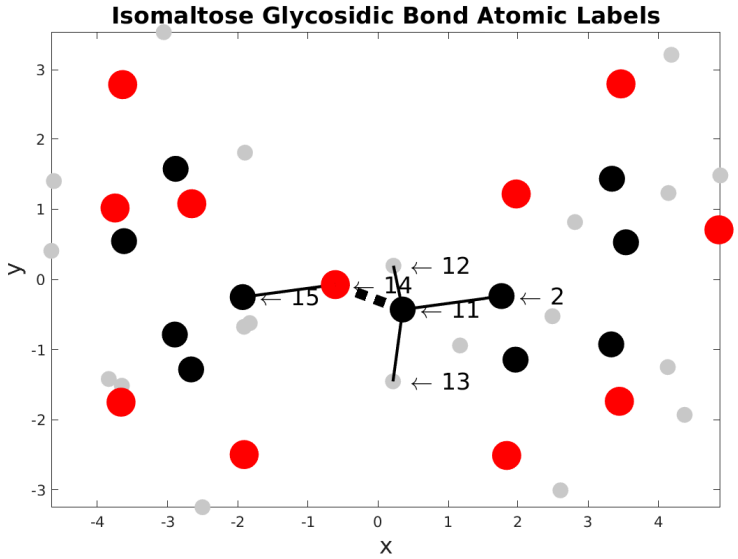

Figure 2.3: A zoom of Fig. 2.2 to show the isomaltose glycosidic link atom labels, the glycosidic linkage atoms are shown with bonding notation, and the dashed line represents the bond that is severed by the catalytic action of MalL. Axes are in units of angstroms ($1\ \mathring{A} = 10^{-10}$ m)

2.3.4 Potential Forces

The draw script, `P_Draw_Harmonic_Potentials`, visualises the linear and quadratic harmonic potential energy coefficients for each atom for each Cartesian coordinate. The linear coefficients are the spatial gradients of the potential energy and are the forces acting on each atom due to the potential. The MATLAB script defines the variable `Force` of size `(1, 3*N_atom)`, which is organised in the atomic xyz labelling defined in (2.3). The GAUSSIAN 09 software defines the molecule equilibrium geometry when the summation of atomic forces is under a defined threshold value that is specified in GAUSSIAN 09. The total force acting on the molecule is on the order of piconewtons and are *vanishingly* small values, which serves to validate the harmonic assumption of setting the linear potential coefficients to zero.

For a comparison, nanonewton ($1\ \text{nN} = 10^{-9}$ N), piconewton ($1\ \text{pN} = 10^{-12}$ N) and femtonewton ($1\ \text{fN} = 10^{-15}$ N) scale forces (as offered by Wolfram Alpha) include: the electrostatic

force exerted by the nucleus on the electron in a hydrogen atom (82 nN); the adhesive force of a single spatula of a gecko's foot (10 nN); the typical force to break a covalent bond (1.6 nN); the typical force to break a non-covalent bond (160 pN); the force needed to pull a DNA molecule apart by pulling each end (65 pN); the force needed to unzip a DNA molecule at room temperature (10 pN); Brownian motion forces acting on an E. coli bacterium averaged over one second (10 fN). Even though these forces are minuscule, the sum of the potential forces acting on the glucose and maltose are on the order of femto- or attonewtons. Sub-attonewton ($< 10^{-18}$ N) measurements have been made on laser-cooled, trapped single ions [110], and optical methods applied to an ultracold atom cloud have approached the quantum limit (Heisenberg uncertainty) achieving force sensitivities on the order of yoctanewtons (10^{-24} N) [111].

2.4 Vibrational Normal Modes are Dynamical Eigenstates

In this section, I demonstrate the computation of the molecular vibrational modes via the solution of the Christoffel equation (eigendecomposition of the dynamical matrix) as populated by the MD data from GAUSSIAN 09 simulations.

2.4.1 Dynamical Eigenvalues

The Christoffel dynamical matrix is constructed in MATLAB via (2.11) and called `Dyn`. The complete set of molecular vibrational modes are given by the eigenstates of `Dyn`, which are computed in MATLAB by the in-built eigendecomposition function, `[eVec_raw, eVal_raw] = eig(Dyn)`. The function's outputs are, `eVec_raw`, the column-wise eigenvector matrix and, `eVal_raw`, the diagonal eigenvalue matrix. The the raw subscript denotes that the output of the `eig` computation is unprocessed. The raw eigenvalues are converted from the internal hartree-amu-bohr unit system used by GAUSSIAN 09 into SI. Fig. 2.4 shows the diagonal elements of `eVal`, and the negative values are indicated by red dots. The eigenvalues are then sorted from smallest to largest and renamed to `eVal`, then that sorting index is used to reorganise the eigenvector matrix columns into `eVec`.

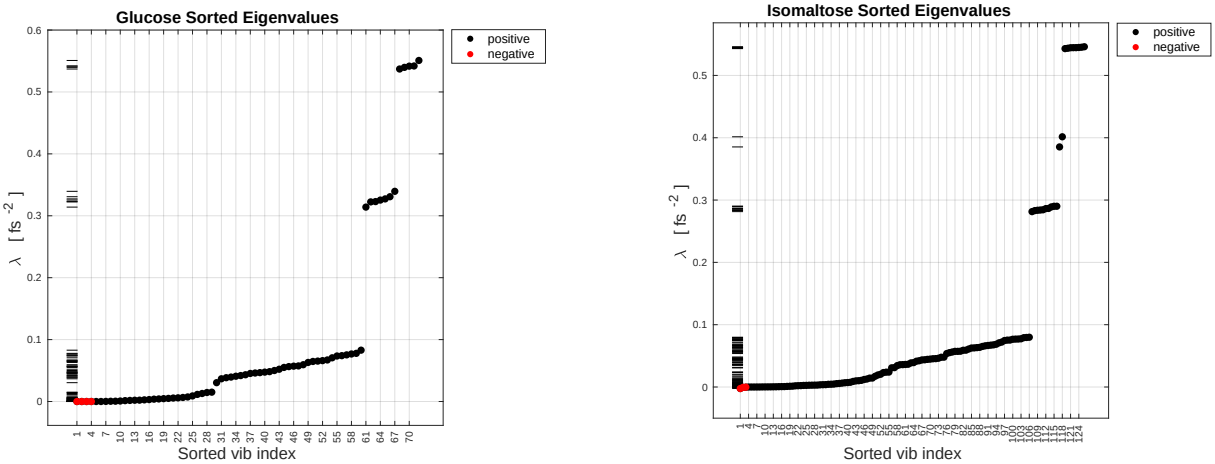

(a) Glucose **(b)** Isomaltose

Figure 2.4: Sorted dynamical eigenvalues for glucose (a) and isomaltose (b) in units of femtosecond^2. Negative eigenvalues (red) are the modes removed in NMA. The eigenvalues are drawn as lines along the y-axis to indicate their distribution.

2.4.2 Harmonic Eigenfrequencies

The vibrational eigenfrequencies are the square-roots of the dynamical eigenvalues. Since the eigenvalues computed by `eig` are given as a diagonal matrix, the frequencies can be calculated and populated into a 1D array by, `freq = sqrt(diag(eVal))`, which is a set of angular frequencies, $[\text{time}]^{-1}$. By the convention of NMA, the modes pertaining to rigid body translations and rotations are removed from the set of eigenmodes. These modes have an eigenvalues that are either positive and close to zero, zero (corresponding to acoustic modes), or negative (corresponding to an imaginary–valued eigenfrequency). For linear molecules, there are five removed modes, and six modes are removed for asymmetric polyatomic molecules [93].

The molecules under study in the thesis, the number of normal modes are $3N - 6$. The eigenmodes of glucose and isomaltose are shown in Fig. 2.5, with the removed modes shown in red. There is a transparent window (no vibrational modes) in the bandwidths 50–90 THz (medium-wavelength IR-C), and 95–115 THz (short-wavelength IR-B).

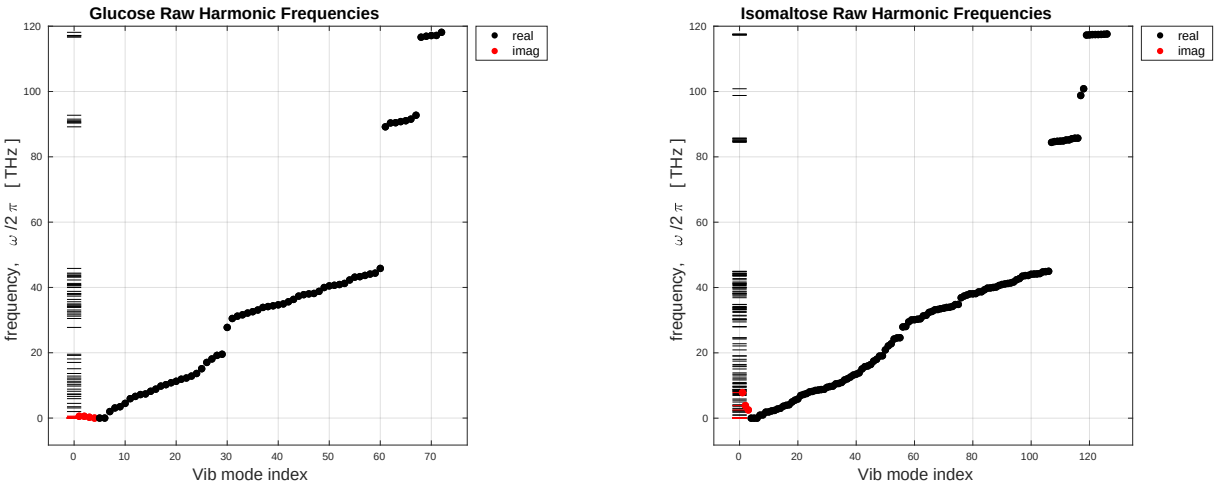

(a) Glucose **(b)** Isomaltose

Figure 2.5: Harmonic dynamical eigenfrequencies, including those with imaginary frequency (red).

2.4.3 Dynamical Eigenvector Matrix

The eigenvector elements are dimensionless by their definition, since the valid eigenvector matrices of `Dyn` are all those that are linearly proportional to `eVec`. However, the eigenvectors of the dynamical matrix have the physical interpretation of atomic polarisations. The element in position (1,1) is the maximum relative deviation of the atom labelled 1 in the x-coordinate due to the motion of the vibrational mode labelled as 1. It is therefore appropriate to endow the eigenvector elements with a spatial dimension in units that are consistent with the equilibrium geometry. The largest eigenvector element is therefore interpreted as the largest atomic displacement; the vibrational mode that moves a particular atom in a particular coordinate the most. Typically, the highest frequency vibrational modes pertaining to oscillations of hydrogen atoms have the largest polarisations.

The rank-3 dynamical eigenvector tensor, $L(rb|k)$, can be populated for mode `k`, atom `b`, in Cartesian coordinate `r` by, `eVec_tensor(r,b,k) = eVec((3*(b-1)+r),k)`, the resultant

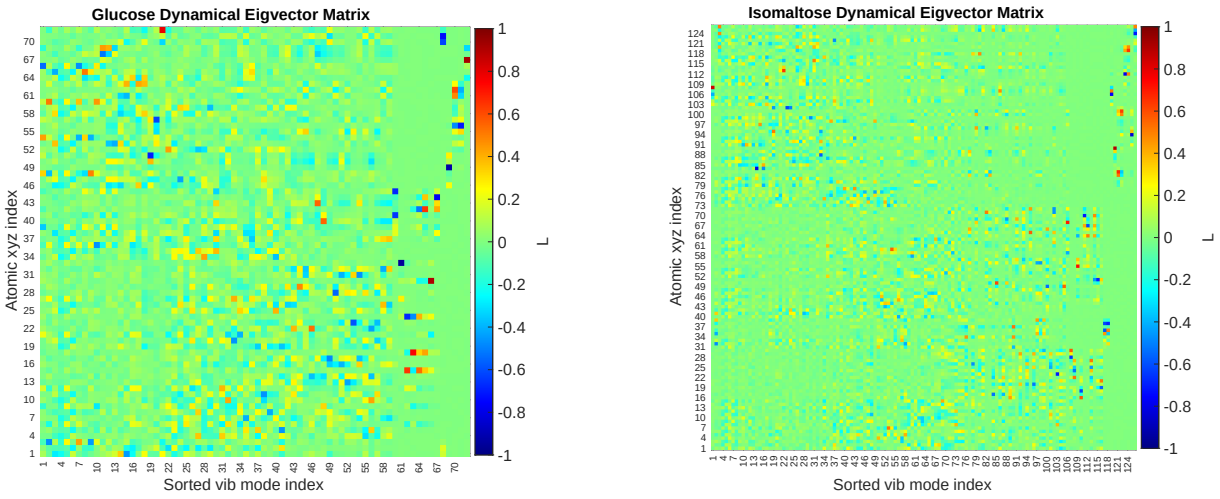

(a) Glucose **(b)** Isomaltose

Figure 2.6: Dynamical eigenvector matrix, **L**, in normalised dimensionless units

tensor has size `(3, N_atom, 3*N_atom)`. This tensor makes it easier to select specific elements, for example, `eVec_tensor(1,2,3)` corresponds to the x-coordinate polarisation of atom 2 due to mode 3.

2.4.4 Atomic Polarisation Magnitudes

The atomic polarisation magnitude, `Atom_Pol(a,m)`, is the absolute magnitude of the eigenvector elements over Cartesian coordinates pertaining to a single atom of one vibrational mode, and has size `(N_atom,3*N_atom)`. In MATLAB, this is calculated for atom `b` and mode `k` by

$$\texttt{Atom\_Pol(b,k)} \;=\; \texttt{P\_0 * sqrt}\left(\;\texttt{sum}\left(\;\texttt{eVec\_tensor(:,b,k).\^{}2}\;\right)\;\right) \tag{2.12}$$

which in tensor notation is

$$P(b|k) \;=\; P_0\,\sqrt{L(xb|k)^2 \;+\; L(yb|k)^2 \;+\; L(zb|k)^2} \tag{2.13}$$

where P_0 is an arbitrary scalar with dimensions of [space]. This measures the maximum extent to which an atom nuclei is displaced by a vibrational mode, without referring to a particular coordinate direction. For example, one of the largest atomic polarisation values for glucose is atom 23 due to the highest-frequency vibrational mode 72 (as indicated by the yellow point in Fig. 2.7), with a smaller polarisation for atom 22. From checking the labelling, atoms 22 and 23 are the hydroxy group on the left of Fig. 2.2a. Therefore the vibrational mode labelled 72 is the oscillatory motion of this hydroxy group while the rest of the glucose is virtually stationary, and has eigenfrequency, $\omega_{72}/2\pi = 118.1$ THz.

2.4.5 Atomic Polarisations

All of the molecule's atomic polarisations are drawn on the equilibrium geometry by my MATLAB script, `P_Draw_Vib_Eigenstates`. Each polarisation element is computed from the eigenvector element by, $P_0\;L(rb|k)$, with $P_0 \;=\; 100$ pm (10^{-10} m $= 1$ Å), and then plotted as a deviation

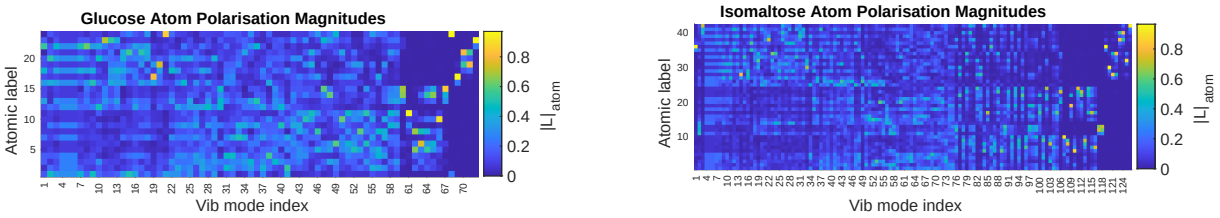

(a) Glucose **(b)** Isomaltose

Figure 2.7: Atomic polarisation magnitudes, as calculated from the dynamical eigenvector elements (2.12)

from the atomic equilibrium (Fig. 2.8). The polarisation (row vector) in 3D for atom b due to mode k is calculated by,

$$u^{\text{pol}}_{rb,k} \;=\; x^{\text{eqm}}_{rb} \;+\; P_0\; L(rb|k) \tag{2.14}$$

and the negative polarisation is given by replacing `+` with `-`, since it is the phase conjugate. The polarisations are drawn as a dot with a line connecting them to their equilibrium. The colouring is due to their frequency, and is selected from a linear scaled rainbow (`colormap jet`); lowest is red, highest is blue. For example, the high frequency hydrogen oscillations can be seen as the long blue lines.

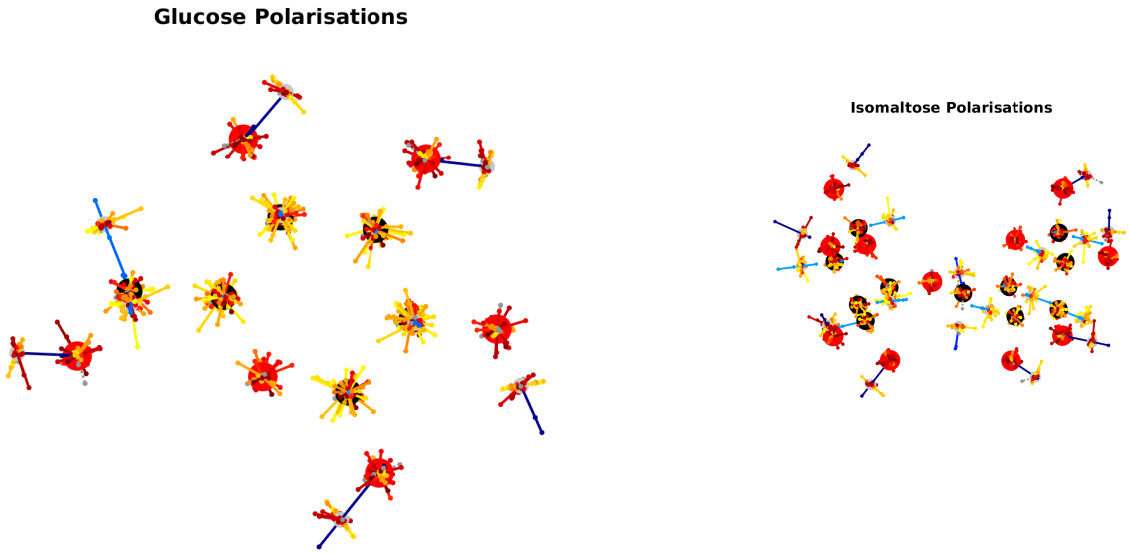

(a) Glucose **(b)** Isomaltose

Figure 2.8: The dynamical eigenvector elements as the vibrational atomic polarisations.

2.5 Normal Mode Analysis in Gaussian 09

In this section, I describe the some of the GAUSSIAN 09 output data that is used in conventional NMA. The draw script `Draw_Normal_Mode_Analysis`, visualises the data offered by GAUSSIAN 09 collectively referred to in the `log` data files as the NMA.

2.5.1 Normal Mode Frequencies

The number of dynamical modes are, $N_{\text{dyn}} = 3\,N_{\text{atom}}$, and for asymmetric molecules composed of three or more atoms, the number of NMA modes is, $N_{\text{nma}} = N_{\text{dyn}} - 6$, since the NMA

algorithm has removed the modes associated with rotations and translations. The process by which these modes are identified by GAUSSIAN 09 is detailed in [99].

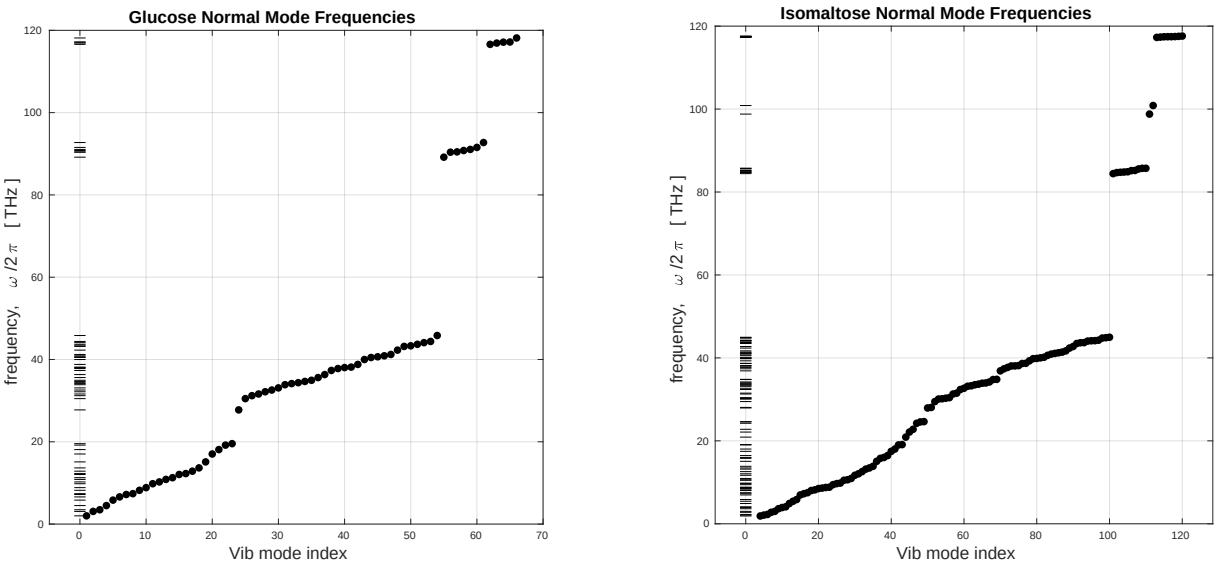

(a) Glucose **(b)** Isomaltose

Figure 2.9: Normal mode frequencies of glucose and isomaltose

2.5.2 Simulated Infrared Absorbance

The GAUSSIAN 09 NMA algorithm also calculates an approximation of the infrared (IR) absorbance spectrum. The procedure of calculating IR absorbance spectra from molecular dynamics is a rich body of work, and the GAUSSIAN 09 documentation utilises the procedure in, for example, [112, 113]. The essential process is the (Fourier) frequency representation of the time auto-correlation of the dipole moment, and is calculated from the Fourier–transformed MD trajectories. As this is not a major aspect of this thesis, I will omit the details here. The output data gives an IR intensity value for each vibrational normal mode in IUPAC conventional absorbance intensity units of km/mol [114]. While the direct physical interpretation of [space][amount]$^{-1}$ is not immediately apparent, it is derived from the integrated molar absorption coefficient, ϵ, defined by

$$\epsilon(\tilde{\nu}) \;=\; \frac{1}{Cd}\int d\tilde{\nu}\;\log_{10}\left(\frac{I_0(\tilde{\nu})}{I(\tilde{\nu})}\right) \;=\; \frac{A(\tilde{\nu})}{Cd} \tag{2.15}$$

where $\tilde{\nu} = \nu/c$ is the linear frequency in spectroscopy units, C is a concentration, d is the optical path distance, A is the integrated value over log intensities, and I and I_0 are the transmitted and incident radiation intensities, respectively.

The plots in Fig. 2.10 are reminiscent to the absorbance spectra as obtained via spectroscopic experiments. The most significant difference in these figures is that the data is *point-like* and not a smooth continuous spectral distribution; this distinction will become apparent throughout this thesis. Typically, in order for the calculated IR spectra to be plotted as a smooth curve, there is an assumption made that each vibrational mode absorbance, ϵ_0, has a Lorentzian resonance

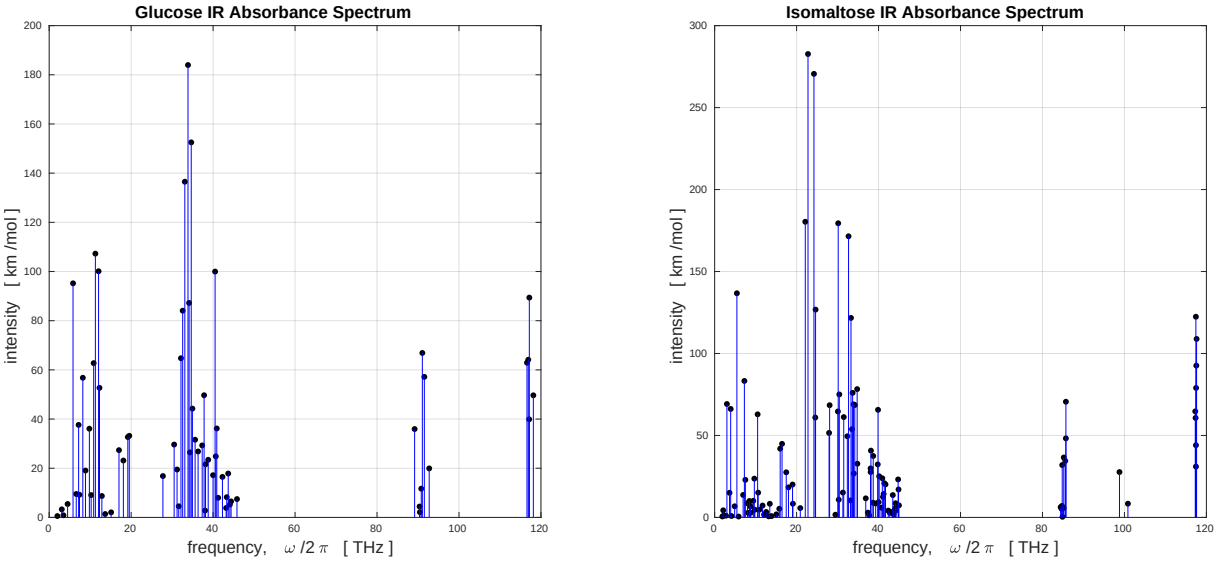

(a) Glucose **(b)** Isomaltose

Figure 2.10: Simulated IR absorbance spectrum for glucose (a) and isomaltose (b). The frequency axis is shown up to 120 THz, which corresponds to a spectroscopic wavenumber of 4,000 cm^{-1}.

distribution for IR intensity

$$\epsilon_0(\tilde{\nu}) \;=\; \frac{2A}{\pi}\;\frac{w}{w^2 \;+\; 4\,(\tilde{\nu} \;-\; \tilde{\nu}_0)^2} \tag{2.16}$$

where, $\tilde{\nu}_0$, is the vibrational mode frequency and w is the full-width-at-half-maximum, and carries the same units as $\tilde{\nu}$. In GAUSSIAN 09, the value for w is arbitrarily set to produce smooth curves, and is not calculated from MD data. This form will be derived from first principles from the quantum harmonic theory for the steady state value of phonon number response (**Chapter 3**), and allows for the identification of w to be due to the vibrational dissipation rate (inverse of lifetime) of the vibrational mode. Essentially, real experimental data does show a smooth distribution due to the inherent molecular vibrational relaxation behaviour, but it is not demonstrated when assuming a value w, and thus I leave the data as point-like. There also exist approximations for resonance curves by using the Gaussian normal distribution; while they may appear similar, they are fundamentally different and there is an intrinsic error of 32% in their integrated areas.

2.5.3 Density of States

A representation of the distribution density of vibrational mode frequencies is to make a histogram plot of their values, and is calculated by `Solve_Density_of_States`. The number of histogram bins is fixed to allow for an unbiased comparison of two molecules. Fig. 2.11 shows the distribution density of vibrational modes as given by the histogram count divided by the number of vibrational normal modes. The number of histogram bins is set to 50, so that over a range of 120 THz, each bin spans 2.4 THz, and is coarse enough to show multiple modes in one bin. For glucose (Fig. 2.11a), the most populated histogram bins occur at [33.1, 35.5, 42.6, 45.0, 92.4, 118.4] THz, with a count of five modes. For isomaltose (Fig. 2.11b), the most populated

vibrational mode histogram bins occur at [10.8, 41.4] THz with a count of nine, and [33.7, 38.8, 87.2, 117.8] THz with a count of eight.

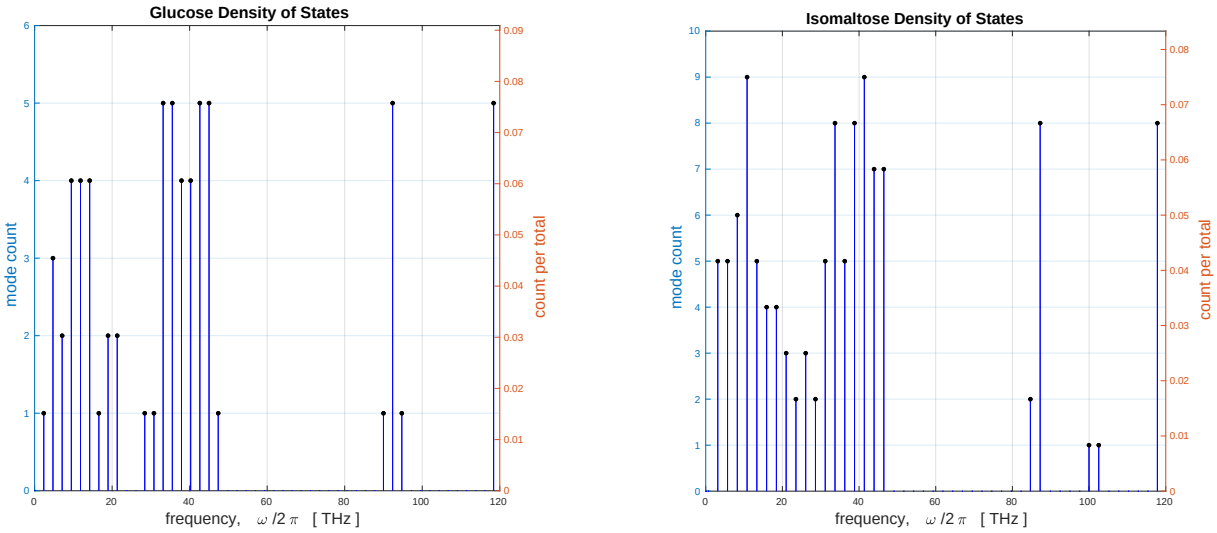

(a) Glucose **(b)** Isomaltose

Figure 2.11: The density of states of glucose and isomaltose as represented by a normalised histogram plot with 50 bins.

The Density of States (DoS) is effectively a normalised count of how many eigenfrequencies are within a given frequency bandwidth. There exist many different context-based interpretations, derivations, and expressions for the quantity called the 'density of states'. For a single molecule in the CHO approximation with a well-defined dynamical matrix (that is to say, the second spatial derivatives of potential energy are known), the states are the vibrational modes obtained via NMA. Thus, the DoS, g, amounts to a count (histogram) which is then scaled by the total number of modes, N_{mode}, for normalisation

$$g(\omega) \;=\; \frac{1}{N_{\text{mode}}} \sum_{k=1}^{N_{\text{mode}}} \delta(\omega \;-\; \omega_k) \tag{2.17}$$

for vibrational mode index k, and the Dirac δ-function is equal to one only for $\omega = \omega_k$, or else is zero. For a fine enough sampling of ω, this is simply a Dirac-comb distribution, each with height, N_{mode}^{-1}, due to normalisation. The DoS for glucose and isomaltose are shown in Fig. 2.11, and essentially what is represented on the y-axis of Fig. 2.5. In **Chapter 3**, I will make use of an approximation for (2.17) to produce a continuous distribution for $g(\omega)$, which I will use to express the enzyme stimulus to the substrate molecule.

2.6 A Closer Inspection of the Glycosidic Bond of Isomaltose

In this section, I will demonstrate some of the insights gained from what has been shown thus far from the MD data and classical harmonic analysis. The central theme of this work is on the enzymatic action of MalL of the catalysis of isomaltose into two glucose by severing of the glycosidic linkage, and so that is what I will expand upon here. What we want to know is which vibrational modes cause the greatest stretching to the glycosidic carbon–oxygen bond, because

I hypothesise that it is these modes that participate the most in the catalytic process.

The general procedure for identifying the principal molecular and enzyme modes involved in catalysis from the raw data presented in this chapter is as follows:

- locate the labelling of relevant atoms
- locate their atomic polarisations
- find modes that stretch their bond the most by taking the difference in their polarisations
- search for resonances of these molecular modes with the enzyme modes

To investigate the catalytic action of MalL on isomaltose, the first step is to identify the labelling of the glycosidic linkage atoms. This is done by observing the atomic labelling (Fig. 2.3), from which the glycosidic oxygen is labelled 14, the carbon in the linkage is 11, the carbon bonded to the glycosidic oxygen that is part of a glucose ring is 15, and the two glycosidic hydrogen atoms are 12 and 13.

```
C_link  = 11;
H_link1 = 12;
H_link2 = 13;
O_gly   = 14;
C_ring  = 15;
```

With atom labels determined, the polarisation magnitudes are extracted from the data structure. The information demonstrated here shows the magnitude to which each atom is deviated from equilibrium due to each vibrational mode, and is essentially another method of visualising the relevant rows of Fig. 2.7. The colours and sizes representing the atoms are equivalent to those used for the equilibrium geometry Fig. 2.1. By sorting the polarisations of the glycosidic oxygen, it is seen that the vibrational modes that deviate this oxygen the most are 24, 56, 29, 28, and 2, sequentially. The motions associated with these particular modes are readily viewable in the animations that are produced by the Molecular Harmonic Vibrations Pack detailed in **§ 2.3**.

The polarisations themselves are not a measure of the stretch between two atoms. To obtain a rudimentary measure of the carbon–oxygen bond stretch, I first extract the 3D atomic polarisations from the eigenvector tensor for the carbon, $L_C = L(r, 11|k)$, and oxygen, $L_O = L(r, 14|k)$, then calculate the absolute difference between the glycosidic oxygen and carbon (Fig. 2.12), from which the magnitude of the stretch due to mode k is given by the (Euclidean) distance, $|L_C - L_O|$, Therefore, I define the measure for the glycosidic carbon–oxygen bond stretch, S_k, due to vibrational mode k to be

$$S_k = \sqrt{\big[L(x,11|k) - L(x,14|k)\big]^2 + \big[L(y,11|k) - L(y,14|k)\big]^2 + \big[L(z,11|k) - L(z,14|k)\big]^2} \tag{2.18}$$

The comparison of the bond stretching are plotted in Fig. 2.13 and are ordered sequentially in Fig. 2.14, which shows that modes 57, 65, 58, and 66 contribute the most to bond stretching, with each occurring within the 20–35 THz bandwidth. The glycosidic hydrogen vibrations are

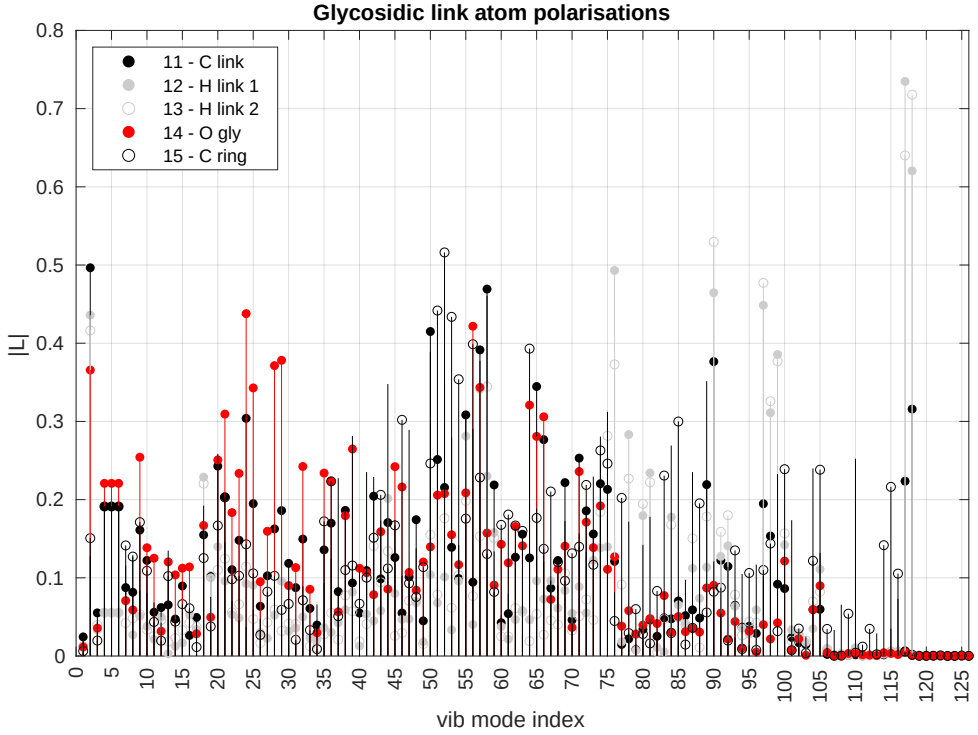

Figure 2.12: The atomic polarisation magnitudes (2.13) (y-axis) are shown for each atom in the glycosidic bond for each vibrational mode (x-axis). The modes that polarises the glycosidic carbon (label 11, solid black circle) are 1, 58, and 50; the modes that polarises the glycosidic oxygen (label 14, solid red circle) the most is 24, 56, and 29. This information alone does not describe the extent of bond stretching.

clearly identified in Fig. 2.12 as the vibrational modes 117 (98.79 THz) and 118 (100.85 THz), since there are no vibrational modes near this frequency in glucose.

A detailed analysis of IR absorbance data has been performed for a monosaccharide (glucose) in comparison with the stretching vibrations of the glycosidic linkages of disaccharides (maltose) and polysaccharides (cellulose) [115]. The results show that the polysaccharide has a low frequency absorbance band (34.5 THz, 1150 cm^{-1}) that is not present in the monosaccharide, whereas each molecular structure has the presence of a glycosidic stretching mode (29.4 THz, 980 cm^{-1}). This provides support for the hypothesis that selective excitation of isomaltose vibrational modes in the 25 to 35 THz bandwidth may contribute to the completion of a reaction.

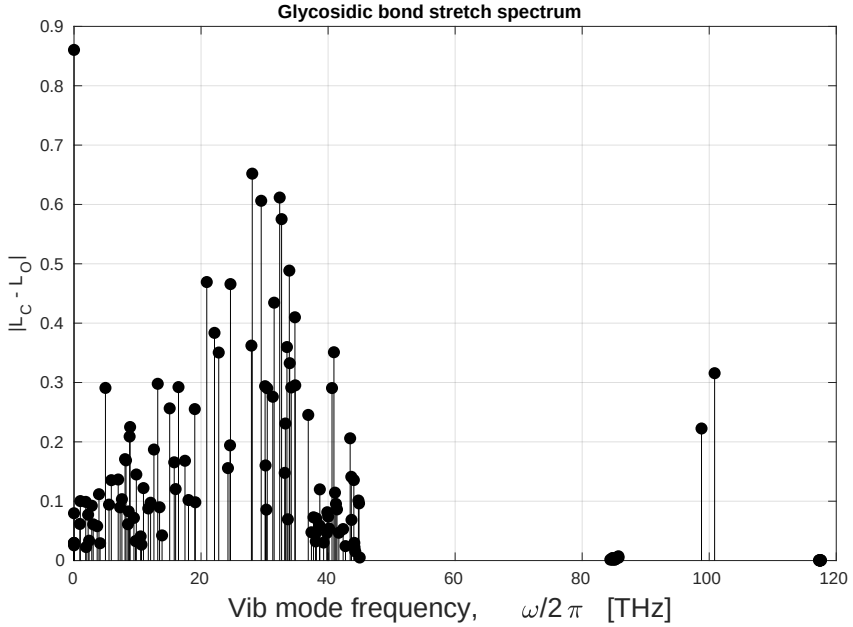

Figure 2.13: Spectral distribution for the isomaltose glycosidic bond stretch (2.18) for each vibrational mode. The large value at $\omega = 0$ pertains to translations and rotations (vibrational modes that are not in the set of normal mode), which do not stretch the bond. The largest values for the bond stretch occur within the 20 to 40 THz bandwidth; and the vibrational modes close to 100 THz are associated with the oscillations of the glycosidic hydrogens (labelled 12 and 13).

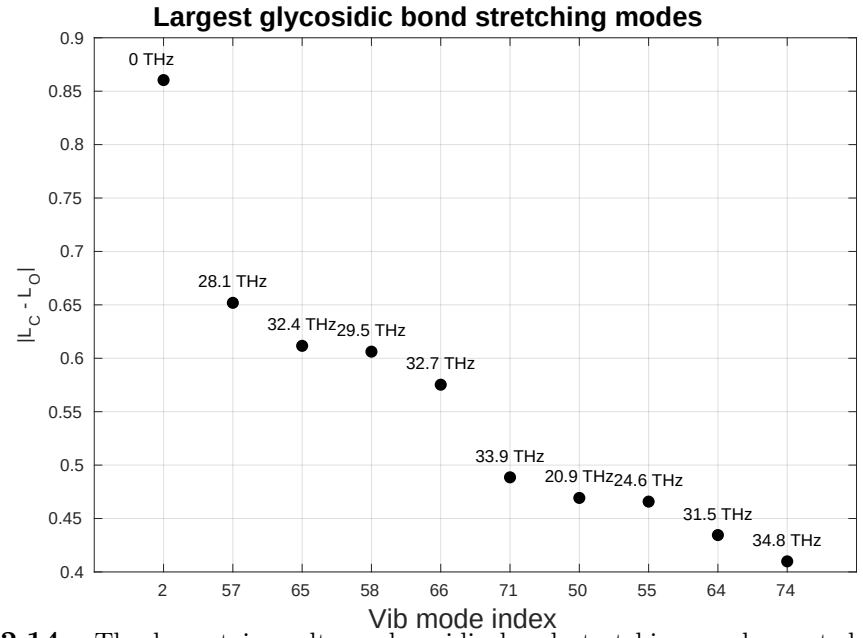

Figure 2.14: The largest isomaltose glycosidic bond stretching modes sorted by (2.18) (y-axis) with their mode index (x-axis) and mode frequencies.

2.7 Vibrational Mode Animations

In this section, I present the mathematical construction for the MATLAB code that I built to animate the molecular vibrational modes from GAUSSIAN 09 MD output data. The full hierarchy

tree is given below,

```
>> Molecule_Harmonic_Vibrations_Pack
    · Get_All_Data
    · Draw_Molecule_Data
    · Animate_Vibrational_Modes
        · Vibrational_Mode_Movie_Maker
```

where the indent depth shows nested functions, and the scripts are listed in the order that they are called. The individual vibrational modes are animated and stored by the Molecular Harmonics Vibration Pack. By running of the package, there will be a new directory created called by the name of the molecule and the time of computation that will contain all figure displayed in the previous chapter. By choosing to also animate and store the vibrational modes, there will be two new folders created that to store the animations for each vibrational mode in two different draw methods: point swarm (figure cleared each frame); and motion smear (new frames are overlaid). A snapshot of the final animation frame is also stored.

2.7.1 Time Evolution of the Normal Modes

In the CHO mode, the deviation of the atomic nuclei from their equilibrium positions at any time duration the oscillation of vibrational mode k is

$$\delta\mathbf{X}_k(t) \;=\; P_0\;\mathbf{L}_k\;\cos\big(\omega_k t \;+\; \phi_0\big) \tag{2.19}$$

where $\mathbf{L}_k$ is the k^{th} column of the eigenvector matrix corresponding to the eigenfrequency ω_k, ϕ_0 is the initial phase state of the vibrational mode, and P_0 is an arbitrary scale with dimensions of [space] which fixes the oscillation envelope amplitude for the sinusoidal oscillation of each atom in each spatial coordinate to $P_0\;\mathbf{L}_k$. The initial phase offset, ϕ_0, defines the initial nuclei positions

$$\delta\mathbf{X}_k(0) \;=\; P_0\;\mathbf{L}_k\;\cos\big(\phi_0\big) \tag{2.20}$$

By choosing $\phi_0 = 0$, the atoms start at their maximum (positive polarisation) displacements, if $\phi_0 = \pi/2$, the molecule is at the equilibrium geometry, and $\phi_0 = \pi$ corresponds to the negative polarisation. The actual positions of the nuclei throughout the animation are then

$$\mathbf{X}_k(t) \;=\; \mathbf{X}_{\text{eqm}} \;+\; \delta\mathbf{X}_k(t) \tag{2.21}$$

where the equilibrium positions are constant and are the same for all vibrational mode. This expression is sufficient to prepare the animations. The deviation of the atom b in the r^{th} Cartesian coordination due to vibrational mode k is given in tensor form by

$$u_{rb,k}(t) \;=\; x_{rb}^{\text{eqm}} \;+\; P_0\;L(rb|k)\;\cos(\omega_k t \;-\; \phi_{0,k}) \tag{2.22}$$

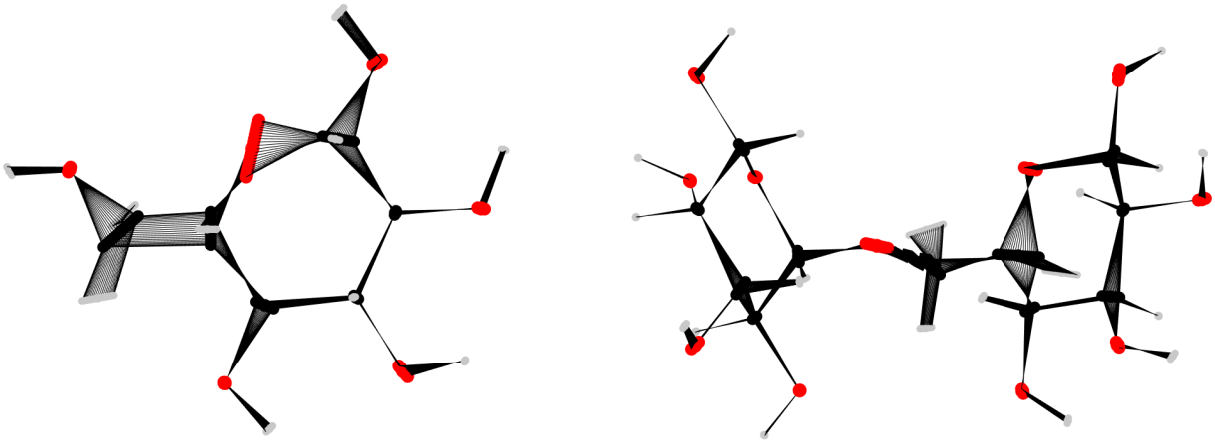

(a) Glucose mode 30, $\omega_{30}^{\text{glu}}/2\pi = 29.4$ THz **(b)** Isomaltose mode 57, $\omega_{57}^{\text{iso}}/2\pi = 28.1$ THz

Figure 2.15: The final frames of an animation of a single vibrational mode over one full cycle for (a) glucose and (b) isomaltose. Mode 57 of isomaltose was identified as the dominant glycosidic stretching mode, and mode 30 of glucose is the closest to the aforementioned oscillation frequency. The locations of the nuclei and the molecular bonds are drawn at a time step defined by the animation duration and frame rate.

This equation is computed for each atom for every animation frame and the bond connections are redrawn. The dominant glycosidic bond stretching mode (57) of isomaltose has a cycle period of $2\pi/\omega_{57} = 35.6$ fs, thus for a five-second animation at 10 frames per second, the time step is 0.714 fs. Vibrational mode 30 of glucose has an oscillation frequency nearest to isomaltose mode 57 ($\omega_{57}^{\text{iso}} \approx \omega_{30}^{\text{glu}}$) and also exhibits large polarisations of the ethanol group, which is the resultant product from hydrolysis of the glycosidic bond in isomaltose (Fig. 2.15). This lends support to the hypothesis that this bandwidth is correlated with the catalytic action of MalL since both reactant and products have vibrational modes at similar frequencies with related undulation patterns.

2.8 Enzyme Vibrational Modes

With the molecule equilibrium and harmonic dynamics calculated, the next step is to perform a similar computation for the enzyme. The enzyme MalL is composed of 9,145 atoms which is vastly larger than the 42 atoms composing isomaltose, and is therefore beyond the reach of the computational ability of Gaussian 09. Thus the enzyme is treated within the Gromacs software as it is specially suited for the harmonic (normal mode) analysis of very large molecules and other atomic structures.

The atomic structure of MalL was determined via X-ray crystallography by the work performed by van der Kamp et al. [116]. This crystal structure was then digitised in Gromacs where an energy minimisation MD simulation was performed to determine the equilibrium configuration of the enzyme in an aqueous environment. The NMA was performed for this resultant structure. The MalL data structures were prepared by Daniel Schipper for the work contributing to his Masters thesis [117]. In this section, I will be comparing the MalL enzyme at a Reaction State (RS) and with a Transition State (TS) analogue. The RS has an isomaltose molecule inserted into the active site of MalL, whose total structure is composed of 9,145 atoms. The

TS features an analogue substrate molecule which is stable in the configuration mimicking the isomaltose at the point of transitions. To achieve this, one of the glucose subunits has been replaced by a nitrated ring which alters the total number of atoms to 9,150. As every additional atom contributes three vibrational modes to the harmonic structure, the RS has 27,435 vibrational eigenmodes and the TS has 27,450.

2.8.1 Extracting Enzyme Data

I built the `Get_Enzyme_Data` script to fetch the data and then compute the enzyme equilibrium structure and vibrational mode frequencies. I have used the GRO2MAT software package [118] to import the GROMACS output data into the MATLAB workspace, and the open-source Atomistic Topology package [119] in order to automate the data processing and enable a visualisation of the equilibrium geometry. This package is able to read `pdb`, `gro`, and `xyz` file types and construct arrays compatible with MATLAB, thus it can take any atomic structure built in GROMACS or even downloaded from the online Protein Database (PDB), making this process general and simple for any enzyme. The Atomistic Topology package is called by, `atom = import_atom(filename)`, where the output structure `atom` is a column array with a number of elements equal to the number of atoms, the fields contained within are: `molid`, residue identification number; `resname`, residue name; `type`, atom name; `fftype`, effectively the same as atom name; `index`, atom number; `neigh`, atomic neighbours; `bond`, the atoms bonded to other atoms; `angle`, the angle at which atoms are bonded, if they exist; `x,y,z,` atomic coordinates; `vx,vy,vz,` atomic velocities, if they exist.

2.8.2 MalL Equilibrium Geometry

The MATLAB script that I have built called `atomistic_topo_unpack` offers a pop-up window to choose the enzyme structure (`xyz`) file, then automates the data fetching, unpacking, and matrix construction of the `atom` structure into equivalent arrays used in the `Molecule_Vibrations_Pack`. The same script used for the visualisation of the molecule, `Draw_Eqm_Geometry`, is used to render the MalL enzyme atoms at equilibrium (Fig. 2.16). The length dimensions of the box containing the whole enzyme is $[5.3 \times 5.8 \times 7.9]$ nanometres.

2.8.3 Dynamical Eigenfrequencies

The GROMACS software constructs the dynamical matrix of MalL and then performs the eigendecomposition that solves the Christoffel equation, thus obtaining all of the harmonic (normal) vibrational modes. Since there are 9,150 atoms in the TS, the dynamical matrix for MalL is a square matrix of size $(27,450 \times 27,450)$, with each element stored in a double-precision floating-point format occupying 64 bits in order to preserve a high level of accuracy in the eigendecomposition. Since the (harmonic) dynamical matrix is symmetric, only the diagonal and lower triangular elements are needed which cuts the total number of stored elements by roughly half, despite this, the file size is over 5 GB when stored as a comma-separated variable (`csv`) text file. Therefore, I make use of the open-source GMX2MATLAB package to process the GROMACS output binary files to prepare the eigenvalue array into a `xvg` filetype that can be

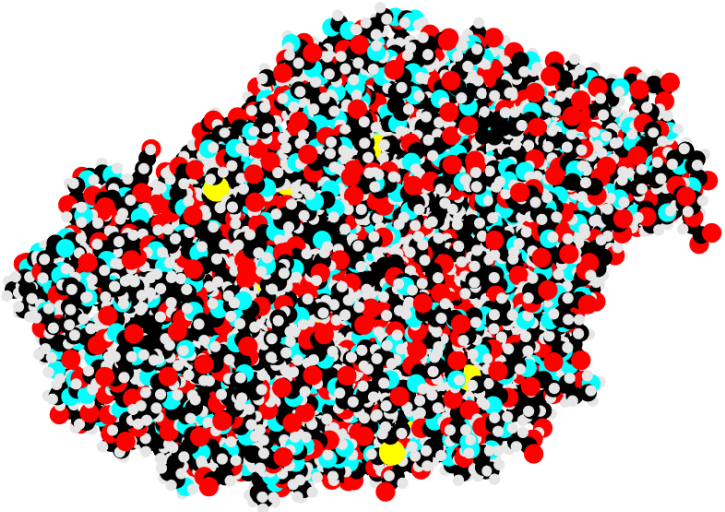

Figure 2.16: MalL equilibrium structure as drawn by `Draw_Eqm_Geometry`, which is composed entirely of hydrogen (grey), carbon (black), oxygen (red), nitrogen (blue), and sulphur (yellow) atoms.

read by MATLAB.

The `Get_Enzyme_Data` script first assumes that the initial structure file chosen has the name of the format, `[enzyme_name '_struct.xyz']`, then, using MalL at the reaction state for example, `'MalL_rs_struct.xyz'`, checks if there exists files within the same folder called, `'MalL_rs_eigenval.xvg'` and `'MalL_rs_eigenfreq.xvg'`. If these files exist, then they are read into MATLAB and prepared using scripts that I built

```
eVal  = Get_XVG_eigenval(  'MalL_rs_eigenval.xvg'  , dir )      (2.23)
eFreq = Get_XVG_eigenfreq( 'MalL_rs_eigenfreq.xvg' , dir )      (2.24)
```

where `dir` is the data directory, and the outputs `eVal, eFreq` are numerical column arrays of double–precision on the order of hundreds of kB, which MATLAB can process rapidly. If these files are not named exactly as above, the user is prompted with a pop-up window to select the appropriate file.

The normal mode frequencies are plotted in Fig. 2.17 using the same method described for Fig. 2.9 with subtle changes to the script. By inspection, the general distribution of vibrational modes for both RS and TS is the same, with the ∼22,000 low–to–mid frequency modes trending over a roughly linear progression up to about 60 THz. The highest mid frequency modes around 60 THz are more compact and at a lower frequency in the TS compared to the RS. There exist only two vibrational modes within the 60–80 THz frequency band and oscillate with a reduced frequency difference in the TS. The highest frequency bands associated with the hydrogen network are also altered subtly.

2.8.4 MalL Density of States

With the vibrational modes of MalL now computed and read into MATLAB, the next step of the `Enzyme_Harmonic_Vibrations_Pack` is to run the script `Solve_Density_of_States` to calculate

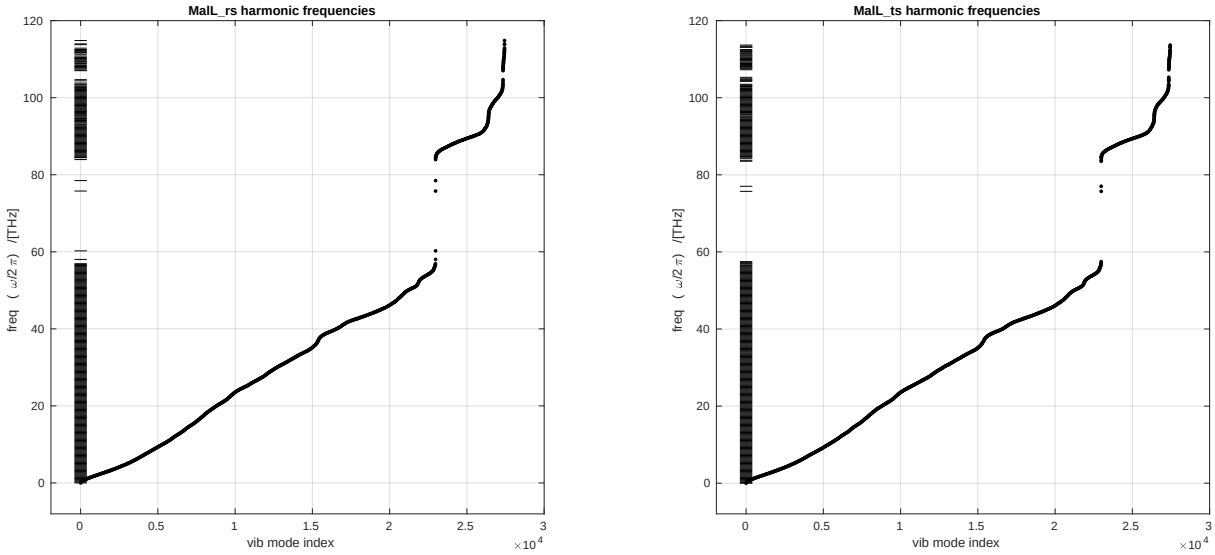

(a) Reaction state **(b)** Transition state

Figure 2.17: MalL harmonic normal mode frequencies

the DoS using 1,000 histograms bins of bandwidth 0.12 THz. The distribution of vibrational states appears equivalent for both the RS and TS states (Fig. 2.18); the main perceivable difference is the modes 22,985 (75.71 THz) and 22,986 (77.03 THz), in the mostly transparent bandwidth between 60-80 THz. Their difference is due to the substrate analogue that has been inserted into the active site, and are perhaps the modes pertaining to the substrate analogue, not the enzyme. In order to locate the vibrational modes most associated with the enzyme's active site, the dynamical eigenvector matrix must be computed. Research performed by Ben-Avraham and colleagues has shown that there is a universality for the DoS of proteins [120], thus for the quantum phonon model, I take these structures to be a general enzyme which stimulates the molecule.

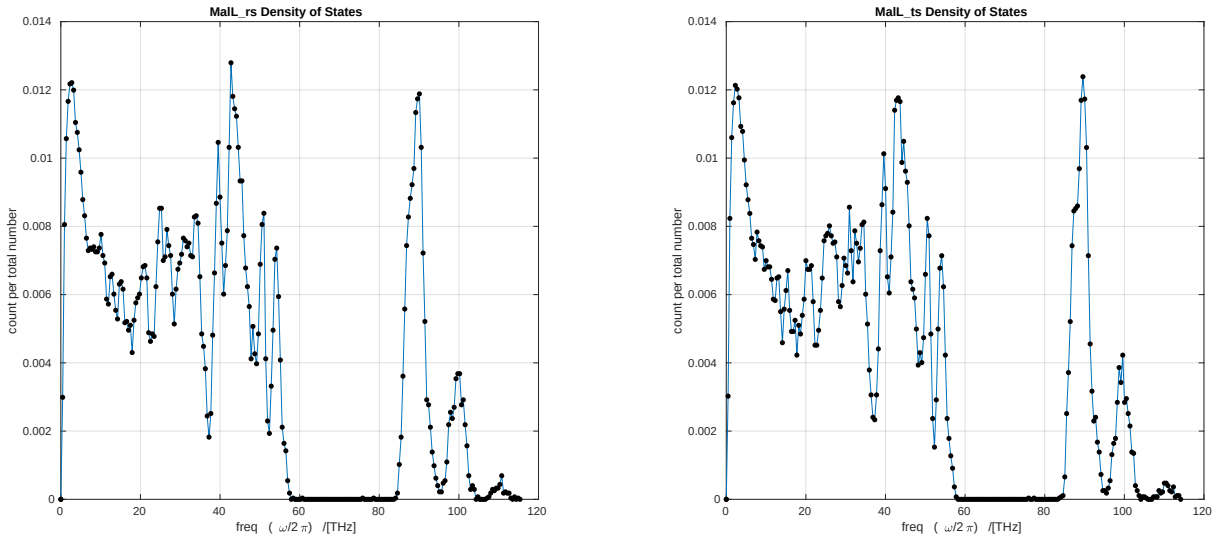

(a) Reaction state **(b)** Transition state

Figure 2.18: MalL density of state

2.9 Conclusions

In this chapter, I have detailed the mathematical foundations of the molecular vibrational NMA as used by GAUSSIAN 09. With the theory established, I have explained how to construct a digitised model and run a MD experiment within the GAUSSIAN 09 software for molecules, and in GROMACS for the enzyme. Then I have heuristically demonstrated the preparatory coding work that I have built in MATLAB to extract and process the raw output data from the MD data, with accompanying figures for the appropriate quantities that will be used in the catalytic EoM solver. I have established a pathway of methodology to use the data for the investigation of the stretching of particular atomic bonds due to each vibrational mode. The data shown has been for glucose and isomaltose, and the discussion was made for glycosidic hydrolysis via the action of the MalL enzyme.

In the next chapter, I will extend the classical harmonic model by utilising the tool set of quantum mechanics in order to determine the response behaviour and thermodynamics of the molecular vibrational modes of isomaltose to the stimulus delivered by MalL.

Chapter 3

Quantum Harmonic Molecular Vibrations

In this chapter, I will explore the Quantum Harmonic Oscillator (QHO) model of a molecule that is driven by a stimulus (enzyme or solvent) and immersed in a thermal environment. I derive the molecular Equations of Motion (EoMs) by inserting the QHO Hamiltonian into a dissipative Quantum Master Equation (QME). I then obtain the EoM steady states and their stability, before analytically solving the EoM for the expectation value of the phonon number operator for each vibrational mode. Finally, I demonstrate the response spectrogram of energy and heat capacity of a QHO model of glucose and isomaltose in response to MalL. I provide a more detailed description of the quantum state and the derivation of the QME in **Appendix A**.

3.1 Preliminary Mathematics

Before I describe the QHO molecule, I will provide an introduction to some of the mathematical tools that I will use throughout this thesis. In particular, I will demonstrate the transformation of classical state space variables into quantum operators, whose non-commutational algebra is central for the derivation of the EoMs for the molecular quantum state.

3.1.1 Non-Commutational Algebra

Is there any condition for when $AB \neq BA$? When dealing with scalars (real and imaginary numbers), the order does not matter — doubling and then tripling (3×2) is the same as tripling then doubling (2×3), and both result in a final state that is six times larger, $2 \times 3 = 3 \times 2$. However, it is possible for $AB \neq BA$ when A and B are *operators* whose *order of operations* is important since the product AB may not result in the same final state as BA — this is true for most real-life processes. The mathematical concept that has been introduced here is *non-commutational algebra*, wherein the order of operations, A and B, leads to different resultant states. The difference is described by the commutation bracket which is defined [63]

$$[A\ ,\ B]\ \equiv\ AB\ -\ BA \tag{3.1}$$

If $[A, B] = 0$, then A and B are said to be *commutative*, and are dynamically distinct since $AB = BA$; if $[A, B] \neq 0$, then the operators are said to be *non-communititive* since $AB \neq BA$,

and are dynamically interrelated. The non-commutational algebra of operators is at the heart of quantum mechanics, as will be seen in this chapter.

3.1.2 Transformation into Quantum Mechanical State Spaces in 1D

In this section, I will demonstrate the quantisations in 1D that result in a Hamiltonian for a QHO. This is a well-known formalism that was developed for general quantum fields and atomic undulations over the early 20^{th} century [59,121] that I will demonstrate in my own procedure for the bosonic operators that describe molecular phonons based upon [58]. In classical Hamiltonian mechanics, the state at some position has an associated conjugate momentum, and necessitates that not only that these measures are inseparable, but hints that there is a state space coordinate where both variables are treated as one. In quantum Hamiltonian mechanics, this coordinate transformation is achieved by the creation and annihilation operators which act on a quantum state. The transformation procedure is known as the first and second quantisations: the first quantisation transforms the position and momentum variables into non-dimensionalised operators; the second quantisation transforms these operators into the creation and annihilation operators, the product of which is the number operator [56, 58]. The Hamiltonian of the QHO model is entirely described by this number operator, and hence the evolution of the quantum state of a QHO molecule is elucidated upon deriving an EoM for the number operator.

I will begin the quantisation of variables by making use of the Schödinger equation for the evolution of an arbitrary quantum wave state in (1+1)-dimensional spacetime, $\Psi(t,x)$

$$i\hbar\,\partial_t\Psi \;=\; \mathcal{H}\;\Psi \tag{3.2}$$

where $i = \sqrt{-1}$ is the imaginary unit, $\hbar$ is the reduced Planck constant (with dimensions [energy][time] = [mass][space]^2[time]$^{-1}$), $\partial_t \equiv \frac{\partial}{\partial t}$ is the operator notation for the partial derivative with respect to time, and the Hamiltonian is the summation of potential and kinetic energies, $\mathcal{H} = \mathcal{T} + \mathcal{V}$. The Hamiltonian, $\mathcal{H}$, for an arbitrary potential energy, $\mathcal{V}$, in terms of the classical scalar position, x, and momentum, p, is

$$\mathcal{H}(x,p) \;=\; \frac{1}{2m}\,p^2 \;+\; \mathcal{V}(x) \tag{3.3}$$

By assuming that a solution to (3.2) is a plane-wave that is proportional to a $(1+1)$-D phasor, $\Psi(t,x) \propto \exp\left[i\,(px/\hbar \;-\; \omega t)\right]$, then upon taking the spatial derivative, $\partial_x\Psi$, and subsequent rearrangement for p, the momentum can be expressed by a differential *operator*, $\tilde{p} = -i\hbar\,\partial_x$, which retains dimensions of [momentum]=[mass][space][time]$^{-1}$. The resultant kinetic energy differential operator is then, $\hat{\mathcal{T}} = -\frac{\hbar^2}{2m}\,\partial_x^2$. This relation can be extended to higher spatial dimensions by replacement of the partial derivative with the del operator: $\tilde{p} = -i\hbar\nabla$. The position operator is simply the scalar-valued position, $\tilde{x} = x$, (with dimensions of [space]) and gives the harmonic potential operator, $\hat{\mathcal{V}} = \frac{1}{2}m\omega^2\;\tilde{x}^2$. The QHO Hamiltonian in $(\tilde{x},\tilde{p})$ state space is then a differential operator, which upon substitution of $\hat{\mathcal{T}}$ and $\hat{\mathcal{V}}$ into (3.2) defines the well-known Schrödinger partial differential equation in time and space for the QHO evolution of state, Ψ. By applying the definition of the commutation bracket (3.1) to an arbitrary wave

function, $\Psi(x)$

$$\begin{aligned}\left[\tilde{x}\ ,\ \tilde{p}\right]\ \Psi\ &=\ \tilde{x}\ \tilde{p}\ \Psi\ -\ \tilde{p}\ \tilde{x}\ \Psi \\ &=\ (-i\hbar)\ x\ \partial_x\Psi\ -\ (-i\hbar)\ \partial_x(x\ \Psi) \\ &=\ i\hbar\ \Big(-\ x\ \partial_x\Psi\ +\ x\ \partial_x\Psi\ +\ \Psi\Big) \\ &=\ i\hbar\ \Psi \end{aligned} \tag{3.4}$$

then by equating the action on Ψ, the commutation bracket is,

$$\left[\tilde{x},\tilde{p}\right]\ =\ i\hbar\,\hat{1} \tag{3.5}$$

where $\hat{1}$ is the unity operator which always commutes since, $\hat{1}\Psi\ =\ \Psi\hat{1}\ =\ \Psi$. This result is known as the position–momentum operator grand canonical commutation relation.

3.1.3 Dimensionless Position and Momentum Operators

The QHO Hamiltonian, $\mathcal{H}(\tilde{x},\tilde{p}) = \frac{1}{2m}\ \tilde{p}^2\ +\ \frac{1}{2}m\omega^2\ \tilde{x}^2$, is a sum of squares and therefore can be expressed in terms of one complex variable, in the manner of $z = u + iv$, with absolute magnitude $|z|^2\ =\ zz^*\ =\ (u+iv)(u-iv)\ =\ u^2+v^2$. By associating position and momentum to be the real and imaginary components of some imaginary-valued operator, a simpler expression for the Hamiltonian is expected. The position and momentum operator commutation relation (3.5) can be non-dimensionalised by division of $\hbar$, then using the commutation identity, $[\hat{A},\hat{B}] = [c\hat{A},\ c^{-1}\hat{B}]$, for any arbitrary operators $\hat{A},\hat{B}$ and scalar c. The $(\tilde{x},\tilde{p})$ commutation relation becomes, $i\,\hat{1} = \left[\frac{c}{\sqrt{\hbar}}\ \tilde{x}\ ,\ \frac{1}{c\sqrt{\hbar}}\ \tilde{p}\right]$, for a parameter c that carries dimensions of $[\text{mass}]^{1/2}[\text{time}]^{-1/2}$. The dimensioned position and momentum operators, $(\tilde{x},\tilde{p})$, can then be transformed into dimensionless operators $(\hat{q},\hat{p})$ by, $\tilde{x} = \frac{\sqrt{\hbar}}{c}\ \hat{q}$ and $\tilde{p} = c\sqrt{\hbar}\ \hat{p}$, with commutation relation, $\left[\hat{q},\hat{p}\right] = i\,\hat{1}$, by construction. The undetermined parameter, c, can be fixed by the QHO Hamiltonian upon substitution of $\hat{q}$, and $\hat{p}$ into (3.3), giving, $\hat{\mathcal{H}}(\hat{q},\hat{p}) = \frac{\hbar\omega}{2}\ \left(\frac{c^2}{m\omega}\ \hat{p}^2 + \frac{m\omega}{c^2}\ \hat{q}^2\right)$. By setting $c = \sqrt{m\omega}$, the dimensionless position and momentum operators are defined to be $\hat{q} = \sqrt{\frac{m\omega}{\hbar}}\ \tilde{x}$ and $\hat{p} = \frac{1}{\sqrt{\hbar m\omega}}\ \tilde{p}$, the 1D QHO Hamiltonian is transformed to

$$\hat{\mathcal{H}}(\hat{q},\hat{p})\ =\ \frac{\hbar\omega}{2}\ \left(\hat{p}^2\ +\ \hat{q}^2\right) \tag{3.6}$$

3.1.4 Creation and Annihilation Operators

Now that the QHO Hamiltonian is expressed as the sum of two squares, a dimensionless imaginary-valued operator can be defined by

$$\hat{a}\ =\ \frac{1}{\sqrt{2}}\ \Big(\hat{q}\ +\ i\hat{p}\Big) \tag{3.7a}$$

$$\hat{a}^\dagger\ =\ \frac{1}{\sqrt{2}}\ \Big(\hat{q}\ -\ i\hat{p}\Big) \tag{3.7b}$$

where $\hat{a}^\dagger$ is the Hermitian conjugate (dagger) transpose operator of $\hat{a}$. The inverse maps to the dimensionless position and momentum operators are

$$\hat{q} \;=\; \frac{1}{\sqrt{2}}\,\Big(\hat{a}^\dagger \;+\; \hat{a}\Big) \tag{3.8a}$$

$$\hat{p} \;=\; \frac{i}{\sqrt{2}}\,\Big(\hat{a}^\dagger \;-\; \hat{a}\Big) \tag{3.8b}$$

The complete transformation from the dimensioned position and momentum operators to these new operators, $(\tilde{x}, \tilde{p}) \mapsto (\hat{a}, \hat{a}^\dagger)$, is

$$\hat{a} \;=\; \frac{1}{\sqrt{2\hbar m\omega}}\,\big(m\omega\;\tilde{x} \;+\; i\,\tilde{p}\big) \tag{3.9a}$$

$$\hat{a}^\dagger \;=\; \frac{1}{\sqrt{2\hbar m\omega}}\,\big(m\omega\;\tilde{x} \;-\; i\,\tilde{p}\big) \tag{3.9b}$$

These are called the annihilation $\hat{a}$, and creation $\hat{a}^\dagger$ operators, which are the fundamental state space coordinates (observables) used in quantum mechanics, whose real and imaginary components represent the position and momentum, respectively. The inverse mapping from creation and annihilation operators to the dimensioned position and momentum operators, $(\hat{a}, \hat{a}^\dagger) \mapsto (\tilde{x}, \tilde{p})$, is performed by

$$\tilde{x} \;=\; \sqrt{\frac{\hbar}{2m\omega}}\;(\hat{a}^\dagger \;+\; \hat{a}) \tag{3.10a}$$

$$\tilde{p} \;=\; i\sqrt{\frac{\hbar m\omega}{2}}\;(\hat{a}^\dagger \;-\; \hat{a}) \tag{3.10b}$$

which will be used in the transformation of the QHO and QAO molecular Hamiltonians. The grand canonical commutation relation of the creation and annihilation operators is found by, $\big[\hat{a},\,\hat{a}^\dagger\big] = \frac{1}{i\hbar}\,\big[\tilde{x},\,\tilde{p}\big]$, then using the commutation relation (3.5) yields

$$\big[\hat{a},\,\hat{a}^\dagger\big] \;=\; \hat{a}\,\hat{a}^\dagger \;-\; \hat{a}^\dagger\,\hat{a} \;=\; \hat{1} \tag{3.11}$$

Thus the $(\hat{a}, \hat{a}^\dagger)$ grand canonical commutation relation is simply the *unity operator*.

3.1.5 Phonon Number Operator

The QHO Hamiltonian can now be transformed to coordinate operators, $\hat{\mathcal{H}}(\hat{a}, \hat{a}^\dagger)$, by substitution of (3.10b) into the kinetic energy operator giving, $\hat{\mathcal{T}} = -\frac{\hbar\omega}{4}\,\big(\hat{a}^\dagger\hat{a} + \hat{a}\hat{a}^\dagger - \hat{a}^\dagger\hat{a}^\dagger - \hat{a}\hat{a}\big)$, and (3.10a) for the QHO potential operator, $\hat{\mathcal{V}} = \frac{\hbar\omega}{4}\,\big(\hat{a}^\dagger\hat{a} + \hat{a}\hat{a}^\dagger + \hat{a}^\dagger\hat{a}^\dagger + \hat{a}\hat{a}\big)$. The Hamiltonian via (3.3) yields $\hat{\mathcal{H}} = \frac{\hbar\omega}{2}\big(\hat{a}^\dagger\hat{a} + \hat{a}\hat{a}^\dagger\big)$, then by making use of (3.11) the QHO Hamiltonian is, $\hat{\mathcal{H}} = \hbar\omega\,\big(\hat{a}^\dagger\hat{a} + \frac{1}{2}\big)$. By defining an operator, $\hat{n} \equiv \hat{a}^\dagger\hat{a}$, the QHO Hamiltonian can be completely expressed in terms of a single operator

$$\hat{\mathcal{H}}(\hat{n}) \;=\; \hbar\omega\,\left(\hat{n} \;+\; \frac{1}{2}\right) \tag{3.12}$$

The operator, $\hat{n}$, is known as the number operator which is Hermition, $\hat{n}^\dagger = \hat{n}$, and the commutation relations with the creation and annihilation operators are

$$[\,\hat{a}\;,\;\hat{n}] \;=\; \hat{a}\,\hat{a}^\dagger\hat{a} \;-\; \hat{a}^\dagger\hat{a}\hat{a} \;\;=\;\; +\,\hat{a} \tag{3.13a}$$

$$[\hat{a}^\dagger,\;\hat{n}] \;=\; \hat{a}^\dagger\hat{a}^\dagger\hat{a} \;-\; \hat{a}^\dagger\hat{a}\hat{a}^\dagger \;\;=\;\; -\,\hat{a}^\dagger \tag{3.13b}$$

where the $(\hat{a}^\dagger, \hat{a})$ commutation relation (3.11) is used to reorganise the order of operations resulting in the cancellation of the terms with three operators.

The action of the number operator, $\hat{n}$, upon the eigenstate, $|n\rangle$, is to give the phonon number eigenvalue, n, via the eigenvalue equation, $\hat{n}|n\rangle = n|n\rangle$. For an eigenstate (ket vector), $|n\rangle$, the eigenvalue is a non-negative integer, $n \in \mathbb{Z}_{\geq 0}$, that describes the quantised number of phonons in that vibrational mode, with $|0\rangle$ representing the unoccupied state that has no phonons, $\hat{n}|0\rangle = 0$, known as the ground state or the vacuum state. The operator $\hat{a}$ acts to lower the number state by one, $\hat{a}|n\rangle = \sqrt{n}|n-1\rangle$, and the conjugate operator $\hat{a}^\dagger$ acts to raise the number state by one, $\hat{a}^\dagger|n\rangle = \sqrt{n+1}|n+1\rangle$, thus earning them their names as the *creation* and *annihilation* operators as they represent the addition and subtraction of a single phonon, respectively. The QHO Hamiltonian (3.12) can be applied to an arbitrary vibrational eigenstate to obtain its energy levels, $\hat{\mathcal{H}}\,|n\rangle = E\,|n\rangle$, and is evaluated by the much simpler eigenvalue equation, $\hat{n}\,|n\rangle = n\,|n\rangle$. The energy of this eigenstate is then, $E_n = \hbar\omega(n + \frac{1}{2})$, showing that the energy levels are evenly spaced by $\hbar\omega$, and the vacuum state $|0\rangle$ has energy $\hbar\omega/2$, which is known as the zero point energy. I provide a more detailed description of the quantum bra-ket notation in **Appendix A**.

3.2 Quantum Harmonic Oscillator Molecular Energetics

In this section, I will demonstrate a QHO molecular Hamiltonian that uses the physical quantities that are obtained by NMA. The subsequent derivation for the 3D Hamiltonian of a harmonic quantum crystal follows the procedure in *'The Physics of Phonons'* by Srivastava [56], a standard reference book within the studies of phonons. Much of Srivastava's work uses the infinite crystal model, wherein a unit cell is tessellated throughout space infinitely, as this simplifies the mathematical treatment. While this approach is useful in the study of (relatively) large objects such as macroscopic regular crystals and semiconductors, an individual molecule cannot be treated as an infinite crystal. I will be demonstrating Srivastava's general derivation for crystalline atomic undulations about an equilibrium in a procedure that is readily extended to account for the anharmonicities, which will be the subject of **Chapter 4**.

3.2.1 The Harmonic Approximation for Molecular Potential Energy

The dynamics of a molecule can be described by a collection of N_{atom} atomic nuclei in 3D Cartesian coordinates, $r \in \{x, y, z\}$. Let the equilibrium position of atom b in coordinate r be x_{rb}^{eqm}, then the deviation from equilibrium is, $u_{rb}(t) \;=\; x_{rb}(t) \;-\; x_{rb}^{\text{eqm}}$. Similarly to the classical harmonic model (**§ 2.2.2**), the 3D potential energy $\mathcal{V}$ is expanded in a second-order Taylor power series with respect to the atomic displacements: $\mathcal{V}_{\text{QHO}} \;=\; \mathcal{V}_0 \;+\; \mathcal{V}_1 \;+\; \mathcal{V}_2$. The zeroth-order

term, $\mathcal{V}_0$, is the scalar-valued equilibrium potential energy, the first-order term describes the potential forces

$$\mathcal{V}_1 \;=\; \sum_{r}^{xyz} \sum_{b=1}^{N_{\text{atom}}} \left(\frac{\partial \mathcal{V}}{\partial u_{rb}} \right) \Bigg|_{\text{eqm}} u_{rb} \tag{3.14}$$

and the second-order term describes the curvature of the potential

$$\mathcal{V}_2 \;=\; \frac{1}{2} \sum_{r,r'}^{xyz} \sum_{b,b'=1}^{N_{\text{atom}}} \left(\frac{\partial^2 \mathcal{V}}{\partial u_{rb}\, \partial u_{r'b'}} \right) \Bigg|_{\text{eqm}} u_{rb}\; u_{r'b'} \tag{3.15}$$

where the summation is over the atom labels, $b \in [1, N_{\text{atom}}] \cap \mathbb{N}$, and each of the 3 Cartesian spatial coordinates $r \in \{x, y, z\}$. The scalar term $\mathcal{V}_0$ describes the minimum of the potential, and can be set to zero by taking it to be the datum by a redefinition: $\mathcal{V} - \mathcal{V}_0 \;\rightarrow\; \mathcal{V}$. The first-order linear term, $\mathcal{V}_1$, is assumed to be zero, since the forces are taken to be zero at the equilibrium under the harmonic approximation, $(\partial_{u_{rb}} \mathcal{V})|_{\text{eqm}} \;=\; 0$. The second-order term $\mathcal{V}_2$ contains the Hessian matrix of second derivatives, and encapsulates the torsion-free local *curvature* of the potential energy field. Therefore, the QHO potential energy is $\mathcal{V}_{\text{QHO}} = \mathcal{V}_2$. The higher-order terms are the anharmonicities and are active (non-zero) if the curvature of the potential energy has a gradient with respect to an atomic displacement (**Chapter 4**).

3.2.2 Molecular Dynamical Matrix and QHO Energy Operators

As was shown in **§ 2.3.3**, the Christoffel dynamical matrix for an atom bound to a molecule has elements, $D(rb|r'b')$, given by (2.11), which composes a square matrix of size $3N_{\text{atom}} \times 3N_{\text{atom}}$. The eigendecompositon of the Christoffel dynamical matrix, $\mathbf{D} = \mathbf{L}\mathbf{\Lambda}\mathbf{L}^{-1}$, defines the eigenvalue $\mathbf{\Lambda}$ and eigenvector $\mathbf{L}$ matrices, from which the eigenfrequencies, ω_k, are

$$\Lambda_{kk'} \;=\; \omega_k^2\, \delta_{kk'} \;=\; \sum_{r,r'}^{xyz} \sum_{b,b'=1}^{N_{\text{atom}}} L^{-1}(rb|k)\; D(rb|r'b')\; L(r'b'|k') \tag{3.16}$$

The deviation operator for atom b in Cartesian coordinate r due to all vibrational modes k can now be expressed in terms of the creation and annihilation operators, or the position operator via (3.10a) to be

$$\hat{u}_{rb} \;=\; \sum_{k=1}^{N_{\text{mode}}^{\text{mol}}} \sqrt{\frac{\hbar}{2\, m_b\, \omega_k}}\; L(rb|k)\; \left(\hat{a}_k^\dagger \;+\; \hat{a}_k \right) \tag{3.17a}$$

$$\;=\; \sum_{k=1}^{N_{\text{mode}}^{\text{mol}}} \sqrt{\frac{\hbar}{m_b\, \omega_k}}\; L(rb|k)\; \hat{q}_k \tag{3.17b}$$

where the eigenvector acts as a projection onto the vibrational mode direction [56]. The subsequent summations over the molecular vibrational modes, $k \;\in\; [1, N_{\text{mode}}^{\text{mol}}] \cap \mathbb{N}$, will be denoted as $\sum_k^{\text{mol}}$ for readability. The quadratic potential term can then be promoted to a quantum operator, $\hat{\mathcal{V}}_2$, in terms of $\hat{a}_k$, $\hat{a}_k^\dagger$ and the dynamical eigenstates via substitution of

(3.17) in (3.15)

$$\hat{\mathcal{V}}_2 \;=\; \frac{1}{4}\sum_{k,k'}^{\text{mol}}\sum_{r,r'}^{xyz}\sum_{b,b'=1}^{N_{\text{atom}}}\frac{\hbar}{\sqrt{\omega_k\;\omega_{k'}}}\;L(rb|k)\;L(r'b'|k')\;D(rb|r'b')\;\left(\hat{a}_k^\dagger\;+\;\hat{a}_k\right)\left(\hat{a}_{k'}^\dagger\;+\;\hat{a}_{k'}\right) \tag{3.18}$$

Upon use of (3.16) and the orthogonality of eigenvectors, the QHO molecular potential energy operator is

$$\hat{\mathcal{V}}_2 \;=\; \sum_{k}^{\text{mol}}\frac{\hbar\omega_k}{4}\;\left(\hat{a}_k^\dagger\;+\;\hat{a}_k\right)^2 \tag{3.19}$$

which is parameterised only by the vibrational mode frequency, with dynamics due to the creation and annihilation operators. A similar procedure reveals the QHO kinetic energy operator to be

$$\hat{\mathcal{T}}_2 \;=\; -\sum_{k}^{\text{mol}}\frac{\hbar\omega_k}{4}\;\left(\hat{a}_k^\dagger\;-\;\hat{a}_k\right)^2 \tag{3.20}$$

By taking the summation of the kinetic and potential energy operators, then using the commutation relation (3.11), the molecular QHO Hamiltonian is

$$\hat{\mathcal{H}}_{\text{mol}} \;=\; \sum_{k}^{\text{mol}}\hbar\omega_k\;\left(\hat{n}_k\;+\;\frac{1}{2}\right) \tag{3.21}$$

The molecular Hamiltonian is given by the summation of the individual vibrational modes, $\hat{\mathcal{H}}_{\text{mol}} = \sum_k^{\text{mol}}\hat{\mathcal{H}}_k$, where each vibrational mode contributes, $\hat{\mathcal{H}}_k$, to the molecule. These are independent oscillators, and as such the QHO molecular vibrational modes do not interact.

3.2.3 Vibrational Energy, ZPE, and Thermal Equilibrium

The energy of a single QHO vibrational mode is given by taking the expectation value of the Hamiltonian, $E_k \;=\; \langle\hat{\mathcal{H}}_k\rangle$, and the energy of a QHO molecule is the expectation value of (3.21)

$$E_{\text{mol}} \;=\; \sum_{k}^{\text{mol}}\hbar\omega_k\;\left(\langle\hat{n}_k\rangle\;+\;\frac{1}{2}\right) \tag{3.22}$$

The QHO molecular energy is scalar-valued a function in terms of, $\langle\hat{n}_k\rangle$, and, ω_k, for each vibrational mode, and is given by the summation of the contributions of each individual vibrational mode, $E_{\text{mol}} \;=\; \sum_k^{\text{mol}} E_k$. I provide a detailed explanation of the expectation values of a quantum observable in **Appendix A**; in the current context, $\langle\hat{n}_k\rangle$ represents the mean average value for the phonon number in vibrational mode k. The energies associated with a single vibrational mode are on the order of zeptojoules (1 zJ $= 10^{-21}$ J $= 602.2$ J.mol^{-1} $= 6.242 \;\times\; 10^{-3}$ eV), and the energy of molecules are on the order of attojoules (1 aJ $= 10^{-18}$ J $= 602.2$ kJ.mol^{-1} $=$ 6.242 eV).

The minimum of potential energy for the molecule is the lowest energy eigenstate of (3.21), characterised by the state wherein all of the molecular vibrational modes have zero phonons (unoccupied), $\hat{n}_k|0\rangle \;=\; 0$, $\forall k \in [1, N_{\text{mode}}^{\text{mol}}] \cap \mathbb{N}$. If this is a stationary state, then it is known as the *ground state* or *vacuum state* in quantum field theory, the corresponding energy value is the

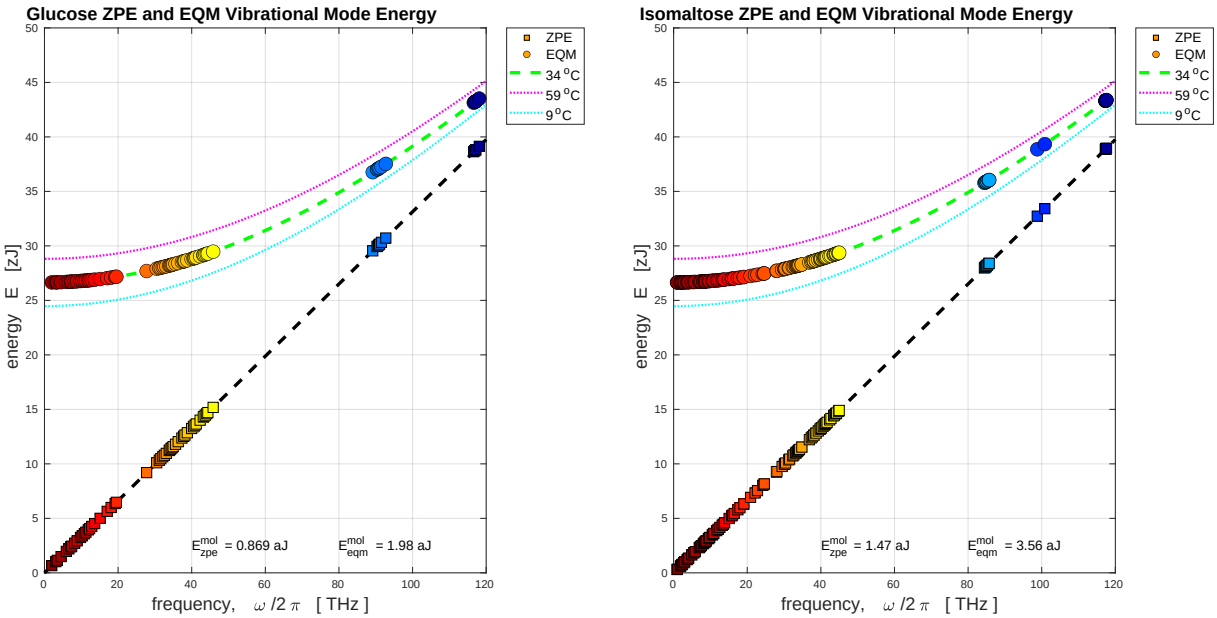

(a) Glucose **(b)** Isomaltose

Figure 3.1: Glucose and Isomaltose vibrational mode QHO ZPE and thermal equilibrium (EQM) energy distributions. The thermal equilibrium (EQM) values lie along the curve (3.25) drawn at temperatures 9°C (cyan), 34°C (dashed green), and 59°C (magenta), and the ZPE values lie on the line $\hbar\omega/2$, which coincides with a thermal equilibrium at absolute zero temperature (0 K) (dashed black).

Zero Point Energy (ZPE) [53,122]; the energy of any excited state will be higher than the ZPE. By setting all phonon occupation number operators in (3.21) to zero, the molecular ZPE is

$$E^{\text{zpe}}_{\text{mol}} \;=\; \sum_{k}^{\text{mol}} \frac{\hbar\omega_k}{2} \tag{3.23}$$

with each vibrational mode contributing, $E^{\text{zpe}}_k = \hbar\omega_k/2$, to the total. Fig. 3.1 shows that the total molecular ZPE for isomaltose is 147 aJ, with the highest frequency vibrational mode (normal mode 120 of frequency $\omega_{120}/2\pi = 117.6$ THz) contributing the most with 39.0 zJ. In comparison, glucose has a ZPE of 869 zJ, and the summation of two glucose molecules is 268 zJ more than a single isomaltose; the ZPE for one molecule of water is 92.2 zJ which accounts for some of this discrepancy. The thermal equilibrium of the molecule is the state where all vibrational modes have an expectation value of phonon occupation number sampled from the Planck distribution, $\langle \hat{n}_k \rangle = \bar{n}_k$, where

$$\bar{n}_k(T) \;\equiv\; \left(\exp\left(\frac{\hbar\omega_k}{k_B T} \right) \;-\; 1 \right)^{-1} \tag{3.24}$$

Physically, the Planck distribution describes the average number of phonons in a vibrational mode k that is at a thermal equilibrium with a harmonic reservoir at temperature, T (in Kelvin), and it is assumed that all vibrational modes of the solid are non-interacting [56]. Therefore, the energy of one vibrational mode at thermal equilibrium is $E^{\text{eqm}}_k = \hbar\omega_k(\bar{n}_k + 1/2)$. The molecular energy at thermal equilibrium is determined by setting $\langle \hat{n}_k \rangle = \bar{n}_k$ for all vibrational modes in

(3.21)

$$E^{\text{eqm}}_{\text{mol}}(T) \;=\; \sum_{k}^{\text{mol}} \hbar\omega_k \;\left(\bar{n}_k(T) \;+\; \frac{1}{2}\right) \tag{3.25a}$$

$$\;=\; \sum_{k}^{\text{mol}} E^{\text{zpe}}_{k} \;\coth\left(\frac{\hbar\omega_k}{2\,k_B T}\right) \tag{3.25b}$$

where $2\bar{n}_k+1 = \coth(\hbar\omega_k/2k_BT)$ has been used to express the vibrational mode thermal equilibrium energy levels in terms of the hyperbolic cotangent ($\coth(x) = 1/\tanh(x)$) and the ZPE. In the limit of absolute zero temperature, $T = 0$ K, the thermal equilibrium is at the ZPE for all vibrational modes ($\coth(\infty) = 1$). The thermal equilibrium energy for isomaltose at a biologically relevant temperature of 34°C is 3.56 aJ, with the highest vibrational mode contributing 43.4 zJ. By raising the temperature to 59°C, the thermal equilibrium isomaltose energy is 3.80 aJ, and when lowering to 9°C, the energy is reduced to 3.33 aJ; a ±7% change for ± 25°C.

3.3 Equations of Motion for the QHO Molecule

In this section, I will derive the quantum state EoMs for the QHO molecular model that experiences an external stimulus from surrounding molecules and dissipation into a thermal environment. The solutions to the model EoMs describe how the expectation values of the molecular vibrational mode quantum states evolve in time. The phonon quantum state space operators for vibrational mode k are the annihilation, creation, and number operators, ($\hat{a}_k,\ \hat{a}^\dagger_k,\ \hat{n}_k$); which can be equivalently described by the position, momentum and number operators, ($\hat{q}_k,\ \hat{p}_k,\ \hat{n}_k$). The vibrational mode EoMs are generated upon evaluating each state space operator in the QME, similarly to the Euler-Lagrange equation of classical mechanics. The catalytic model is constructed once the EoMs for all quantum state operators for each vibrational mode are determined.

The total QME contains contributions from the free behaviour, a response to stimulus and dissipation

$$\partial_t\langle\hat{\mathcal{M}}\rangle \;=\; \partial_t\langle\hat{\mathcal{M}}\rangle_{\text{free}} \;+\; \partial_t\langle\hat{\mathcal{M}}\rangle_{\text{int}} \;+\; \partial_t\langle\hat{\mathcal{M}}\rangle_{\text{diss}} \tag{3.26}$$

where the angled braces denote the expectation value, defined as the trace over the reduced density operator, $\langle\hat{\mathcal{M}}\rangle = \text{Tr}[\hat{S}\,\hat{\mathcal{M}}]$, and behave as scalar-valued classical functions. This expression is similar to the Ehrenfest theorem for the temporal derivative of the expectation value of an arbitrary system observable; if the observables are position and velocity, then this result is closely related to the Liouvelle theorem of classical mechanics [60]. Details on the QME are in **Appendix A**.

3.3.1 Free Behaviour of the QHO Molecule

The free QHO QME for state space operator, $\hat{\mathcal{M}} = \hat{\mathcal{M}}(t;\, \hat{a}_k(t))$, for vibrational mode k is

$$\partial_t \langle \hat{\mathcal{M}}(t) \rangle_{\text{free}} \;=\; \frac{1}{i\hbar} \left\langle \Big[\hat{\mathcal{M}} \;,\; \hat{\mathcal{H}} \Big] \right\rangle \tag{3.27}$$

This is derived from the von Neumann equation that describes the evolution of a quantum state density operator, however the commutation is reversed due to performing the trace. Inserting the vibrational mode Hamiltonian, $\hat{\mathcal{H}}_k \;=\; \hbar\omega_k \left(\hat{n}_k + \frac{1}{2}\right)$, into the free QME generates the free EoM for the expectation value of $\hat{\mathcal{M}}$

$$\partial_t \langle \hat{\mathcal{M}}(t) \rangle_{\text{free}} \;=\; -\, i\omega_k \left\langle \Big[\hat{\mathcal{M}} \;,\; \hat{n}_k \Big] \right\rangle \tag{3.28a}$$

The ZPE contribution vanishes since scalars always commute, $[\hat{\mathcal{M}}, E_k^{\text{zpe}}] = E_k^{\text{zpe}}[\hat{\mathcal{M}}, \hat{1}] = 0$. Therefore the problem of deriving the free QHO EoMs boils down to computing the commutation bracket of $\hat{\mathcal{M}}$ with the phonon number operator $\hat{n}_k$. Upon using the commutation relations (3.13), the free QHO EoMs are

$$\partial_t \langle \hat{a}_k(t) \rangle_{\text{free}} \;=\; -\, i\omega_k \, \langle \hat{a}_k(t) \rangle \tag{3.29a}$$

$$\partial_t \langle \hat{a}_k^\dagger(t) \rangle_{\text{free}} \;=\; +\, i\omega_k \, \langle \hat{a}_k^\dagger(t) \rangle \tag{3.29b}$$

$$\partial_t \langle \hat{n}_k(t) \rangle_{\text{free}} \;=\; 0 \tag{3.29c}$$

These are uncoupled first-order ODEs whose solutions, $\langle \hat{a}_k(t) \rangle_{\text{free}} \;=\; \langle \hat{a}_k(0) \rangle \, e^{-i\omega_k t} \;=\; \langle \hat{a}_k^\dagger(t) \rangle_{\text{free}}^\dagger$, show that the creation and annihilation operators evolve in time as counter-rotating phasors at frequency, ω_k, with a constant complex amplitude set by the initial state, and the phonon number (and hence the energy) remains constant.

3.3.2 QHO Interaction Hamiltonian

The substrate molecule is perturbed from its free behaviour due to its external surroundings, which can be taken to be the enzyme, a solvent, or the aqueous internal contents of a biological cell. The total Hamiltonian for two interacting QHO systems can be partitioned as two distinct QHOs and their interaction, $\hat{\mathcal{H}} = \hat{\mathcal{H}}_{\text{mol}} + \hat{\mathcal{H}}_{\text{ext}} + \hat{\mathcal{H}}_{\text{int}}$. The QHO Hamiltonian for the external system is

$$\hat{\mathcal{H}}_{\text{ext}} \;=\; \sum_{j}^{\text{ext}} \hbar\omega_j \, \left(\hat{b}_j^\dagger \hat{b}_j \;+\; \frac{1}{2} \right) \tag{3.30}$$

where $\hat{b}_j$ ($\hat{b}_j^\dagger$) is the annihilation (creation) operator that pertains to the removal (addition) of one phonon in mode j with frequency ω_j, and the summation is over all external modes, $j \in [1, N_{\text{mode}}^{\text{ext}}] \cap \mathbb{N}$. The molecule and external operators are commutative $[\hat{a}_k,\; \hat{b}_k^\dagger] = 0$, meaning that they are dynamically distinct. The interaction Hamiltonian between all molecular modes

k and all modes j of the external system is

$$\hat{\mathcal{H}}_{\text{int}} \;=\; \sum_{k}^{\text{mol}} \sum_{j}^{\text{ext}} \hbar \chi_{kj} \; \left(\hat{a}_k^\dagger \; \hat{b}_j \;+\; \hat{a}_k \; \hat{b}_j^\dagger \right) \; \delta(\omega_k \;-\; \omega_j) \tag{3.31a}$$

$$= \; \hbar \sum_{k}^{\text{mol}} \left(\hat{a}_k^\dagger \; \hat{B}_k^{\text{qho}} \;+\; \hat{a}_k \; (\hat{B}_k^{\text{qho}})^\dagger \right) \tag{3.31b}$$

where the operator product, $\hat{a}_k^\dagger \hat{b}_j$, states that a molecular phonon is created in mode k by the annihilation of an external phonon in mode j, with a coupling strength is χ_{kj}; and vice versa for the $\hat{a}_k \hat{b}_j^\dagger$ term. The interacting external system can be taken to be any molecular system, with the distinction being the coupling χ_{kj}, and the vibrational modes available to it. This description of the interaction assumes the rotating wave approximation, which can be justified by assuming a weak coupling condition such that fast, high-order oscillations quickly average to zero and can be neglected [123]. The frequency-matching resonance condition is captured by the Kronecker-like δ-function, defined

$$\delta(\omega_k \;-\; \omega_j) \;=\; \begin{cases} 1, & \text{if } \; \omega_k = \omega_j \\ 0, & \text{if } \; \omega_k \neq \omega_j \end{cases} \tag{3.32}$$

For a valid one-for-one (harmonic) exchange of phonons the resonance condition, $\omega_k = \omega_j$, must be satisfied, and therefore the molecule and external phonons must have the same frequency. However, this condition can be relaxed by allowing slight variations in oscillation frequency due to the environment, $\omega_k + \varphi_k = \omega_j$, as will be discussed in the dissipation section (**§ 3.3.5**). The QHO interaction Hamiltonian is recast into (3.31b) by defining a stimulus superoperator

$$\hat{B}_k^{\text{qho}} \;\equiv\; \sum_{j}^{\text{ext}} \chi_{kj} \; \hat{b}_j \; \delta(\omega_k \;-\; \omega_j) \tag{3.33}$$

that acts as a quantum mechanical stimulating force (with dimensions of $[\text{time}]^{-1}$) to create a molecular phonon in mode k. An interaction Hamiltonian with an equivalent expression to (3.31b) arises in the context of the exchange of phonons and photons, where the equivalent of B_k is called the Rabi frequency and is the product of the (complex) electric field amplitude and dipole moment, divided by $\hbar$ [56].

3.3.3 QHO Stimulus to the Molecule

The strict resonance condition imposed by (3.32) requires that interacting modes must have precisely equal oscillation frequencies. This condition can be relaxed by invoking a smearing frequency, φ_k, whereby interactions can occur if

$$\left| \omega_k \;-\; \omega_j \right| \;\leq\; \varphi_k \tag{3.34}$$

A more detailed treatment of this approximation will be described in forthcoming sections. The smeared resonance condition has been applied to the study of vibrational dissipation in proteins

over a range of smearing frequencies: cytochrome C (0.09 to 0.9 THz, 3 to 30 cm^{-1}) [86], myoglobin [124] and green fluorescent protein (0.015 to 0.3 THz, 0.5 to 10 cm^{-1}) [125, 126].

The count of resonant interactions between isomaltose and MalL that satisfy (3.34) is shown in Fig. 3.2, for a smearing frequency $\varphi_k/2\pi = 0.25$ THz, allowing for 2.37×10^4 interactions, 0.72% of the total possible, $N^{\text{isom}}_{\text{mode}} N^{\text{MalL}}_{\text{mode}} = 3.29 \times 10^6$ combinations. Repeating the calculation for the isomaltose–MalL system over a rage of smearing frequencies up to 1 THz shows that the number of harmonic resonant interaction is linearly proportional to smearing with a constant of 9.60×10^4 THz^{-1}.

It can be seen that the two modes pertaining to the glycosidic link hydrogen oscillations at 100 THz correspond to a spike in the MalL DoS. The highest eight isomaltose vibrational modes that are clustered around 117.5 THz do not show any resonant interaction due to the removal of MalL states at that bandwidth in the data.

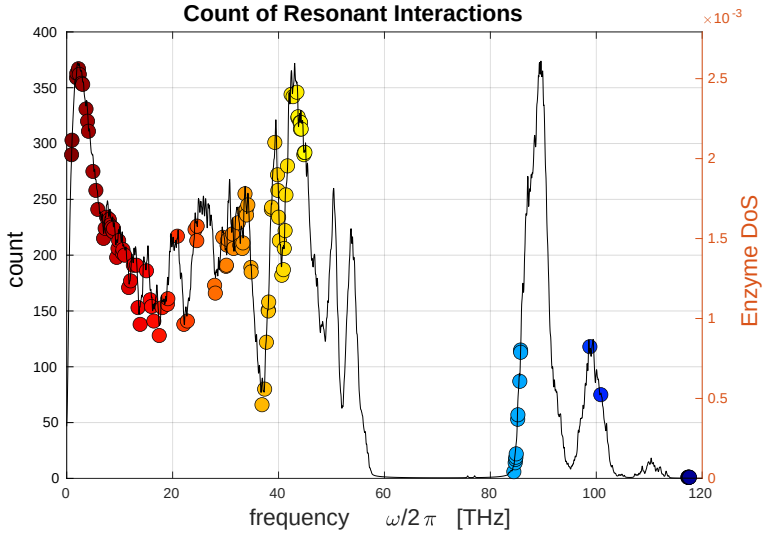

Figure 3.2: Count of the QHO valid interactions between MalL and each vibrational mode of isomaltose. The normalised enzyme DoS(black line) is drawn using (3.45) with $\varphi/2\pi = 0.25$ THz, and the isomaltose vibrational modes are linearly coloured by their frequency from red to blue. The highest frequency enzyme modes were removed in the processing of the MalL MD data, which artificially shows that there are zero resonant interactions with the highest modes of isomaltose (dark blue at 117 THz).

Let the interaction Hamiltonian for a one-for-one phonon exchange between the molecule and the enzyme to be of the form (3.31b), with substrate–enzyme coupling strength, Ξ_{kj}. The QME for the QHO interaction is found by substitution of (3.31b) into (3.27) yielding

$$\partial_t \langle \hat{\mathcal{M}}(t) \rangle^{\text{QHO}}_{\text{int}} = \frac{1}{i\hbar} \left\langle \left[\hat{\mathcal{M}} \, , \, \hat{\mathcal{H}}^{\text{int}}_k \right] \right\rangle \tag{3.35}$$

and since operators that act on distinct phonon modes commute, $[\hat{a}_k, \hat{b}^\dagger_j] = 0$, then

$$\partial_t \langle \hat{\mathcal{M}}(t) \rangle^{\text{QHO}}_{\text{int}} = -i \sum_j^{\text{enz}} \Xi_{kj} \left\langle \left[\hat{\mathcal{M}} \, , \, \hat{a}^\dagger_k \right] \hat{b}_j + \left[\hat{\mathcal{M}} \, , \, \hat{a}_k \right] \hat{b}^\dagger_j \right\rangle \delta(\omega_k - \omega_j) \tag{3.36}$$

The contributions to the molecule's EoMs due to QHO interactions with an enzyme are found by the commutation relations

$$\partial_t \langle \hat{a}_k(t) \rangle_{\text{int}} \;=\; -\,i \sum_{j}^{\text{enz}} \Xi_{kj} \; \langle \hat{b}_j \rangle \; \delta(\omega_k \;-\; \omega_j) \tag{3.37a}$$

$$\partial_t \langle \hat{a}_k^\dagger(t) \rangle_{\text{int}} \;=\; +\,i \sum_{j}^{\text{enz}} \Xi_{kj} \; \langle \hat{b}_j^\dagger \rangle \; \delta(\omega_k \;-\; \omega_j) \tag{3.37b}$$

$$\partial_t \langle \hat{n}_k(t) \rangle_{\text{int}} \;=\; -\,i \sum_{j}^{\text{enz}} \Xi_{kj} \; \Big(\langle \hat{a}_k^\dagger \rangle \; \langle \hat{b}_j \rangle \;-\; \langle \hat{a}_k \rangle \; \langle \hat{b}_j^\dagger \rangle \Big) \; \delta(\omega_k \;-\; \omega_j) \tag{3.37c}$$

whose contributions introduce a constant offset to the free EoMs, resulting in a coupled set of inhomogeneous first-order ODEs. The interaction Hamiltonian can be written more simply by defining a QHO enzyme stimulus operator (3.33) which carries dimensions of $[\text{time}]^{-1}$. With this stimulus superoperator, $\hat{B}_k^{\text{qho}}$, the QHO QME is then

$$\partial_t \langle \hat{\mathcal{M}}(t) \rangle_{\text{int}}^{\text{QHO}} \;=\; -\,i \Big\langle \Big[\hat{\mathcal{M}} \;,\; \hat{a}_k^\dagger \Big] \; \hat{B}_k^{\text{qho}} \;+\; \Big[\hat{\mathcal{M}} \;,\; \hat{a}_k \Big] \; (\hat{B}_k^{\text{qho}})^\dagger \Big\rangle \tag{3.38}$$

By defining the traced value of the QHO stimulus superoperator,

$$\langle \hat{B}_k^{\text{qho}} \rangle \;\equiv\; \sum_{j}^{\text{enz}} \Xi_{kj} \; \langle \hat{b}_j \rangle \; \delta(\omega_k - \omega_j) \tag{3.39}$$

then the QHO enzyme response EoMs are

$$\partial_t \langle \hat{a}_k(t) \rangle_{\text{enz}} \;=\; -\,i \; \langle B_k^{\text{qho}} \rangle \tag{3.40a}$$

$$\partial_t \langle \hat{a}_k^\dagger(t) \rangle_{\text{enz}} \;=\; +\,i \; \langle (B_k^{\text{qho}})^\dagger \rangle \tag{3.40b}$$

$$\partial_t \langle \hat{n}_k(t) \rangle_{\text{enz}} \;=\; -\,i \; \Big(\langle \hat{a}_k^\dagger \rangle \; \langle B_k^{\text{qho}} \rangle \;-\; \langle \hat{a}_k \rangle \; \langle (B_k^{\text{qho}})^\dagger \rangle \Big) \tag{3.40c}$$

The influence of the enzyme contributions when added to the free EoMs, are to couple the phonon state EoMs, and to shift the centre of phasor rotation in the creation and annihilation states, which results in $\langle \hat{n}_k \rangle$ evolving in time.

3.3.4 Simplifying the QHO Stimulus

The molecule–enzyme interaction can be simplified by making a semiclassical approximation, where it assumed that the enzyme operators can be treated as classical field amplitudes. The semiclassical approximation is used in quantum optics to describe atomic excitations due to the electromagnetic field [53], and in the Davydov theory for proteins [127]. First, the enzyme annihilation operator is moved into the interaction picture by the application of a QHO unitary time translation, $\hat{b}_j(t) \;\to\; \hat{b}_j \; e^{-i\omega_j \, t}$, which eliminates the explicit time dependence of the enzyme operator. Then the semiclassical approximation for the number operator is, $\langle \hat{b}_j^\dagger \hat{b}_k \rangle \;\mapsto\; n_j^e$, where, n_j^e, is an scalar amplitude representing the number of phonons in vibrational mode j. The annihilation operator is then approximated by, $\hat{b}_j \;\to\; \sqrt{n_j^e}$. The enzyme interaction

superoperator under the semiclassical assumption becomes, $\hat{B}_k \;\mapsto\; \tilde{B}_k(t)$, where

$$\tilde{B}_k(t) \;=\; \sum_j^{\text{enz}} \Xi_{kj}\, \sqrt{n_j^e}\; e^{-i\omega_j t}\; \delta(\omega_k \;-\; \omega_j) \tag{3.41}$$

The sinusoidal oscillations of the enzyme stimulus field are removed by transforming the state into a rotating frame at frequency ω, which is taken to be equal to the enzyme frequency, ω_j, for a valid interaction. The molecular $\hat{a}_k$ is now in the interaction picture, $\langle \hat{a}_k(t) \rangle \;\mapsto\; \langle \hat{a}_k(t) \rangle\; e^{-i\omega_j\, t}$, whose temporal derivative is, $\partial_t \big(\langle \hat{a}_k(t) \rangle\; e^{-it\,\omega_j} \big)$. Thus the EoMs are transformed into the rotating frame, $e^{-it\,\omega_j} \left[\partial_t \;-\; i\omega_j \right] \langle \hat{a}_k(t) \rangle = -i\;\omega_k\; \langle \hat{a}_k(t) \rangle\; e^{-it\,\omega_j} - i\,\tilde{B}_k(t)$. Upon multiplication by $e^{+it\,\omega_j}$, the enzyme-stimulated annihilation EoM in the rotating frame is obtained

$$\partial_t\; \langle \hat{a}_k(t) \rangle_{\text{enz}} \;=\; -\,i(\omega_j \;-\; \omega_k)\; \langle \hat{a}_k \rangle \;-\; i\,B_k \tag{3.42}$$

The enzyme stimulus, $B_k = e^{i\omega_j t}\, \tilde{B}_k(t)$, is now a static real-valued scalar classical field, and $\omega_j - \omega_k$ acts a *detuning* parameter. The number EoM in the rotating frame is

$$\partial_t\; \langle \hat{n}_k(t) \rangle_{\text{enz}} \;=\; -\,iB_k\; \Big(\langle \hat{a}_k^\dagger(t) \rangle \;-\; \langle \hat{a}_k(t) \rangle \Big) \tag{3.43}$$

A significant feature that has been removed by the semiclassical assumption made for B_k is that the enzyme's vibrational mode phonon numbers remain constant throughout an exchange with the molecule. The enzyme acts like a 'phonon laser' that supplies a consistent flow of phonons to the molecule at a rate that is proportional to the square root of the number of phonons in the enzyme vibrational modes. The solution to (3.42) is a phasor that is centred at, $B_k/(\omega_j - \omega_k)$, with a frequency, $\omega_j - \omega_k$; when this solution is inserted into the number EoM (3.43), the RHS becomes zero, indicating that the phonon number remains constant. The response amplitude of $\langle \hat{n}_k \rangle$ can be set to be $B_k^2/(\omega_j - \omega_k)^2$, which exhibits zero impedance at $\omega_j = \omega_k$, resulting in an infinite spike in amplitude.

The resonance condition for the QHO molecule–enzyme interaction can be smeared out by approximating the δ-function by a Lorentzian distribution (with dimensions of [time])

$$\delta(\omega) \;\approx\; \frac{1}{\pi}\; \frac{\varphi}{\varphi^2 \;+\; \omega^2} \tag{3.44}$$

where, φ, is the linewidth (half width at half maximum). In the coding work, I have specified viable interactions only if, $|\omega_k - \omega_j| < \varphi_k$. Since the DoS, $g(\omega_k)$, is taken to be a Dirac comb (summation of δ-functions) due to the continuum approximation for replacing a summation with an integral (details in **§ 3.3.5**), the product $d\omega_k\, g(\omega_k)$ is interpreted to be the number of modes in the range $[\omega_k,\, \omega_k + d\omega_k]$, then by allowing $d\omega_k \approx \varphi_k$, the number of enzyme modes that can interact with molecular mode k is approximately

$$n_k^e \;\approx\; \varphi_k\; g(\omega_k) \;=\; \frac{1}{\pi\, N_{\text{mode}}^{\text{enz}}} \sum_j^{\text{enz}} \frac{\varphi_k^2}{\varphi_k^2 \;+\; (\omega_k \;-\; \omega_j)^2} \tag{3.45}$$

The QHO enzyme stimulus is then approximated to be at thermal equilibrium such that each

enzyme mode, j, has an occupation number from the Planck thermal distribution, $\bar{n}_j$; then since a molecular mode k will interact with an enzyme mode j if, $\omega_k \approx \omega_j$, the occupation number of the enzyme mode will be approximately $\bar{n}_k$. A further approximation can be made by taking the coupling strength of molecular mode k with all enzyme modes j to be equal, $\Xi_{kj} = \Xi_{kk}$. These simplifications allow, $\Xi_{kj}\sqrt{n_j^e} \approx \Xi_{kk}\sqrt{\bar{n}_k}$, which can be taken out of the summation in (3.41), and the resultant expression for the stimulus to each molecular mode k from all QHO interactions with the enzyme is

$$B_k \;=\; \Xi_{kk}\,\sqrt{\bar{n}_k}\;\varphi_k\;g(\omega_k) \tag{3.46}$$

In general, there is a temperature dependence in the stimulus due to the phonon exchanges between the enzyme and solvent as well as the changes to the enzyme vibrational modes due to an altered equilibrium geometry, however these dynamics are not present in (3.46). The approximation retains a temperature dependence due to $\bar{n}_k$, and as will be shown in **§ 3.5**, has a contribution to the molecular heat capacity.

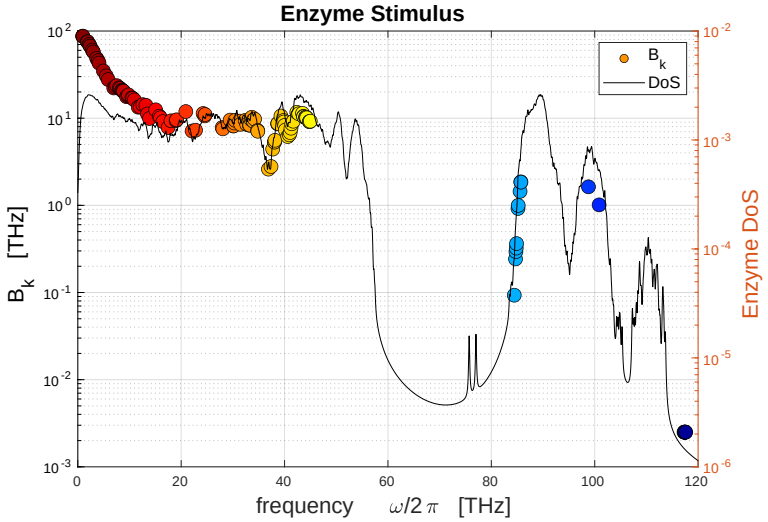

Figure 3.3: QHO stimulus, B_k, of isomaltose due to MalL at 34°C. The coupling is set to, $\Xi_{kj}/2\pi = 5,000$ THz, for all interactions and the smearing frequency is, $\varphi_k/2\pi = 0.25$ THz for all isomaltose modes. The MalL DoS (black) and vibrational mode stimulus (coloured circles) are plotted in log scale.

The stimulus of the vibrational modes of isomaltose due to the MalL enzyme is shown in Fig. 3.3 for equal coupling strengths. It can be seen that the largest stimulus is delivered to the lowest frequency molecular modes, with a decreasing trend for higher frequencies, due to the thermal equilibrium assumption for the enzyme modes. The contour of the DoS modulates the magnitude of B_k, due to the presence of multiple MalL vibrational modes participating in phonon exchange for each molecular mode; a spike in DoS imparts a larger stimulus to the molecule. In reality, the matrix of coupling strengths, Ξ_{kj}, has different values for each of the interactions, $\omega_k \approx \omega_j$, with their magnitudes changing in time due to the motions of the molecule and enzyme. This allows for a specificity of the enzyme to selectively excite particular vibrational modes in the substrate.

3.3.5 Environmental Vibrational Dissipation Rate

In this section I will introduce energy dissipation to the molecular model which allows for an excited state to relax into a thermal equilibrium with its surrounding environment. As was introduced in **§ 1.7**, the evolution of a system's state can be tracked by the Schrödinger equation, and a simplified treatment is achieved by partitioning the total system into a molecular subsystem and a thermal reservoir composed of QHOs. The behaviour of the reduced molecular subsystem is then captured by a dissipative QME after performing a trace over the reservoir. Therefore, there is a distinction between the external molecular stimulus and the dissipative environment subsystems. The derivation follows Louisell's treatment for an atom in a radiation field [53], which I claim is valid in the context of enzyme catalysis since photons and phonons are both fermions with equivalent mathematical expressions. Similar treatments are used in the study of the vibrational behaviour of the Davydov molecular model [127] and proteins [74, 86].

The dissipative QME has coefficients due to the Spectral Density Integrals (SDI) of the molecule's surrounding environment, and invoke a shift to the molecular vibrational mode frequencies as well as a Vibrational Dissipation Rate (VDR) which allows for an excited molecular mode to relax. I provide a detailed description of the QME in **Appendix A**. The dissipative QME for a QHO thermal reservoir with amnesia (Markov approximation) is given approximately by

$$\partial_t \langle \hat{\mathcal{M}} \rangle_{\text{diss}} \;\approx\; \Gamma_{\hat{a}_k} \left\langle \hat{\mathcal{D}}[\hat{a}_k](\hat{\mathcal{M}}) \right\rangle \;+\; \Gamma_{\hat{a}_k^\dagger} \left\langle \hat{\mathcal{D}}[\hat{a}_k^\dagger](\hat{\mathcal{M}}) \right\rangle \;-\; i\,\varphi_k \left\langle \left[\hat{\mathcal{M}},\, \hat{n}_k\right] \right\rangle \tag{3.47}$$

where the rate of dissipation of the annihilation operator is $\Gamma_{\hat{a}_k} = 2\,\Re[w_{12}]\;\delta(\omega_1 + \omega_2)$, and the creation operator has an equivalent expression with w_{21}. There is a perturbation to the vibrational mode natural frequency called the Lamb shift, $\varphi_k = \Im[w_{12} + w_{21}]\;\delta(\omega_1 + \omega_2)$. The dissipation superoperator, $\hat{\mathcal{D}}$, is a modification that I have made to the Lindbladian formalism in order to take the expectation value, (**§ A.2.4**)

$$\hat{\mathcal{D}}[\hat{A}](\hat{\mathcal{M}}) \;=\; -\frac{1}{2}\,\Big(\left[\hat{\mathcal{M}},\, \hat{A}^\dagger\right]\, \hat{A} \;-\; \hat{A}^\dagger\, \left[\hat{\mathcal{M}},\, \hat{A}\right] \Big) \tag{3.48a}$$

where $\hat{A}$ is either the annihilation or creation operator. The imaginary component can be taken to be a smearing of the resonant frequency condition (energy conservation) for each molecular vibrational mode with a Lorentzian resonance distribution

$$\delta(\omega_k \;-\; \omega_{k'}) \;\approx\; \frac{1}{\pi}\,\frac{\varphi_k}{\varphi_k^2 \;+\; (\omega_k \;-\; \omega_{k'})^2} \tag{3.49}$$

This smeared resonance condition physically represents a small deviation of the natural oscillation frequency due to the Lamb shift, φ_k, which in general is distinct for each molecular mode [128]. The four SDIs, $w_{ij}^{\pm}$, are the force–force correlation of the stimulus superoperator integrated over correlation time. Each term is defined in **§ A.2.3** and was used in the derivation of (3.47), here I demonstrate the calculation of w_{12}^{+} for a general external QHO stimulus superoperator of the form (3.33) and subsequently give the results for the remaining three. The

SDI w_{12}^{+} for the stimulus, $\hat{B}_k^{\text{qho}}$, with coupling, χ_{kj}, is given by

$$w_{21}^{+} \;=\; \int_0^{\infty} d\tau \; e^{-i\omega_k \tau} \; \left\langle \left(\hat{B}_k^{\text{qho}}(\tau) \right)^{\dagger} \; \hat{B}_k^{\text{qho}} \right\rangle \tag{3.50}$$

and carries dimensions of $[\text{time}]^{-1}$. Upon substitution of (3.31b) and then assuming that the operators evolve in time as a QHO, $\hat{b}_\alpha(\tau) \mapsto \hat{b}_\alpha \, e^{-i\omega_\alpha \tau}$, the SDI is

$$w_{21}^{+} \;=\; \sum_{\alpha,\beta}^{\text{env}} \chi_{k\alpha}^{*} \; \chi_{k\beta} \; \langle \hat{b}_\alpha^{\dagger} \; \hat{b}_\beta \rangle \; \int_0^{\infty} d\tau \; e^{-i(\omega_\alpha \; - \; \omega_k)\tau} \tag{3.51}$$

and the summation is over environmental modes. I take the expectation phonon number to be at thermal equilibrium (Planck distribution), $\langle \hat{b}_\alpha^{\dagger} \hat{b}_\beta \rangle = \bar{n}_\alpha \delta_{\alpha\beta}$, and perform the correlation time τ-integral via the Cauchy principal component

$$\int_0^{\infty} d\tau \; e^{\pm i\Omega\tau} \;=\; \pi \; \delta(\Omega) \;\pm\; i\mathcal{P}\Omega^{-1} \tag{3.52}$$

the SDI can then be expressed as

$$w_{21}^{+} \;=\; \sum_{\alpha}^{\text{env}} |\chi_{k\alpha}|^2 \; \bar{n}_\alpha \; \left(\pi \; \delta(\omega_k - \omega_\alpha) \;-\; i\mathcal{P}(\omega_k - \omega_\alpha)^{-1} \right) \tag{3.53}$$

By further assuming that the environmental modes are packed sufficiently closely, the summation can be replaced with an integral by invoking the DoS. By setting $d\omega \, g(\omega_k)$ to be the number of phonons contained within the infinitesimal bandwidth, $[\omega_k, \, \omega_k + d\omega]$, then the SDI is solved

$$w_{21}^{+} \;=\; |\chi_{kk}|^2 \; \bar{n}_k \; \left(\pi \; g(\omega_k) \;-\; i\varphi_{21} \right) \tag{3.54}$$

The term, φ_{21}, is a contribution to the environmental Lamb shift to the vibrational mode natural frequency that is taken to be part of the smearing parameter in (3.44). A similar method for the SDI, w_{12}^{+}, yields

$$w_{12}^{+} \;=\; |\chi_{kk}|^2 \; (\bar{n}_k \;+\; 1) \; \left(\pi \; g(\omega_k) \;+\; i\varphi_{12} \right) \tag{3.55}$$

and it can be shown that, $(w_{ij}^{-})^{*} = w_{ij}^{+}$. Upon substitution of the SDI, the dissipative QHO QME is

$$\partial_t \langle \hat{\mathcal{M}} \rangle_{\text{diss}} \;=\; -\, i\varphi_k \; \left\langle \left[\hat{\mathcal{M}} \; , \; \hat{n}_k \right] \right\rangle \;+\; \Upsilon_k^{\text{qho}} \; (\bar{n}_k \;+\; 1) \; \left\langle \hat{\mathcal{D}}[\hat{a}_k](\hat{\mathcal{M}}) \right\rangle \;+\; \Upsilon_k^{\text{qho}} \; \bar{n}_k \; \left\langle \hat{\mathcal{D}}[\hat{a}_k^{\dagger}](\hat{\mathcal{M}}) \right\rangle \tag{3.56}$$

where the Lamb shift is $\varphi_k = |\chi_{kk}|^2 \big((\bar{n}_k + 1) \, \varphi_{12} - \bar{n}_k \, \varphi_{21} \big)$, and $\Upsilon_k^{\text{qho}} = \pi \; g(\omega_k) \; |\chi_{kk}|^2$, is the VDR, which is independent of temperature. These results are given in [53] for when the DoS in unknown; to calculate the values using NMA data, I smear out the resonance condition by (3.44), then the QHO VDR is approximately

$$\Upsilon_k^{\text{qho}} \;=\; |\chi_{kk}|^2 \; \sum_{j}^{\text{env}} \frac{\varphi_k}{\varphi_k^2 \;+\; (\omega_k \;-\; \omega_j)^2} \tag{3.57}$$

The VDR of isomaltose into MalL (with coupling χ_{kj}, which is not equal to the stimulus coupling Ξ_{kj}) is shown in Fig. 3.4. The dissipative EoMs are found by evaluating (3.56) for each vibrational mode operator, yielding

$$\partial_t \langle \hat{a}_k \rangle_{\text{diss}} = -(\Upsilon_k + i\varphi_k)\,\langle \hat{a}_k \rangle \tag{3.58a}$$
$$\partial_t \langle \hat{a}_k^\dagger \rangle_{\text{diss}} = -(\Upsilon_k - i\varphi_k)\,\langle \hat{a}_k^\dagger \rangle \tag{3.58b}$$
$$\partial_t \langle \hat{n}_k \rangle_{\text{diss}} = -2\Upsilon_k\,\big(\langle \hat{n}_k \rangle - \bar{n}_k\big) \tag{3.58c}$$

The environmental EoMs are uncoupled, linear first-order inhomogeneous ODEs that capture the relaxation dynamics of an initially excited vibrational mode towards a thermal equilibrium with a QHO Markovian reservoir — a molecule in an ocean of consistent background noise, that has no internal dynamics and is not interacting with anything else. The dissipative contribution to the EoMs in isolation are uncoupled and so each EoM can be solved separately, yielding

$$\langle \hat{a}_k(t) \rangle_{\text{diss}} = \langle \hat{a}_k(0) \rangle\, e^{-(\Upsilon_k + i\varphi_k)t} \tag{3.59a}$$
$$\langle \hat{a}_k^\dagger(t) \rangle_{\text{diss}} = \langle \hat{a}_k^\dagger(0) \rangle\, e^{-(\Upsilon_k - i\varphi_k)t} \tag{3.59b}$$
$$\langle \hat{n}_k(t) \rangle_{\text{diss}} = \bar{n}_k + \big(\langle \hat{n}_k(0) \rangle - \bar{n}_k\big)\, e^{-2\Upsilon_k t} \tag{3.59c}$$

The creation and annihilation states are complex conjugates and follow counter-rotating exponential spiral paths in imaginary spacetime ($\mathbb{C}\times\mathbb{R}$) starting from their initial states and trending towards the origin at rate Υ_k, with an oscillation frequency given by the Lamb shift φ_k; the number state evolves exponentially from its initial state, $\langle \hat{n}_k(0) \rangle$, to thermal equilibrium with its environment, $\bar{n}_k$, at a rate $2\Upsilon_k$.

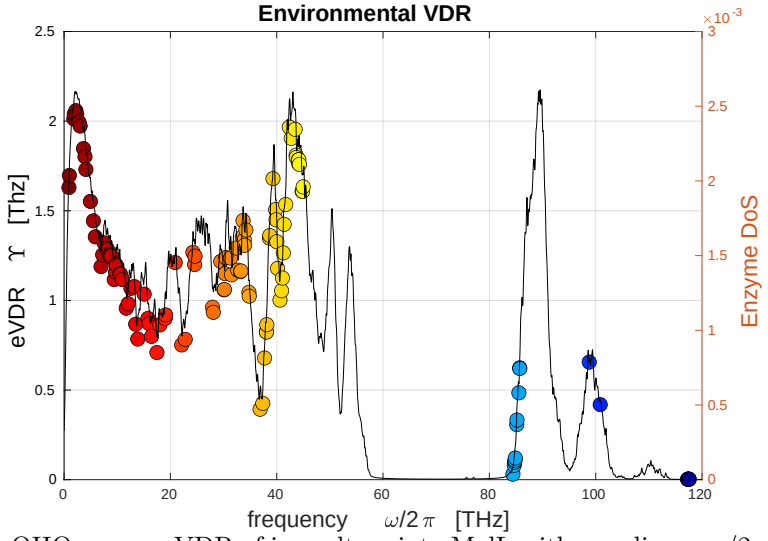

Figure 3.4: QHO enzyme VDR of isomaltose into MalL with coupling $\chi_{kj}/2\pi = 7$ THz for all interactions, and resonance smearing, $\varphi_k/2\pi = 0.25$ THz for all isomaltose modes. The VDR values are closely correlated to the distribution of the MalL DoS since all couplings are set to be equal; it would be expected that for realistic coupling strengths that there would be departure from this tight correlation.

3.4 Full QHO Catalytic Model

The full QHO model EoMs are thus obtained upon the summation of the free (3.29), stimulated (3.42, 3.43), and dissipation (3.59) behaviours. Thus the QHO QME (3.26) generates the set of EoMs for the substrate molecule vibrational modes

$$\partial_t \langle \hat{a}_k(t) \rangle \;=\; -\left(\Upsilon_k \;-\; i\Omega_k\right) \langle \hat{a}_k \rangle \;-\; iB_k \tag{3.60a}$$

$$\partial_t \langle \hat{a}_k^\dagger(t) \rangle \;=\; -\left(\Upsilon_k \;+\; i\Omega_k\right) \langle \hat{a}_k(t) \rangle \;+\; iB_k \tag{3.60b}$$

$$\partial_t \langle \hat{n}_k(t) \rangle \;=\; -\,2\Upsilon_k \;\left(\langle \hat{n}_k(t) \rangle \;-\; \bar{n}_k\right) \;-\; iB_k \;\Big(\langle \hat{a}_k^\dagger(t) \rangle \;-\; \langle \hat{a}_k(t) \rangle\Big) \tag{3.60c}$$

with detuning frequency, $\Omega_k = \omega - (\omega_k + \varphi_k)$, for a stimulating frequency of, ω, that I take to be a free parameter. These EoMs are a coupled set of inhomogeneous first-order linear ODEs in time which are analytically solvable. The most direct approach is to solve the creation and annihilation EoMs and then substitute them into the number EoM, which results in a time dependent inhomogeneous linear ODE that can be solved. The solution that I will present in **§ 3.4.2** makes use of a position–momentum state space matrix representation.

3.4.1 QHO Steady States

The QHO Steady States (QHOSS) are found in the standard way of setting the temporal derivatives of the EoMs to zero then rearranging, which yields the creation and annihilation QHOSS expectation values

$$\langle \hat{a}_k \rangle^{\text{qhoss}} \;=\; \frac{B_k}{\Omega_k \;+\; i\,\Upsilon_k} \;=\; \left(\langle \hat{a}_k^\dagger \rangle^{\text{qhoss}}\right)^* \tag{3.61}$$

At perfect tuning, $\Omega_k = 0$, the QHOSS of the annihilation operator is, $-iB_k/\Upsilon_k$. The phonon number QHOSS excitation above thermal equilibrium, $\langle \delta\hat{n}_k \rangle = \langle \hat{n}_k \rangle - \bar{n}_k$, is

$$\langle \delta\hat{n}_k \rangle^{\text{qhoss}} \;=\; \frac{B_k^2}{\Omega_k^2 \;+\; \Upsilon_k^2} \tag{3.62}$$

showing that the vibrational mode response to the enzyme stimulus is a Lorentzian resonance distribution centred at frequency, $\omega_k + \varphi_k$, with peak height, B_k^2/Υ_k^2, and linewidth, Υ_k. This represents an excited state of the molecule, and is dependent on the stimulus frequency, ω. The phonon number QHOSS for isomaltose are shown in Fig. 3.5, relative to their thermal equilibrium values. The QHOSS for the position and momentum operators are

$$\langle \hat{q}_k \rangle^{\text{qhoss}} \;=\; +\sqrt{2}\,\frac{\Omega_k}{B_k}\,\langle \delta\hat{n}_k \rangle^{\text{qhoss}} \tag{3.63a}$$

$$\langle \hat{p}_k \rangle^{\text{qhoss}} \;=\; -\sqrt{2}\,\frac{\Upsilon_k}{B_k}\,\langle \delta\hat{n}_k \rangle^{\text{qhoss}} \tag{3.63b}$$

whose resonant peak values are

$$\langle \hat{n}_k \rangle^{\text{qhoss}}\big|_{\Omega_k=0} = \frac{B_k^2}{\Upsilon_k^2} \tag{3.64a}$$

$$\langle \hat{q}_k \rangle^{\text{qhoss}}\big|_{\Omega_k=0} = 0 \tag{3.64b}$$

$$\langle \hat{p}_k \rangle^{\text{qhoss}}\big|_{\Omega_k=0} = -\sqrt{2}\,\frac{B_k}{\Upsilon_k} \tag{3.64c}$$

which shows that the QHOSS position state is the equilibrium geometry, and the QHOSS momentum state is negative, in contrast to the CHO model which has zero velocity at SS. The quantity, $\langle \hat{p}_k \rangle$, is the expectation for the phonon's crystal pseudo-momentum and is related to the wave-vector or group velocity of a wave in a solid, not the ballistic trajectory momentum of classical mechanics. The concept of a pseudo-momentum arises from Bloch's Theorem for the plane-wave solution to Schrödinger's equation, which was used in **§ 3.1**, from which the crystal momentum is defined to be the product of a wave-vector (of dimensions $[\text{space}]^{-1}$) multiplied by $\hbar$. The wave-vector can be used to characterise the wave-packet for the motion of electrons in a solid, and by conservation of (crystal) momentum, a negative wave-vector for the phonons describes a resistance to heat flow [56]. Therefore, $\langle \hat{p}_k \rangle^{\text{qhoss}} < 0$ could be interpreted as a restoring 'flow' towards thermal equilibrium in response to the impact of the stimulus. Fig. 3.6 shows the QHOSS distribution of (q, p) for the isomaltose vibrational modes for stimulus (Fig. 3.3) and VDR (Fig. 3.4).

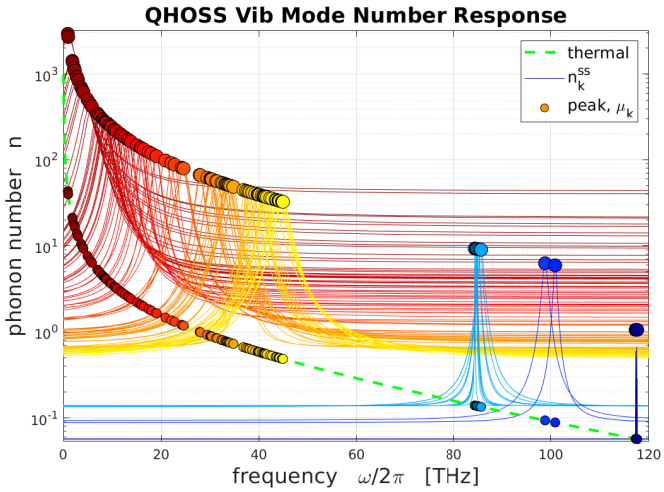

Figure 3.5: QHOSS distributions of the number operators, $\langle \hat{n}_k \rangle = \bar{n}_k + \langle \delta\hat{n}_k \rangle$, for isomaltose (coloured by vibrational mode frequency) with stimulus (Fig. 3.3) and VDR (Fig. 3.4). The peak values (large dots) are plotted above their thermal equilibrium values (smaller dots) that are distributed along $\bar{n}(\omega)$ (green) at 34°C.

Plotting the creation and annihilation QHOSS over a range of ω draws two perfect circles on the imaginary plane, $\mathbb{C}$: the creation QHOSS is a circle in the positive-imaginary portion of $\mathbb{C}$ that is symmetric about the imaginary axis, centred at $+iB_k/2\Upsilon_k$, with radius $B_k/2\Upsilon_k$, and coincides with the origin; the annihilation QHOSS is a circle in the negative-imaginary portion of $\mathbb{C}$ that is centred at $-iB_k/2\Upsilon_k$, with the same radius. The creation and annihilation QHOSS distributions coincide at the origin, $\langle \hat{a}_k \rangle^{\text{ss}} = \langle \hat{a}_k^\dagger \rangle^{\text{ss}} = 0$, for infinite detuning, $\Omega_k = \pm\infty$.

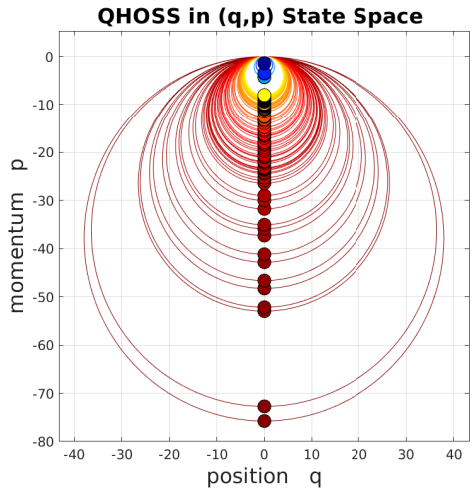

Figure 3.6: QHOSS distributions of the position and momentum operators for isomaltose (circles, (3.63)) and their peak values (filled circles, (3.64)). The same method of colouring the vibrational modes is used. The origin $(0, 0)$ corresponds to a vibrational mode with infinite detuning, $\Omega_k \to \infty$, or the unstimulated $B_k = 0$ case. The lowest frequency modes (red) exhibit the largest variations in position and momentum.

Therefore the annihilation QHOSS can be expressed by the circle

$$\langle \hat{a}_k \rangle^{\text{qhoss}} \;=\; -\,i\,\frac{B_k}{2\,\Upsilon_k}\,\left(e^{i\,\theta(\omega)}\;+\;1\right) \tag{3.65}$$

with the creation QHOSS being the complex conjugate, which coincides with the annihilation QHOSS at the origin on $\mathbb{C}$. The position and momentum QHOSS distribution can be expressed as the circles

$$\langle \hat{q}_k \rangle^{\text{qhoss}} \;=\; \frac{B_k}{\sqrt{2}\;\Upsilon_k}\;\sin\theta \tag{3.66a}$$

$$\langle \hat{p}_k \rangle^{\text{qhoss}} \;=\; -\,\frac{B_k}{\sqrt{2}\;\Upsilon_k}\;(\cos\theta\;+\;1) \tag{3.66b}$$

The angle of rotation is a function of detuning, $\theta(\omega) = \tan^{-1}\left(2\,\Omega_k\,\Upsilon_k/(\Upsilon_k^2 - \Omega_k^2)\right)$, however, the utility of (3.65) and (3.66) is that the SS distribution can be drawn continuously by $\theta \in [-\pi, +\pi]$. The QHOSS perfect circles (3.65) are plotted in Fig. 3.6, and in subsequent figures. If the resting state of a simulation lies on the circle, then is at SS; if the resting state is deviated away from the QHOSS, then the vibrational mode has not reached a SS.

3.4.2 QHO Equations of Motion Solution

The direct solution to the phonon number EoM (3.60c) can be found by first solving (3.60a) and (3.60b)

$$\langle \hat{a}_k(t) \rangle \;=\; \langle \hat{a}_k \rangle^{\text{qhoss}} \;+\; \left(\langle \hat{a}_k(0) \rangle \;-\; \langle \hat{a}_k \rangle^{\text{qhoss}}\right)\,e^{-(\Upsilon_k \;-\; i\Omega_k)\,t} \tag{3.67a}$$

$$\;=\; \langle \hat{a}_k^\dagger(t) \rangle^\dagger \tag{3.67b}$$

and then the inserting them into (3.60c). However, the resultant solution is the same as taking a different approach that uses only real-valued quantities. The evolution of the vibrational mode quantum state is equivalently captured by a transformation into the (dimensionless) position and momentum operators by (3.8),

$$\partial_t \langle \hat{q}_k \rangle \;=\; -\,\Upsilon_k\,\langle \hat{q}_k \rangle \;-\; \Omega_k\,\langle \hat{p}_k \rangle \tag{3.68a}$$

$$\partial_t \langle \hat{p}_k \rangle \;=\; +\,\Omega_k\,\langle \hat{q}_k \rangle \;-\; \Upsilon_k\,\langle \hat{p}_k \rangle \;-\; \sqrt{2}\,B_k \tag{3.68b}$$

The number EoM can be expressed in terms of the momentum operator

$$\partial_t \langle \hat{n}_k \rangle \;=\; -\,2\Upsilon_k\,\big(\langle \hat{n}_k(t) \rangle \;-\; \bar{n}_k\big) \;-\; \sqrt{2}\,B_k\,\langle \hat{p}_k(t) \rangle \tag{3.69}$$

showing that the evolution of the number operator is sourced by the response of momentum due to the stimulus. The solution to (3.60c) satisfies, $\langle \hat{n}_k(t) \rangle = \langle \hat{n}_k(t) \rangle_{\text{th}} + \langle \delta\hat{n}_k(t) \rangle$, where the environmental thermal equilibration is the solution to (3.69) in the absence of a stimulus, $B_k = 0$,

$$\langle \hat{n}_k(t) \rangle_{\text{th}} \;=\; \bar{n}_k \;+\; \big(\bar{n}_k^0 \;-\; \bar{n}_k\big)\; e^{-2\Upsilon_k t} \tag{3.70}$$

which accounts for an initial thermal equilibrium, $\bar{n}_k^0$, at a different temperature.

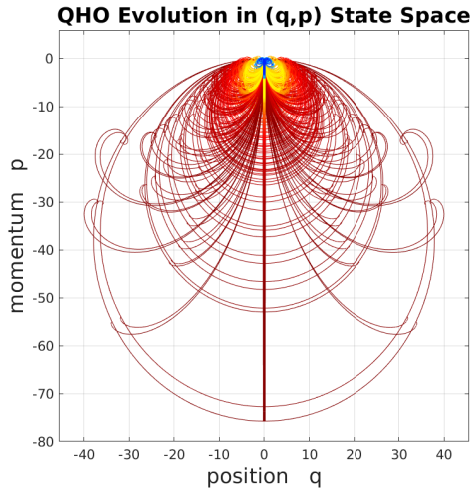

Figure 3.7: QHO evolution in position and momentum state space, (q, p), for the excitation of isomaltose from an initial thermal equilibrium due to a SS with a MalL stimulus. Traces are shown for each molecular vibrational mode over a range of detuning values $\Omega_k/2\pi = m$ THz, for integers on the interval $m \in [-3, +3]$. The peak values evolve exponentially along $q = 0$, and the non-resonant traces ($\Omega_k \neq 0$) exhibit relaxation oscillations towards their SS with a direction due to the sign of Ω_k.

The excitation dynamics are captured by $\langle \delta\hat{n}_k(t) \rangle$, which can be equivalently represented as

$$\langle \delta\hat{n}_k(t) \rangle \;=\; \langle \hat{a}_k^\dagger(t) \rangle\,\langle \hat{a}_k(t) \rangle \;=\; \frac{1}{2}\Big(\langle \hat{q}_k(t) \rangle^2 \;+\; \langle \hat{p}_k(t) \rangle^2\Big) \;=\; \frac{1}{2}\,\mathbf{\Psi}^\dagger(t)\mathbf{\Psi}(t) \tag{3.71}$$

I have confirmed this equivalence by deriving exact solutions to the number QHO EoM via each pathway. The coupled position and momentum EoMs (3.68) can be collected into a matrix

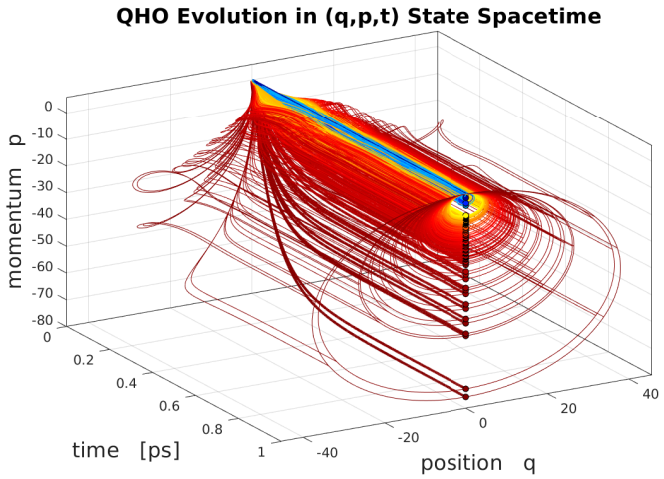

Figure 3.8: QHO evolution of isomaltose in position and momentum state spacetime, (t, q, p); effectively, a rotation of Fig. 3.7 in time. The traces project out of the initial state of thermal equilibrium, and migrate towards their QHOSS.

equation by defining a (q, p) state space vector, $\boldsymbol{\Psi} = [\langle \hat{q}_k \rangle, \langle \hat{p}_k \rangle]^{\mathrm{T}}$, giving

$$\partial_t \boldsymbol{\Psi} = \begin{bmatrix} -\Upsilon_k & +\Omega_k \\ -\Omega_k & -\Upsilon_k \end{bmatrix} \boldsymbol{\Psi}(t) + \begin{bmatrix} 0 \\ -\sqrt{2}\, B_k \end{bmatrix} \tag{3.72}$$

This is a linear inhomogeneous matrix ODE of the form, $\partial_t \boldsymbol{\Psi} = \mathbf{M}\boldsymbol{\Psi} + \mathbf{b}$, whose solution is, $\boldsymbol{\Psi}(t) = \boldsymbol{\Psi}^{\mathrm{ss}} + \exp(\mathbf{M}\, t)(\boldsymbol{\Psi}_0 - \boldsymbol{\Psi}^{\mathrm{ss}})$, where $\mathbf{M}$ is the matrix of linear internal dynamics, the initial state is, $\boldsymbol{\Psi}_0$, and SS, $\boldsymbol{\Psi}^{\mathrm{ss}}$. The matrix exponential is computed by the eigendecomposition, $\exp(\mathbf{M}t) = \mathbf{L}\exp(\boldsymbol{\Lambda}t)\mathbf{L}^{-1}$, which after matrix multiplication yields, $\exp(\mathbf{M}\, t) = e^{-\Upsilon_k t}\, \mathbf{R}(\Omega_k t)$, where

$$\mathbf{R}(\Omega_k t) = \begin{bmatrix} \cos(\Omega_k t) & -\sin(\Omega_k t) \\ +\sin(\Omega_k t) & \cos(\Omega_k t) \end{bmatrix} \tag{3.73}$$

is the 2D counter-clockwise rotation matrix for angle $\Omega_k t$. Therefore the solution to (3.72) is

$$\boldsymbol{\Psi}(t) = \boldsymbol{\Psi}^{\mathrm{ss}} + e^{-\Upsilon_k t}\, \mathbf{R}(\Omega_k t)\, (\boldsymbol{\Psi}_0 - \boldsymbol{\Psi}^{\mathrm{ss}}) \tag{3.74}$$

which evolves as a circular exponential spiral from the initial state towards the resting state $\boldsymbol{\Psi}^{\mathrm{ss}}$, at a relaxation rate, Υ_k, with frequency Ω_k and whose rotation direction depends on the sign of Ω_k. At zero detuning, $\omega = \omega_k + \varphi_k$, the rotational matrix is equal to the 2D identity matrix, $\mathbf{1}_2$, and the evolution is purely exponential with no relaxation oscillations. The evolutions of the position and momentum operators are the first and second elements of (3.74), respectively

$$\langle \hat{q}_k(t) \rangle = \langle \hat{q}_k \rangle^{\mathrm{ss}} + e^{-\Upsilon_k t} \Big(\big(\langle \hat{q}_k(0) \rangle - \langle \hat{q}_k \rangle^{\mathrm{ss}} \big) \cos(\Omega_k t) - \big(\langle \hat{p}_k(0) \rangle - \langle \hat{p}_k \rangle^{\mathrm{ss}} \big) \sin(\Omega_k t) \Big) \tag{3.75a}$$

$$\langle \hat{p}_k(t) \rangle = \langle \hat{p}_k \rangle^{\mathrm{ss}} + e^{-\Upsilon_k t} \Big(\big(\langle \hat{q}_k(0) \rangle - \langle \hat{q}_k \rangle^{\mathrm{ss}} \big) \sin(\Omega_k t) + \big(\langle \hat{p}_k(0) \rangle - \langle \hat{p}_k \rangle^{\mathrm{ss}} \big) \cos(\Omega_k t) \Big) \tag{3.75b}$$

which are related to the real and imaginary components of the creation and annihilation operators. The evolution of the vibrational modes of isomaltose from thermal equilibrium to a strongly excited state are shown in Fig. 3.7 and Fig. 3.8.

3.4.3 QHO Evolution of Phonon Number Response

The solution to the excited phonon number response is the inner product of two counter-rotating, exponentially decaying phasors, $\langle \delta\hat{n}_k(t)\rangle = \frac{1}{2}\,\mathbf{\Psi}^\dagger(t)\mathbf{\Psi}(t)$. The derivation makes use of the following properties of the rotation matrix: direction reversal, $\mathbf{R}^\dagger(\theta) = \mathbf{R}(-\theta)$; identity, $\mathbf{R}(+\theta)\ \mathbf{R}(-\theta) = \mathbf{1}_2$; and additive scaling, $\mathbf{R}(+\theta) + \mathbf{R}(-\theta) = 2\,\cos(\theta)\,\mathbf{1}_2$. After performing the inner products, the evolution of the phonon number excitation is

$$\begin{aligned}\langle \delta\hat{n}_k(t,\omega)\rangle^{\text{qho}} \;=\; &\Big(\langle \hat{n}_k(0,\omega)\rangle \;-\; \bar{n}_k\Big)\; e^{-2\Upsilon_k t} \\ &+\; \langle \delta\hat{n}_k(\omega)\rangle^{\text{qhoss}} \Bigg[1 \;+\; e^{-2\Upsilon_k t} \;-\; 2\,\cos(\Omega_k t)\; e^{-\Upsilon_k t} \\ &\qquad +\; 2\,e^{-\Upsilon_k t}\,\Big(\Re[z(\omega)]\,\big(\cos(\Omega_k t) \;-\; e^{-\Upsilon_k t}\big) \;-\; \Im[z(\omega)]\;\sin(\Omega_k t)\Big)\Bigg]\end{aligned} \tag{3.76}$$

where $z(\omega) = \langle \hat{a}_k(0,\omega)\rangle / \langle \hat{a}_k(\omega)\rangle^{\text{qhoss}}$, is the ratio of the initial-to-QHOSS for the annihilation operator, and the stiminitial state, $\langle \hat{n}_k(0,\omega)\rangle$, can be taken to be at a different temperature than for $t > 0$ and hence can have a different thermal occupation number. The EoM solution for the phonon number is function of time as well as stimulus frequency due to the detuning, $\Omega_k(\omega) \;=\; \omega \;-\; (\omega_k \;+\; \varphi_k)$ as well as the initial and SS spectral distributions of the quantum states. In the case of perfect tuning, $\Omega_k = 0$, the square braces reduces to the monotonically increasing function, $(1 \;-\; e^{-\Upsilon_k t})^2$; the response is oscillatory for all $\Omega_k \neq 0$.

The QHO EoM solutions show that the vibrational mode relaxation rate is governed by Υ_k, whose inverse is the vibrational lifetime. The transient response dynamics are approximately quiesced after five lifetimes, $t \;=\; 5\Upsilon_k^{-1}$ (since $e^{-5} \;\approx\; 0$), wherein the vibrational mode is near its steady state. After five lifetimes of the vibrational mode with the smallest VDR, all modes will be approximately in their steady states and the molecule vibrates in a consistent manner at a constant energy.

3.4.4 QHO Molecular Energy Response Spectrogram

The total QHO molecular energy response is constructed by insertion of (3.76) into the QHO energy (3.22)

$$E_{\text{mol}}(t,\omega) \;=\; \sum_k^{\text{mol}} \hbar\omega_k \;\left(\langle \delta\hat{n}_k(t,\omega)\rangle^{\text{qho}} \;+\; \bar{n}_k \;+\; \frac{1}{2}\right) \tag{3.77}$$

This energy response is a spectrogram since it describes a response that evolves with time and is dependent on the stimulating frequency. The vibrational modes in the QHO model do not interact with each other, and therefore the energy response of each mode is distinct; however, the molecular energy response spectrogram is the superposition of all modes and thus provides

an insightful description of a molecule–enzyme simulation. A simulation of a dissipative QHO molecule's response to an external stimulus is performed by `QHO_EoM_Solver`, which I have constructed in MATLAB. The QHO simulation parameters are the temperature and resonance smearing frequency as well as the stimulus and VDR coupling Ξ_{kj}, χ_{kj} in dimensions of $[\text{time}]^{-1}$. The figures presented throughout this chapter have been computed and visualised via (3.77) for the response of isomaltose to a stimulus from MalL.

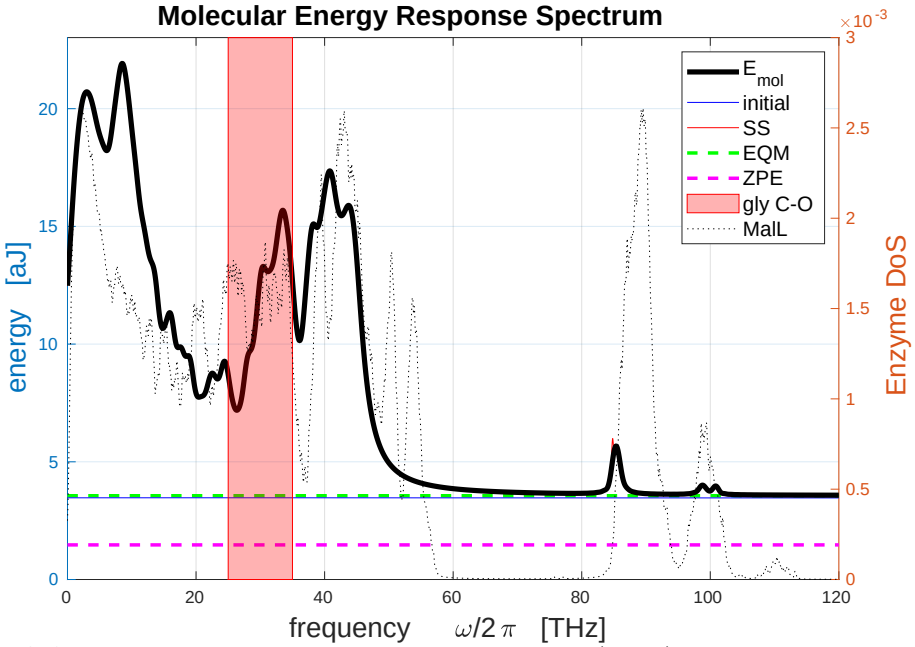

Figure 3.9: The isomaltose energy response spectrum (black) after 1 picosecond of MalL stimulus, with the thermal equilibrium (EQM, dashed green), QHOSS (red, largely overlapped by the simulated response), and the ZPE (dashed magenta); the enzyme DoS (dotted black) is measured along the right y-axis. The bandwidth containing the glycosidic carbon–oxygen bond stretching modes is denoted by the red region. The initial state is at a colder thermal equilibrium (blue), and the persisting high-frequency hydrogen oscillations can be inferred by the red peak near 85 THz where there is a deviation from the QHOSS.

The simulations demonstrated in this chapter are set to a biologically relevant temperature of 34°C, with a resonance smearing frequency set to 0.25 THz for all isomaltose–MalL interactions. In reality, I anticipate that each interaction would have a distinct value which is temperature dependent, and marks a direction of further study. The VDR, Υ_k, is computed by `Solve_Enzyme_Dissipation_Rate` with a coupling of 7 THz for all interactions (Fig. 3.4), and the stimulus, B_k, is computed by `Solve_Enzyme_Stimulus` with a coupling of 5,000 THz for all interactions (Fig. 3.3). I set the simulation duration to 1 ps so that the molecule is approximately in its SS with the enzyme. After this time, only the hydrogen undulations persist, as can be seen by the SS spectrum (red in Fig. 3.9 around 85 THz).

I prepared this simulation in order to exhibit the excitation behaviour of an individual isomaltose molecule from a cold thermal equilibrium to a SS with a MalL stimulus at a higher temperature. To achieve this, I set the initial state to be a SS at 24°C with a raised VDR coupling (35 THz) and reduced stimulus coupling (1,000 THz), which appears flat compared to the final SS. I account for a change in the vibrational mode oscillation frequencies due to a change in the dissipative environment by setting an initial Lamb shift whose vales are normally distributed

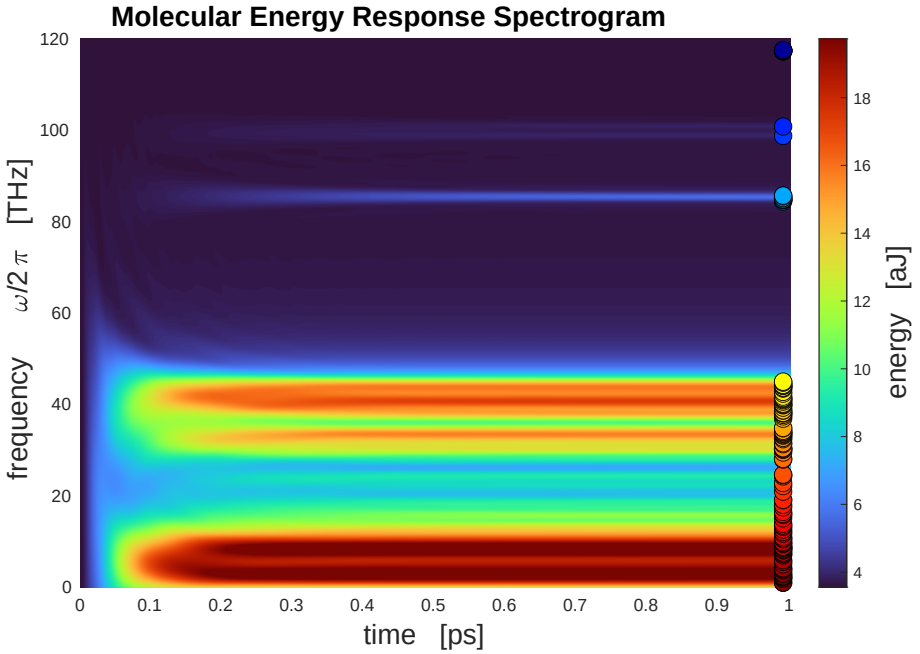

Figure 3.10: Transient QHO isomaltose energy response spectrogram (3.77) over 1 picosecond of MalL stimulus. The initial molecular state is relatively close to thermal equilibrium (3.6 aJ), the lowest frequency modes become noticeably excited after 0.05 ps and are approximately at SS from 0.25 ps, with a peak of 20 aJ in the sub-10 THz bandwidth; the higher-frequency hydrogen oscillation modes have a slower response compared to the lower-frequency bulk motions. The isomaltose vibrational modes are plotted along the right side of the figure.

random numbers scaled by 5 THz. Therefore, the simulation demonstrates the response due to a sudden change at $t = 0$ in temperature, VDR, stimulus, and Lamb shift.

The QHOSS energy response of isomaltose due to MalL, under these conditions (Fig. 3.9) shows a strong response in the lowest frequency modes pertaining to bulk motion, as well at the highest mid-frequency modes that represent the localised stretching of atomic bonds. The transient evolution of energy response (Fig. 3.10) shows a peak in the 28–33 THz bandwidth, which corresponds to the modes that are related stretching of the glycosidic bond (**§ 2.6**); however, higher peaks are contained in the < 10 THz and 40–50 THz bandwidths. It will be shown in **§ 5.4** that the inclusion of anharmonic effects causes these peaks to migrate towards the glycosidic bond stretching bandwidth. The process by which this occurs is called phonon hardening and softening, which I will describe in **§ 4.6**.

3.5 QHO Phonon Thermodynamics

In order to connect the behaviour of phonons to catalytic rate theory, in particular MMRT, the thermodynamics of vibrational modes must be determined. As I introduced in **§ 1.3**, the rate of a enzyme-catalysed reaction is determined by the change in Gibbs free energy between the reaction and transition states of an enzyme, called the activation free energy, $\Delta G^{\ddagger}$, which is composed of enthalpic and entropic contributions, $\Delta H^{\dagger}$, $\Delta S^{\ddagger}$. The MMRT equation makes use of temperature dependent activation enthalpy and entropy which leads to a description of $\Delta G^{\ddagger}$ that incorporates an activation heat capacity, $\Delta C_{\mathrm{p}}^{\ddagger}$ (1.4).

It has been observed that there is temperature-dependence for enzyme catalytic rates due to a non-zero (typically negative) activation heat capacity, $\Delta C_{\mathrm{p}}^{\ddagger}$ [16, 21]. Recent work on the cooperative conformational transitions of an enzyme during catalysis proposes the existence of a finite-size phase transition arising from a narrowing of the conformational landscape along the reaction coordinate [85]. This model results in a sigmoidal temperature dependence for $\Delta C_{\mathrm{p}}^{\ddagger}$, and it is suggested that this is analogous to a 2^{nd} order phase transition.

In this section, I demonstrate that the transient excitation heat capacity for a QHO vibrational mode, $\delta C_{\mathrm{p},k}$, follows a sigmoidal shape in time from its initial to steady state; however, more work is required to connect the vibrational mode heat capacity with the enzymatic activation heat capacity. It is well-known that the heat capacity, C_{p}, of materials varies dramatically at a phase transition (for example melting or vaporisation), and it is perhaps a phase transition in the enzyme during catalysis that drives a phase transition in the substrate which results in bond rearrangement. More support of this claim will be discussed for the anharmonic model.

In macroscopic classical thermodynamics, the heat capacity, C_{p}, is the incremental change in heat energy due to an infinitesimal change in temperature. The heat capacity of a phonon is given by the differentiation of vibrational energy ($E = \langle \hat{\mathcal{H}} \rangle$) with temperature, $C_{\mathrm{p}} = \partial_T E$. Therefore, the heat capacity of vibrational mode k is obtained directly from its Hamiltonian,

$$C_{\mathrm{p},k} = \partial_T \langle \hat{\mathcal{H}}_k \rangle \tag{3.78}$$

In order to make use of this phonon description with MMRT, the enzyme must itself be treated as a quantum system from which $\Delta C_{\mathrm{p}}^{\ddagger}$ can be computed as the difference in heat capacity for the substrate–enzyme complex at the RS and TS. This work lies outside the scope of this thesis, but is a vital component of connecting theory to experiment.

The other thermodynamic quantities that characterise the MMRT for catalysis are enthalpy and entropy. The activation enthalpy for phonons can be described as energy barriers (at zero pressure) and are used in the study atomic diffusion and defect formation in crystals [129]. The Gibbs entropy pertaining to classical statistical mechanics is extended to quantum statistical mechanics via the von Nuemann entropy defined, $S = -\mathrm{Tr}[\rho \ln(\rho)]$, for density operator ρ, and Tr denotes the trace. An equivalent expression for the entropy of a vibrational mode has been derived in [53], however I will omit its discussion since I will not be making use of entropy in this thesis. The quantum thermodynamic quantities of activation mark an avenue of further

study in the role of phonon exchange during enzyme catalysis; the theoretical treatment of an excitation heat capacity in this section will provide the initial direction.

3.5.1 QHO Heat Capacity

In this section, I will derive an exact analytic expression for the response spectrogram of molecular heat capacity by making use of the QHO EoM solutions. The heat capacity of a molecular vibrational mode is the temperature derivative of the expectation value of the Hamiltonian (3.78), and the QHO molecular heat capacity is derived by performing the derivative of (3.22) with temperature

$$C_{\mathrm{p,mol}} \;=\; \sum_{k}^{\mathrm{mol}} \hbar\omega_k \;\partial_T \;\langle \hat{n}_k \rangle \tag{3.79}$$

The vibrational mode heat capacity, $C_{\mathrm{p},k}$, is such that, $C_{\mathrm{p,mol}} = \sum_k C_{\mathrm{p},k}$. The response of the heat capacity for each vibrational mode can be tracked by specifying $\langle \hat{n}_k \rangle$. Note that the ZPE (3.23) does not contribute to the QHO heat capacity since $\partial_T E^{\mathrm{zpe}}_{\mathrm{mol}} \;=\; 0$.

3.5.2 QHO Thermal Equilibrium Heat Capacity

The heat capacity of a QHO molecule at thermal equilibrium is computed by setting, $\langle \hat{n}_k \rangle \;=\; \bar{n}_k$, for all modes in (3.79). The contribution of a single mode is $\bar{C}_{\mathrm{p},k} \;=\; \hbar\omega_k \;\partial_T \bar{n}_k$, whose solution is found by performing the derivative of $\bar{n}_k$

$$\bar{C}_{\mathrm{p},k} \;=\; k_B \;\left(\frac{\hbar\omega_k}{k_B T}\right)^2 \;\bar{n}_k \;(\bar{n}_k \;+\; 1) \tag{3.80a}$$

$$\;=\; k_B \;\left(\frac{\hbar\omega_k}{2\,k_B T}\right)^2 \;\mathrm{csch}^2\left(\frac{\hbar\omega_k}{2\,k_B T}\right) \tag{3.80b}$$

I use the over bar to represent the thermal equilibrium value. This is the Einstein heat capacity (1.11) introduced in **§ 1.8**. The total molecule heat capacity at thermal equilibrium is then the summation of all vibrational modes, $\bar{C}_{\mathrm{p,mol}} \;=\; \sum_k^{\mathrm{mol}} \bar{C}_{\mathrm{p},k}$.

3.5.3 QHOSS Excited Heat Capacity

Now by taking the molecule to be an excited state, $\langle \hat{n}_k \rangle = \bar{n}_k + \langle \delta\hat{n}_k \rangle$, the vibrational mode heat capacity is raised above thermal equilibrium, $C_{\mathrm{p},k} = \bar{C}_{\mathrm{p},k} + \delta C_{\mathrm{p},k}$, due to an excitation heat capacity, $\delta C_{\mathrm{p},k} = \hbar\omega_k \,\partial_T \langle \delta\hat{n}_k \rangle$. By evaluating, $\langle \delta\hat{n}_k \rangle$, at the QHOSS (3.62), and assuming that the Lamb shift, φ_k is independent on temperature, the temperature dependence of the phonon number response is due entirely to the stimulus, $B_k(T)$, the excitation heat capacity is

$$\delta C_{\mathrm{p},k} \;=\; 2\,\hbar\omega_k \;\langle \delta\hat{n}_k \rangle^{\mathrm{ss}} \;\partial_T \ln B_k \tag{3.81}$$

The simplified QHO enzyme stimulus (3.46) has a temperature dependence due to $\bar{n}_k$, and upon performing the derivative leads to

$$\partial_T \ln B_k = \frac{1}{B_k}\,\partial_T\,\left(\Xi_{kk}\,\sqrt{\bar{n}_k}\,\varphi_k\,g(\omega_k)\right) \tag{3.82a}$$

$$= \frac{1}{2}\,\partial_T \ln \sqrt{\bar{n}_k} \tag{3.82b}$$

$$= \frac{\bar{C}_{\mathrm{p},k}}{2\,\hbar\omega_k\,\bar{n}_k} \tag{3.82c}$$

Therefore, the QHOSS excitation vibrational mode heat capacity is

$$\delta C_{\mathrm{p},k} = \frac{\langle\delta\hat{n}_k\rangle^{\mathrm{ss}}}{\bar{n}_k}\,\bar{C}_{\mathrm{p},k} \tag{3.83}$$

and the total QHOSS molecular heat capacity is

$$C_{\mathrm{p,mol}} = \sum_k^{\mathrm{mol}}\left(1 + \frac{\langle\delta\hat{n}_k\rangle^{\mathrm{ss}}}{\bar{n}_k}\right)\,\bar{C}_{\mathrm{p},k} \tag{3.84}$$

If there is no enzyme stimulus, $B_k = 0$, then the thermal equilibrium value is recovered. A simulation of the QHOSS heat capacity of isomaltose under the conditions described in **§ 3.4.4** is shown in Fig. 3.11.

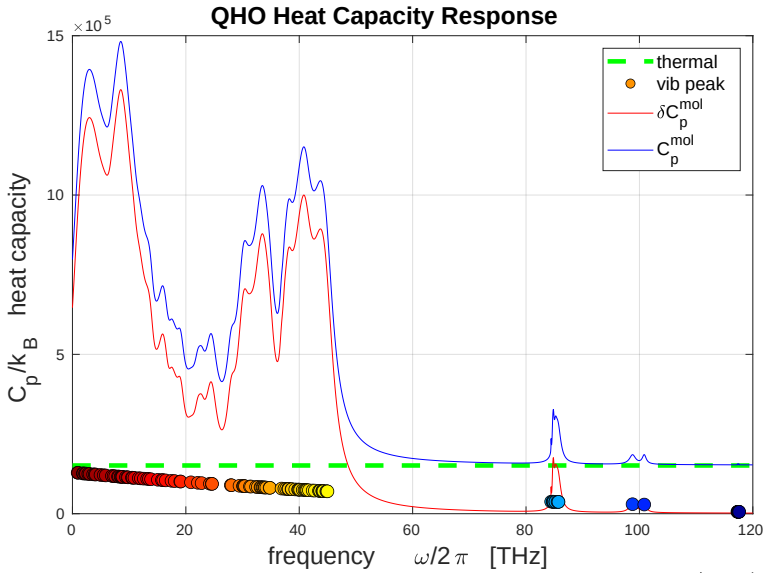

Figure 3.11: Isomaltose QHOSS heat capacity response plotted in C_p/k_B (dimensionless). The excitation heat capacity, $\delta C_{\mathrm{p,mol}}$ (red), raises the total molecular heat capacity (blue) above the thermal equilibrium value (green). The peak values for each vibrational mode (dots) show a decreasing trend for higher frequencies

3.5.4 QHO Transient Heat Capacity Evolution

The time evolution of the transient QHO heat capacity can be tracked by insertion of the number EoM solution (3.76) into (3.79), then by assuming that the initial conditions are independent of

temperature, the thermal equilibration heat capacity due to (3.70) is

$$\bar{C}_{\mathrm{p},k}(t) \;=\; \bar{C}_{\mathrm{p},k}\;\left(1\;-\;e^{-2\,\Upsilon_k\,t}\right) \tag{3.85}$$

The excitation portion of the heat capacity by (3.76) is

$$\begin{aligned}\delta C_{\mathrm{p},k}(t) \;=\; \bar{C}_{\mathrm{p},k}\;\frac{\langle\delta\hat{n}_k\rangle^{\mathrm{ss}}}{\bar{n}_k}\;\Bigg[1\;+\;e^{-2\Upsilon_k t}\;-\;2\,\cos(\Omega_k t)\,e^{-\Upsilon_k t}\\ +\;e^{-\Upsilon_k t}\left(\Re[z]\,\left(\cos(\Omega_k t)\;-\;e^{-\Upsilon_k t}\right)\;+\;\Im[z]\,\sin(\Omega_k t)\right)\Bigg]\end{aligned} \tag{3.86}$$

The total response in heat capacity is the summation of the thermal equilibration and excitation contributions. This is a related description to the activation heat capacity that is used in the MMRT model. In MMRT, the activation heat capacity, $\Delta C_p^{\ddagger}$, measures the difference in the heat capacity of an enzyme–substrate complex and its catalytic transition state, where as, $\delta C_{\mathrm{p,mol}}$, is the change in the heat capacity of the substrate molecule due to the enzyme. The change in the enzyme conformational state is probably the dominant effect for MMRT, however, this theoretical treatment is readily applicable to the enzyme upon specification of a VDR and stimulus for the enzyme. This is outside the scope of this thesis and marks a direction for future work.

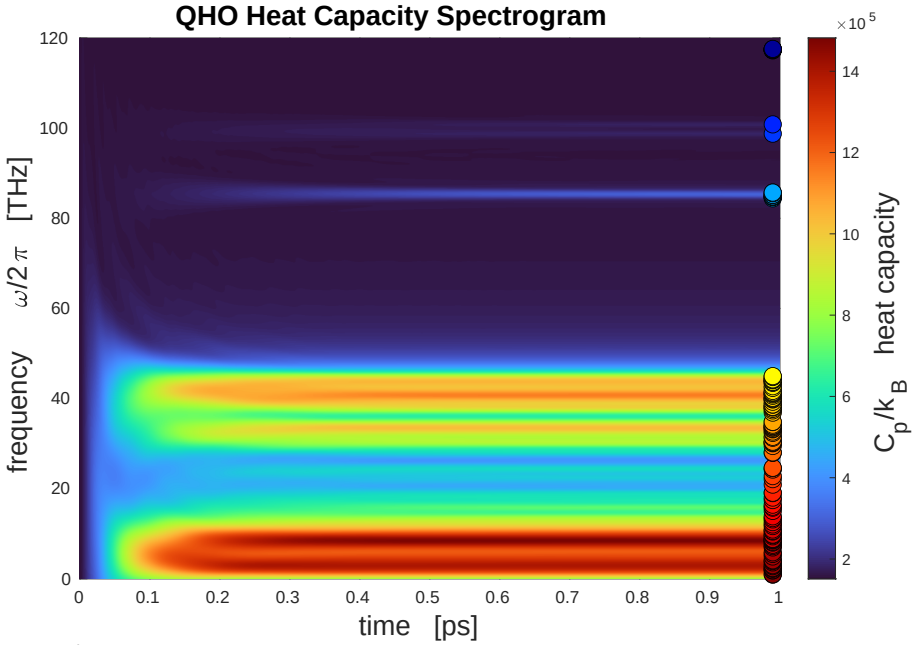

Figure 3.12: Isomaltose QHO heat capacity response spectrogram.

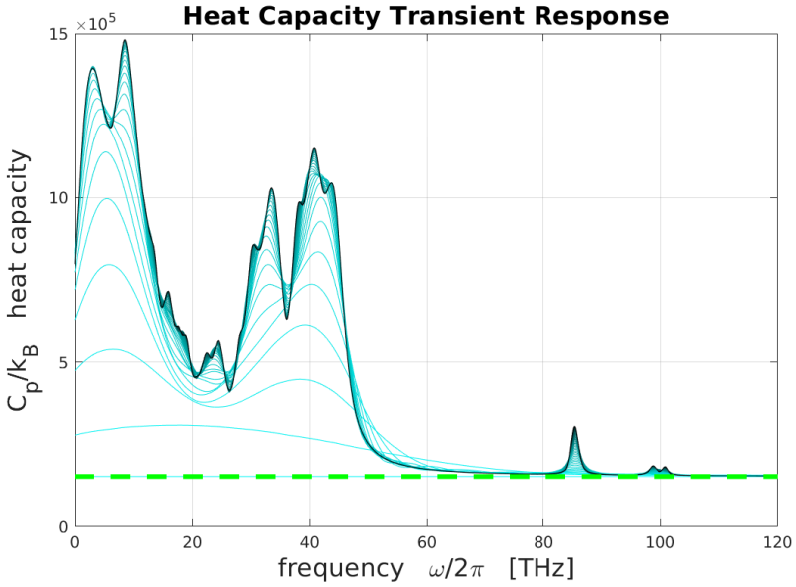

Figure 3.13: The spectral response of isomaltose heat capacity is drawn at regular intervals of 20 femtoseconds from thermal equilibrium (green) up to the QHOSS (black).

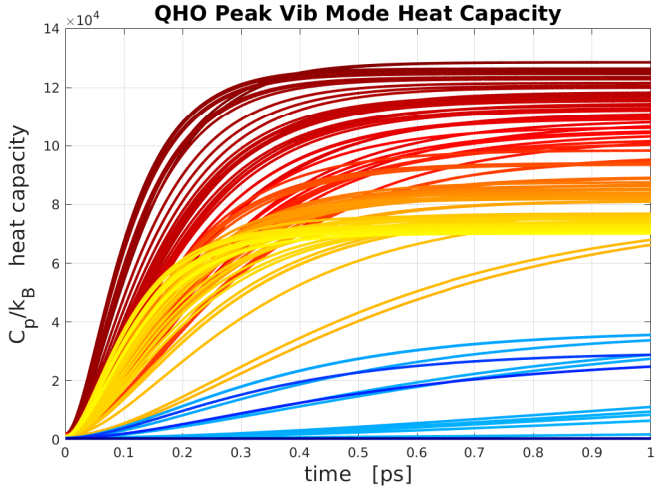

Figure 3.14: Transient evolution of isomaltose vibrational mode QHO heat capacity response over 1 ps.

3.6 Conclusion

In this chapter, I described a QHO model for a dissipative molecule in 3D space that is driven by an external stimulus. The EoMs for the evolution of the substrate's quantum state were then obtained for the free substrate, the enzyme stimulated response, and the dissipative behaviour; the full QHO model is the inclusion of each dynamical behaviour. The interaction with the enzyme is treated as a classical field with a consistent stimulus and smeared resonance condition, and thus behaves as a 'phonon laser', and the dissipative environment is treated as a Markovian thermal reservoir of QHOs.

Exact expressions for the evolution of the expectation values for the vibrational mode phonon numbers were elucidated via the analytic solutions of the QHO EoMs. The QHOSS response

spectra of the expectation value of the phonon number are a Lorentzian resonance distribution with the following characteristics:

- the peak is centred at the normal mode frequency plus an environmental Lamb shift
- the peak height is the ratio of the squares of stimulus to dissipation rate
- the half width at half maximum is the dissipation rate

The phonon number EoM solution was then used to construct the molecular energy response spectrogram and the transient excitation heat capacity. I demonstrated the results of a simulation that I built in MATLAB to show the excitation response of isomaltose due to the sudden application of MalL; the resultant expectation energy response spectrogram was analysed in the context of the glycosidic bond. I set the coupling strength for each viable interaction to be equal for all modes; this is a crude approximation and therefore highlights an important aspects of future work.

Chapter 4

Quantum Anharmonic Molecular Vibrations

In this chapter, I will be demonstrating a Quantum Anharmonic Oscillator (QAO) model of a dissipative molecule interacting with an enzyme that was first derived by Professor Moira Steyn-Ross then adapted by me for use with the Hamiltonian used in GAUSSIAN 09 for simulating anharmonic spectroscopy. Non-linearities are introduced into the model by including three-phonon processes for the substrate's free behaviour and dissipation, as well as the molecule–enzyme interaction. The mathematical description for a QAO and its interactions have been developed for an atom with a radiation field [53, 79], and the QAO description of three-phonon dissipation (also known as linewidth or vibrational lifetime) has been developed under the infinite crystal approximation in 1D [71] and 3D [56], and more recently for the vibrational relaxation in proteins [86]. I will be applying the semiclassical approximation to the stimulus and so the enzyme is treated as a QHO 'phonon laser' to a QAO molecule. The QAO catalytic model is obtained upon substitution of an anharmonic Hamiltonian into the QAO QME, whose computational simulation will be the subject of **Chapter 5**.

In this chapter, the QAO EoMs will be derived then subsequently explored by determining the QAO Steady States (QAOSS) and performing a stability analysis. I will then analytically locate the minimum stimulus requirements for phase transition behaviour in the substrate, and derive an approximate expression for the boundary of the phase transition region for larger stimuli. The anharmonic data presented in this chapter are for benzene as a proxy substrate, except for the map of viable QAO resonant interactions which requires only the harmonic normal mode frequencies. I recast the QAO model into a Non-Dimensionalised, One-Parameter (ND1P) model in **Appendix B**, wherein I follow a parallel methodology in a mathematically simpler context which exhibits equivalent theoretical results to those derived throughout this chapter. The ND1P parameter is used in the approximation of the phase transition boundary in the dimensioned QAO model and also serves as an *a priori* test for phase transition behaviour before performing a simulation.

4.1 Molecular Anharmonic Vibrations Pack

I have built the `Molecular_Anharmonic_Vibrations_Pack` in MATLAB to visualise and analyse the anharmonic data obtained from an anharmonic GAUSSIAN 09 MD simulation. The figures presented in this chapter are generated by this code package. The data presented in this chapter are used in the full QAO EoM simulation, which will be the subject of **Chapter 5**. The code hierarchy tree is as follows:

```
>> Molecular_Anharmonic_Vibrations_Pack
    · Get_All_Data
        · (detailed in Chapter 2)
    · Solve_Enzyme_Stimulus
    · Solve_Molecular_Dissipation_Rate
    · Solve_Enzyme_Dissipation_Rate
    · Solve_SS3
    · Save_all_plots
        · Plot_save_function
```

4.2 Quantum Anharmonic Oscillator Molecule Energetics

The derivation of an anharmonic molecular Hamiltonian is an involved and non-trivial task. The general procedure is similar to the derivation for the QHO molecule: perform a power expansion of the potential energy to the desired order, then apply an appropriate quantisation to transform the Hamiltonian to be in terms of the phonon number operator. Here, I will simply present the potential energy and the Hamiltonian that is used in GAUSSIAN 09; a more detailed discussion for an anharmonic molecule is provided in [79].

For the infinite Taylor power series expansion of potential energy, $\mathcal{V} = \sum_{m=0}^{\infty} \mathcal{V}_m$, the terms up to the second-order encapsulate the harmonic oscillations and one-for-one phonon exchanges (**Chapter 3**), while all higher-order terms are referred to as the anharmonic contributions or perturbations. The third- and fourth-order terms collectively account for the two-for-one exchange of phonons, and thus represent the simplest anharmonic treatment for a vibrational mode. Therefore, the required anharmonic molecular potential energy is, $\mathcal{V}_{\text{qao}} = \mathcal{V}_{\text{qho}} + \mathcal{V}_3 + \mathcal{V}_4$, where $\mathcal{V}_{\text{qho}}$ is the QHO potential (2.2) and the cubic and quartic terms are given by [56]

$$\mathcal{V}_3 = \frac{1}{6} \sum_{\{b\}}^{N_{\text{atom}}} \sum_{\{r\}}^{\text{xyz}} \left(\frac{\partial^3 \mathcal{V}}{\partial u_{r_1 b_1} \, \partial u_{r_2 b_2} \, \partial u_{r_3 b_3}} \right) \Bigg|_{\text{eqm}} u_{r_1 b_1} \; u_{r_2 b_2} \; u_{r_3 b_3} \tag{4.1a}$$

$$\mathcal{V}_4 = \frac{1}{24} \sum_{\{b\}}^{N_{\text{atom}}} \sum_{\{r\}}^{\text{xyz}} \left(\frac{\partial^4 \mathcal{V}}{\partial u_{r_1 b_1} \, \partial u_{r_2 b_2} \, \partial u_{r_3 b_3} \, \partial u_{r_4 b_4}} \right) \Bigg|_{\text{eqm}} u_{r_1 b_1} \; u_{r_2 b_2} \; u_{r_3 b_3} \; u_{r_4 b_4} \tag{4.1b}$$

where the summations are over the number of molecular atoms, $b_i \in [1, N_{\text{atom}}] \cap \mathbb{N}$, in the three Cartesian coordinates, $r_i \in \{x, y, z\}$. The cubic and quartic contributions to the potential can be transformed in terms of the creation and annihilation operators by use of the deviation operator, $\hat{u}_{rb}(\hat{a}_k)$ (3.17), which will result in terms with products of up to four operators, such as $\hat{a}_k^\dagger \, \hat{a}_k \, \hat{a}_j^\dagger \, \hat{a}_j = \hat{n}_k \, \hat{n}_j$, where k, j are the molecular vibrational mode index; eventually, the fourth-order potential can be expressed in terms of the phonon number operators. The Hamiltonian for an anharmonic molecule in the bilinear form as used in the GAUSSIAN 09 anharmonic MD package [130] is

$$\hat{\mathcal{H}}_{\text{mol}} \; = \; \hbar\xi_0 \, \hat{1} \; + \; \sum_{k=1}^{N_{\text{mode}}^{\text{mol}}} \hbar\omega_k \left(\hat{n}_k \; + \; \frac{1}{2}\right) \; + \; \sum_{k=1}^{N_{\text{mode}}^{\text{mol}}} \sum_{j \geq k}^{N_{\text{mode}}^{\text{mol}}} \hbar\xi_{kj} \left(\hat{n}_j \; + \; \frac{1}{2}\right)\left(\hat{n}_k \; + \; \frac{1}{2}\right) \tag{4.2}$$

whose terms, respectively, are the zero-point energy (ZPE), QHO, and the anharmonic contributions; for readability, the subsequent summations over the molecular vibrational modes will be denoted as, $\sum_k^{\text{mol}}$. The Hamiltonian coefficients, $\{\omega_k, \xi_0, \xi_{kj}\}$ have dimensions of $[\text{time}]^{-1}$; the summation over k are over all vibrational eigenmodes available to the molecule; the $j = k$ contribution describes self-energy; the indices run over $j \geq k$ to suppress double counting of the symmetries, $\xi_{kj} = \xi_{jk}$; and the phonon number operator of the k^{th} mode is $\hat{n}_k$. Hamiltonians of this form have been used to investigate anharmonic potential energy landscapes for many years [131], including to explore semiclassical TST tunnelling probabilities [132]. In the simplest approximation, the anharmonic Hamiltonian coefficients, ξ_{kk}, are given by functions of the equilibrium values of the third- and fourth-spatial derivatives in (4.1), as well as the harmonic dynamical eigenfrequencies, ω_k. The anharmonic coefficients computed in the GAUSSIAN 09 MD package also incorporate contributions from angular momentum that impart a Coriolis force and centrifugal distortion.

4.2.1 QAO Zero-Point Energy and Thermal Equilibrium

The ZPE represents the minimum of vibrational energy for a molecule. The anharmonic perturbation from the QHO Hamiltonian is to alter the ZPE and the natural oscillation frequency. In **Chapter 3**, the total Hamiltonian for the harmonic molecule is the superposition of all individual vibrational mode Hamiltonians, $\hat{\mathcal{H}}_{\text{mol}}^{\text{qho}} \; = \; \sum_k^{\text{mol}} \hat{\mathcal{H}}_k^{\text{qho}}$, however, this is not true when taking anharmonics into account due to the zeroth-order coefficient, ξ_0, arising from the total contributions to the ZPE. The Hamiltonian of the anharmonic molecule can be partitioned as, $\hat{\mathcal{H}}_{\text{mol}} \; = \; \hat{\mathcal{H}}_{\text{zpe}} \; + \; \sum_k^{\text{mol}} \hat{\mathcal{H}}_k$, where the ZPE Hamiltonian is, $\hat{\mathcal{H}}_{\text{zpe}} \; = \; \hbar\xi_0 \, \hat{1}$, and each vibrational mode contributes

$$\hat{\mathcal{H}}_k \; = \; \hbar\left[\omega_k \; + \; \sum_{j \geq k}^{\text{mol}} \xi_{kj} \left(\hat{n}_j \; + \; \frac{1}{2}\right)\right] \left(\hat{n}_k \; + \; \frac{1}{2}\right) \tag{4.3}$$

The square braces representing an oscillation frequency that is dependent on the phonon number states of all of the other modes available to the molecule, including itself ($j = k$). The expectation value for total energy of the molecule is found by taking the trace of the molecular Hamiltonian over the system states, $E_{\text{mol}} \; = \; \langle \hat{\mathcal{H}}_{\text{mol}} \rangle \; = \; E_{\text{zpe}} \; + \; \sum_k^{\text{mol}} \langle \hat{\mathcal{H}}_k \rangle$, where the zeroth-order ZPE term has energy, $E_{\text{zpe}} \; = \; \hbar\xi_0$. The energy evolution of the molecule can be determined once

the expectation values for the phonon number operator of each vibrational mode, $\{\langle\hat{n}_k\rangle\}$, have been found. The time evolutions of $\langle\hat{n}_k\rangle$ are found by the EoMs as derived from the QME in the same way that was done in **Chapter 3**. The anharmonic vibrational mode energy for the unoccupied ground state, $\langle\hat{n}_k\rangle = 0$, is $E_k^{\text{gnd}} = \frac{1}{2}\hbar\omega_k + \frac{1}{4}\sum_{j\geq k}^{\text{mol}}\hbar\xi_{kj}$, from which the ground state energy of the molecule is, $E_{\text{mol}}^{\text{gnd}} = E_{\text{zpe}} + \sum_k^{\text{mol}} E_k^{\text{gnd}}$. Since the anharmonic coefficients can be positive or negative, the ground state molecular energy may lowered or raised relative to the QHO ground state, $\sum_k^{\text{mol}}\frac{1}{2}\hbar\omega_k$. The thermal equilibrium energy is found by setting $\langle\hat{n}_k\rangle = \bar{n}_k$, throughout the Hamiltonian (4.2).

The ZPE and thermal equilibrium energy for benzene is shown in Fig. 4.1. Generally speaking, the influence of anharmonics is to raise the energy of the low frequency modes and reduce the higher frequency modes; the total energy value for benzene is anharmonically perturbed by 1.75% and 1.4% from the QHO ZPE and thermal equilibrium energy values, respectively.

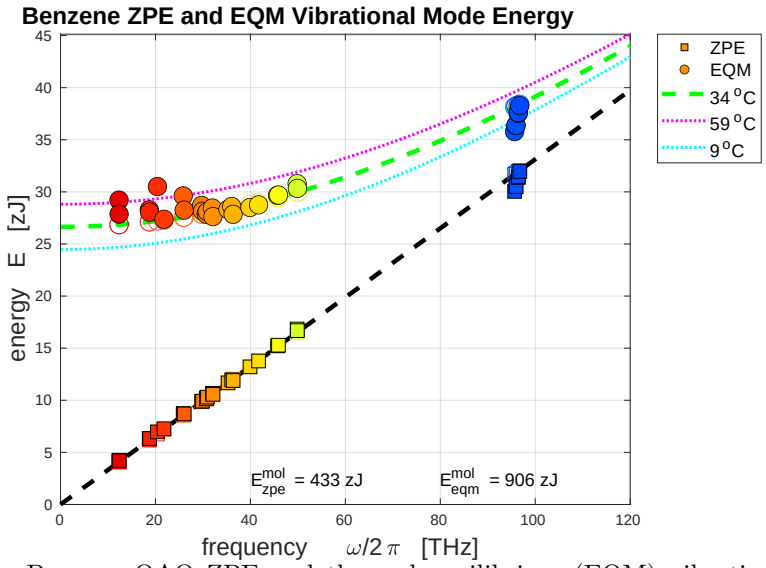

Figure 4.1: Benzene QAO ZPE and thermal equilibrium (EQM) vibrational energy (in zeptojoules), showing how the QAO values (filled) are perturbed from the QHO values (hollow). The QHO ZPE is 440.7 zJ (265.4 kJ.mol^{-1}), and EQM is 904.7 zJ (544.8 kJ.mol^{-1}).

4.3 QAO Free Behaviour

The free QAO EoMs for the vibrational mode quantum state operators, $\hat{\mathcal{M}}(t;\hat{a}_k(t))$, are derived via substitution of the QAO molecular Hamiltonian (4.2) into the free QME (3.27), in a similar manner to **Chapter 3**. To simplify the derivation to the EoM solutions, I will proceed by treating each term of $\hat{\mathcal{H}}_k$ (4.2) separately,

$$\partial_t\langle\hat{\mathcal{M}}\rangle_{\text{free}} = \partial_t\langle\hat{\mathcal{M}}\rangle_{\text{free}}^{\text{ZPE}} + \partial_t\langle\hat{\mathcal{M}}\rangle_{\text{free}}^{\text{QHO}} + \partial_t\langle\hat{\mathcal{M}}\rangle_{\text{free}}^{\text{QAO}} \tag{4.4}$$

4.3.1 QAO Zero-Point Energy Contribution

Since scalars always commute with operators, $[\hat{\mathcal{M}}, \hat{1}] = 0$, the zeroth-order term vanishes from the QME

$$\partial_t \langle \hat{\mathcal{M}}(t) \rangle_{\text{free}}^{\text{ZPE}} \;=\; \frac{1}{i\hbar} \left\langle \Big[\hat{\mathcal{M}} \;,\; \hbar \xi_0 \; \hat{1} \Big] \right\rangle \;=\; 0 \tag{4.5}$$

Therefore, the scalar zeroth-order Hamiltonian term does not directly contribute to the dynamical behaviour of the free molecule in this model. This is analogous to the assumption for taking the constant coefficient for the classical potential energy expansion to be zero since it does not affect the output of the classical Euler-Lagrange equation.

4.3.2 Anharmonic Quantum Master Equation

The QHO contribution is the same as in **§ 3.3.1**,

$$\partial_t \langle \hat{\mathcal{M}}(t) \rangle_{\text{free}}^{\text{QHO}} \;=\; -\, i\, \omega_k \left\langle \Big[\hat{\mathcal{M}} \;,\; \hat{n}_k \Big] \right\rangle \tag{4.6}$$

The derivation of the free EoMs for the QAO contribution is more involved due to the higher-order process that result in terms with operator products. By inserting the QAO portion of the Hamiltonian into the free QME, the anharmonic contribution to the state EoM is

$$\partial_t \langle \hat{\mathcal{M}}(t) \rangle_{\text{free}}^{\text{QAO}} \;=\; -\, i \left\langle \left[\hat{\mathcal{M}} \;,\; \left(\hat{n}_k \;+\; \frac{1}{2} \right) \sum_{j \geq k}^{\text{mol}} \xi_{kj} \left(\hat{n}_j \;+\; \frac{1}{2} \right) \right] \right\rangle \tag{4.7}$$

Since phonon operators that act on different vibrational modes are dynamically distinct, two operators of different indices always commute, $[\hat{a}_k \;,\; \hat{a}_j^\dagger] = \delta_{kj}$, as captured by the Kronecker δ-function (2.9). Therefore, the summation over the commutations of mode k with all the other modes j has only one surviving term: $[\hat{\mathcal{M}} \;,\; \sum_{j\geq k}^{\text{mol}} \hat{n}_j] = \sum_{j\geq k}^{\text{mol}} [\hat{\mathcal{M}} \;,\; \hat{n}_j] = [\hat{\mathcal{M}} \;,\; \hat{n}_k]$. Any arbitrary operator acting on vibrational mode k only commutes with another operator acting on k, all others are zero. Separating the self-interaction term, $j = k$, from the summation in (4.2) by, $\sum_{j\geq k}^{\text{mol}} \xi_{kj} \big(\hat{n}_j + 1/2 \big) = \xi_{kk} \, \big(\hat{n}_k + 1/2 \big) + \hat{\eta}_k$, allows the contribution to mode k from the other modes, $j \neq k$, to be encapsulated by

$$\hat{\eta}_k \;\equiv\; \sum_{j>k}^{\text{mol}} \xi_{kj} \;\left(\hat{n}_j \;+\; \frac{1}{2} \right) \tag{4.8}$$

which carries dimensions of $[\text{time}]^{-1}$, and has the property that $[\hat{\mathcal{M}}(\hat{a}_k), \hat{\eta}_k] = 0$, since $\hat{\eta}_k$ is dynamically distinct to $\hat{\mathcal{M}}(\hat{a}_k)$. Thus the free QAO QME can be written

$$\partial_t \langle \hat{\mathcal{M}}(t) \rangle_{\text{free}}^{\text{QAO}} \;=\; -\, i \left\langle \hat{\eta}_k \Big[\hat{\mathcal{M}} \;,\; \hat{n}_k \Big] \;+\; \xi_{kk} \left[\hat{\mathcal{M}} \;,\; \big(\hat{n}_k \;+\; 1/2 \big)^2 \right] \right\rangle \tag{4.9}$$

The multi-phonon self-interaction (higher octave) term of frequency ξ_{kk} imparts dynamical contributions due to the commutation with the square of number operator. By expanding the round brackets and then the commutation brackets by using the identity, $[a, bc] = [a, b]c + b[a, c]$, the

summation of the QHO and QAO contributions to the free QME are found

$$\begin{aligned}\partial_t\langle\hat{\mathcal{M}}(t)\rangle_{\text{free}} \;=\; -\,i\,\Big\langle\big(\omega_k \;+\; \hat{\eta}_k\big)\Big[\hat{\mathcal{M}}\;,\;\hat{n}_k\Big] \\ +\;\xi_{kk}\,\Big(\Big[\hat{\mathcal{M}}\;,\;\hat{n}_k\Big]\,\hat{n}_k \;+\; \hat{n}_k\,\Big[\hat{\mathcal{M}}\;,\;\hat{n}_k\Big] \;+\; \Big[\hat{\mathcal{M}}\;,\;\hat{n}_k\Big]\Big)\Big\rangle\end{aligned} \tag{4.10}$$

To derive the free EoMs, only the commutation of $\hat{\mathcal{M}}$ with $\hat{n}_k$ needs to be evaluated. This is the general free QAO QME for an arbitrary operator acting on molecular vibrational mode k.

4.3.3 Free Equations of Motion for the Annihilation and Creation Operators

Starting with the annihilation operator, $\hat{\mathcal{M}} = \hat{a}_k$, whose commutation with $\hat{n}_k$ is, $[\hat{a}_k\;,\;\hat{n}_k] = \hat{a}_k$, the EoM from the free QME (4.10) is

$$\partial_t\langle\hat{a}_k(t)\rangle_{\text{free}} \;=\; -\,i\,\Big\langle\big(\omega_k \;+\; \hat{\eta}_k\big)\,\hat{a}_k \;+\; \xi_{kk}\,\Big(\hat{a}_k\hat{n}_k \;+\; \hat{n}_k\hat{a}_k \;+\; \hat{a}_k\Big)\Big\rangle \tag{4.11}$$

The commutation relation, $\hat{a}\hat{n} = \hat{n}\hat{a} + [\hat{a},\hat{n}] = \hat{n}\hat{a} + \hat{a}$, is then used to reorganise the operator products into normal order (creation operators to the left)

$$\partial_t\langle\hat{a}_k(t)\rangle_{\text{free}} \;=\; -\,i\,\Big\langle\big(\omega_k \;+\; \hat{\eta}_k\big)\,\hat{a}_k \;+\; 2\xi_{kk}\,\Big(\hat{n}_k\hat{a}_k \;+\; \hat{a}_k\Big)\Big\rangle \tag{4.12}$$

To perform the trace over the operators, let $\langle\hat{\eta}_k\hat{a}_k\rangle = \eta_k\,\langle\hat{a}_k\rangle$, where the *traced* frequency shift of mode k due to all other modes is defined to be

$$\eta_k \;\equiv\; \langle\hat{\eta}_k\rangle \;=\; \sum_{j\neq k}^{\text{mol}}\xi_{kj}\,\left(\langle\hat{n}_j\rangle \;+\; \frac{1}{2}\right) \tag{4.13}$$

Since operators acting on different modes commute, the separation, $\langle\hat{n}_j\hat{a}_k\rangle = \langle\hat{n}_j\rangle\langle\hat{a}_k\rangle = \langle\hat{a}_k\rangle\langle\hat{n}_j\rangle$, is always valid (note that traced operators act as scalars, and so their ordering is equivalent, i.e., they commute). By assuming that the higher-order correlations can be neglected, the trace over three operators is separable by, $\langle\hat{a}_k^\dagger\hat{a}_k\hat{a}_k\rangle = \langle\hat{n}_k\rangle\langle\hat{a}_k\rangle = \langle\hat{a}_k\rangle\langle\hat{n}_k\rangle$, (a common assumption in modelling anharmonic molecules [53, 79]) then (4.12) can be factorised

$$\partial_t\langle\hat{a}_k(t)\rangle_{\text{free}} \;=\; -\,i\,\Big(\omega_k \;+\; \eta_k \;+\; 2\xi_{kk}\,\big(\langle\hat{n}_k(t)\rangle \;+1\big)\Big)\,\langle\hat{a}_k(t)\rangle \tag{4.14}$$

This is the free EoM for the expectation value of the annihilation operator. Upon performing an equivalent process for, $\hat{\mathcal{M}} = \hat{a}_k^\dagger$, the creation free EoM is confirmed to be the dagger (Hermitian conjugate) pair of the annihilation operator, $\partial_t\langle\hat{a}_k^\dagger\rangle_{\text{free}} = (\partial_t\langle\hat{a}_k\rangle_{\text{free}})^\dagger$

4.3.4 Free Equation of Motion for the Phonon Number

The main vibrational quantum state of interest is the number operator, $\hat{\mathcal{M}} = \hat{n}_k = \hat{a}_k^\dagger\hat{a}_k$; however, since the commutation of anything with itself is always zero, the free EoM for the phonon number is, $\partial_t\langle\hat{n}_k(t)\rangle_{\text{free}} = 0$, which shows that the phonon number for the free QAO molecule is constant for all time and for all molecular vibrational modes, just as with the QHO model.

4.3.5 Exploration of the Free QAO Equation of Motion

The free QAO EoMs are thus found to be

$$\partial_t \langle \hat{a}_k(t) \rangle_{\text{free}} \;=\; -\,i\,\Big(\omega_k \;+\; \eta_k \;+\; 2\xi_{kk}\,\big(\langle \hat{n}_k(t) \rangle \;+1\big)\Big)\,\langle \hat{a}_k(t) \rangle \tag{4.15a}$$

$$\partial_t \langle \hat{a}_k^\dagger(t) \rangle_{\text{free}} \;=\; +\,i\,\Big(\omega_k \;+\; \eta_k \;+\; 2\xi_{kk}\,\big(\langle \hat{n}_k(t) \rangle \;+1\big)\Big)\,\langle \hat{a}_k^\dagger(t) \rangle \tag{4.15b}$$

$$\partial_t \langle \hat{n}_k(t) \rangle_{\text{free}} \;=\; 0 \tag{4.15c}$$

Physically, this model represents an individual molecule in a void — a vibrational mode that exchanges phonons with itself and all other vibrational modes of the molecule, but does not interact with anything else. The dynamics of this model are elucidated by solving the coupled set of first-order nonlinear ODEs, which do have an exact solution. Since the phonon number must be a constant (4.15c), without loss of generality set $\langle \hat{n}_k \rangle = n_0$, then the creation and annihilation EoM is of the form,

$$\partial_t \langle \hat{a}_k(t) \rangle_{\text{free}} \;=\; -\,i\;\varpi_{\text{free}}\;\langle \hat{a}_k \rangle \tag{4.16a}$$

$$\partial_t \langle \hat{a}_k^\dagger(t) \rangle_{\text{free}} \;=\; +\,i\;\varpi_{\text{free}}\;\langle \hat{a}_k^\dagger \rangle \tag{4.16b}$$

where the free natural QAO oscillation frequency is, $\varpi_{\text{free}} \equiv \omega_k + \eta_k + 2\xi_{kk}(n_0 + 1)$. Since the phonon number is constant, the EoMs can be solved separately, yielding

$$\langle \hat{a}_k(t) \rangle_{\text{free}} \;=\; a_0\;e^{-it\;\varpi_{\text{free}}} \tag{4.17a}$$

$$\langle \hat{a}_k^\dagger(t) \rangle_{\text{free}} \;=\; a_0^*\;e^{+it\;\varpi_{\text{free}}} \tag{4.17b}$$

$$\langle \hat{n}_k(t) \rangle_{\text{free}} \;=\; n_0 \tag{4.17c}$$

for initial annihilation state, $\langle \hat{a}_k(0) \rangle = a_0$, and since the creation and annihilation operators are dagger pairs, their traced initial states must be complex conjugate pairs, $\langle \hat{a}_k^\dagger(0) \rangle = a_0^*$; the initial phonon number state is the absolute magnitude, $n_0 = |a_0|^2$. These solutions are counter-rotating phasors whose trajectories travel along the same circular paths on the imaginary plane $\mathbb{C}$ at a distance from the origin set by the initial state, a_0, which revolve with a constant complex-amplitude at frequency ϖ_{free}. The expectation value for the total energy of the free QAO molecule is

$$E_{\text{free}} \;=\; \hbar\xi_0 \;+\; \hbar \sum_{k=1}^{N_{\text{mode}}} \;\left(\Big(\omega_k \;+\; \eta_k^0\Big)\Big(n_0 \;+\; \frac{1}{2}\Big) \;+\; \xi_{kk}\,\Big(n_0 \;+\; \frac{1}{2}\Big)^2\right) \tag{4.18}$$

where η_k^0 is taken to have constant phonon number values for all other vibrational modes. The presence of anharmonics acts to raise or lower the free QHO energy, depending on the signs of the anharmonic coefficients. Thus the energy of the free molecule is constant for all time due to the fact that the number of phonons in each vibrational mode does not change.

4.4 QAO Molecule and Enzyme Interactions in a Void

In this section, I describe the QAO Catalysis-in-a-Void (CV) model that represents a molecule–enzyme complex in the absence of a dissipative thermal environment. With the free behaviour of the QAO molecule found, an external stimulus can be applied to represent an enzyme. The QAO molecule and the enzyme are able to exchange phonons one-for-one (QHO), but also two-for-one (first-order anharmonics). The inclusion of multi-phonon interactions allows vibrational modes of different frequencies to engage in phonon exchange via spontaneous absorption/emission or by scattering processes.

4.4.1 QAO Catalytic Interaction — Two-for-one Phonon Exchange

The QHO resonance condition for a one-for-one phonon exchange requires that there is a vibrational mode of the enzyme that has the exact same frequency as a vibrational mode of the substrate molecule, $\omega_k = \omega_j$. The set of viable interactions can be extended to allow for the two-for-one exchange of phonons between the enzyme and molecule via the Hamiltonian

$$\begin{aligned}\hat{\mathcal{H}}_{\text{enz}}^{\text{QAO}} \;=\; \sum_{k=1}^{N_{\text{mode}}^{\text{mol}}} \sum_{\alpha,\beta=1}^{N_{\text{mode}}^{\text{enz}}} \hbar\,\kappa_{k\alpha\beta} \Big[&\hat{a}_k^\dagger \hat{b}_\alpha \hat{b}_\beta \;\delta(+\omega_k - \omega_\alpha - \omega_\beta) \;+\; \hat{a}_k^\dagger \hat{b}_\alpha^\dagger \hat{b}_\beta \;\delta(+\omega_k + \omega_\alpha - \omega_\beta) \\ &+\; \hat{a}_k^\dagger \hat{b}_\alpha \hat{b}_\beta^\dagger \;\delta(+\omega_k - \omega_\alpha + \omega_\beta) \;+\; \hat{a}_k \hat{b}_\alpha^\dagger \hat{b}_\beta \;\delta(-\omega_k + \omega_\alpha - \omega_\beta) \\ &+\; \hat{a}_k \hat{b}_\alpha \hat{b}_\beta^\dagger \;\delta(-\omega_k - \omega_\alpha + \omega_\beta) \;+\; \hat{a}_k \hat{b}_\alpha^\dagger \hat{b}_\beta^\dagger \;\delta(-\omega_k + \omega_\alpha + \omega_\beta) \Big]\end{aligned} \tag{4.19}$$

where the summation is over the molecular modes with index k and two enzyme phonons with vibrational mode index α, β, which runs over the integers from 1 to the number of enzyme modes, $N_{\text{mode}}^{\text{enz}}$, subsequently denoted $\sum_{\alpha\beta}^{\text{enz}}$. The coupling strength coefficients, $\kappa_{k\alpha\beta}$, compose a rank-3 tensor that modulates the scattering amplitude of the interactions. The terms in the square brackets describe, respectively: $\hat{a}_k^\dagger \hat{b}_\alpha \hat{b}_\beta$, the creation of one high-frequency molecule phonon due to the simultaneous annihilation of two lower frequency enzyme phonons (absorption); $\hat{a}_k^\dagger \hat{b}_\alpha^\dagger \hat{b}_\beta$, $\hat{a}_k^\dagger \hat{b}_\alpha \hat{b}_\beta^\dagger$, the creation of one molecule phonon and one enzyme phonon due to the annihilation of one high-frequency enzyme phonon (scattering); $\hat{a}_k \hat{b}_\alpha \hat{b}_\beta^\dagger$, $\hat{a}_k \hat{b}_\alpha^\dagger \hat{b}_\beta$ the creation of a high-frequency enzyme phonon due to the annihilation of one molecule phonon and one enzyme phonon (scattering); and, $\hat{a}_k \hat{b}_\alpha^\dagger \hat{b}_\beta^\dagger$, the annihilation of one high-frequency molecule phonon which creates two phonons in the enzyme (emission). The Dirac δ-functions in the interaction are the resonance conditions, and can equivalently be expressed as a statement of *energy conservation* by multiplication of the mode frequencies with $\hbar$. The mutual creation of one molecular phonon and two enzyme phonons, $\hat{a}_k^\dagger \hat{b}_\alpha^\dagger \hat{b}_\beta^\dagger$, and the mutual annihilation, $\hat{a}_k \hat{b}_\alpha \hat{b}_\beta$, do not conserve energy and have been omitted since, $\delta(\omega_k + \omega_\alpha + \omega_\beta) \;=\; 0$, for non-zero, positive frequencies.

Since the dynamics of the molecule are of most interest, the QAO interaction Hamiltonian can be rewritten in terms of that which annihilates or creates a phonon in molecular vibrational

mode k by

$$\hat{\mathcal{H}}_{\text{enz}}^{\text{QAO}} \;=\; \hbar \sum_{k}^{\text{mol}} \Big(\hat{a}_k^\dagger \; \hat{B}_k^{\text{qao}} \;+\; \hat{a}_k \; (\hat{B}_k^{\text{qao}})^\dagger \Big) \tag{4.20}$$

which is of the same general form as the QHO interaction (3.31b). The symmetry, $\delta(-x) \;=\; \delta(x)$, has been used to show that there are only two distinct resonant conditions, $\omega_k \;=\; |\omega_\beta \pm \omega_\alpha|$. Therefore, a valid exchange of phonons occurs via absorption/emission when $\omega_k \;=\; \omega_\alpha + \omega_\beta$ (one high-frequency molecule mode for two lower frequency enzyme modes), and for scattering processes with $\omega_k + \omega_\alpha = \omega_\beta$ (one high frequency enzyme mode scattering into a lower frequency mode in the molecule, and into the enzyme). The inclusion of multi-phonon interactions allows for many enzyme modes over a range of frequencies to participate in the time evolution of each molecular mode. The general resonance condition for a two-for-one exchange of phonons is, $\delta(\omega_k - |\omega_\alpha \pm \omega_\beta|)$.

The QAO stimulus superoperator can then be identified as

$$\begin{aligned} \hat{B}_k^{\text{qao}} \;\equiv\; \sum_{\alpha\beta}^{\text{enz}} \kappa_{k\alpha\beta} \; \Big(& \hat{b}_\alpha \hat{b}_\beta \; \delta(\omega_k - \omega_\alpha - \omega_\beta) \\ & +\; \hat{b}_\alpha^\dagger \hat{b}_\beta \; \delta(\omega_k + \omega_\alpha - \omega_\beta) \;+\; \hat{b}_\alpha \hat{b}_\beta^\dagger \; \delta(\omega_k - \omega_\alpha + \omega_\beta) \Big) \end{aligned} \tag{4.21}$$

The first term represents the type-1 Fermi resonance, $\omega_k = \omega_\alpha + \omega_\beta$, which describes spontaneous emission and absorption; the other two terms are the type-2 Fermi resonances, $\omega_k = |\omega_\alpha - \omega_\beta|$, which describe scattering processes [133]. Therefore, a valid three-phonon QAO interaction satisfies the resonance condition

$$\omega_k \;=\; |\omega_\alpha \;\pm\; \omega_\beta| \tag{4.22}$$

for a molecular mode k, with two enzyme modes α, β, where absorption/emission is described by $(+)$, and scattering by $(-)$.

4.4.2 QAO Interactions of Isomaltose and MalL

The viable resonant interactions between isomaltose and MalL can be elucidated from Fig. 4.2. The low- to mid-frequency modes of the isomaltose and MalL (< 60 THz) are readily able to exchange phonons via all processes, as can be seen by the many white and coloured lines crossing the lower left bright region. The lowest frequency isomaltose modes (bulk motion) interact with some of the highest frequency enzyme modes (hydrogen network) via scattering, as can be seen from the red lines adjacent to the leading diagonal passing through a bright patch in the top left corner. For example, the high-frequency glycosidic hydrogen oscillations of isomaltose (100 THz) can exchange with MalL via scattering (for example, $\omega_\alpha = 110$ THz and $\omega_\beta = 10$ THz, indicated by the blue lines crossing the bright region), and emission/absorption in the 45–55 THz bandwidth of enzyme modes (white lines crossing crossing the lower left square region). Of particular interest are the glycosidic bond stretching modes near 30 THz (orange). These isomaltose modes can be seen to interact with many MalL mode combinations in the < 30 THz bandwidth via emission/absorption (white), and are able to exchange phonons via

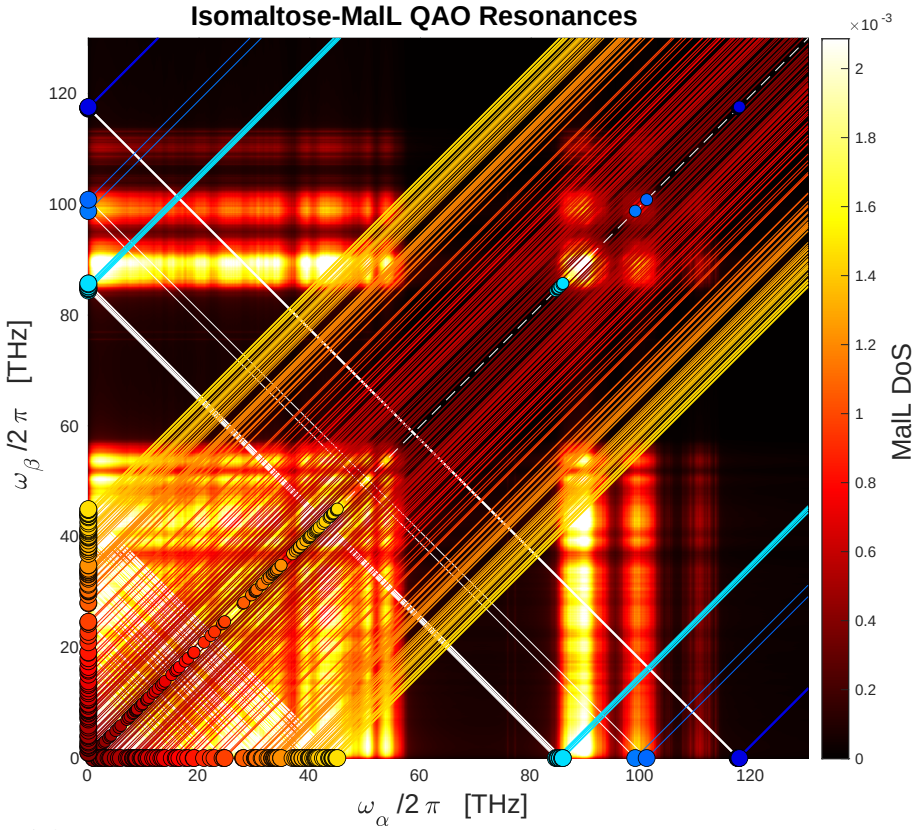

Figure 4.2: QAO interactions for isomaltose and MalL; this map is constructed using the normal mode frequencies for the substrate and enzyme, and does need require explicit resonance calculations or anharmonic MD simulation data. The heatmap surface is produced by the square root of the outer-product matrix of the DoS with $\varphi_k/2\pi = 0.1$ THz, the leading diagonal slice is the MalL DoS (Fig. 3.2); the bright regions indicate the presence of enzyme modes, and there are no enzyme modes in the black regions. The dots indicate the isomaltose modes and are coloured for their natural NMA frequencies, ω_k. The QHO interaction zones are equally represented: along the x-axis, $\omega_\alpha = \omega_k$; along the y-axis, $\omega_\beta = \omega_k$; and on the leading diagonal (dashed white line), $\omega_\alpha = \omega_\beta = \omega_k$. The QAO interaction zones are represented by the lines radiating from the QHO mode frequencies: the white downwards diagonal lines (with ω_α) are the regions of emission/absorption, $\omega_k = \omega_\beta + \omega_\alpha$; and the coloured upwards diagonals are the regions of scattering, $\omega_k = |\omega_\beta - \omega_\alpha|$.

scattering with the combinations of enzyme bond stretching modes (55 THz) and the hydrogen network (85 THz).

The total number of possible QAO interactions between one molecular mode and two enzyme modes is $N_{\text{mode}}^{\text{mol}}\,(N_{\text{mode}}^{\text{enz}})^2$. For the interaction between isomaltose (126 modes) and the MalL enzyme (27,450 modes) there are 9.49×10^{10} opportunities for anharmonic phonon exchange (Fig. 4.2). By smearing out the δ-function into a Lorentzian resonance distribution with a small smearing frequency (spectral linewidth) via (3.44), the number of interactions that approximately satisfy the resonance conditions (4.22) can be computed. Therefore a smearing frequency of φ_k allows interactions between substrate mode k and enzyme modes α, β to exchange phonons if

$$\big|\omega_k \;-\; |\omega_\alpha \;\pm\; \omega_\beta|\big| \;\leq\; |\varphi_k| \tag{4.23}$$

By setting $\varphi_k/2\pi = 0.1$ THz for all substrate modes, the smallest value used in the literature (**§ 3.3.3**), the total number of viable isomaltose–MalL QAO interactions is 3.63×10^8, or 0.38%

of the total. Fig. 4.3 shows the number of combinations of enzyme modes that resonate with each molecular mode, and Fig. 4.4 shows the number of molecular modes that resonate with each combination of enzyme modes for a smearing of 0.1 THz. In the same manner as the harmonic case in **§ 3.3.3**, the number of viable anharmonic interactions is linearly proportional to the smearing frequency up to 1 THz, with a constant of 3.61×10^9 THz^{-1}. This is a surprising result considering the 9.49×10^{10} calculations leading to their values, and allows for the number of viable interactions to be determined without performing the computation.

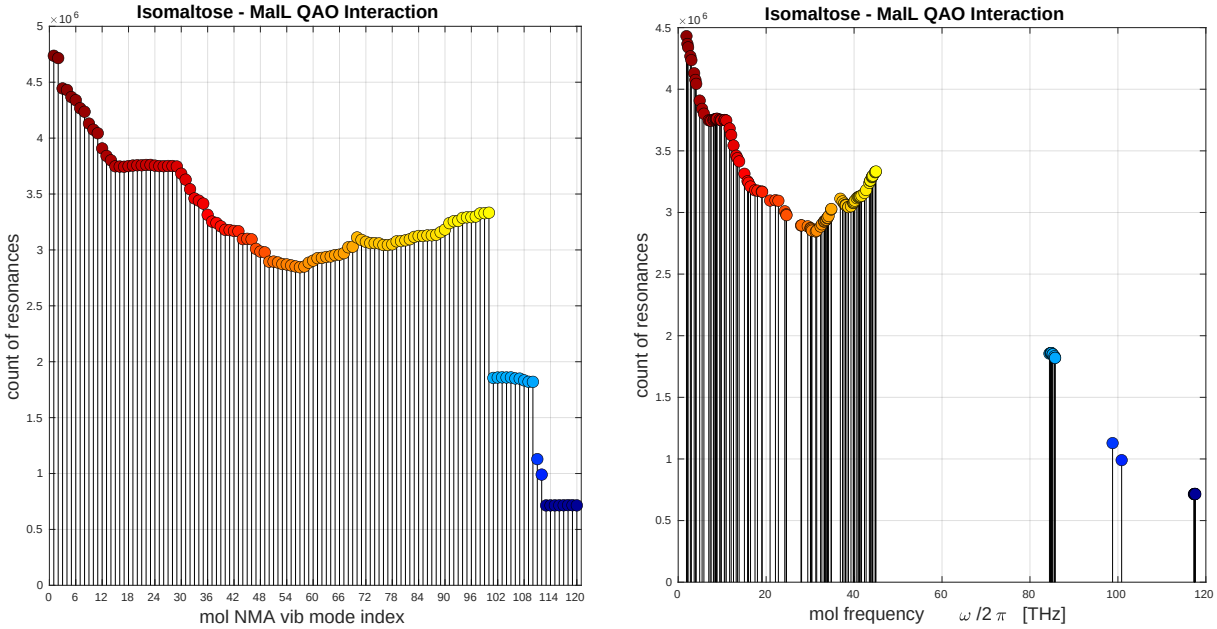

(a) QAO interaction — mode index **(b)** QAO interaction — spectral distribution

Figure 4.3: The number of isomaltose–MalL QAO interactions is calculated by (4.23), the total number of combinations of enzyme modes, $(\alpha\,\beta)$, that satisfy the smeared resonance conditions for each molecular mode k. The smearing frequency is set to, $\varphi_k/2\pi = 0.1$ THz.

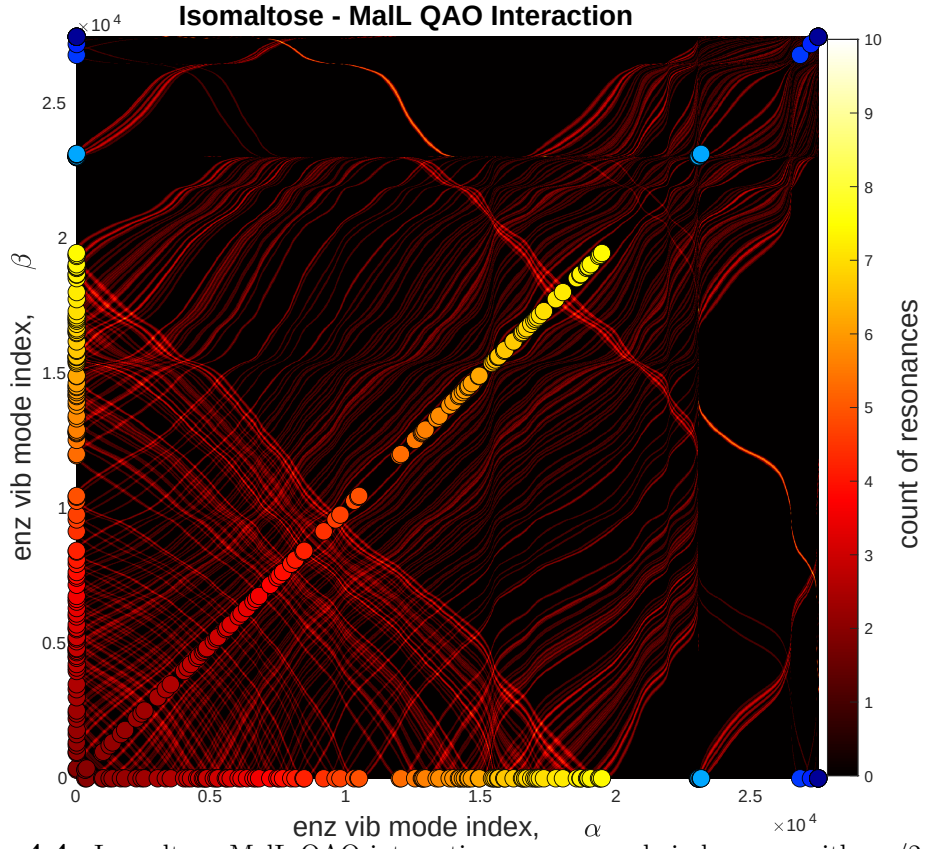

Figure 4.4: Isomaltose–MalL QAO interaction enzyme mode index map with $\varphi_k/2\pi = 0.1$ THz; this map is the computed equivalent to Fig. 4.3. Each pixel represents a combination of enzyme modes (α, β), whose colour denotes the total number of molecular vibrational modes that satisfy the QAO resonance conditions (4.23). The axes are the enzyme vibrational mode indicies. The black regions indicate combinations of MalL modes (α, β) that have no resonance with isomaltose modes, and the brighter regions indicate viable interactions. The isomaltose modes are plotted as dots along the axes where, $\omega_k = \omega_\alpha$. Absorption/emission processes for a given molecular mode are represented by the lines that trend down from left to right; scattering processes project upwards. The high frequency molecular modes around 85 THz (light blue) can be seen to participate in many scattering exchanges, and the higher frequency modes (100 THz) pertaining the glycosidic hydrogen atoms can be seen to interact with much lower frequency modes in the enzyme due to absorption.

4.4.3 The Simplest Interaction Model for Anharmonic Phonon Exchange

The total molecule–enzyme interaction Hamiltonian is the summation of the harmonic one-for-one and anharmonic two-for-one phonon exchange processes. The total external stimulus superoperator that results in the creation of one molecule phonon in vibrational mode k is the summation of the QHO (3.33) and QAO (4.21) contributions, $\hat{B}_k = \hat{B}_k^{\text{qho}} + \hat{B}_k^{\text{qao}}$. With this definition, the total interaction Hamiltonian is

$$\hat{\mathcal{H}}_{\text{mol}}^{\text{int}} = \sum_k^{\text{mol}} \hbar \left(\hat{a}_k^\dagger \, \hat{B}_k + \hat{a}_k \, \hat{B}_k^\dagger \right) \tag{4.24}$$

To simplify the treatment of how the molecule experiences an external stimulus, it can be assumed that the phonon numbers of the external system are unaffected by the exchange. This is achieved by the semiclassical assumption whereby the quantum annihilation operators are

replaced by classical phasors, $\hat{b}_\alpha \mapsto \sqrt{n_\alpha^{\text{ext}}}\, e^{-it\,\omega_\alpha}$, with the creation operator being the complex conjugate. The creation and annihilation operators are classical counter-rotating phasors under this approximation. The value of n_α^{ext} is the number of phonons in vibrational mode α of the external system, and is a non-negative real-valued scalar. The phasor frequency, ω_α, is equal to the external vibrational mode frequency, and the amplitude, $\sqrt{n_\alpha^{\text{ext}}}$, is purely real. This choice for the replacement is such that the number operator for the external system is non-oscillatory, $\hat{b}_\alpha^\dagger \hat{b}_\alpha \mapsto n_\alpha^{\text{ext}}$. This semiclassical approximation for the exchange of quanta is commonly used in quantum optics for photons whereby the EM field is treated classically [60], and also in Davydov's theory of the energy transfer in proteins [127, 134]. Thus, the external stimulus superoperator is replaced with the classical field

$$\begin{aligned}\tilde{B}_k(t) \;=\; & \sum_{k'}^{\text{ext}} \Xi_{kk'}\, \sqrt{n_{k'}^{\text{ext}}}\; e^{-it\,\omega_{k'}}\; \delta(\omega_k - \omega_{k'}) \\ & +\; \sum_{\alpha\beta}^{\text{ext}} \kappa_{k\alpha\beta}\, \sqrt{n_\alpha^{\text{ext}}\; n_\beta^{\text{ext}}}\, \Big(e^{-it\,(\omega_\alpha\; +\; \omega_\beta)}\; \delta(\omega_k - \omega_\alpha - \omega_\beta) \;+\; e^{-it\,(\omega_\beta\; -\; \omega_\alpha)}\; \delta(\omega_k + \omega_\alpha - \omega_\beta) \Big)\end{aligned} \tag{4.25}$$

and is an imaginary-valued scalar, $\tilde{B}_k^* \neq \tilde{B}_k$. The total interaction Hamiltonian for vibrational mode k is then encapsulated by

$$\hat{\mathcal{H}}_k^{\text{int}} \;=\; \hbar \left(\hat{a}_k^\dagger\; \tilde{B}_k(t) \;+\; \hat{a}_k\; \tilde{B}_k^*(t) \right) \tag{4.26}$$

The contribution of the external stimulus to the EoMs is elucidated via substitution of (4.26) into the free QME (4.10)

$$\partial_t \langle \hat{\mathcal{M}}(t) \rangle_{\text{int}} \;=\; -\,i\,\tilde{B}_k(t)\, \left\langle \left[\hat{M}\;,\; \hat{a}_k^\dagger \right] \right\rangle \;+\; i\,\tilde{B}_k^*(t)\, \left\langle \left[\hat{M}\;,\; \hat{a}_k \right] \right\rangle \tag{4.27}$$

from which the EoMs are

$$\partial_t \langle \hat{a}_k(t) \rangle_{\text{int}} \;=\; -\,i\tilde{B}_k(t) \tag{4.28a}$$

$$\partial_t \langle \hat{a}_k^\dagger(t) \rangle_{\text{int}} \;=\; +\,i\tilde{B}_k^*(t) \tag{4.28b}$$

$$\partial_t \langle \hat{n}_k(t) \rangle_{\text{int}} \;=\; -\,i \left(\tilde{B}_k(t)\; \langle \hat{a}_k^\dagger(t) \rangle \;-\; \tilde{B}_k^*(t)\; \langle \hat{a}_k(t) \rangle \right) \tag{4.28c}$$

The stimulus introduces a time-dependent inhomogeneity to the creation and annihilation EoMs, and a time-dependent coupling to the number operator.

4.4.4 The Dynamics of Catalysis in a Void

I call the QAO EoMs for vibrational mode k of a molecule as it interacts with an enzyme in the absence of dissipation the Catalysis-in-a-Void (CV) model. The QAO CV EoMs are the

combination of the free (4.15) and stimulated (4.28) behaviours

$$\partial_t\langle\hat{a}_k(t)\rangle_{\rm cv} \;=\; -\,i\,\Big(\varpi_{\rm cv} \;+\; 2\xi_{kk}\,\langle\hat{n}_k(t)\rangle\Big)\,\langle\hat{a}_k(t)\rangle \;-\; i\,\tilde{B}_k(t) \tag{4.29a}$$

$$\partial_t\langle\hat{a}_k^\dagger(t)\rangle_{\rm cv} \;=\; +\,i\,\Big(\varpi_{\rm cv} \;+\; 2\xi_{kk}\,\langle\hat{n}_k(t)\rangle\Big)\,\langle\hat{a}_k^\dagger(t)\rangle \;+\; i\,\tilde{B}_k(t) \tag{4.29b}$$

$$\partial_t\langle\hat{n}_k(t)\rangle_{\rm cv} \;=\; -\,i\,\Big(\tilde{B}_k(t)\,\langle\hat{a}_k^\dagger(t)\rangle \;-\; \tilde{B}_k^*(t)\,\langle\hat{a}_k(t)\rangle\Big) \tag{4.29c}$$

where the ground state oscillation frequency of the QAO CV mode is, $\varpi_{\rm cv} \equiv \omega_k + \eta_k + 2\xi_{kk}$. The QAO CV EoMs for one vibrational mode are a system of three coupled first-order, nonlinear inhomogeneous ODEs which cannot be solved analytically; furthermore, the phonon number state of the other molecular modes ($j \neq k$) affects the evolution of mode k via the η_k term. As was done in the QHO chapter, the sinusoidal factors of the external stimulus can be eliminated via a transformation to a rotating frame of reference at frequency, ω, such that the creation and annihilation operators are moved from the Heisenberg picture into the interaction picture. By observing the inhomogeneity in the rotating frame

$$\begin{aligned}\tilde{B}_k(t)\;e^{+it\,\omega} \;=\; &\sum_{k'}^{\rm ext}\Xi_{kk'}\,\sqrt{n_{k'}^{\rm ext}}\;e^{it\,(\omega-\omega_{k'})}\;\delta(\omega_k-\omega_{k'})\\ &+\;\sum_{\alpha\beta}^{\rm ext}\kappa_{k\alpha\beta}\,\sqrt{n_\alpha^{\rm ext}\;n_\beta^{\rm ext}}\;\Big(e^{it\,(\omega\;-\;\omega_\alpha\;-\;\omega_\beta)}\;\delta(\omega_k-\omega_\alpha-\omega_\beta)\\ &\qquad\qquad+\;e^{it\,(\omega\;+\;\omega_\beta\;-\;\omega_\alpha)}\;\delta(\omega_k+\omega_\alpha-\omega_\beta)\Big)\end{aligned} \tag{4.30}$$

it can be seen that since each of these exchanges of phonons occur distinctly from the others, when the rotating frame frequency ω is such that a resonance condition is met, the phase of the associated phasor will be zero ($e^0 = 1$); this means that and that when one of these exchanges occurs, the stimulus is not dependent on time. The exchanges are independent of each other since each value of ω can only satisfy a single resonance condition, and the other processes will be suppressed via the δ-function. The QAO stimulus in the rotating frame can then be given as

$$\begin{aligned}B_k \;=\; &\sum_{k'}^{\rm ext}\Xi_{kk'}\,\sqrt{n_{k'}^{\rm ext}}\;\delta(\omega_k-\omega_{k'})\\ &+\;\sum_{\alpha\beta}^{\rm ext}\kappa_{k\alpha\beta}\,\sqrt{n_\alpha^{\rm ext}\;n_\beta^{\rm ext}}\;\Big(\delta(\omega_k-\omega_\alpha-\omega_\beta)\;+\;\delta(\omega_k+\omega_\alpha-\omega_\beta)\Big)\end{aligned} \tag{4.31}$$

which is a real-valued scalar, $B_k^* = B_k$, that is independent of time. The QHO portion can be expressed in the form shown in **§ 3.3.4** (3.46); the QAO portion can then be approximated in a similar fashion by smearing the resonance condition and setting the external system to be at thermal equilibrium, $n_\alpha^{\rm ext} = \bar{n}_\alpha$, resulting in

$$B_k^{\rm qao} \;=\; \frac{1}{\pi N_{\rm mode}^{\rm env}}\;\sum_{\pm}\sum_{\alpha\beta}^{\rm env}\kappa_{k\alpha\beta}\,\sqrt{\bar{n}_\alpha\;\bar{n}_\beta}\;\frac{\varphi_k^2}{\varphi_k^2\;+\;(\omega_k\;-\;|\omega_\alpha\;\pm\;\omega_\beta|)^2} \tag{4.32}$$

where the DoS has been used to express the number of external modes. The QAO CV EoMs can then be written

$$\partial_t\langle\hat{a}_k(t)\rangle_{\rm cv} \;=\; +\,i\,\phi_{\rm cv}\,\langle\hat{a}_k(t)\rangle \;-\; i2\xi_{kk}\,\langle\hat{n}_k(t)\rangle\,\langle\hat{a}_k(t)\rangle \;-\; i\,B_k \tag{4.33a}$$

$$\partial_t\langle\hat{a}_k^\dagger(t)\rangle_{\rm cv} \;=\; -\,i\,\phi_{\rm cv}\,\langle\hat{a}_k^\dagger(t)\rangle \;+\; i2\xi_{kk}\,\langle\hat{n}_k(t)\rangle\,\langle\hat{a}_k^\dagger(t)\rangle \;+\; i\,B_k \tag{4.33b}$$

$$\partial_t\langle\hat{n}_k(t)\rangle_{\rm cv} \;=\; -\,i\,B_k\,\Big(\langle\hat{a}_k^\dagger(t)\rangle \;-\; \langle\hat{a}_k(t)\rangle\Big) \tag{4.33c}$$

with a detuning frequency, $\phi_{\rm cv}(\omega) \equiv \omega - \varpi_{\rm cv}$. These EoMs are a coupled set of first-order ODEs that cannot be solved analytically due to the products $\langle\hat{n}_k\rangle\langle\hat{a}_k\rangle$ and $\langle\hat{n}_k\rangle\langle\hat{a}_k^\dagger\rangle$.

4.4.5 QAO Catalysis in a Void Steady States

I will now perform a SS analysis on the QAO CV model EoMs (4.33). The SS of the creation and annihilation operators are equal and purely real

$$\langle\hat{a}_k\rangle_{\rm cv}^{\rm ss} \;=\; \langle\hat{a}_k^\dagger\rangle_{\rm cv}^{\rm ss} \;=\; \frac{B_k}{\phi_{\rm cv} \;-\; 2\xi_{kk}\,\langle\hat{n}_k\rangle_{\rm cv}^{\rm ss}} \tag{4.34}$$

and therefore the number EoM at SS reveals no information; however, since the the CV model has the property, $\partial_t(\langle\hat{a}_k^\dagger\rangle_{\rm cv}\langle\hat{a}_k\rangle_{\rm cv}) = \partial_t\langle\hat{n}_k\rangle_{\rm cv}$, and that number operator is the product of the creation and annihilation operators, the number SS value could be set to

$$\langle\hat{n}_k\rangle_{\rm cv}^{\rm ss} \;=\; \langle\hat{a}_k^\dagger\rangle_{\rm cv}^{\rm ss}\langle\hat{a}_k\rangle_{\rm cv}^{\rm ss} \;=\; \frac{B_k^2}{\big(\phi_{\rm cv} \;-\; 2\xi_{kk}\,\langle\hat{n}_k\rangle_{\rm cv}^{\rm ss}\big)^2} \tag{4.35}$$

Rearrangement reveals a cubic polynomial in the number SS, which means that there are at most *three* valid SS for the molecular vibrational mode at a given detuning frequency. For readability, let $N \equiv \langle\hat{n}_k\rangle_{\rm cv}^{\rm ss}$, then the SS conditional relation is

$$0 \;=\; \big(\phi_{\rm cv} \;-\; 2\xi_{kk}\,N\big)^2\,N \;-\; B_k^2 \tag{4.36}$$

If the enzyme stimulus is removed ($B_k = 0$), then the SS is at $N = 0$ (unoccupied state), or along $N = \phi_{\rm cv}/2\xi_{kk}$ (dashed line in Fig. 4.5).

The solutions of the cubic polynomial can either have three real roots, or one real root and two complex conjugate pairs. Since a valid SS for the molecular vibrational mode phonon number must be real and positive, $N \in \mathbb{R}_{\geq 0}$, there are two distinct regimes characterised by the stimulus frequency:

- **SS1**: frequency bands with one valid number SS
- **SS3**: frequency bands with three valid number SS

their boundary has repeated roots, and is represented as the vertical blue line in Fig. 4.5. The SS distribution can be plotted by rearrangement the (4.36) for $\phi_{\rm cv}$ in terms of N

$$\phi_{\rm ss}^{\pm}(N) \;=\; 2\xi_{kk}\,N \;\pm\; \frac{B_k}{\sqrt{N}} \tag{4.37}$$

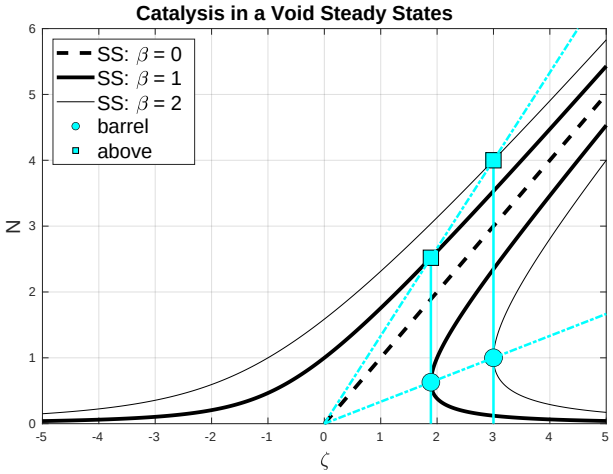

Figure 4.5: QAO Catalysis in a Void SS distribution, plotted using dimensionless detuning frequency $\zeta = \phi_{\rm cv}/2\xi_{kk}$ and stimulus $\beta = B_k/2\xi_{kk}$. SS curves are drawn for $\beta = 0$ (dashed), $\beta = 1$ (thick black), and $\beta = 2$ (thin black), along with the associated barrel point (cyan circle) and above-barrel point (cyan square) which denote the SS1/SS3 boundary. The barrel points (circles) at varying β lie along the line $N = \zeta/3$, and the above-barrel points (squares) lie long $N = 4\zeta/3$.

without using a root solving algorithm, and has been used in Fig. 4.5. The positive branch, $\phi^{+}_{\rm ss}$, is the lower portion of the SS in Fig. 4.5, whose curl marks the boundary. The point where the lower portion curls over is the saddle-node bifurcation point (cyan circle), which is a neutral state delicately balanced between stability and instability (zero stability eigenvalue), as will be seen in the next section. I will call this the *barrel* point since the non-dissipative SS distribution on the detuning–number plane has a shape that resembles a surfable ocean wave, and the barrel point indicates the ideal place to ride the wave. The location of the saddle-node bifurcation point will migrate towards the spine ($N = \phi_{\rm cv}/2\xi_{kk}$) for increasing dissipation, as will be shown in a later section, which motivates the distinction for the naming convention. It will be shown later in this chapter that the inclusion of dissipation creates a second saddle-node bifurcation point at the 'crest' of the wave.

The barrel point coordinates are found by taking the extrema of the positive branch (4.94), $0 = \partial_N \phi^{\pm}_{\rm ss}$, which upon rearrangement reveals the barrel phonon number, $N = \nu_k$, where

$$\nu_k \;\equiv\; \left(\frac{B_k}{4\,|\xi_{kk}|}\right)^{2/3} \tag{4.38}$$

where the absolute value ensures that ν_k is real. This result that will be used throughout the subsequent sections. The barrel point detuning frequency is then found by setting $N = \nu_k$ in (4.37), and using $B_k = 4\xi_{kk}\,\nu_k^{3/2}$, giving, $\phi_\nu = 6\xi_{kk}\,\nu_k$. Thus the barrel point (saddle node bifurcation for the QAO CV model) has coordinates

$$(\phi_{\rm cv}\ ,\ N)_{\rm barrel} \;=\; (6\xi_{kk}\,\nu_k\ ,\ \nu_k) \tag{4.39}$$

It can be seen in Fig. 4.5 that for larger $\beta = B_k/2\xi_{kk}$, the barrel point occurs at a higher $\phi_{\rm cv}$ and N. The detuning frequency is plotted using the dimensionless $\zeta = \phi_{\rm cv}/2\xi_{kk}$, the barrel point is always at a positive value, but when using the dimensioned quantities ξ_{kk} and B_k can be positive

or negative. Where there are repeated roots for the phonon number in the solution of the QAO CV SS conditional relation (4.36) the low solution is the barrel point where there is repeated roots (cyan circle in Fig. 4.5); the high solution is above the barrel at a higher N (square). By the fundamental theorem of algebra, a cubic polynomial can be expressed as the product, $(x-r_1)(x-r_2)(x-r_3)$, where the r_i are the distinct roots; in the case of repeated roots, $r_2 = r_3$, the factorisation is $(x-r_1)(x-r_2)^2$. To find the point above the barrel, the SS conditional relation (4.36) is set to $\phi_{\rm cv} = 6\xi_{kk}\,\nu_k$ and then equated to repeated root factorisation, noting that the repeated root phonon number is ν_k, then $0 \;=\; (3\nu_k - N)^2 N - \beta^2 \;=\; (N-\nu_k)^2(N-N_{\rm nr})$, where $N_{\rm nr}$ is the non-repeated root. By expanding the brackets and equating coefficients, the above-barrel phonon number is, $N_{\rm nr} = 4\,\nu_k$. Therefore, the point above the barrel has coordinates

$$(\phi_{\rm cv}\;,\;N)_{\rm above} \;=\; (6\xi_{kk}\,\nu_k\;,\;4\nu_k) \tag{4.40}$$

and is plotted in Fig. 4.5 as the cyan squares for $\beta = \{1, 2\}$. Thus the boundary of SS1 & SS3 regimes has been found analytically, and is dependent on the anharmonic self-interaction frequency, ξ_{kk}, and the stimulus, B_k. The boundary grows linearly with increasing β (dashed cyan lines), where the line threading through the barrel points for varying β is plotted by $N = \frac{1}{3}\zeta$, and the line threading through the above barrel points is $N = \frac{4}{3}\zeta$.

The frequencies for a certain phonon number, N, which experience a SS is given by (4.37), $\omega_{\rm ss}^{\pm}(N) \;=\; \varpi_{\rm cv} \;+\; \phi_{\rm ss}^{\pm}(N)$. The boundary occurs at barrel frequency, $\omega_{\rm barrel} \;=\; \varpi_{\rm cv} \;+\; 6\,\xi_{kk}\,\nu_k$, which occurs at a higher (lower) frequency than the vibrational mode oscillation frequency, $\varpi_{\rm cv}$, if the anharmonic self-interaction frequency, ξ_{kk}, is positive (negative). With the SS1 & SS3 boundary determined, it can be seen that the SS1 region occurs for low frequencies such that $\zeta < 3\nu_k$, and the SS3 region occurs where $\zeta \geq 3\nu_k$. In the dimensioned quantities, if $\xi_{kk} > 0$, then the SS3 region occurs where $\omega > \omega_{\rm barrel}$, and if $\xi_{kk} < 0$ then the SS3 region is $\omega < \omega_{\rm barrel}$. The value of ξ_{kk} controls the angle of N response amplitude; for negative values, the SS curve leans towards lower frequencies, and for positive values the SS leans towards higher frequency. This is described by phonon softening and hardening, respectively.

For the following discussion, let $\xi_{kk} > 0$. If the molecular vibrational mode is driven at a frequency lower than the oscillation, $\omega < \varpi_{\rm cv}$ (negative detuning), and is gradually increased, the SS phonon number will monotonically increase along the upper $\omega_{\rm ss}^{\pm}$ curve without bound. In the absence of noise, if the vibrational mode begins at a low phonon number ($N < \zeta$) and is driven at a higher frequency, $\omega > \varpi_{\rm cv}$ (positive detuning), and then is tuned down, the SS phonon number will slowly increase until the boundary, $\omega = \omega_{\rm barrel}$, where the phonon number will discontinuously *jump* from the barrel point to the point above it; by continually lowering ω, the vibrational mode will travel further into the SS1 regions, however, if ω were to be increased *after* the jump, the state will travel back into the SS3 region along the upper branch. In the presence of a stochastic background due to thermal noise the jump will occur before the saddle-node point [1]. This jump behaviour is a central feature of the classical cubic anharmonic oscillator Duffing equation [50]. I will return to this discussion in **§ 4.6** once the complete QAO catalytic model is constructed.

4.4.6 Catalysis in a Void Stability Analysis

The solutions to the QHO model EoMs are single-valued functions with trivial stability behaviour: when released from an arbitrary initial state, the evolution of the transient state is attracted towards the SS while exhibiting relaxation oscillations with an exponentially decaying amplitude. By including anharmonic behaviour, the EoMs are not analytically tractable and so an exact solution cannot be found; instead, a stability analysis will be applied to the EoMs which will elucidate the stability of the SS. Defining a vibrational mode quantum state expectation value vector,

$$\mathbf{\Psi}(t) \;\equiv\; \begin{bmatrix} \langle \hat{a}_k(t) \rangle \\ \langle \hat{a}_k^\dagger(t) \rangle \\ \langle \hat{n}_k(t) \rangle \end{bmatrix} \tag{4.41}$$

allows the QAO CV EoMs (4.33) to be collected into a matrix form

$$\partial_t \mathbf{\Psi}_{\text{cv}} \;=\; \mathbf{M}_{\text{cv}}\; \mathbf{\Psi} \;+\; \mathcal{N}_{\text{cv}}(\mathbf{\Psi}) \;+\; \mathbf{b}_{\text{cv}} \tag{4.42}$$

The matrix containing the linear dynamics is

$$\mathbf{M}_{\text{cv}} \;=\; \begin{bmatrix} +i\phi_{\text{cv}} & 0 & 0 \\ 0 & -i\phi_{\text{cv}} & 0 \\ +iB_k & -iB_k & 0 \end{bmatrix} \tag{4.43}$$

the constant offset (inhomogeneity), $\mathbf{b}_{\text{cv}} = iB_k \left[-1, +1, 0 \right]^{\text{T}}$, acts as a source term and the matrix containing the non-linear dynamics is, $\mathcal{N}_{\text{cv}} = i\, 2\xi_{kk} \langle \hat{n}_k \rangle \left[-\langle \hat{a}_k \rangle, +\langle \hat{a}_k^\dagger \rangle, 0 \right]^{\text{T}}$. A non-linear matrix EoM can only be solved exactly in very restrictive circumstances [135, 136]; therefore, I perform a linear stability analysis in order to explore the dynamical behaviour of the QAO CV model. The Jacobian stability matrix is a linear approximation of the EoMs taken at the SS. For the QAO CV model, the Jacobian stability matrix is

$$\mathbf{J} \;=\; \left(\frac{\partial(\partial_t \mathbf{\Psi})}{\partial \mathbf{\Psi}} \right) \Bigg|_{\text{ss}} \tag{4.44}$$

whose elements are the quantum state EoMs differentiated with the states, which are then evaluated at SS,

$$\mathbf{J} \;=\; \begin{bmatrix} \dfrac{\partial(\partial_t \langle \hat{a}_k \rangle)}{\partial \langle \hat{a}_k \rangle} & \dfrac{\partial(\partial_t \langle \hat{a}_k \rangle)}{\partial \langle \hat{a}_k^\dagger \rangle} & \dfrac{\partial(\partial_t \langle \hat{a}_k \rangle)}{\partial \langle \hat{n}_k \rangle} \\ \dfrac{\partial(\partial_t \langle \hat{a}_k^\dagger \rangle)}{\partial \langle \hat{a}_k \rangle} & \dfrac{\partial(\partial_t \langle \hat{a}_k^\dagger \rangle)}{\partial \langle \hat{a}_k^\dagger \rangle} & \dfrac{\partial(\partial_t \langle \hat{a}_k^\dagger \rangle)}{\partial \langle \hat{n}_k \rangle} \\ \dfrac{\partial(\partial_t \langle \hat{n}_k \rangle)}{\partial \langle \hat{a}_k \rangle} & \dfrac{\partial(\partial_t \langle \hat{n}_k \rangle)}{\partial \langle \hat{a}_k^\dagger \rangle} & \dfrac{\partial(\partial_t \langle \hat{n}_k \rangle)}{\partial \langle \hat{n}_k \rangle} \end{bmatrix}_{\text{ss}} \tag{4.45}$$

After computing each element, and letting the SS variables be, $\langle \hat{a}_k \rangle_{\rm cv}^{\rm ss} = \alpha = \langle \hat{a}_k^\dagger \rangle_{\rm cv}^{\rm ss}$, and $\langle \hat{n}_k \rangle_{\rm cv}^{\rm ss} = N$, for readability, the QAO CV Jacobian stability matrix is

$$\mathbf{J}_{\rm cv} \;=\; \begin{bmatrix} +i(\phi_{\rm cv} - 2\xi_{kk}\,N) & 0 & -i2\xi_{kk}\,\alpha \\ 0 & -i(\phi_{\rm cv} - 2\xi_{kk}\,N) & +i2\xi_{kk}\,\alpha \\ +iB_k & -iB_k & 0 \end{bmatrix} \tag{4.46}$$

The Jacobian stability matrix is a 3×3 matrix and so has three stability eigenvalues, found in the standard way, $0 = \det[\mathbf{J} - \mathbf{\Lambda}]$, yielding the characteristic equation

$$0 \;=\; -\lambda\,\left(\lambda^2 \;+\; (\phi_{\rm cv} \;-\; 2\xi_{kk}\,N)^2\right) \;+\; 4\xi_{kk}\,B_k\,\alpha\;\lambda \tag{4.47}$$

The first term is the main leading diagonal (top left to bottom right), and the second term is the combination of the anti-diagonals (bottom to top). These terms can be factorised

$$0 \;=\; -\lambda\,\left(\lambda^2 \;+\; (\phi_{\rm cv} \;-\; 2\xi_{kk}\,N)^2 \;-\; 4\xi_{kk}\,B_k\,\alpha\right) \tag{4.48}$$

Making use of the QAOSS conditional relation in the form, $\alpha^2 = N$ (4.35), to eliminate α, it can be seen from (4.34) that, $\alpha B_k = (\phi_{\rm cv} - 2\xi_{kk}\,N)N$, and the characteristic equation can be expressed as

$$0 \;=\; -\lambda\,\Big(\lambda^2 \;+\; (\phi_{\rm cv} \;-\; 2\xi_{kk}\,N)(\phi_{\rm cv} \;-\; 6\xi_{kk}\,N)\Big) \tag{4.49}$$

The three stability eigenvalues are: $\lambda_{\rm cv}^0 = 0$, which does not contribute any information about the SS stability; and a pair

$$\lambda_{\rm cv}^{\pm} \;=\; \pm\sqrt{-(\phi_{\rm cv} \;-\; 2\xi_{kk}\,N)(\phi_{\rm cv} \;-\; 6\xi_{kk}\,N)} \tag{4.50}$$

which carry dimensions of $[\text{time}]^{-1}$ and can be either purely real or purely imaginary depending on the sign under the squareroot. These eigenvalues can be non-dimensionalised by division of $2\xi_{kk}$, and expressed in terms of the dimensionless detuning parameter, ζ, by

$$\tilde{\lambda}_{\rm cv}^{\pm} \;=\; \pm\sqrt{-(\zeta \;-\; N)(\zeta \;-\; 3N)} \tag{4.51}$$

where $\tilde{\lambda} = \lambda/2\xi_{kk}$ is dimensionless. The bifurcation of stability is the boundary between the stable and unstable regions, which occurs where the real component of the stability eigenvalue is zero, $\Re[\tilde{\lambda}_{\rm cv}^{\pm}] = 0$. For a given ζ, there will be two values of N for which there is a stability bifurcation point, $N_{s,\rm cv}^{\pm} = \left(\frac{2\pm1}{3}\right)\,\zeta$. The stability eigenvalue is real–valued at a particular ζ between these phonon numbers, and the $N_{\rm uns} \in \left[N_{s,\rm cv}^{-}\;,\; N_{s,\rm cv}^{+}\right]$, and are imaginary–valued outside of this bounded region. For the SS to be *unstable*, one of the stability eigenvalues must have a *positive* real component; if the phonon number is within the $N_{\rm uns}$ bounds, then $\tilde{\lambda}_{\rm cv}^{+}$, will by *destabilising*. Therefore, the molecule vibrational mode is unstable in the coloured region of fig. Fig. 4.6, and is stable everywhere else.

This completes the discussion on the QAO CV model. While there were important dynamical results obtained within, to properly capture catalytic behaviour there needs to a pathway for the dissipation of energy to allow for relaxation behaviour.

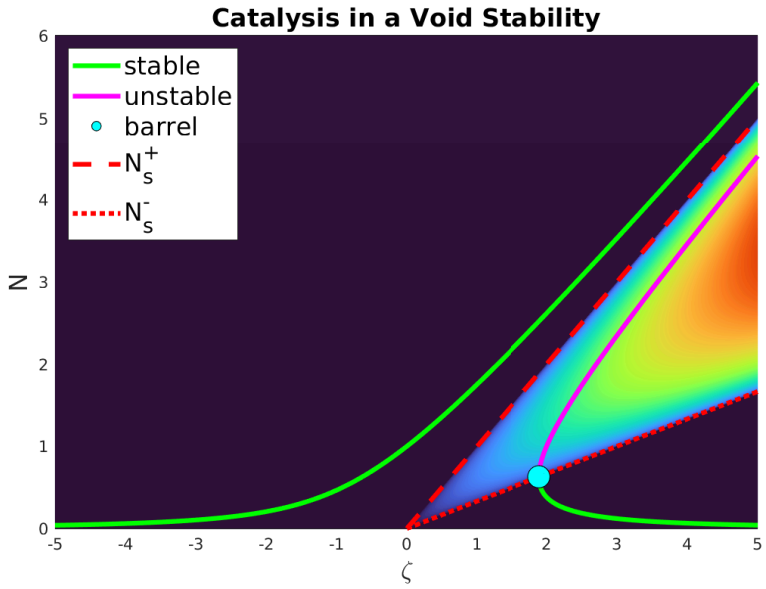

Figure 4.6: Catalysis in a Void Stability. The stable region (green) and unstable (magenta) regions of the SS distribution are shown for $\beta = 1$, along with the barrel point (cyan circle), and the stability bifurcation lines ($N^{+}_{s,\mathrm{cv}}$ is dashed red, $N^{-}_{s,\mathrm{cv}}$ is dot-dashed red). The background is coloured by $\Re[\tilde{\lambda}^{\pm}_{\mathrm{cv}}]$, and is dark blue where $\tilde{\lambda}^{\pm}_{\mathrm{cv}}$ is imaginary–valued.

4.5 QAO Molecule in an Dissipative Environment

The free QME describes motion in a void, whereby the molecule does not exhibit dissipative behaviour. The final step in the model building process is to immerse the molecule–enzyme complex in a thermal environment that facilitates an exchange of energy, thus providing a relaxation mechanism via a dissipation pathway. The modelling of quantum anharmonic phonon dissipation is varied, resulting in many expressions for the Vibrational Dissipation Rate (VDR). In quantum optics, an anharmonic crystal [137] can be excited by an IR laser (semiclassical radiation field) [138], and has been used in the study of the nanocrystals for semi conductor design [139–141]. Expressions for the VDR of biolmolecules have been derived from classical NMA data [72], and laser excitation [142]. I will be using a description derived for an individual protein [86], and adapt it for a substrate molecule that participates in multi-phonon exchanges with its environment as well as anharmonic dissipation pathways throughout the molecule. Therefore, the total VDR is the summation of QHO and QAO environmental VDR (eVDR), as well as an intramolecular VDR (iVDR)

4.5.1 Environmental Vibrational Dissipation Rate

The thermal equilibration and relaxation dynamics of the anharmonic are governed by the dissipative QME (3.47) whose coefficients are derived from the SDIs. The treatment of dissipation presented here follows the derivation in [86] for the vibrational relaxation of proteins, which stems from the work in [143] on the lifetime of phonons in 1D crystals. The real component of the difference in the SDIs of the environment is the eVDR of the molecule into a thermal environment,

$$\Upsilon^{\mathrm{e}}_{k} \equiv \frac{1}{2}\,\Re[w_{12} - w_{21}] = \Upsilon^{\mathrm{e,qho}}_{k} + \Upsilon^{\mathrm{e,qao}}_{k} \tag{4.52}$$

which is the summation of the QHO term from **§ 3.3.5**, $\Upsilon_k^{\rm e,qho} = \pi g(\omega_k)|\chi_{kk}^{\rm qho}|^2$, and QAO contributions. The QAO SDIs, $w_{ij}^{\pm}$, are determined by the integral over the force–force correlation of the QAO stimulus superoperator with coupling $\chi_{k\alpha\beta}$, one of which is

$$w_{21}^{+} \;=\; \int_0^{\infty} d\tau\; e^{-i\omega_k\tau}\; \left\langle \left(\hat{B}_k^{\rm qao}(\tau)\right)^{\dagger}\; \hat{B}_k^{\rm qao} \right\rangle \tag{4.53}$$

By inserting the QAO portion of the environmental stimulus superoperator with different coupling strengths, (4.21), and evolving the operators in time by the QHO unitary time translation operator (as was done in **§ 3.3.5**) the QAO SDI becomes

$$\begin{aligned} w_{21}^{+} \;=\; \sum_{\alpha\beta,\alpha'\beta'}^{\rm env} \chi_{k\alpha\beta}^{*}\; \chi_{k\alpha'\beta'}\; \Big[& \;\langle \hat{b}_\alpha^\dagger \hat{b}_\beta^\dagger \hat{b}_{\alpha'} \hat{b}_{\beta'} \rangle\; I(\omega_k - \omega_\alpha - \omega_\beta) \\ & +\; \langle \hat{b}_\alpha \hat{b}_\beta^\dagger (\hat{b}_{\alpha'} \hat{b}_{\beta'}^\dagger + \hat{b}_{\alpha'}^\dagger \hat{b}_{\beta'}) \rangle\; I(\omega_k - \omega_\alpha + \omega_\beta) \\ & +\; \langle \hat{b}_\alpha^\dagger \hat{b}_\beta (\hat{b}_{\alpha'} \hat{b}_{\beta'}^\dagger + \hat{b}_{\alpha'}^\dagger \hat{b}_{\beta'}) \rangle\; I(\omega_k + \omega_\alpha - \omega_\beta) \;\Big] \end{aligned} \tag{4.54}$$

where terms that do not conserve energy (traces over an odd number of operators) have been omitted, and the τ-integral over the resonance conditions performed via the Cauchy principle component

$$I(\Omega) \;=\; \int_0^{\infty} d\tau\; e^{-i\Omega\tau} \;=\; \pi\;\delta(\Omega) \;-\; i\mathscr{P}\Omega^{-1} \tag{4.55}$$

The traces over four operators are decomposed via Wick's decomposition

$$\langle \hat{b}_\alpha^\dagger \hat{b}_\beta^\dagger \hat{b}_{\alpha'} \hat{b}_{\beta'} \rangle \;=\; n_\alpha^e\; n_\beta^e\; \left(\delta_{\alpha\alpha'}\delta_{\beta\beta'} \;+\; \delta_{\alpha\beta'}\delta_{\beta\alpha'}\right) \tag{4.56a}$$

$$\langle \hat{b}_\alpha \hat{b}_\beta^\dagger (\hat{b}_{\alpha'} \hat{b}_{\beta'}^\dagger + \hat{b}_{\alpha'}^\dagger \hat{b}_{\beta'}) \rangle \;=\; (n_\alpha^e \;+\; 1)\; n_\beta^e\; \left(\delta_{\alpha\alpha'}\delta_{\beta\beta'} \;+\; \delta_{\alpha\beta'}\delta_{\beta\alpha'}\right) \;+\; (n_\alpha^e \;+\; 1)(2\,n_{\alpha'}^e \;+\; 1)\;\delta_{\alpha\beta}\;\delta_{\alpha'\beta'} \tag{4.56b}$$

$$\langle \hat{b}_\alpha^\dagger \hat{b}_\beta (\hat{b}_{\alpha'} \hat{b}_{\beta'}^\dagger + \hat{b}_{\alpha'}^\dagger \hat{b}_{\beta'}) \rangle \;=\; n_\alpha^e\; (n_\beta^e \;+\; 1)\; \left(\delta_{\alpha\alpha'}\delta_{\beta\beta'} \;+\; \delta_{\alpha\beta'}\delta_{\beta\alpha'}\right) \;+\; n_\alpha^e\; (2\,n_{\alpha'}^e \;+\; 1)\;\delta_{\alpha\beta}\;\delta_{\alpha'\beta'} \tag{4.56c}$$

where, $\langle \hat{b}_\alpha^\dagger \hat{b}_\beta \rangle = n_\alpha^e\;\delta_{\alpha\beta}$, and, $\langle \hat{b}_\alpha \hat{b}_\beta^\dagger \rangle = (n_\alpha^e + 1)\,\delta_{\alpha\beta}$, have been used. By making use of the Kronecker δ-functions to collapse the summations, and using the symmetry of the coupling strength tensor, $\chi_{k\alpha\beta} = \chi_{k\beta\alpha}$, the SDI under observation reduces to

$$\begin{aligned} w_{21}^{+} \;=\; & 2\pi \sum_{\alpha\beta} |\chi_{k\alpha\beta}|^2 \;\Big[n_\alpha^e\; n_\beta^e\; \delta(\omega_k - \omega_\alpha - \omega_\beta) \\ & \qquad +\; (n_\alpha^e \;+\; 1)\; n_\beta^e\; \delta(\omega_k - \omega_\alpha + \omega_\beta) \\ & \qquad +\; n_\alpha^e\; (n_\beta^e \;+\; 1)\; \delta(\omega_k + \omega_\alpha - \omega_\beta) \Big] \\ & +\; \pi \sum_{\alpha\alpha'} \chi_{k\alpha\alpha}^{*}\; \chi_{k\alpha'\alpha'}\; (2\,n_\alpha^e \;+\; 1)(2\,n_{\alpha'}^e \;+\; 1)\;\delta(\omega_k) \end{aligned} \tag{4.57}$$

By omitting the dynamical eigenfrequencies of the molecule that pertain to translations and rotations (restricting to NMA eigenstates, $\omega_k \in \mathbb{R}_{>0}$), the final term vanishes due to $\delta(\omega_k) = 0$ for non-zero ω_k. This contribution also cancels due to (4.52), and thus the eigenmodes that are not normal modes do not experience an eVDR in this model. By repeating the process for the alternate SDI, w_{12}^{+}, results in a similar expression after the replacement, $n_\alpha^e \leftrightarrow n_\alpha^e + 1$. The QAO VDR is thus obtained upon evaluation of the QAO portion of (4.52)

$$\Upsilon_k^{\mathrm{e,abs}} = \sum_{\alpha\beta}^{\mathrm{env}} |\chi_{k\alpha\beta}|^2 \; (n_\alpha^e + n_\beta^e + 1) \; \pi \; \delta(\omega_k - (\omega_\alpha + \omega_\beta)) \tag{4.58a}$$

$$\Upsilon_k^{\mathrm{e,sca}} = \sum_{\alpha\beta}^{\mathrm{env}} |\chi_{k\alpha\beta}|^2 \; |n_\beta^e - n_\alpha^e| \; \pi \; \delta(\omega_k - |\omega_\alpha - \omega_\beta|) \tag{4.58b}$$

whose terms account for the spontaneous absorption/emission ($\omega_k = \omega_\alpha + \omega_\beta$) and scattering ($\omega_k = |\omega_\alpha - \omega_\beta|$) processes, respectively. If the occupation numbers are taken at QHO thermal equilibrium ($n_\alpha^e \approx \bar{n}_\alpha$), the Maradudin–Fein formula is obtained [71]. A significant feature of $\Upsilon_k^{\mathrm{qao}}$ that is not present in $\Upsilon_k^{\mathrm{qho}}$ is the dependence on *temperature*, due to the phonon numbers n_α^e, which will contribute to the *heat capacity*.

4.5.2 Intramolecular Vibrational Dissipation Rate

In the QHO model, only modes of the same frequency can exchange phonons, whereas, in the QAO model there is an intramolecular VDR (iVDR) due to two-for-one phonon exchanges between the molecular modes $k, \alpha,$ and β if the resonance condition, $\omega_k = |\omega_\alpha \pm \omega_\beta|$, is satisfied. By also allowing for a slight detuning due to the environment (Lamb shift, φ_k), there is the ability for molecular phonons to dynamically distribute across the other vibrational modes available to the molecule.

The iVDR of a molecule is governed by an integral over a force–force correlation function, for the quantum mechanical force applied to each vibrational bond, for example, a stretching mode in proteins [144]. Since the correlation function is difficult to compute numerically, there exists a range of approximations, including taking the classical limit (Landau-Teller-Zwanzig formula), applying a quantum correction factor [145], and the thermal equilibrium quantum mechanical treatment (Maradudin-Fein formula) for the decay and collision processes. The expression that I have implemented in the numerical solution of the QAO EoMs uses the Maradudin-Fein formula, but can be extended to account for excited phonon number states; this provides an avenue for future work.

Single-Mode Relaxation Time

An approximation for first-order anharmonic is given by Srivastava [56] for a Single-Mode Relaxation Time (SMRT). The SMRT method is the simplest picture for anharmonic intramolecular phonon interactions; the relaxation rate of phonons in mode k is made on the assumption that

all other phonon modes are at their equilibrium distribution, and is given by

$$\Upsilon_k^{\text{smrt}} = \frac{\Upsilon_0}{\bar{n}_k\ (\bar{n}_k + 1)} \tag{4.59a}$$

$$= 4\,\Upsilon_0\ \sinh^2\left(\frac{\hbar\omega_k}{2\ k_B T}\right) \tag{4.59b}$$

with Υ_0 (carrying dimensions of $[\text{time}]^{-1}$) being the diagonal part of a phonon collision operator that includes anharmonic processes. Since there is dependence on temperature, the SMRT iVDR will contribute to the heat capacity of the molecule. Srivastava also derives an expression for vibrational lifetime in terms of the memory effects endowed by the presence of anharmonicity in the context of lattice thermal conductivity for an infinite crystal.

iVDR from Intramolecular Force–Force Correlation

An exact expression for the collision operator in the SMRT model cannot be implemented using anharmonic MD data, therefore a more detailed description is required. By taking the third-order potential to be a perturbation to the harmonic behaviour, an approximation of the iVDR can be derived via a force–force correlation in a similar manner to the eVDR. The following derivation is motivated by the work performed by [86] for the study of the vibrational relaxation of proteins. Take the interaction Hamiltonian of one mode to the others to be given by the third-order potential energy operator

$$\hat{\mathcal{V}}_3 = \sum_{\{b_i\}=1}^{N_{\text{atom}}} \sum_{\{r_i\}}^{xyz} V_{\{rb\}}^{(3)}\ \hat{u}_{r_1 b_1}\ \hat{u}_{r_2 b_2}\ \hat{u}_{r_3 b_3} \tag{4.60}$$

where the summation notation represents a sum over each b_i and r_i giving six in total, and $\hat{u}_{r_i b_i}$ is the position operator for the deviation from equilibrium of atom b_i in the r_i^{th} Cartesian coordinate evaluated at equilibrium given by (3.17). The coefficient, $V_{\{rb\}}^{(3)}$, is the third derivative of the potential energy with the deviation evaluated at the molecular equilibrium conformation

$$V_{\{rb\}}^{(3)} \equiv \left(\frac{\partial^3\ \mathcal{V}}{\partial u_{r_1 b_1}\ \partial u_{r_2 b_2}\ \partial u_{r_3 b_3}}\right)\Bigg|_{\text{eqm}} \tag{4.61}$$

which carries dimensions of $[\text{energy}][\text{space}]^{-3}$, and is obtained from the anharmonic GAUSSIAN 09 output data. The deviation operator describes the perturbation of an atomic nuclei due to all vibrational modes, with an amplitude that is dependent of the atom's mass, m_{b_i}, the vibrational mode natural harmonic frequency, ω_k, the dynamical eigenvector (polarisation) $L(r_i b_i|k)$, and the phonon position operator, $\hat{q}_k = \frac{1}{\sqrt{2}}\,(\hat{a}_k^\dagger + \hat{a}_k)$. Substitution of the deviation operator into (4.60) allows for a projection of $V_{\{rb\}}^{(3)}$ into vibrational mode coordinates by the atomic polarisation (dynamical eigenvector elements)

$$V_{k\alpha\beta}^{(3)} = \sum_{\{b_i\}=1}^{N_{\text{atom}}} \sum_{\{r_i\}}^{xyz} V_{\{rb\}}^{(3)}\ \frac{L(r_1 b_2|k)\ L(r_2 b_2|\alpha)\ L(r_3 b_3|\beta)}{\sqrt{m_{b_1}\ m_{b_2}\ m_{b_3}}} \tag{4.62}$$

The third-order potential energy term (4.60) can be expressed as

$$\hat{\mathcal{V}}_3 \;=\; \sum_{k\alpha\beta}^{\text{mol}} \Phi_{k\alpha\beta} \left(\hat{a}_k^\dagger \;+\; \hat{a}_k\right)\left(\hat{a}_\alpha^\dagger \;+\; \hat{a}_\alpha\right)\left(\hat{a}_\beta^\dagger \;+\; \hat{a}_\beta\right) \tag{4.63}$$

where the intramolecular anharmonic interaction strength coefficient is a rank-3 tensor

$$\Phi_{k\alpha\beta} \;\equiv\; V^{(3)}_{k\alpha\beta} \sqrt{\frac{\hbar^3}{8\,\omega_k\,\omega_\alpha\,\omega_\beta}} \tag{4.64}$$

which carries dimensions of $[\text{time}]^{-1}$. The third-order potential energy term (4.60) can then be expressed in the form of an interaction Hamiltonian,

$$\hat{\mathcal{V}}_3 \;=\; \hbar \sum_{k}^{\text{mol}} \left(\hat{a}_k^\dagger\, \hat{\mathcal{F}}_k \;+\; \hat{a}_k\, \hat{\mathcal{F}}_k^\dagger\right) \tag{4.65}$$

similar to the treatment of the eVDR, from which the quantum force (with dimensions of $[\text{time}]^{-1}$) is

$$\hat{\mathcal{F}}_k \;\equiv\; \sum_{\alpha\beta}^{\text{mol}} \Phi_{k\alpha\beta} \left(\hat{a}_\alpha^\dagger \;+\; \hat{a}_\alpha\right)\left(\hat{a}_\beta^\dagger \;+\; \hat{a}_\beta\right) \tag{4.66}$$

and represents the strength of the exchanges that create one phonon in mode k due to the interactions with all combinations of other molecular modes, α, β. The iVDR is derived via the reservoir spectral density integrals

$$w_{21}^{+} \;=\; \int_0^\infty d\tau\; e^{-i\omega_k \tau} \left\langle \hat{\mathcal{F}}_k^\dagger(\tau)\; \hat{\mathcal{F}}_k \right\rangle \tag{4.67}$$

and similarly for the other three intramolecular force-force correlations, $w_{ij}^{\pm}$. The result of these calculations shows

$$\begin{aligned} \Upsilon_k^{\text{mol}} \;=\; \pi \sum_{\alpha\beta}^{\text{mol}} |\Phi_{k\alpha\beta}|^2 \Bigg\{ & \left(\langle \hat{n}_\alpha \rangle \;+\; \langle \hat{n}_\beta \rangle \;+\; 1\right) \delta(\omega_k - (\omega_\alpha + \omega_\beta)) \\ & +\; \left|\langle \hat{n}_\alpha \rangle \;-\; \langle \hat{n}_\beta \rangle\right| \delta(\omega_k - |\omega_\alpha - \omega_\beta|) \Bigg\} \end{aligned} \tag{4.68}$$

is equivalent to the Maradudin–Fein formula used for the eVDR (4.58), but crucially all parameters are defined by MD data, atomic properties, and the molecular phonon numbers of the other vibrational modes. The first term in the brackets represents the absorption and emission processes while the second term describes scattering. The phonon numbers could be taken to be dynamic in time, $\langle \hat{n}_k \rangle = \langle \hat{n}_k(t) \rangle$ and incorporated into the numerical solution for the EoM; however, this would drastically increase the computational time. For this reason, I make the thermal equilibrium approximation by setting $\langle \hat{n}_k \rangle = \bar{n}_k$, and leave a numerical solution with dynamically updated iVDR phonon numbers for future work. Therefore, the iVDR can be approximated using the Maradudin–Fein formula, and can be determined entirely by data

extracted from an anharmonic GAUSSIAN 09 MD run.

The resonance conditions can be 'smeared' out by the approximation of taking the Dirac δ-functions to follow a Lorentzian resonance distribution (3.44), where φ_k is a linewidth parameter, physically representing that each vibrational modes should have a lifetime $2\pi/\varphi_k$. I take φ_k to be a phenomenological parameter arising from a Lamb shift since it is difficult to derive from first principles. The Maradudin–Fein equation has been applied for the iVDR of proteins [86], where they choose values of 3 and 30 cm^{-1} (0.09 and 0.90 THz), which result in a vibrational lifetime of several picoseconds, with some experiments showing a range of lifetime values up to several hundred picoseconds.

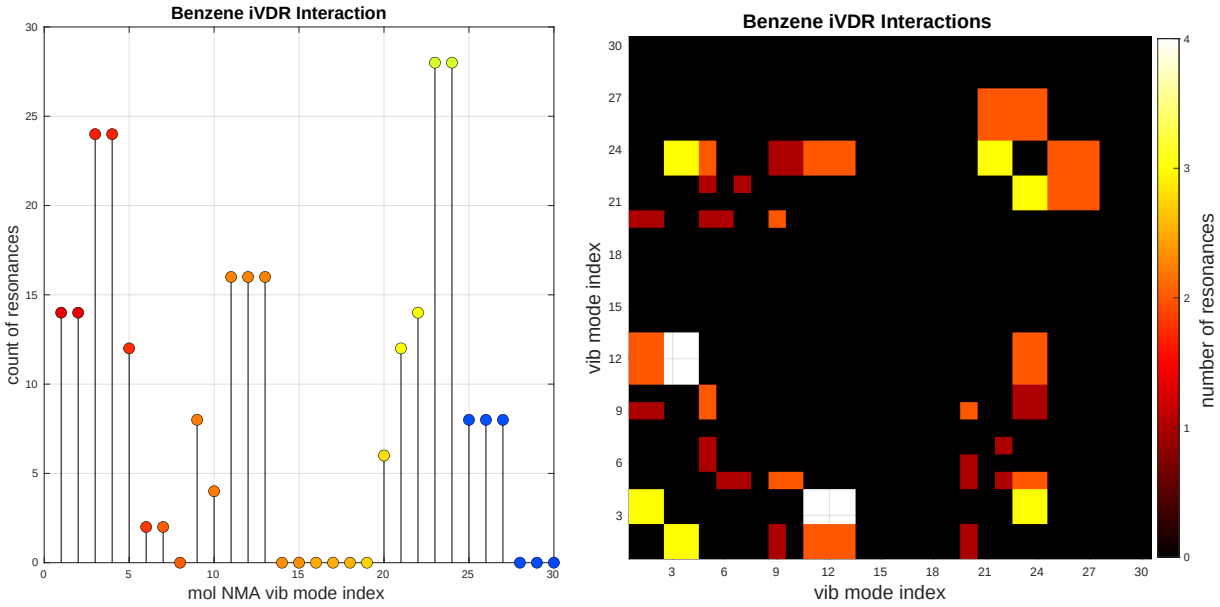

(a) Interactions per mode **(b)** Interaction map

Figure 4.7: Viable QAO intramolecular dissipation pathways for benzene due to anharmonic resonant phonon exchanges with smearing $\varphi_k/2\pi = 0.1$ THz.

The viable intramolecular interactions for benzene with a smearing frequency of 0.1 THz are shown in Fig. 4.7; the high-frequency modes 23 and 24 have the highest count of resonances since both permit 28 interactions, with the low-frequency modes 3 and 4 having the second highest count at 24 (Fig. 4.7a); the combination of modes, $(\omega_\alpha, \omega_\beta)$ that permit the highest count of interactions are modes 11 to 13 with modes 3 to 4 (and their symmetries) which permit four interactions with the other modes (white patches in Fig. 4.7b). The iVDR for benzene shown in Fig. 4.8 indicates that scattering processes (green squares) dominate the low-frequency modes, and absorbance/emission processes (red squares) dominate the high-frequency modes, and absorbance for the higher frequency modes. The largest iVDR is mode 12, whose atomic deviations are all perpendicular to the hexagonal planar ring of benzene.

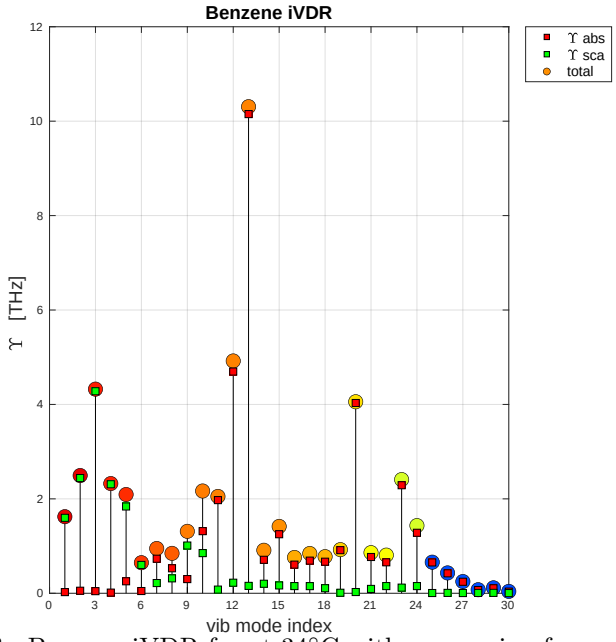

Figure 4.8: Benzene iVDR for at 34°C with a smearing frequency 0.1 THz.

4.5.3 Dissipative QAO Equations of Motion

The form of the dissipative QAO EoMs is in an equivalent expression to the QHO model for the creation and annihilation operators. The number EoM is

$$\partial_t \langle \hat{n}_k(t) \rangle_{\text{diss}} \;=\; -\,2\Upsilon_k \,\langle \hat{n}_k(t) \rangle \;+\; \Re[w_{21}] \tag{4.69}$$

which can be factorised by evaluating, $\Re[w_{21}]/\Upsilon_k$, since each interaction is independent on all others and must occur at resonant frequencies for a valid exchange of phonons, the term is simply equal to the reservoir (Planck distribution) phonon number of the molecular vibrational mode, $\Re[w_{21}]/\Upsilon_k = \bar{n}_k$. Therefore, the environmental dissipative EoMs are

$$\partial_t \langle \hat{a}_k \rangle_{\text{diss}} \;=\; -\,(\Upsilon_k \;+\; i\varphi_k)\,\langle \hat{a}_k \rangle \tag{4.70a}$$

$$\partial_t \langle \hat{a}_k^\dagger \rangle_{\text{diss}} \;=\; -\,(\Upsilon_k \;-\; i\varphi_k)\,\langle \hat{a}_k^\dagger \rangle \tag{4.70b}$$

$$\partial_t \langle \hat{n}_k \rangle_{\text{diss}} \;=\; -\,2\,\Upsilon_k \,\big(\langle \hat{n}_k \rangle \;-\; \bar{n}_k\big) \tag{4.70c}$$

which are similar in appearance and dynamics to the QHO model, but with the adjusted QAO VDR due to the anharmonic phonon exchange with the environment and intramolecular dissipation. The total VDR is the summation of iVDR as well as QHO and QAO eVDR

$$\Upsilon_k \;=\; \Upsilon_k^{\text{iVDR}} \;+\; \Upsilon_k^{\text{qho}} \;+\; \Upsilon_k^{\text{eVDR}} \tag{4.71}$$

4.6 Equations of Motion for the QAO Catalytic Model

In this section, I will be investigating the complete catalytic model QAO EoMs. The full QAO catalytic model is the combination of the free behaviour of the molecule (4.15) and its interactions with the enzyme (4.33) and the environment (4.70). By the adding these dynamical

contributions, the full set of QAO EoMs for the quantum state of molecular vibrational mode k are

$$\partial_t\langle\hat{a}_k(t,\omega)\rangle \;=\; -\Big(\Upsilon_k \;-\; i\phi_k(t,\omega)\Big)\,\langle\hat{a}_k(t,\omega)\rangle \;-\; i\,2\xi_{kk}\,\langle\hat{n}_k(t,\omega)\rangle\,\langle\hat{a}_k(t,\omega)\rangle \;-\; iB_k \tag{4.72a}$$

$$\partial_t\langle\hat{a}_k^\dagger(t,\omega)\rangle \;=\; -\Big(\Upsilon_k \;+\; i\phi_k(t,\omega)\Big)\,\langle\hat{a}_k(t,\omega)\rangle \;+\; i\,2\xi_{kk}\,\langle\hat{n}_k(t,\omega)\rangle\,\langle\hat{a}_k^\dagger(t,\omega)\rangle \;+\; iB_k \tag{4.72b}$$

$$\partial_t\langle\hat{n}_k(t,\omega)\rangle \;=\; -\,2\Upsilon_k\,\Big(\langle\hat{n}_k(t,\omega)\rangle \;-\; \bar{n}_k\Big) \;-\; iB_k\,\Big(\langle\hat{a}_k^\dagger(t,\omega)\rangle \;-\; \langle\hat{a}_k(t,\omega)\rangle\Big) \tag{4.72c}$$

with detuning frequency, $\phi_k(t,\omega) = \omega - \varpi_k(t,\omega)$, from the QAO vibrational mode oscillation frequency

$$\varpi_k(t,\omega) \;=\; \omega_k \;+\; 2\xi_{kk} \;+\; \eta_k(t,\omega) \;+\; \varphi_k \tag{4.73}$$

whose contributions, respectively, are the QHO natural eigenfrequency, ω_k; QAO self-interaction, ξ_{kk}; total frequency shift due to all other molecular vibrational modes, $\eta_k(t,\omega)$; and the environmental Lamb shift, φ_k. These equations cannot be solved exactly due to the nonlinear products $\langle\hat{n}_k\rangle\langle\hat{a}_k\rangle$ and $\langle\hat{n}_k\rangle\langle\hat{a}_k^\dagger\rangle$. Furthermore, the phonon numbers of all other modes, $\langle\hat{n}_j(t,\omega)\rangle$, act to shift the oscillation frequency, η_k, which must be updated in the numerical solution. The EoMs can be expressed in terms of the quantum state space vector

$$\partial_t\;\boldsymbol{\Psi} \;=\; \mathbf{M}\;\boldsymbol{\Psi} \;+\; \mathcal{N}(\boldsymbol{\Psi}) \;+\; \mathbf{b} \tag{4.74}$$

where the linear dynamics are contained in

$$\mathbf{M} \;=\; \begin{bmatrix} -(\Upsilon_k - i\phi_k) & 0 & 0 \\ 0 & +(\Upsilon_k + i\phi_k) & 0 \\ +iB_k & -iB_k & -2\Upsilon_k \end{bmatrix} \tag{4.75}$$

the nonlinear dynamics are $\mathcal{N} = i2\xi_{kk}\,\langle\hat{n}_k\rangle\,\big[-\langle\hat{a}_k\rangle,\,+\langle\hat{a}_k^\dagger\rangle,\,0\big]^{\mathrm{T}}$, and the constant inhomogeneous source term is $\mathbf{b} = \big[-iB_k,\,+iB_k,\,2\Upsilon_k\,\bar{n}_k\big]^{\mathrm{T}}$. To investigate the dynamics encapsulated in this model, the steady states and their stability are to be determined.

4.6.1 QAO Steady States

The QAOSS of the molecular vibrational mode quantum states are found by setting the temporal derivatives in (4.72) to zero. To simplify the notation, let

$$N \;\equiv\; \langle\hat{n}_k\rangle^{\mathrm{ss}} \tag{4.76a}$$

$$\mathcal{A} \;\equiv\; \langle\hat{a}_k\rangle^{\mathrm{ss}} \tag{4.76b}$$

$$\mathcal{A}^* \;=\; \langle\hat{a}_k^\dagger\rangle^{\mathrm{ss}} \;=\; \big(\langle\hat{a}_k\rangle^{\mathrm{ss}}\big)^* \tag{4.76c}$$

noting that the QAOSS creation and annihilation expectation values are complex conjugate pairs. The QAOSS are then determined by the simultaneous solutions of

$$0 \;=\; -\left(\Upsilon_k \;-\; i\phi_k\right)\,\mathcal{A} \;-\; i\,2\xi_{kk}\;N\,\mathcal{A} \;-\; iB_k \tag{4.77a}$$

$$0 \;=\; -\left(\Upsilon_k \;+\; i\phi_k\right)\,\mathcal{A}^* \;+\; i\,2\xi_{kk}\;N\,\mathcal{A}^* \;+\; iB_k \tag{4.77b}$$

$$0 \;=\; -\,2\Upsilon_k\,\Big(N \;-\; \bar{n}_k\Big) \;-\; i\;B_k\,\Big(\mathcal{A}^* \;-\; \mathcal{A}\Big) \tag{4.77c}$$

The annihilation operator QAOSS $\mathcal{A}$ as a function of N and ω is from (4.77a)

$$\text{at SS:}\quad \mathcal{A}(\omega,\,N) \;=\; \frac{B_k}{i\Upsilon_k \;+\; \phi_k(\omega) \;-\; 2\xi_{kk}N} \tag{4.78}$$

the creation SS is the complex conjugate, $\mathcal{A}^*$. The absolute square is

$$|\mathcal{A}|^2 \;=\; \frac{B_k^2}{\Upsilon_k^2 \;+\; (\phi_k \;-\; 2\xi_{kk}N)^2} \tag{4.79}$$

from which the real and imaginary components are

$$\Re[\mathcal{A}] \;=\; (\phi_k \;-\; 2\xi_{kk}N)\;\frac{|\mathcal{A}|^2}{B_k} \tag{4.80a}$$

$$\Im[\mathcal{A}] \;=\; -\,\Upsilon_k\;\frac{|\mathcal{A}|^2}{B_k} \tag{4.80b}$$

Finally, the spectral distribution for the QAOSS phonon number, $N(\omega)$, is to be determined by substitution of (4.80b) into the number EoM SS (4.77c)

$$0 \;=\; -\,2\Upsilon_k\,\Big(N \;-\; \bar{n}_k \;-\; |\mathcal{A}|^2\Big) \tag{4.81}$$

which is valid for $\Upsilon_k \neq 0$ (finite vibrational lifetime), for all N such that

$$N \;=\; \bar{n}_k \;+\; |\mathcal{A}|^2 \tag{4.82}$$

The QAOSS number value above thermal equilibrium is

$$\delta N_{\text{qao}}(\omega,\,N) \;=\; |\mathcal{A}|^2 \;=\; \frac{B_k^2}{\Upsilon_k^2 \;+\; (\phi_k \;-\; 2\xi_{kk}\,N)^2} \tag{4.83}$$

The QAOSS detuning in terms of the QHOSS detuning is, $\phi_k(\omega) = \phi_{\text{qho}}(\omega) - (2\xi_{kk} + \eta_k)$, stating that the QAO includes the frequency shift due to all other molecular modes including itself. The expression for $|\mathcal{A}|^2$ is similar to the result obtained from the QHO SS in **§ 3.4.1** (3.62), where the SS number above thermal equilibrium is

$$\delta N_{\text{qho}}(\omega) \;=\; \frac{B_k^2}{\Upsilon_k^2 \;+\; \phi_{k,\text{qho}}^2} \tag{4.84}$$

which is a Lorentzian resonance peak centred at $\phi_{k,\text{qho}}(\omega) = \omega - (\omega_k + \varphi_k)$, with height B_k^2/Υ_k^2, and half width at half maximum Υ_k. The peak height (at perfect tuning, $\phi_{k,\text{qho}} = 0$) above

thermal background is $\delta N_{\text{peak}} = B_k^2/\Upsilon_k^2$, and the phonon number is $N_{\text{peak}} = \bar{n}_k + \delta N_{\text{peak}}$, for both the QHO and QAOSS spectra, however the peak tips occur at different frequencies, as can be seen in Fig. 4.9. Therefore, the QAOSS response spectrum for phonon number is a *skew* Lorentzian resonance distribution.

4.6.2 QAO Steady State Conditional Relation

The QAOSS conditional equation (4.82) is a transcendental equation in N which can be solved numerically, however, analytic exploration yields useful and insightful results. Rearrangement of (4.83) to one line yields

$$\Big(\Upsilon_k^2 \; + \; \big(\phi_k(\omega) \; - \; 2\xi_{kk}\; N\big)^2\Big)\Big(N \; - \; \bar{n}_k\Big) \; = \; B_k^2 \tag{4.85}$$

where the RHS is the environmental stimulus, and the LHS is the molecular vibrational mode's response. This is a cubic polynomial in N and quadratic in ω, that determines the spectral distribution of (trace-averaged) phonon number at SS. Defining the stimulus-free portion of the SS conditional statement by the LHS of (4.85) as $S(\omega,\, N)$, allows the SS conditional statement to be expressed as $S(\omega,\, N) = B_k^2$. Any value of N that satisfies this condition at a particular ω is a valid SS phonon number for vibrational mode k at the stimulus frequency ω. Note that $S = 0$ on the thermal equilibrium background phonon number $N = \bar{n}_k$, for which the SS condition requires that $B_k = 0$; equivalently stated, in the absence of an external stimulus, the SS (spectral distribution of expectation values) vibrational mode phonon number is at thermal equilibrium with its environment. If the phonon number is below the background, $N < \bar{n}_k$, then $S < 0$, then there is a valid SS only for imaginary-valued stimulus; by restricting $B_k \in \mathbb{R}_{\geq 0}$, then all valid SS phonon numbers *must* be above the thermal background, $\bar{n}_k$. A comparison of the QHOSS and QAOSS features is shown in Fig. 4.9. The SS conditional relation (4.85) is the basis for the establishment of the Non-Dimensionalised, One-Parameter (ND1P) QAO model that I detail in **Appendix B**. The core dynamics and central theoretical results for the the QAO model EoMs (4.72) can be analysed more simply in the ND1P model, and I found it to be invaluable in the construction of the QAO molecule simulations presented in **Chapter 5**.

An equivalent SS conditional relation has been obtained within the classical anharmonic oscillator framework by performing the homotopy analysis method, or harmonic balance, on the Duffing equation with nonlinear stiffness [50, 146]. The resultant magnification factor for the frequency–amplitude-response equation can be recast into an equivalent form of (4.85), and has been used to study the resonance jump behaviour in nonlinear oscillations [147]. The response of micro/nano-electro-mechanical resonators to nonlinear sources has been measured experimentally, which lead to the discovery of inherent behaviours including softening and hardening frequency responses, chaos, and bistability [148]; each of these dynamics are also present in the QAO model.

4.6.3 Stability of QAO Steady States

With the QAOSS phonon number curve determined, the next step in exploring the dynamics is to ascertain the stability along the SS curve. The stability of the QAOSS is elucidated by the

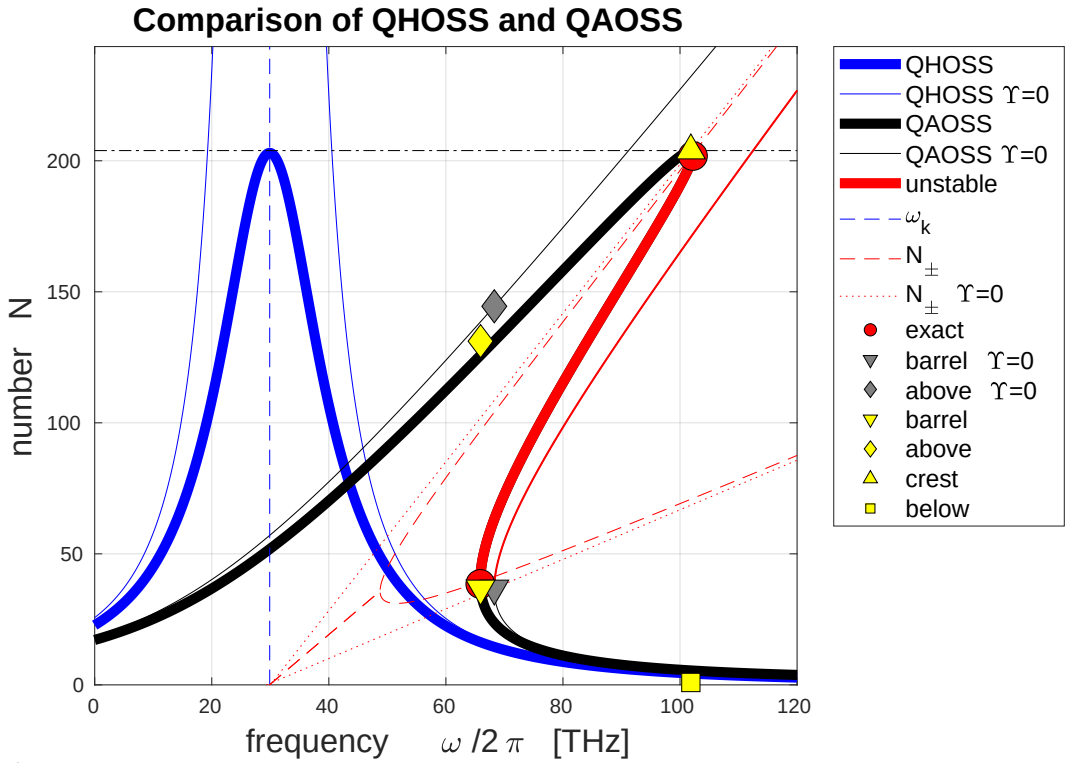

Figure 4.9: A comparison of the QHOSS (thick blue) and QAOSS (thick black is stable and red is unstable) phonon number response curves, along with non-dissipative models, $\Upsilon_k = 0$ (thin), for mode 10 of benzene with $\xi_{10,10}/2\pi = 0.176$ THz, $\Upsilon_{10}/2\pi = 10.6$ THz, $B_{10}/2\pi = 151.5$ THz. I detail the other physical properties of this particular vibrational mode at the end of **§ 4.6**. The anharmonic effects shift and tilt the QHOSS distribution while preserving peak height ($\bar{n}_k + \mu_k$, dot-dashed) and width (Υ_k); the tilt angle is $\tan^{-1}(2\xi_{kk})$ from the QHOSS. The intramolecular frequency shift is computed such that all modes are at thermal equilibrium, and under these conditions, the harmonic natural (normal mode) (dashed blue, $\omega_{10}/2\pi = 29.90$ THz) and anharmonically adjusted oscillation frequencies ($\varpi_{10}/2\pi = 30.02$ THz) are indistinguishable. The non-dissipative barrel (grey down-triangle) and above (grey diamond) points are shown in comparison to the exact bifurcation points (red circle) and the approximate expressions for the dissipative barrel (yellow down-triangle) and above (yellow diamond) points as well as the crest (yellow up-triangle) and below (yellow square) points. The stability bifurcation, $N_\pm$, (4.91) (dashed red) coincides with the SS bifurcation (exact crest and barrel) points (red circles), and stability bifurcation for the non-dissipative, $\Upsilon_k = 0$, case (dotted red) coincides with the maximum response (approximately at the crest) and the bifurcation ($\Upsilon_k = 0$ barrel) point (grey down-triangle).

eigenvalues of the Jacobian stability matrix of EoM derivatives (4.45). Computing each EoM derivative and evaluating at SS yields the Jacobian

$$\mathbf{J} = \begin{bmatrix} \big(-\Upsilon_k + i(\phi_k - 2\xi_{kk}\,N)\big) & 0 & -i\,2\xi_{kk}\,\mathcal{A} \\ 0 & \big(-\Upsilon_k - i(\phi_k - 2\xi_{kk}\,N)\big) & +i\,2\xi_{kk}\,\mathcal{A}^* \\ +iB_k & -iB_k & -2\Upsilon_k \end{bmatrix} \tag{4.86}$$

The stability eigenvalues λ are found via characteristic equation of (4.86),

$$\begin{aligned} 0 = & -\big(\lambda + 2\Upsilon_k\big)\Big((\lambda + \Upsilon_k)^2 + (\phi_k - 2\xi_{kk}\,N)^2\Big) \\ & + 2\xi_{kk}\,B_k\,\Big((\lambda + \Upsilon_k)(\mathcal{A} + \mathcal{A}^*) + i(\phi_k - 2\xi_{kk}\,N)(\mathcal{A} - \mathcal{A}^*)\Big) \end{aligned} \tag{4.87}$$

where the first term is the leading diagonal and the second term is the combination of the anti-diagonals. By expressing, $\mathcal{A}$, in terms of the real and imaginary components, the anti-diagonal term is, $4\xi_{kk}\,B_k\big((\lambda+\Upsilon_k)\,\Re[\mathcal{A}]\,-\,(\phi_k\,-\,2\xi_{kk}\,N)\,\Im[\mathcal{A}]\big)$, then by using $\Re[\mathcal{A}]$ and $\Im[\mathcal{A}]$ in terms of the absolute square (4.80), the anti-diagonal term is, $4\xi_{kk}\,(\lambda\,+\,2\Upsilon_k)(\phi_k\,-\,2\xi_{kk}\,N)\,|\mathcal{A}|^2$, which allows the characteristic equation to be factorised. Finally, by using the SS conditional relation in the form, $|\mathcal{A}|^2 = N - \bar{n}_k$, (4.82) the eigenstability characteristic equation is found to be

$$0 \;=\; \big(\lambda\;+\;2\Upsilon_k\big)\Big((\lambda\;+\;\Upsilon_k)^2\;+\;\big(\phi_k\;-\;2\xi_{kk}\,N\big)\,\big(\phi_k\;-\;2\xi_{kk}\,(3N\;-\;2\,\bar{n}_k)\big)\Big) \tag{4.88}$$

from which the three stability eigenvalues are immediately

$$\lambda_0 \;=\; -\,2\Upsilon_k \tag{4.89}$$

$$\lambda_{\pm}(\omega,N) \;=\; -\,\Upsilon_k\;\pm\;\sqrt{-(\phi_k\;-\;2\xi_{kk}\,N)\,(\phi_k\;-\;2\xi_{kk}\,(3N\;-\;2\,\bar{n}_k))} \tag{4.90}$$

The dissipative environment acts to lower the real component when compared to the QAO CV model. Since $\lambda_0 \in \mathbb{R}_{<0}$ (finite vibrational lifetime must be real and positive) and constant for all frequencies and phonon numbers, it is always stabilising. The eigenvalues $\lambda_{\pm}$ can be purely real or complex conjugate pairs depending on the sign of the discriminant under the squareroot: if $\lambda_{\pm} \in \mathbb{C}$, then the SS is a *stable focus node* type equilibrium (since the real component is always negative); if $\lambda_{\pm} \in \mathbb{R}$, then the SS is non-oscillatory, furthermore, if any eigenvalue has a positive real component, then the equilibrium is an *unstable source node*. The boundary for the unstable region is where the stability eigenvalues are zero, which are revealed upon solving (4.90) for N,

$$N_{k,\pm}(\omega) \;=\; \bar{n}_k\;+\;\frac{1}{3\xi_{kk}}\;\left(\phi_k(\omega)\;-\;2\xi_{kk}\,\bar{n}_k\;\pm\;\frac{1}{2}\,\sqrt{\big(\phi_k(\omega)\;-\;2\xi_{kk}\,\bar{n}_k\big)^2\;-\;3\Upsilon_k^2}\;\right) \tag{4.91}$$

whose branches bifurcate ($N_{k,+} = N_{k,-}$) at the critical detuning,

$$\phi_{k,\mathrm{crit}} \;=\; 2\xi_{kk}\;\bar{n}_k\;+\;\sqrt{3}\;\Upsilon_k \tag{4.92}$$

which corresponds to a critical stimulus frequency, $\omega_{k,\mathrm{crit}} = \varpi_k + \phi_{k,\mathrm{crit}}$. The critical bifurcation phonon number is given upon substitution of (4.92) into (4.91)

$$N_{k,\mathrm{crit}} \;=\; \bar{n}_k\;+\;\frac{\Upsilon_k}{\sqrt{3}\;|\xi_{kk}|} \tag{4.93}$$

These expressions locate the critical point in (ω, N) where the saddle-node bifurcation (crest and barrel) points coincide at the critical minimum stimulus.

4.6.4 Minimum Stimulus for Phase Transition Behaviour

The choice of appropriate enzyme stimulus is crucial in order to establish a numerical solution for the catalytic QAO EoMs to be in the SS3 regime for which a phase transition dynamic is present. For demonstration purposes in lieu of experimental data, I have set stimulus coupling strengths to be large enough to ensure SS3 behaviour in the glycosidic stretch bandwidth. By specifying the critical minimum stimulus for SS3, $B_{k,\mathrm{crit}}$, *a priori* allows the coupling strength

values to be adjusted upon computing, B_k, before a simulation is performed. I will discuss this topic further in **Chapter 5**, in this section I will derive an approximate expression for the critical minimum stimulus for phase transition behaviour, which is in close agreement with numerically determined values.

The critical minimum stimulus, $B_{k,\mathrm{crit}}$, to reach the SS3 regime for a dissipative mode at a given detuning is found in a similar way to method by which the barrel point (4.38) was located. Rearranging the QAOSS relation (4.85) for detuning frequency

$$\phi_{\mathrm{ss}}^{\pm}(N) \;=\; 2\xi_{kk}\,N \;\pm\; \sqrt{\frac{B_k^2}{N-\bar{n}_k} \;-\; \Upsilon_k^2} \tag{4.94}$$

allows the QAOSS to be plotted without using a root solving algorithm, which I have used in several figures including Fig. 4.9. The extrema of $\phi_{\mathrm{ss}}^{\pm}(N)$ corresponds to the point where the QAOSS number distribution folds over (yellow down-triangle in Fig. 4.9), and is found by differentiating (4.94) with N then setting to zero, which yields a quartic polynomial in $\delta N = N - \bar{n}_k$ upon rearrangement

$$\Upsilon_k^2\;\delta N^4 \;-\; B_k^2\;\delta N^3 \;+\; \frac{B_k^4}{16\;\xi_{kk}^2} \;=\; 0 \tag{4.95}$$

In the region of SS3, this polynomial has two real roots that correspond to the excitation phonon number, δN, at the SS1/SS3 boundaries (saddle-node bifurcation points). Note that in the limit of zero VDR (infinite lifetime), the quartic term vanishes, leaving $N \;=\; \bar{n}_k \;+\; \nu_k$, which is the barrel point from the QAO CV model that locates the only bifurcation point but raised by the thermal equilibrium value, $\bar{n}_k$. By defining the maximum peak excitation phonon number to be

$$\mu_k \;\equiv\; \frac{B_k^2}{\Upsilon_k^2} \tag{4.96}$$

then (4.95) can be written in terms of the 'crest' (μ_k) and 'barrel' (ν_k) phonon numbers

$$\delta N^4 \;-\; \mu_k\;\delta N^3 \;+\; \mu_k\;\nu_k^3 \;=\; 0 \tag{4.97}$$

This polynomial has a turning point at $\delta N = \frac{3}{4}\mu_k$ and two degenerate turning points at $\delta N = 0$. By evaluating (4.97) at the non-trivial turning point, then rearranging leads to

$$\left.\frac{\mu_k}{\nu_k}\right|_{\mathrm{min}} \;=\; \frac{2^{8/3}}{3} \;\approx\; 2.117 \tag{4.98}$$

In order for the vibrational mode to experience SS3, the peak-to-barrel ratio must be larger than this critical value. Back substitution of the material parameters allows the minimum enzyme stimulus for SS3 to be determined

$$B_{k,\mathrm{crit}} \;=\; \frac{2}{3^{3/4}}\;\sqrt{\frac{\Upsilon_k^3}{|\xi_{kk}|}} \tag{4.99}$$

below this stimulus, the vibrational mode cannot experience SS3, and the QAOSS distribution is single-valued (Fig. 5.8a). This is a significant result as it determines the stimulus required to push a vibrational mode into SS3 for its given VDR, without the requirement of numerically computing the SS spectra and greatly facilitates the establishment of a QAO molecular simulation. For stimuli above $B_{k,\mathrm{crit}}$, the saddle-node bifurcation points diverge and the region of the QAOSS between these values is unstable, which indicates a first-order phase transition. The maximum excitation phonon number response for the QAOSS at critical stimulus, is located by substituting $B_{k,\mathrm{crit}}$ into μ_k (4.96), giving

$$\mu_{k,\mathrm{crit}} \;=\; \frac{4\;\Upsilon_k}{3^{3/2}\;|\xi_{kk}|} \tag{4.100}$$

By inspection of data for benzene in **Chapter 5**, shows that the high-frequency hydrogen network oscillations will almost certainly be in SS3 regime; while some of the mid-frequency modes require excitation peaks with thousands of phonons and are expected to remain in SS1 and do not exhibit a phase transition.

Thus, an approximate analytic expression for the critical bifurcation point frequency (4.92), phonon number (4.93), and stimulus (4.99) has been derived

$$(\omega, N, B)_{\mathrm{crit}} \;=\; \left(\varpi_k \;+\; 2\xi_{kk}\,\bar{n}_k \;+\; \sqrt{3}\Upsilon_k \;,\;\; \bar{n}_k \;+\; \frac{\Upsilon_k}{\sqrt{3}\;|\xi_{kk}|} \;,\;\; \frac{2}{3^{3/4}}\sqrt{\frac{\Upsilon_k^3}{|\xi_{kk}|}} \right) \tag{4.101}$$

4.6.5 Phase Transition Region Boundary

Finally, I will derive approximate algebraic relations for determining the boundary of the phase transition region as a function of the stimulus for vibrational modes in the SS3 regime, ($B_k \;>\; B_{k,\mathrm{crit}}$), as well as the non-repeated roots associated with the discontinuous jump at both bifurcation points. To simplify the discussion, I will call the low- and high-N saddle-node bifurcation points the barrel and crest; I call the non-repeated root for the barrel the 'above' point, and the non-repeated root for the crest is the 'below' point. I describe a parallel theoretical derivation for the Non-Dimensionalised, One Parameter (ND1P) model in **Appendix B**, whose parameter I will make use of in this section.

The general procedure for locating the bifurcation point is by taking the extrema of, $\phi_{\mathrm{ss}}^{\pm}$ (4.94), and the non-repeated roots are found by equating the SS conditional relation (4.85) to $4\xi_{kk}^2\;(N \;-\; N_{\mathrm{r}})^2\;(N \;-\; N_{\mathrm{nr}}) \;=\; 0$, by making use of the fundamental theorem of algebra for the roots of polynomials. Upon expanding the brackets, matching the polynomial coefficients in N, and rearranging for the unknown non-repeating root, N_{nr}, in terms of the specified repeated root, N_{r} and corresponding detuning, the second- and zeroth-order relations are

$$N_{\mathrm{nr}}^{(2)} \;=\; \bar{n}_k \;+\; \frac{\phi_k}{\xi_{kk}} \;-\; 2\,N_{\mathrm{r}} \tag{4.102a}$$

$$N_{\mathrm{nr}}^{(0)} \;=\; \frac{(\phi_k^2 \;+\; \Upsilon_k^2)\;\bar{n}_k \;+\; B_k^2}{4\xi_{kk}^2\;N_r^2} \tag{4.102b}$$

In the non-dissipative QAO CV case under investigation of **§ 4.4**, there is only one saddle-node bifurcation (barrel) point and is given by the dimensionless, ν_k, (4.38). The QAO CV model can be immersed in an environment which will have a non-zero thermal equilibrium by setting $\Upsilon_k = 0$ (physically representing an infinite vibrational lifetime) throughout the full QAO model. I locate the non-dissipative bifurcation point of this model by setting $\Upsilon_k = 0$ in $\phi_{\rm ss}^{\pm}$ (4.94), then computing its extrema gives the phonon number of this bifurcation phonon number, $N_{\rm barrel}^{\Upsilon_k=0} = \bar{n}_k + \nu_k$, then substituting this value back in (4.94) gives the bifurcation detuning frequency, $\phi_{\rm barrel}^{\Upsilon_k=0} = 2\xi_{kk}(\bar{n}_k + 3\nu_k)$; the point above the bifurcation is found by (4.102a), giving $\bar{n}_k + 4\nu_k$. Therefore, the phase transition boundary of the non-dissipative model is

$$\phi_{\rm barrel}^{\Upsilon_k=0} \;=\; 2\,\xi_{kk}\;(\bar{n}_k \;+\; 3\nu_k) \tag{4.103a}$$

$$N_{\rm barrel}^{\Upsilon_k=0} \;=\; \bar{n}_k \;+\; \nu_k \tag{4.103b}$$

$$N_{\rm above}^{\Upsilon_k=0} \;=\; \bar{n}_k \;+\; 4\nu_k \tag{4.103c}$$

The non-dissipative barrel point is denoted by the grey downwards-pointing triangle in Fig. 4.9, and the above point by the grey diamond; the SS1 and SS3 regimes occur at either sides of this point, depending on the sign of ξ_{kk}. The inclusion of dissipation results in a second bifurcation point at a higher N, which corresponds to the largest detuning such that the QAOSS is multi-valued, therefore the phase transition is bounded between the crest and barrel frequencies. I approximate the crest by the maximum value of the QAOSS response, therefore $N_{\rm crest} \approx \bar{n}_k + \mu_k$, and upon inserting this value into (4.94) gives a detuning of, $\phi_{\rm crest} \approx 2\xi_{kk}(\bar{n}_k + \mu_k)$, and the point below the crest is located by (4.102b), giving $N_{\rm below} \approx \bar{n}_k + \Upsilon_k^2/(4\xi_{kk}^2\, N_{\rm crest}^2)$, which is slightly raised above thermal equilibrium; thus the high-N phase transition boundary is

$$\phi_{\rm crest} \;\approx\; 2\,\xi_{kk}\;(\bar{n}_k \;+\; \mu_k) \tag{4.104a}$$

$$N_{\rm crest} \;\approx\; N_{\rm max} \;=\; \bar{n}_k \;+\; \mu_k \tag{4.104b}$$

$$N_{\rm below} \;\approx\; \bar{n}_k \;+\; \frac{\Upsilon_k^2}{4\,\xi_{kk}^2\;(\bar{n}_k \;+\; \mu_k)} \;\approx\; \bar{n}_k \tag{4.104c}$$

Attempting to determine the low-N boundary barrel point by taking the extrema value of $\phi_{\rm ss}^{\pm}$ leads to the quartic polynomial (4.95). Therefore, I approximate the dissipative barrel phonon number by the non-dissipative value, $N_{\rm barrel} \approx N_{\rm barrel}^{\Upsilon_k=0} = \bar{n}_k + \nu_k$; I then approximate the barrel detuning by evaluating $\phi_{\rm ss}^{+}$ at $N_{\rm barrel}^{\Upsilon_k=0}$, giving $\phi_{\rm barrel} \approx 2\xi_{kk}\left(\bar{n}_k + \nu_k\left(1 + 2\sqrt{1 - \gamma_k^2}\right)\right)$, which departs from the non-dissipative value for $\gamma_k \in [0, 1]$, where γ_k is the parameter of the ND1P model (**§ B.1**), defined

$$\gamma_k \;\equiv\; \frac{\Upsilon_k}{\sqrt[3]{4\,|\xi_{kk}|\;B_k^2}} \tag{4.105}$$

which characterises the response behaviour. Finally, the above-barrel point is found by evaluating (4.102a) with the aforementioned values, giving, $N_{\rm above} \approx \bar{n}_k + 4\nu_k\sqrt{1 - \gamma_k^2}$. Thus,

the low-N phase transition boundary approximately occurs at

$$\phi_{\text{barrel}} \approx 2\,\xi_{kk}\left(\bar{n}_k + \nu_k\left(1 + 2\sqrt{1-\gamma_k^2}\,\right)\right) \tag{4.106a}$$

$$N_{\text{barrel}} \approx N_{\text{barrel}}^{\Upsilon_k=0} = \bar{n}_k + \nu_k \tag{4.106b}$$

$$N_{\text{above}} \approx \bar{n}_k + 4\,\nu_k\,\sqrt{1-\gamma_k^2} \tag{4.106c}$$

These approximations have been used in Fig. 4.9 to locate the bifurcation and non-repeated root points, as well as in Figs. 4.10–4.12 to approximate the phase transition boundary over a range of stimulus. For a vibrational mode excited into the SS3 regime, the maximum resting response will occur within the detuning frequency bandwidth $\phi_k \in [\phi_{\text{barrel}}, \phi_{\text{crest}}]$, and have a phonon number expectation value in the range, $N \in [N_{\text{above}}, N_{\text{crest}}]$.

4.6.6 QAOSS Phonon Number Response Manifold

Of particular interest in a model of catalysis are the vibrational modes that pertain to the stretching of the bond that is severed. A central hypothesis of this thesis is that the appropriate enzyme provides a sufficient stimulus to these substrate vibrational modes which results in a SS3 phase transition behaviour that is unlikely to occur in a solvent. The next chapter will show a comparison of the numerical solution of the catalytic QAO model for benzene under the influence of the MalL enzyme and a water solvent. Here, I describe the QAOSS manifold for a vibrational mode within the 20 to 35 THz bandwidth that has been identified to contain the glycosidic bond stretch of isomaltose in **§ 2.6**.

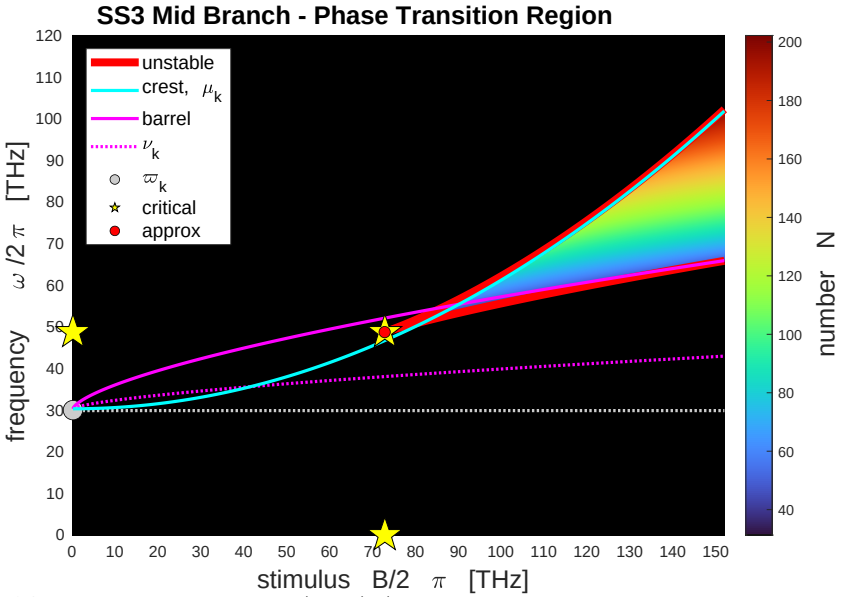

Figure 4.10: The SS3 region in (ω, B) (coloured by the mid branch phonon number), its boundary (red lines), and the SS1 region (black) for the $k = 10$ normal mode of benzene. The peak maximum (crest, μ_k, in cyan), the $\Upsilon_k = 0$ bifurcation point (ν_k, in dotted magenta), and the barrel point (magenta) evolve with increasing stimulus from ϖ_k (grey circle) at zero stimulus, cross paths, and then are in good agreement with the boundary. The critical minimum SS3 stimulus bifurcation point is drawn by the approximate expression (4.101) (yellow star), and the exact numeric result (red), which show a close agreement.

The manifold is constructed using the MATLAB script, `Solve_SS3`, that I built by using a root-solving algorithm on the SS conditional relation (4.85) over a range of frequencies and stimuli values. I then organise the roots into the low, mid, and high sheets: the mid sheet corresponds to the unstable region of the QAOSS manifold; the high sheet lies above the unstable region; and the low sheet is below. The QAOSS phonon number response manifold in (ω, N)-space for the 10^{th} normal mode of benzene is shown in Fig. 4.10, Fig. 4.11, and Fig. 4.12. The various parameters are calculated by using the same conditions that will be used in the QAO EoM simulation **Chapter 5**:

- the harmonic normal mode frequency is $\omega_{10}/2\pi = 29.90$ THz (grey circle)
- the temperature is set to 34°C, giving a thermal equilibrium phonon number $\bar{n}_{10} = 0.906$
- the total VDR is $\Upsilon_{10}/2\pi = 10.63$ THz, with iVDR accounting for 8.36 THz
- the Hamiltonian coefficient for the self energy is, $\xi_{10,10}/2\pi = 0.176$ THz, and since the value is positive the mode experiences phonon hardening
- the intramolecular frequency shift is computed by assuming all other modes are at thermal equilibrium giving, $\eta_{10}/2\pi = -0.236$ THz
- the anharmonically adjusted oscillation frequency is then, $\varpi_{10}/2\pi = 30.02$ THz, a total shift of +0.117 THz

The boundary of the unstable mid sheet is determined numerically from (4.97) via a root-solving algorithm over a range of stimulus values (red lines). The approximate critical point (4.101) is represented by the yellow diamonds, and the numerically determined value by the red circles. It can be seen that the approximate analytic expression is in good agreement with the location of true value in (ω, B, N). Under these conditions, the critical point occurs at:

- $B_{10,\text{crit}}/2\pi = 72.49$ THz ($\hbar B_{10,\text{crit}} = 48.03$ zJ $= 28.93$ kJ.mol^{-1})
- $\phi_{10,\text{crit}}/2\pi = 18.74$ THz
- $\omega_{10,\text{crit}}/2\pi = 48.75$ THz
- $\delta N_{10,\text{crit}} = 34.85$
- $N_{10,\text{crit}} = 35.76$

The transition state stabilisation energy for MalL–isomaltose is 166 zJ (100 kJ.mol^{-1}), which breaks the glycosidic bond, and so the requirement of $\hbar B_{10,\text{crit}}$ seems reasonable. In **Chapter 5**, I simulate the response of benzene due to MalL under conditions where this particular mode is provided sufficient stimulus for phase transition behaviour. I will also provide a detailed discussion of the comparison of the energetics of carbon–oxygen bond breaking in **§ 5.4**.

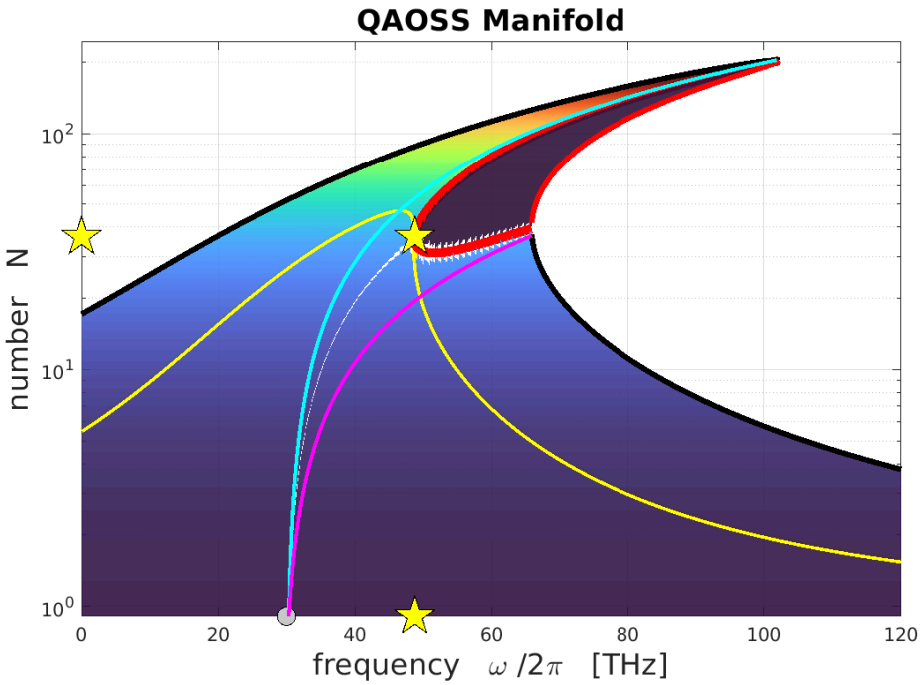

Figure 4.11: The QAOSS phonon number response manifold in (ω, N) for the tenth normal mode of benzene, a rotation of Fig. 4.12, and with phonon number in log scale. The features are labelled in the same manner as Fig. 4.10. The critical QAOSS distribution for $B_{k,\text{crit}}$ (yellow) is SS1 (single-valued), the SS1 region has $B_k < B_{k,\text{crit}}$ is the area under the critical curve, and the SS3 region with $B_k > B_{k,\text{crit}}$ occurs above up to the QAOSS for $B_k/2\pi = 150$ THz (black). The unstable mid-branch is the darker region with a red boundary.

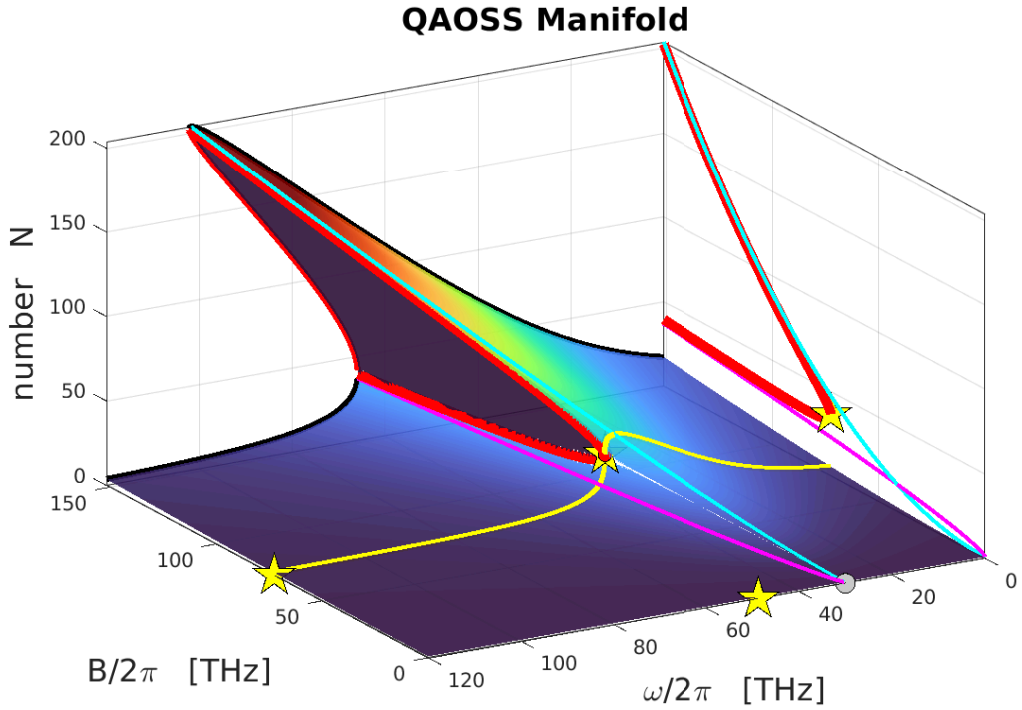

Figure 4.12: The QAOSS phonon number response manifold in (ω, B, N). The features are labelled in the same manner as Fig. 4.10. The boundary of the unstable region (red), crest (cyan) and barrel (magenta) points are projected onto the back wall.

4.7 Conclusion

In this chapter, I have described a quantum anharmonic phonon-based model of catalysis. The non-linear three-phonon processes in the substrate's free behaviour permit intramolecular exchanges of phonons between all vibrational modes, including self-interaction, which results in a perturbation to oscillation frequency as well as an iVDR. The non-linearities in the stimulus permits substrate–enzyme phonon exchanges to occur over a range of frequencies. Thus, the introduction of anharmonicity into the catalytic model allows for vibrational modes to interact with other modes across the spectrum. Of particular interest for catalysis is that the bond stretching modes of the substrate can be stimulated by the low-frequency bulk motions and high-frequency hydrogen network oscillations of the enzyme.

I derived the EoMs for the vibrational quantum state of the substrate molecule via a dissipative QME for the anharmonic Hamiltonian that is used by Gaussian 09 to simulate anharmonic IR spectroscopy. Since there are no exact analytic solutions to the QAO EoMs, I derived exact expressions for the steady states and linear stability.

The QAO model was evaluated under the following cases

Model	Stimulus	Dissipation
Free	×	×
Void	✓	×
Full	✓	✓

The dynamics for each case can be characterised as

- **Free QAO molecule**: constant molecular energy since the vibrational phonon numbers are static
- **QAO Catalysis in a Void**: a single saddle-node bifurcation (barrel) point in the QAOSS expectation phonon number response spectra marks the border between the SS1 & SS3 regimes, and an exact analytic expression was derived
- **Full QAO model**: the inclusion of dissipation introduces a second saddle-node bifurcation (crest) point, thus the SS3 regime is contained within a band of detuning frequencies between the crest and barrel points. A quartic polynomial was derived whose real roots are both bifurcation points

The QAOSS for the phonon number response spectra is a skew Lorentzian resonance distribution with the following characteristics:

- the peak height for the QHOSS and QAOSS are equal; the peak height for the QAO CV model is at infinity
- the half width at half maximum for the QHOSS and QAOSS are equal
- the QAOSS peak is shifted due to anharmonic intramolecular interactions
- the skew angle is due to self-energy, ξ_{kk}, where a positive (negative) value represents phonon hardening (softening) towards higher (lower) frequencies

The SS3 regime is the bandwidth wherein the QAOSS phonon number response spectra is multi-valued and whose boundary locates the bifurcation points; in the naming convention motivated by ocean waves, this region is bounded by the barrel and crest points. The over-hanging mid-branch of the SS3 region is unstable, while both the lower and higher branches are stable, attracting nodes; therefore a SS3 state will tend to a high-energy or low-energy resting state due to the stimulus from intramolecular modes and enzyme stimulus. The discussion for an isolated QAO vibrational mode in the ND1P is in **Appendix B**, which allows the core dynamics and theoretical results to be observed in a simpler manner than the dimensioned molecular QAO response.

I constructed a map for determining the viable two-for-one resonant phonon exchanges between molecules based upon their mode frequencies, which can be applied to the intramolecular interactions as well as the substrate–enzyme interactions. I then computed the viable interactions by assuming a 'smearing' frequency that relaxes the resonance conditions.

I derived a simplified semi-classical description of the stimulus to account for the QAO interactions with the substrate, that is parameterised by the selection of coupling strengths, smearing frequency, and temperature. A fully quantum treatment of the anharmonic intramolecular and environmental vibrational dissipation rate was implemented by the Maradudin–Fein formula upon setting all modes to thermal equilibrium; these dissipation rates can be extended to be dependent on phonon numbers that are simulated by the EoMs, which marks a focus for future work. The intramolecular VDR for benzene is computed using data obtained from GAUSSIAN 09, as well as specifying a temperature of 34°C and a smearing frequency of 0.1 THz (3.3 cm^{-1}). I derived an exact expression for the critical minimum stimulus for SS3 behaviour, which shows that the critical minimum phonon number is proportional to the total dissipation rate (Υ_k) and inversely proportional to the self-energy (ξ_{kk}).

Chapter 5

Anharmonic Catalysis Model Simulation

In this chapter, I will be demonstrating the numerical solution to the catalytic QAO EoMs via the function `Catalytic_QAO_EoM_Solver`, that I have constructed in MATLAB. I will compare the simulations of the response of benzene at thermal equilibrium to the sudden application of water and MalL. The first section details the extraction of the anharmonic Hamiltonian coefficients from the anharmonic IR spectroscopy data computed by GAUSSIAN 09. Performing a quantum mechanical MD simulation of the glycosidic linkage in isomaltose is not only computationally expensive, but is highly sensitive to the molecular conformation since the force field parameterisation will identify many potential minima [149]. While computational anharmonic IR spectroscopy has been performed for isomaltose and glucose [150], I was unable to successfully complete their anharmonic MD in GAUSSIAN 09. Due to this, I will be using the data from an MD simulation of benzene throughout this chapter as a proxy substrate molecule. Despite using this proxy substrate for the MalL enzyme, there are significant conclusions that can be drawn from the results of the QAO EoM solution. Further developments of computational power and quantum MD code efficiency will allow for the quantum anharmonic treatment of molecules and proteins to become more robust and more readily accessible. Therefore, I am demonstrating a methodology and insight in lieu of obtaining the appropriate anharmonic MD data for the catalysis of isomaltose by MalL. As the coding work that I have constructed is generalised to handle data for any molecule and enzyme, this may serve as a guide and a tool for future research outside the scope of this thesis.

In order to perform a numerical solution of the QAO EoMs, the following must be defined additionally to the MD data:

- The initial quantum state of the molecule
- The environmental VDR coupling and smearing for each molecular mode
- The stimulus coupling and smearing for each phonon exchange between the molecule and external system (water or MalL)

I will be addressing these items in their appropriate sections in this chapter, along with a discussion for the considerations behind the decisions that I made for their implementations.

5.1 Simulated Anharmonic Infrared Spectroscopy in Gaussian 09

The harmonic Hamiltonian coefficients are the set of natural oscillation frequencies of each vibrational mode, $\{\omega_k\}$, and are obtained by the procedure of standard NMA (**Chapter 2**). The

procedure for obtaining the set of anharmonic Hamiltonian coefficients, $\{\xi_0, \xi_{ij}\}$, is considerably more involved as it requires the computation of the third- and fourth-order spatial derivatives of potential energy, and functions of the dynamical eigenvalues. I will introduce the mathematical treatment for the calculation of the anharmonic contributions that are used in Gaussian 09 [130], and explain how I extract the anharmonic Hamiltion coefficients from the output data.

A conventional motivation for performing anharmonic MD in Gaussian 09 is to simulate anharmonic IR and Raman spectroscopy. In anharmonic IR spectroscopy, the harmonic natural vibrational mode frequencies are perturbed due to the anharmonic contributions, their IR absorbance is computed, and a spectral distribution of absorbance is drawn using a Lorentzian resonance distribution by assuming a spectral linewidth (Fig. 5.1). The whole algorithm has been included in Gaussian 09 as a 'black box' procedure whereby the user does not need to interact with the intermediate steps [112]; however, it is the set of anharmonic coefficients that is required for use in the catalytic model EoM under inspection in this thesis. Therefore, I have written scripts to extract the necessary data from the raw data files in order to 'reverse-engineer' the values of ξ_0 and ξ_{kj}.

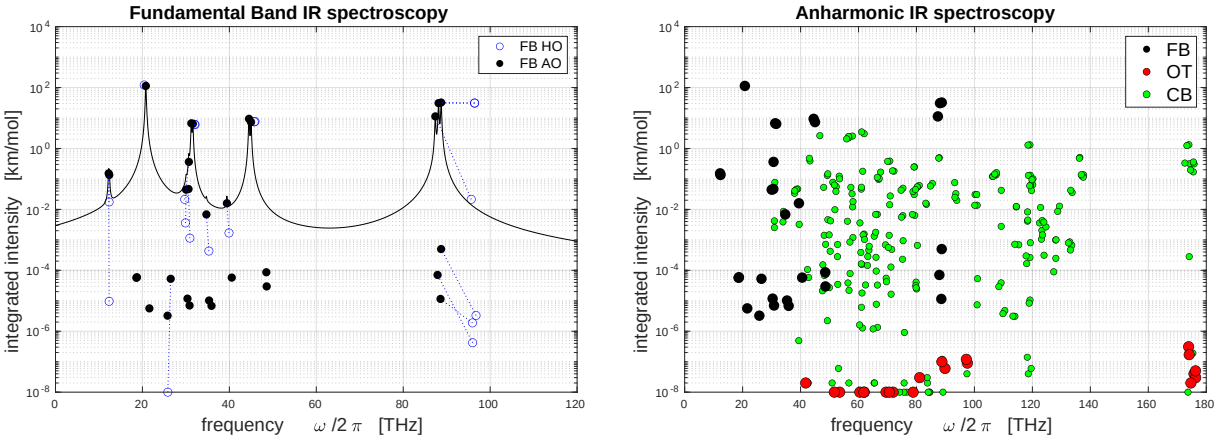

(a) QAO FB IR spectroscopy **(b)** QAO IR spectroscopy

Figure 5.1: Anharmonic IR spectroscopy of benzene as computed by Gaussian 09: panel (a) shows the fundamental band (FB) (black) of the harmonic and anharmonically adjusted frequencies; panel (b) shows the anharmonically adjusted IR absorbance of the FB, overtone (OT), and combination bands (CB). The continuous absorbance spectra is plotted by a normalised Lorentzian distribution, $\sum_k^{\text{mol}} I_k \, \varphi_k^2 \, (\varphi_k^2 + (\omega - \omega_k)^2)^{-1}$, where I_k is the integrated intensity value of mode k, and φ_k is set to 0.1 THz. The largest IR absorbance in benzene occurs for the low-frequency FB modes, with the OT modes exhibiting the smallest. The hydrogen oscillation OTs have a frequency of nearly 180 THz ($6,000$ cm^{-1})

In the terminology of IR spectroscopy, the anharmonically adjusted frequencies are categorised into three distinct frequency bands: the frequency of the transition from the ground state to the first excited state are called the Fundamental Band (FB) frequencies, $[\nu_k]$; the overtone (OT) frequencies represent the transition from the ground state to the second excited state, and have a frequency approximately double that of the FB, denoted by $[2\,\nu_k]$, where the square braces denote the overtone and does not imply that $[2\,\nu_k] = 2\,[\nu_k]$ (Fig. 5.2); and the Combination Band (CB), $[\nu_k\,\nu_j]$, describes the simultaneous excitation of two distinct vibrational modes. The anharmonic frequencies for benzene are shown in Fig. 5.3.

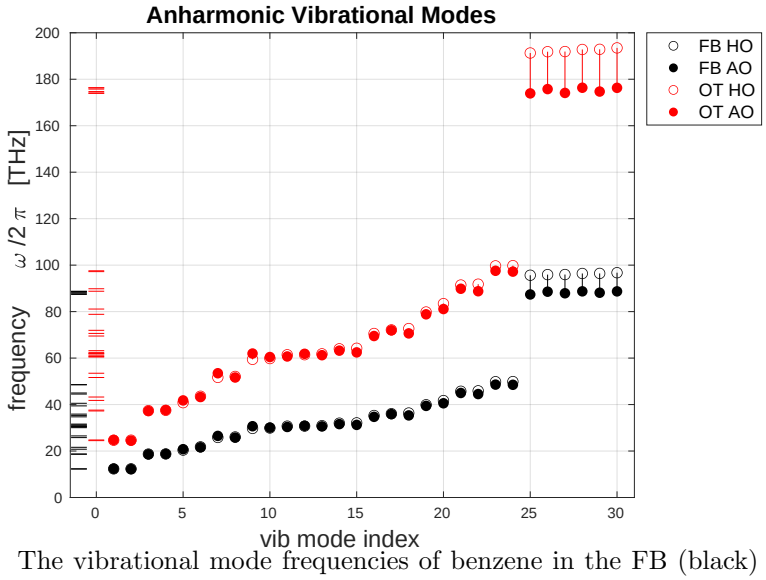

Figure 5.2: The vibrational mode frequencies of benzene in the FB (black) and OT (red) are shown with their harmonic natural (hollow) and anharmonically adjusted values (filled); frequencies are shown as dashes on the left to represent the DoS. It can be seen that the highest frequency modes corresponding to the hydrogen oscillations are perturbed the most due to anharmonic processes. The FB hydrogen oscillation frequencies are in the same range as the mid-range OT, implying viable IR absorbance within the harmonic transparent window in the bandwidth spanning 50–70 THz.

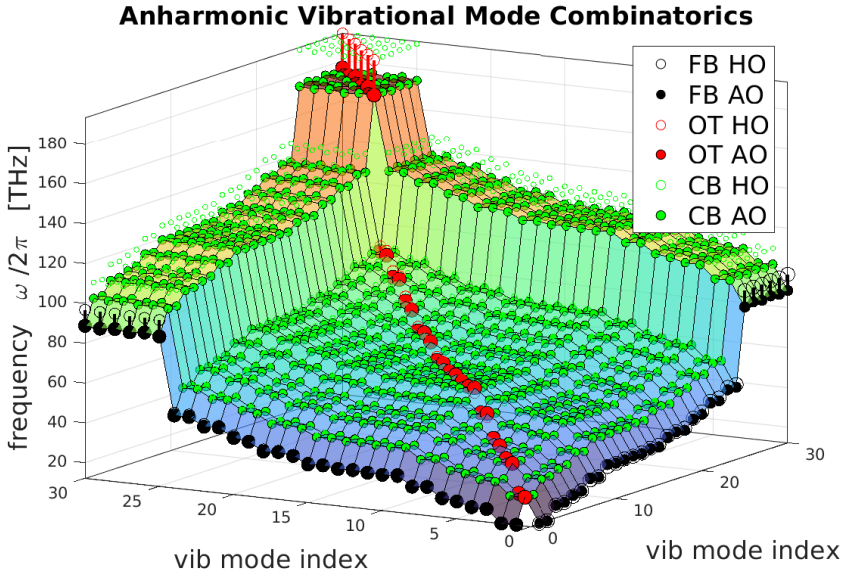

Figure 5.3: All frequencies given in the GAUSSIAN 09 QAO IR data for benzene. The CB (green) corresponds to the combination of two modes and has a frequency between the FB (black) and OT (red). Harmonic values (hollow) are shown in comparison to their anharmonically adjusted values (filled).

The FB frequencies are defined, $[\nu_k] = \omega_k + 2\xi_{kk} + \frac{1}{2}\sum_{j>k}^{\text{mol}} \xi_{kj}$, and as such the anharmonically adjusted vibrational mode frequencies are no longer indexed in ascending order since each mode is perturbed by a varying amount due to the values of ξ_{kj} (Fig. 5.2). The vibrational OT have frequencies given by, $[2\,\nu_k] = 2[\nu_k] + 2\xi_{kk}$; while in the harmonic case, the OT is precisely double the FB, this is not true when accommodating for anharmonic self-energy, ξ_{kk}; the CB has frequencies, $[\nu_k\,\nu_j] = [\nu_k] + [\nu_j] + \xi_{kj}$; and the vibrational ZPE frequency ($E/\hbar$) is, $[\nu_{\text{zpe}}] = \xi_0 +$

$\frac{1}{2}\sum_k^{\text{mol}}(\omega_k + \frac{1}{2}\xi_{kk} + \frac{1}{2}\sum_{j>k}^{\text{mol}}\xi_{kj})$.

5.1.1 Extracting the Hamiltonian Coefficients

The relevant anharmonic spectroscopy data are extracted and processed into the Hamiltonian coefficients by `Solve_Xi_Anharmonic_Hamiltonian` as part of the `Get_Molecule_Data` script. I reverse-engineer the Hamiltonian coefficients by inverting the definitions of the FB, OT, and CB frequencies, and are computed as part of the top-level procedure script `Get_All_Data`. The self-energy (diagonal) coefficients are recovered by, $\xi_{kk} = \frac{1}{2}[2\nu_k] - [\nu_k]$, the mode mixing (off-diagonal) coefficients are, $\xi_{kj} = [\nu_k\nu_j] - [\nu_k] - [\nu_j]$. Generally speaking, the highest frequency modes undergo phonon softening ($\xi_{kk} < 0$), and the lower frequency modes undergo phonon hardening ($\xi_{kk} > 0$), with the hydrogen oscillations having the largest magnitude of self-energy (Fig. 5.4). The off-diagonal anharmonic Hamiltonian coefficients pertaining to hydrogen oscillations also show the largest values (Fig. 5.5). The zeroth-order Hamiltonian coefficient, ξ_0, is obtained by extracting the ZPE energy then rearranging the definition of $[\nu_{\text{zpe}}]$. The ZPE in the GAUSSIAN 09 data includes the harmonic and anharmonic contributions as well as (Watson) Coriolis effects and the modes with imaginary frequencies (negative-valued dynamical eigenvalues).

For the benzene structure demonstrated in this chapter, the highest frequency vibrational normal mode has the largest ZPE at $\frac{1}{2}\hbar\omega_{30} = 64.1$ zeptojoules (64.1 zJ $= 64.1 \times 10^{-21}$ J $=$ 38.6 kJ/mol), and mode 25 has the largest anharmonic perturbation at $\sum_{j\geq 25}^{30}\frac{1}{4}\hbar\xi_{25,j} = -1.65$ zJ (-0.992 kJ/mol). The total molecular ZPE is 432.6 zJ (250.5 kJ/mol), accommodating a total anharmonic perturbation of -8.122 zJ (4.891 kJ/mol), and it will be shown that the enzyme-excited molecular energies are on the order of attojoules (1 aJ $= 10^{-18}$ J $= 602.2$ kJ/mol).

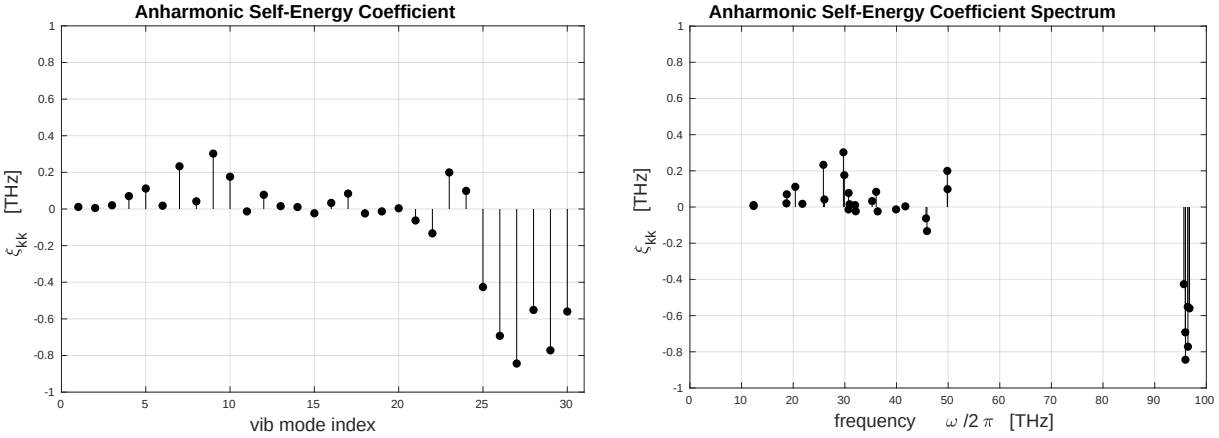

(a) Self-energy coefficients, ξ_{kk} **(b)** Self-energy spectral distribution

Figure 5.4: QAO self-energy coefficient for benzene. Panel (a) shows the values for each vibrational mode, and (b) is plotted using the vibrational mode natural harmonic frequencies to indicate spectral distribution. The hydrogen oscillation (highest six) modes show a strong influence of the anharmonic contributions (< 0.9 THz), and the largest ratio, $|\xi_{kk}/\omega_k|$, is 1.0% for mode $k = 9$, with the mean being 0.33%.

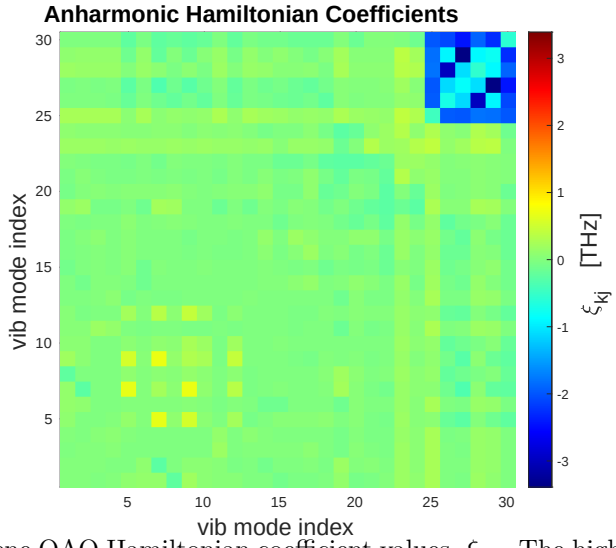

Figure 5.5: Benzene QAO Hamiltonian coefficient values, ξ_{kj}. The highest frequency modes show the largest impact due to anharmonics, and there is significant mixing contributions of the hydrogen network with low-frequency modes, as seen by the bands along the top and right. The largest ratio, $|\xi_{kj}/\omega_k|$, is 3.5% for mode combination $(k, j) = (29, 27)$, with the mean being 0.31%.

5.2 Numerical Model Simulation Establishment

This section details the numerical integration of the catalytic model QAO EoMs (4.72). The simulation conditions are defined in an external launch script, which are then passed into the main QAO EoM solving function, `Catalytic_QAO_EoM_Solver`. The computation is performed, and the results are then packaged into a data structure for visualisation and storage. When running the uppermost EoM solver script, the user will be prompted with a pop-up window to choose the molecule and enzyme data, as implemented via, `Get_All_Data`, which produces a structure that contains the necessary molecular, enzyme, and the general quantities that have been detailed in **Chapter 2**. The required data for the QAO EoM solver are then extracted and processed for use in the numerical solution scheme.

The set of options for the simulation conditions of the full catalytic QAO EoM solver are:

- molecule and enzyme data
- temperature
- simulation duration
- enzyme stimulus coupling strengths (QHO and QAO)
- enzyme VDR coupling strengths (QHO and QAO)
- smearing frequency (QHO and QAO for stimulus and eVDR; QAO for iVDR)
- maximum initial environmental Lamb shift
- number of sampled forcing frequency states
- number of spline interpolation points for solution trajectories

5.2.1 Code Hierarchy

The code hierarchy tree for the MATLAB scripts of `Catalytic_QAO_EoM_Solver` are given below. The list of the script is organised into their order of execution, and the indent depth represents nested functions. The simulation conditions are defined in `Launch_QAO_EoM`, which then executes `Catalytic_QAO_EoM_Solver`.

```
>> Launch_QAO_EoM
  · Catalytic_QAO_EoM_Solver
    · Get_All_Data
      · (Harmonic data § 2.3.1)
      · Solve_Xi_Anharmonic_Hamiltonian
    · Solve_Enzyme_Stimulus
    · Solve_Molecular_Dissipation_Rate
    · Solve_Enzyme_Dissipation_Rate
    · Solve_SS3
    · Save_all_plots
      · Plot_save_function
```

The launch script allows the conditions for different molecules and stimuli to be saved individually, which allows the solver script to be generalised. For this thesis, I have composed two scripts for interaction of benzene with MalL, and benzene with water.

5.2.2 Selection of Molecular Vibrational Modes to Simulate

All molecule and enzyme data are read in by `Get_All_Data` and collected into the structure, `P`, the core components are then extracted for coding convenience. The vibrational mode harmonic natural frequencies, ω_k, are the dynamical eigenmodes with real and positive oscillation frequencies. For generality, the difference in the number of eigenmodes, `w_dyn`, and NMA modes, `w_nma`, is used to clip the first few elements from the set of eigenmodes: `w_vib=w_dyn(clip+1:end)`. The total number of modes to solve, `N_vib`, is then defined by the number of elements of `w_vib`. For most molecules, there are six elements that are removed. The clipped set of dynamical eigenmodes are used instead of the NMA modes as there may be the presence of negative frequencies in, `w_nma`, due to further processing of the dynamical eigenfrequencies by GAUSSIAN 09. The zero-point Hamiltonian coefficient, ξ_0, is extracted by `xi_0=P.MOL.XI0`, and the square matrix of anharmonic coefficients, ξ_{kj}, with `xi=P.MOL.XI`, from which the diagonal elements are the self-interaction Hamiltonian frequencies, ξ_{kk}.

5.2.3 Environmental Conditions

The environment is treated as a constant Markovian QHO reservoir, and thus has a thermal equilibrium given by the Planck spectral distribution, whose values are set by the simulation temperature, `T_sim`. For the purposes of probing biologically relevant catalysis, a temperature of

307.15 K (34°C) is selected. The option to define an initial Lamb shift, φ_k^0, for each vibrational mode allows for phase relaxation due to a varying environment to be observed. This quantity arises from the QAO interaction of a molecule with a Markovian QHO thermal reservoir which imparts a detuning to the natural frequency of a vibrational mode. This is treated as an additional degree of freedom to the smearing frequencies, φ_k, which used to soften the resonance conditions. The initial Lamb shift could be treated as time-dependent random variable, obeying some fluctuation–dissipation relation, that continuously perturbs the system in order to stimulate chaotic behaviour. As a simplest first approach, a scaling value is set to 5 THz, and then the shift to all vibrational modes is a random scalar, `w_lamb_vib=w_lamb_max*randn(size(w_vib))`, where `randn` produces an array whose elements are drawn from the standard normal distribution. In order to treat the Lamb shift as a time evolving variable its values must be updated in the ODE solver, which is not currently implemented in `Catalytic_QAOEoM_Solver` and marks a region of future investigation.

5.2.4 Vibrational Dissipation Rates

The total VDR, Υ_k, for each molecular vibrational mode is the summation of the intramolecular (4.68), QHO (3.57) and QAO (4.58) environmental dissipation pathways. The expectation values of the phonon numbers in each expression is taken to be at thermal equilibrium ($\bar{n}_k$), and therefore have a temperature dependence. The extent of the resonance smearing frequency for each vibrational mode can be associated with temperature via a Lamb shift mechanism that affects the vibrational lifetime, but are most simply implemented by selecting their values as a phenomenological parameter related to the simulation time resolution and letting all modes have the same value. I have chosen values <1 THz as informed by the literature on VDR processes in proteins (**§ 3.3.3**). In physical systems, the interaction coupling strength tensors will also be dynamic and temperature-dependent, which would require reevaluation of the equilibrium structures of the molecule and enzyme at varying temperatures. However, since the computation of the QAO VDR values are computationally expensive, the iVDR is computed for the harmonic equilibrium geometry, and the eVDR coupling strengths are treated as constant scalars.

Intramolecular VDR

The iVDR is computed using (4.68) by the script `Solve_Molecular_Dissipation_Rate`, whose input options are temperature and resonance smearing frequency. The coupling strength tensor for iVDR processes, $\mathbf{\Phi}_{k\alpha\beta}$, is due to the third spatial derivative of the potential (4.64), and is computed entirely from data provided by anharmonic MD data in Gaussian 09. The iVDR for benzene at 34°C with a smearing frequency of 0.25 THz allows for 96 intramolecular resonant interactions, with the largest coupling constant being 3.18 THz, and a mean value of 0.13 THz. The iVDR (green diamonds in Fig. 5.6) shows that mode 13 has the largest iVDR at 9.14 THz (0.017 ps lifetime), and the highest frequency mode has the smallest at 0.099 THz (1.61 ps lifetime).

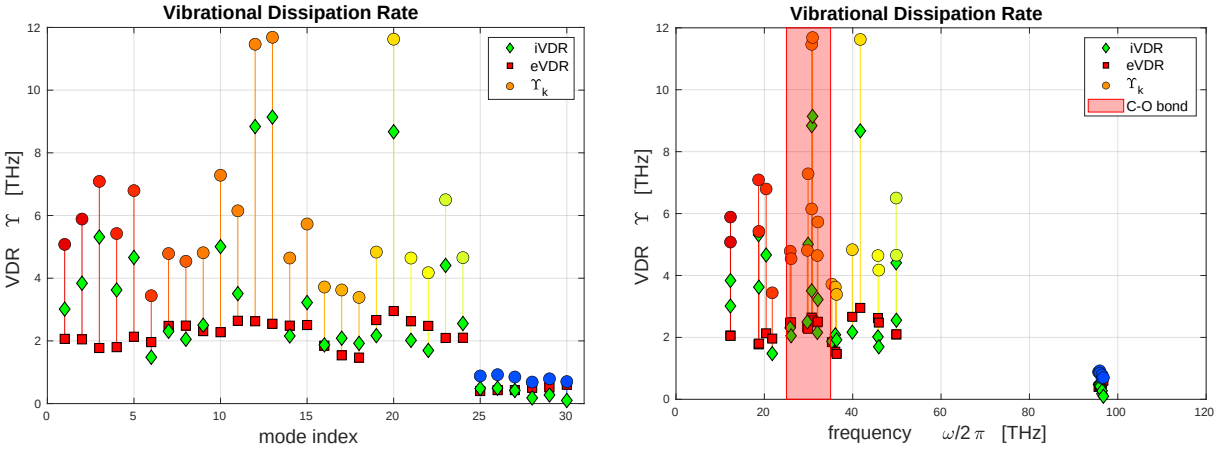

(a) Total VDR by mode **(b)** Total VDR by frequency

Figure 5.6: Total VDR (circles coloured by mode frequency) of benzene due to intramolecular (green diamonds) and enzyme (red square) dissipation pathways. The largest VDR is for mode 13 with a value of 1.69 THz (0.013 ps lifetime), and mode 28 is the smallest at 0.687 THz (0.232 ps lifetime). The red patch in (b) shows the frequency bandwidth that contains the glycosidic bond stretching modes identified in **§ 2.6**.

Environmental VDR

The eVDR is computed using `Solve_Enzyme_Dissipation_Rate`, whose input options are the temperature, as well as the coupling strengths and smearing frequencies for both the QHO and QAO processes. In lieu of obtaining experimentally informed values, all QHO and QAO coupling strengths are set to 7 THz and 0.02 THz, respectively. By reducing the tensor arrays to scalars, each molecule–enzyme dissipation pathway is taken to have the same interaction strength, which is a significant reduction in capturing real world dynamics. The variation in the contribution of each pathway to the eVDR under this assumption is then due to the enzyme phonon numbers and the resonance condition. The smearing frequency for the QHO resonances is set to 0.25 THz which allows 5×10^3 resonant interactions between benzene and MalL, and the QAO resonance is smeared by 0.1 THz allowing 8.17×10^7 interactions. The eVDR coupling strengths are chosen to be approximately double the iVDR strengths on the assumption that the dissipation into the enzyme is dominant compared to intramolecular pathways. The QHO and QAO eVDR coupling strengths are adjusted such that they contribute a similar amount to Υ_k. A more detailed treatment for the eVDR would take the resonances between the substrate molecule and the active site of the enzyme to have the larger coupling strengths than the other regions of the enzyme; this marks an avenue for future work. The eVDR (red squares in Fig. 5.6) shows that mode 20 of benzene has the largest value at 2.95 THz (0.053 ps lifetime), and mode 25 has the smallest value at 0.40 THz (0.40 ps lifetime).

5.2.5 Simulation Duration

The vibrational lifetimes are the inverse of the VDR, Υ_k^{-1}, which represent the time-constants of the vibrational dynamics, and are used to define the duration of the simulation ODE solver time integration window. The time taken for the isolated QHO relaxation oscillations of mode k to be approximately quiesced is $5\Upsilon_k^{-1}$ (since $e^{-5} \approx 0$), the time for the QHO molecule to become relaxed is taken to be five times the inverse of the smallest VDR value. Since the VDR values

in Fig. 5.6 show that the hydrogen oscillations have much longer lifetimes ($5\Upsilon_{30}^{-1} = 1.1$ ps) than the lower frequency modes ($5\Upsilon_{24}^{-1} = 0.17$ ps), if the simulation duration were to capture the relaxation oscillations of the hydrogen oscillations, the evolution of the bond-stretches would occupy a small window of the simulation. Therefore, the simulation duration is set by specifying a percentage of the largest $5\Upsilon_k^{-1}$; for the results presented in this chapter, this percentage is set to 60% which defines a simulation duration of 0.70 ps.

5.2.6 Enzyme Stimulus to each Molecular Vibrational Mode

In this thesis, the enzyme is treated as a classical static object taken at its equilibrium geometry that supplies a consistent stimulus to the substrate molecule like a 'phonon laser'. The enzyme stimulus, B_k, is parameterised by the enzyme vibrational mode phonon number expectation values, as well as the QHO and QAO coupling strengths. In the simplest modelling of the enzyme stimulus, the number of phonon modes is given by a smeared DoS multiplied by the smearing frequency, then by taking the enzyme to be at thermal equilibrium, the expectation values and therefore the temperature-dependence of the stimulus is governed by the Planck distribution. This assumption means that the enzyme vibrational mode parameters (VDR and enzyme–solvent stimulus) need not be determined, and the stimulus is set by the coupling strengths, smearing frequencies, and the temperature. A more detailed analysis of the enzyme would treat the enzyme as a dynamic QHO that is in a coherent state with a solvent environment, which would allow the enzyme phonon number expectation values and the molecule–enzyme coupling strengths to evolve.

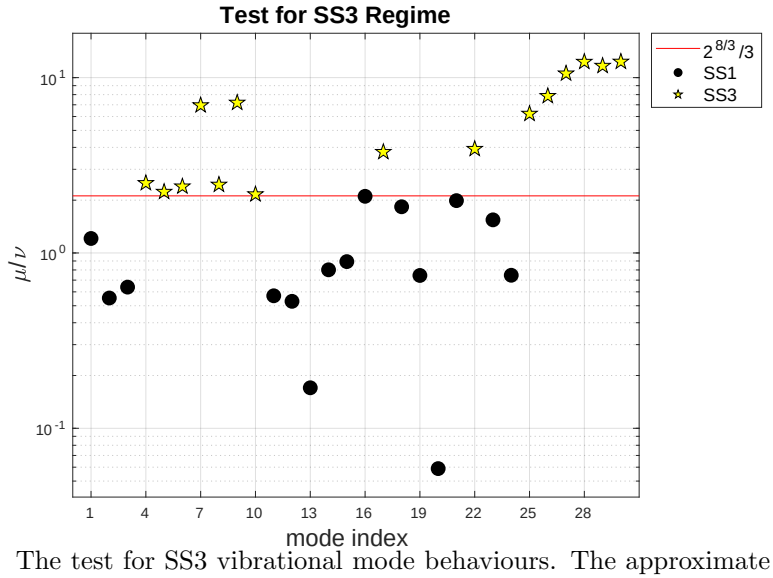

Figure 5.7: The test for SS3 vibrational mode behaviours. The approximate critical value is given by (4.98); enzyme stimuli that are above the critical value indicate that the mode QAOSS is SS3, and below, the QAOSS distribution is SS1 (single-valued).

In **Chapter 4**, it was shown that the critical condition for the vibrational mode QAOSS distribution to be at the border between SS1 and SS3 regimes is when the crest-to-barrel ratio is, $(\mu_k/\nu_k)\big|_{\min} = 2^{8/3}/3$ (Fig. 5.7). Rearrangement shows that the minimum stimulus for SS3 is due to the total VDR and the self-energy (4.99), which corresponds to a minimum peak phonon number (Fig. 5.10). Therefore, in lieu of experimentally determined values, the stimulus

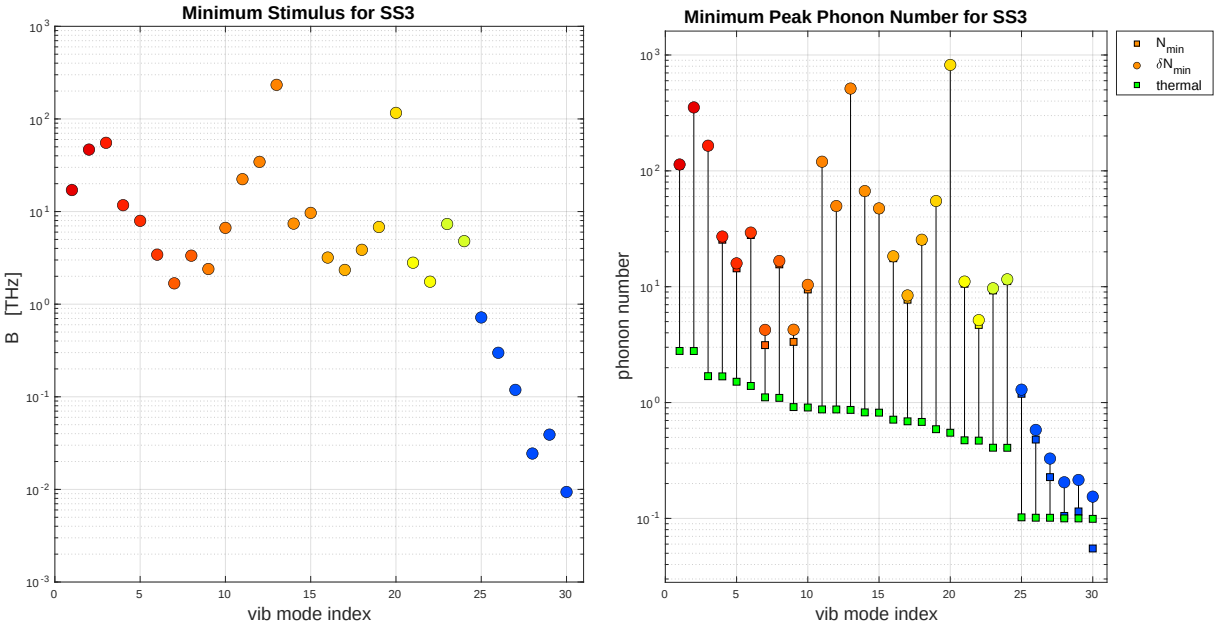

(a) Critical minimum stimulus **(b)** Critical phonon number values

Figure 5.8: Critical minimum conditions for SS3, whose values are coloured by the normal mode frequencies. Panel (a) shows the minimum stimulus, and panel (b) shows the minimum excitation phonon numbers (coloured squares) in comparison to the thermal equilibrium phonon numbers (green squares), whose summation, $N_{k,\min} = \bar{n}_k + \delta N_{k,\min}$, gives the total values (circles).

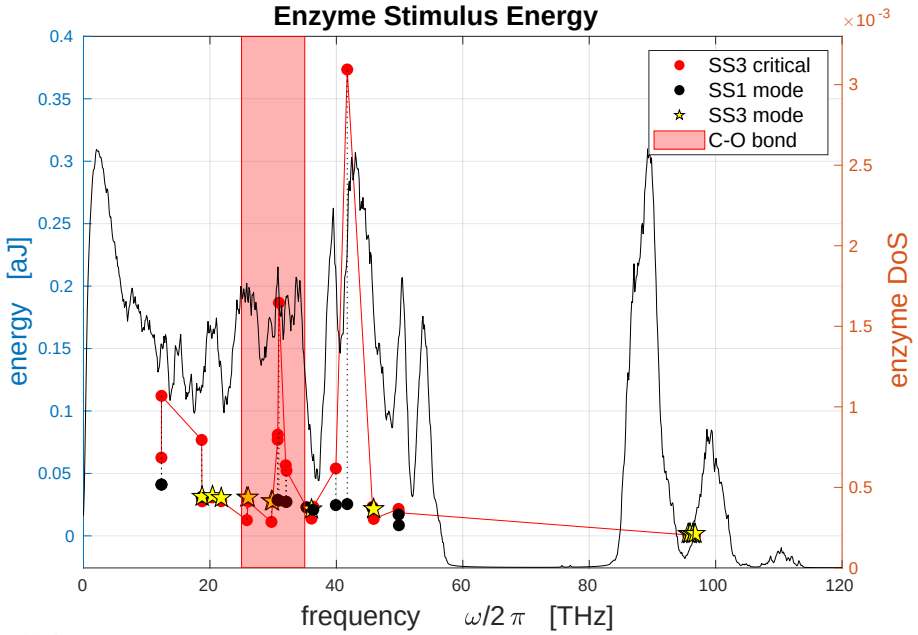

Figure 5.9: Enzyme stimulus energy spectral distribution of benzene due to MalL (left y-axis) plotted alongside the MalL enzyme DoS (right y-axis). The critical values for the SS3 regime (red) are drawn as a continuous line, with the under-stimulated modes in SS1 (black circle) being under this line, and the over-stimulated modes in SS3 (yellow star) are above.

coupling strengths are chosen to ensure there is SS3 vibrational response. A hypothesis of this thesis is that the QAO phonon interactions between the substrate and enzyme during the course of catalysis prompt a phase-transition dynamic in the molecule. Therefore, the simulations that are the most compelling are where the vibrational modes pertaining to a carbon–oxygen bond

stretch (**Chapter 2**) are in the SS3 regime.

The benzene modes 7 through to 15 have natural harmonic frequencies within the bandwidth identified to pertain to stretching the carbon–oxygen glycosidic bond of isomaltose (25 to 35 THz). Under the simulation parameters demonstrated in this chapter, modes 7 (25.84 THz) to 10 (29.90 THz) are in the SS3 regime , while modes 11 to 15 require significantly more stimulus for SS3. From this data, there are vibrational modes in the carbon–oxygen bond stretching bandwidth that do exhibit phase transition behaviour.

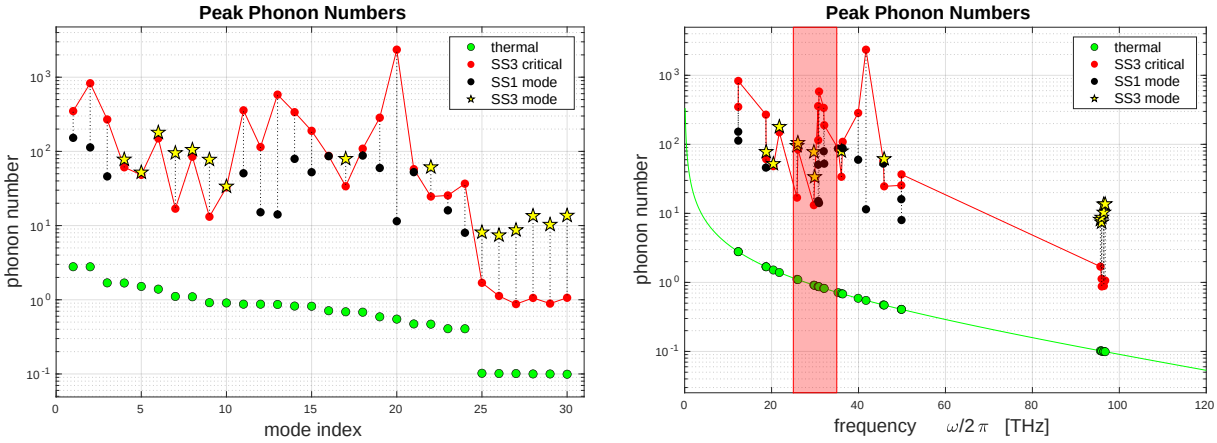

(a) Peak phonon numbers by mode **(b)** Peak phonon numbers by frequency

Figure 5.10: Vibrational mode peak phonon numbers, plotted using the same method as Fig. 5.9, along with the thermal (Planck distribution) values (green).

The total enzyme stimulus is the summation of QHO (3.46) and QAO (4.32) contributions. The QHO and QAO interaction strengths are set to 5000 THz and 0.5 THz, respectively, and the highest six modes pertaining to hydrogen oscillations are reduced by half. The smearing frequencies are set to be the same as for the eVDR calculation, and therefore allow the same number of resonant interactions. Under these conditions, the lowest frequency mode of benzene has the largest stimulation at 62.1 THz ($\hbar B_1 = 41.2$ zJ $= 24.8$ kJ.mol^{-1}), and the least stimulated is mode 27 at 2.49 THz ($\hbar B_{27} = 1.64$ zJ $= 0.988$ kJ.mol^{-1}). Fig. 5.9 shows that while the enzyme stimulus is contained below 40 zJ, the minimum stimulus for SS3 for some modes are significantly larger (for example, mode 20 with 370 zJ, 223 kJ/mol) and are not expected to have sufficient stimulus to be in the SS3 regime; whereas the hydrogen oscillations require a relatively small stimulus to be SS3 (<8 zJ, <4.8 kJ.mol^{-1}). The red patch denotes the frequency band that contains the carbon–oxygen bond stretching modes that were identified in **Chapter 2**, which shows that there is a low stimulus requirement for SS3 for the modes between 25 and 30 THz (834 to 1,000 cm^{-1}). The large variation in minimum stimulus is likely related to the *specificity* of the enzyme to selectively excite certain of bonds in the substrate molecule. Experimental determination of the enzyme stimulus and eVDR would provide a clearer indication of this mechanism.

5.2.7 Initial Anharmonic Frequency Shifts

Before the QAOSS distributions can be drawn, the vibrational mode frequency shift due to the intramolecular anharmonic interactions, η_k, (4.13) must be calculated. The value for η_k is

dependent on the phonon mode expectation values of all modes, which evolve in time due to a particular forcing frequency, $\{\langle \hat{n}_k(t,\omega)\rangle\}$, and would therefore need to be computed by the QAO EoM numerical solution. I obtain an initial value of η_k by setting all modes to thermal equilibrium, $\langle \hat{n}_k\rangle = \bar{n}_k$, resulting in most modes experiencing a negative perturbation with a magnitude less than 0.4 THz, and the hydrogen oscillation modes are perturbed to the greatest extent with values between -1.4 and -1.2 THz. The initial QAO vibrational mode oscillation frequencies are then, $\varpi_k^0 = \omega_k + 2\xi_{kk} + \eta_k^0 + \varphi_k^0$, from which the detuning frequency is, $\phi_k^0 = \omega - \varpi_k^0$, for forcing frequency ω.

5.2.8 Initial Phonon Number Steady State Distributions

The function call, `Solve_SS3`, is used to calculate the distribution of the phonon number QAOSS for each vibrational mode. A pseudo-continuous array is defined over a range of forcing frequencies (0 to 120 THz), with the number of elements chosen such that the SS distribution approaches the saddle-node bifurcation points, while not being so large as to take up storage. A `for` loop over vibrational modes k is performed, and the polynomial coefficients of the SS conditional relation (4.85) and enzyme stimulus are updated in the parameter structure by

```
P_SS3.p3 = 4 *xi(k,k)^2
P_SS3.p2 = @(w) - 4 *xi(k,k)^2 *n_pl_vib(k) - 4 *xi(k,k) *phi(w)
P_SS3.p1 = @(w) 4 *xi(k,k) *phi(w) *n_pl_vib(k) + phi(w).^2 + Y_vib(k)^2
P_SS3.p0 = @(w) - ( phi(w).^2 + Y_vib(k)^2 ) *n_pl_vib(k) - B_vib(k)^2
```
(5.1)

where `phi = @(w) w - w_qao_peak`. The output structure for each mode k is collected into a cell array by an external function call, `SS3_vib{k} = Solve_SS3(P_SS3)`, which uses a root solving algorithm to determine the QAOSS distribution, and then organises the results into high (stable), middle (unstable), and low (stable) branches.

In Fig. 5.11, the three discontinuous regions are plotted with the unstable mid branch shown in red; the high and low branches are the regions that are above and below the mid branch, respectively. Continuous curves are drawn by the rearrangement of the SS conditional relational for detuning frequency, $\omega_{\rm ss}^{\pm}$ (4.94), to fill the gaps near the saddle-node bifurcation point that the root solver cannot reach.

5.2.9 Selection of Initial Molecule Conditions

The initial quantum state of the molecule is a significant choice when performing a simulation. By defining an initial number state, `num0` $\equiv \langle \hat{n}_k(0,\omega)\rangle$, where '$\equiv$' in this context denotes an equivalence in mathematical and code notations, the initial creation and annihilation states can be defined by using the QAOSS conditional statement. I will be demonstrating the QAO EoM behaviour for a benzene molecule that is initially at thermal equilibrium in the absence of an external stimulus by setting all modes to $\langle \hat{n}_k(0,\omega)\rangle = \bar{n}_k$ for all forcing frequencies. I then choose to define forcing frequency dependent initial annihilation state vectors by using the associated

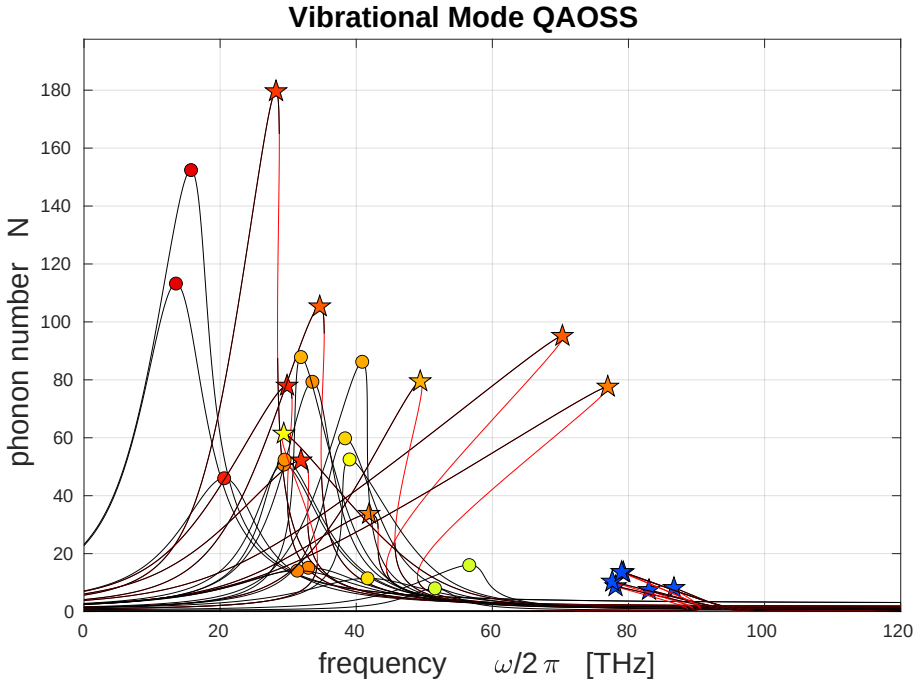

Figure 5.11: Vibrational mode QAOSS distributions for each mode of benzene, with peaks coloured by their natural frequency, ω_k. The stable branches (black) and unstable mid branch (red) are shown with the peaks plotted as circles for SS1 and stars for SS3 (coloured by vibrational mode frequency). The angle of the QAOSS peak is due to self-energy, ξ_{kk}, with phonon softening indicated by a lean towards lower frequencies, and phonon hardening by a lean towards higher frequencies.

QAOSS distributions

$$\texttt{ann0} \equiv \langle \hat{a}_k(0,\omega) \rangle = \frac{B_k}{\omega - \varpi_k - \varphi_k^0 - 2\xi_{kk} \langle \hat{n}_k(0,\omega) \rangle + i\Upsilon_k} \tag{5.2}$$

and the creation states are the complex conjugates, $\texttt{cre0} \equiv \langle \hat{a}_k^\dagger(0,\omega) \rangle = \langle \hat{a}_k(0,\omega) \rangle^*$. The initial quantum states are packaged into a superset array `X0` by the concatenation

$$\texttt{X0} = \begin{bmatrix} \texttt{ann0} \\ \texttt{cre0} \\ \texttt{num0} \end{bmatrix} \tag{5.3}$$

whose rows are vibrational modes indices, and the columns are sampled forcing frequencies.

5.3 Substrate Molecule in Water

The rates of reaction for a molecule in the presence of the appropriate enzyme is far greater than in an aqueous environment. Therefore, I have performed a rudimentary QAO simulation of benzene in water for a comparison with the benzene-MalL results. Dettori, et al, have published the DoS for liquid water by applying a velocity autocorrelation function to MD data on a system of 343 molecules at 300 K [151]. I have approximated their data by the summation of three Lorentzian resonance distributions characterised by:

Mode Type	Centre [THz]	HWHM [THz]	Height [arb.]
Librations	18.53	4.347	0.0233
Bending	42.87	1.973	0.0161
Stretching	97.13	3.957	0.0156

where the Half-Width-at-Half-Maximum (HWHM) is the inverse of the vibrational lifetime, and the DoS peak heights are expressed in arbitrary normalised units. In this simple approximation, I have omitted the low-frequency modes (< 10 THz) with DoS peak heights < 0.005 that correspond to multi-atomic bulk motion of the liquid water; however, these modes would interact anharmonically with the substrate. The simulation of liquid water as a QAO stimulus provides a topic for future research and an application of my coding work.

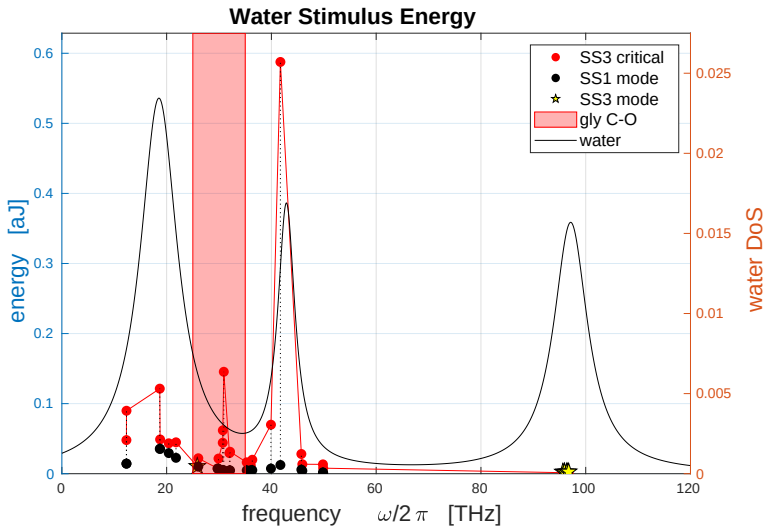

Figure 5.12: The stimulus energy from water to vibrational modes of benzene, in comparison to the approximated DoS of water (black). The SS1 modes (black circle) are below the critical minimum stimulus (red), and the SS3 modes (yellow star) are above.

For a fair comparison, all simulation conditions are set to the same values as was defined for MalL throughout this chapter, however the QAO eVDR coupling strength are increased to 0.7 THz (from 0.02 THz for MalL) in order to increase the contributions of the anharmonic dissipation pathways. The resultant stimulus energy from water to benzene is shown in Fig. 5.12. The critical minimum stimulus (red) is higher than the delivered stimulus (black circle) in comparison to the MalL stimulus. The only modes that are stimulated into SS3 (yellow star) are the six high-frequency hydrogen oscillation modes (clustered around 96 THz) and mode 8 (26.05 THz), which lies in the bandwidth associated with the isomaltose glycosidic carbon–oxygen bond stretch (red patch).

5.4 QAO EoM Simulations for Benzene with MalL and Water

Perhaps the most informative results of the QAO EoM solution in relation to bond breaking behaviour is the molecular response energy spectrogram. For a given forcing frequency, the molecule's energy will evolve from its initial state to a resting state that is larger than the thermal equilibrium due to the enzyme stimulus. The inclusion of anharmonic effects leads to a

redistribution of the QHOSS energy response spectrogram (Fig. 3.9). The altered response spectrum occurs because the low-frequency modes (<10 THz) undergo phonon hardening towards higher-frequency spectral regions, and some of the mid-frequency modes (35–45 THz) undergo phonon softening towards lower-frequency regions; collectively, these processes result in a peak molecular response closer to the glycosidic bond stretching bandwidth.

I have selected the QAO EoM simulation conditions based upon the energetics involved in experimentally measured catalytic dynamics. The binding energy of MalL to a transition state analogue is 0.1183 aJ (110 kJ/mol), which breaks the glycosidic carbon–oxygen bond. The carbon–oxygen single bond dissociation energy (change in enthalpy for a reaction, ΔH) has the maximum value for carbon monoxide at 1.788 aJ (1,077 kJ/mol), and the glycosidic linkages have values around 0.581 aJ (350 kJ/mol) [152]. In Fig. 5.13, there is a peak of 9 aJ precisely where the dominant isomaltose glycosidic stretch vibrational mode is ($\omega_{57}/2\pi = 28.1$ THz). This amount of energy is *significantly* higher than the energy required to cleave a carbon–oxygen bond, and therefore implies a specificity of the MalL enzyme to drive the glycosidic bond to breakage. I anticipate that the coupling strengths of the substrate to enzyme modes pertaining to vibrations of the active-site mode will be the largest; therefore, by reducing the coupling strengths of the other modes, the substrate energy response will have a value closer to the bond dissociation energy and perhaps greater specificity for the glycosidic bond.

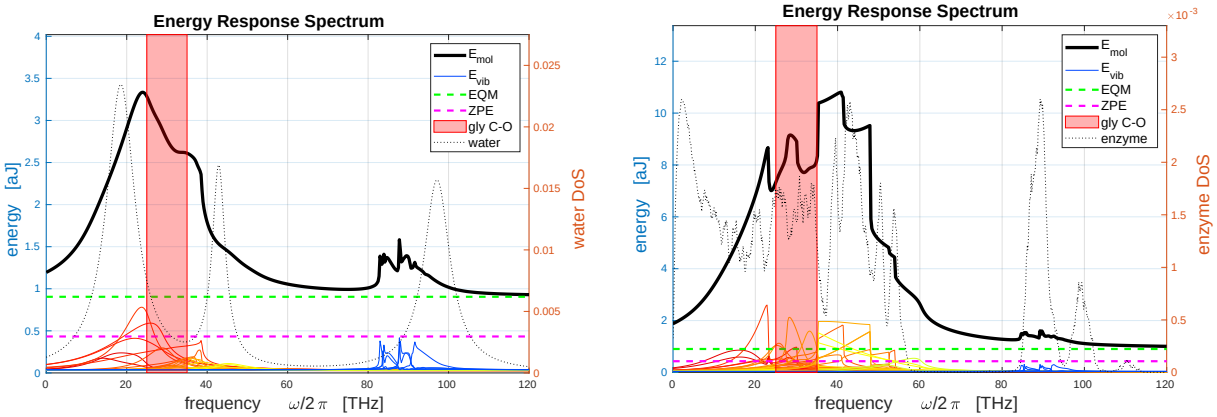

(a) water **(b)** MalL

Figure 5.13: Final molecular energy response spectrum of benzene when initially at thermal equilibrium and then stimulated by water (a) and MalL (b), along with the contributions from each mode (coloured). The benzene ZPE is 0.432 aJ (260 kJ/mol) (magenta), and the thermal equilibrium value is 0.907 aJ (546 kJ/mol) (green). The DoS of the stimulus (dotted black) corresponds to the right y-axis. The red patch represents the bandwidth containing the bond-stretching modes of the glycosidic bond in isomaltose.

The persisting dynamics are shown in Fig. 5.14, where the first 40% of the simulation is clipped in order to suppress the initial relaxation oscillations. In the benzene–water simulation, it can be seen in Fig. 5.14a that only the high-frequency hydrogen oscillations of benzene are still noticeably excited (blue trajectories), and the lower-frequency are all quiesced (dots lying on the QHOSS distribution). This shows that for water, in this simulation, there is no phase transition in the bond-stretching modes behaviour, which is expected since there is only one

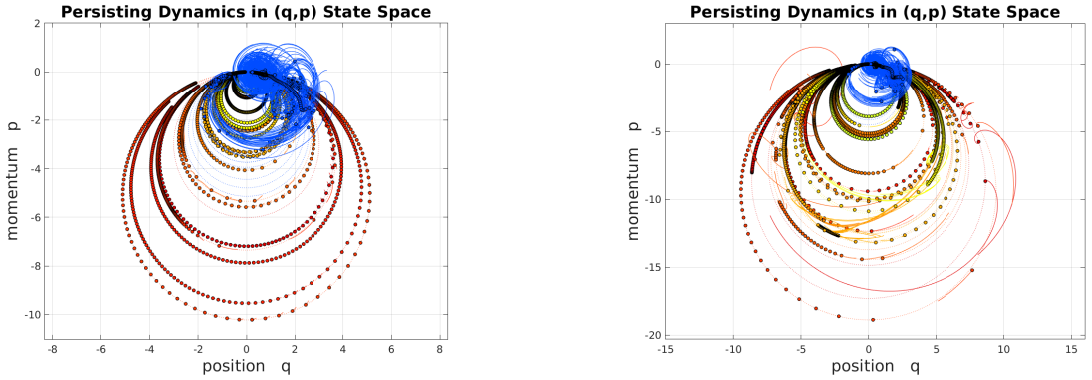

(a) water **(b)** MalL

Figure 5.14: Persisting dynamics of the vibrational mode responses in position–momentum state space after 40% of the simulation time has passed; the traces represent dynamical motion of the vibrational mode that have not quiesced at this time. The large circles are the QHOSS distribution, and the resting states are shown as dots (coloured by vibrational mode frequency).

SS3 mode in this bandwidth (Fig. 5.12). The persisting dynamics for benzene due to the MalL stimulus (Fig. 5.14b) does show a continuation of the relaxation oscillations of modes spanning the low- (red), mid- (green) and high-frequency (blue) modes; their trajectories are also deviated from the QHOSS response, which is verification of anharmonic behaviour along with the SS3 peaks in Fig. 5.11.

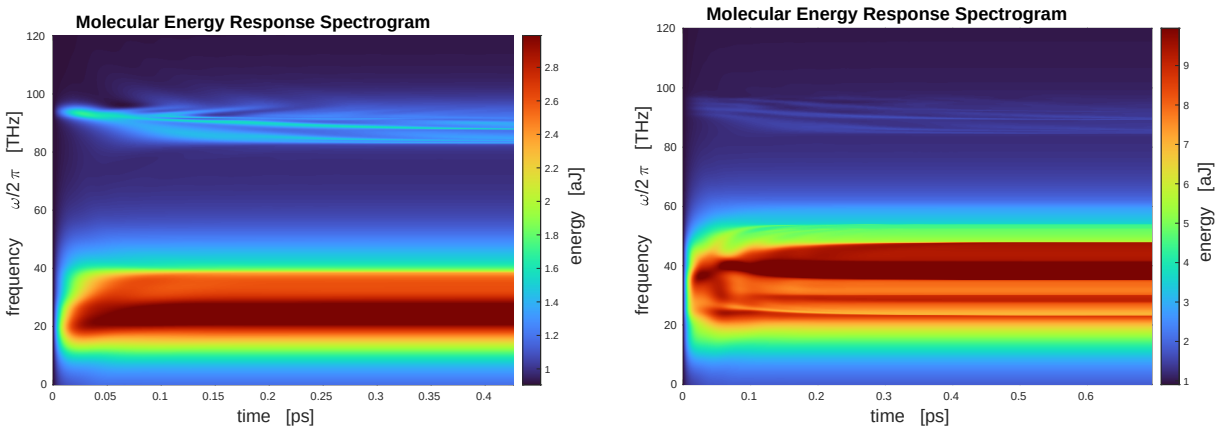

(a) water **(b)** MalL

Figure 5.15: Benzene energy response spectrogram. The thermal equilibrium initial state (at time zero) rises from the minimum value to a resting state due to stimulus from water (a) and MalL (b).

The molecular energy response spectrograms for each simulation are shown in Fig. 5.15 and Fig. 5.16; the resting energy response spectra for benzene in the presence of water and MalL is shown in Fig. 5.13, along with the contributions of each vibrational mode (coloured traces). In the benzene–water simulation, the low-frequency mode responses are merged into a broad peak spanning 10 to 50 THz (333 to 1668 cm^{-1}) with an amplitude of 3.3 aJ (1,987 kJ/mol), 2.4 aJ (1,445 kJ/mol) above thermal equilibrium, which lies in between the libration and bending peaks of the water DoS (Fig. 5.13a). The bandwidth of the glycosidic bond shows a decreasing amplitude for higher frequencies. The low-frequency peak appears to monotonically increase from the initial thermal equilibrium state, whereas the high-frequency modes show a

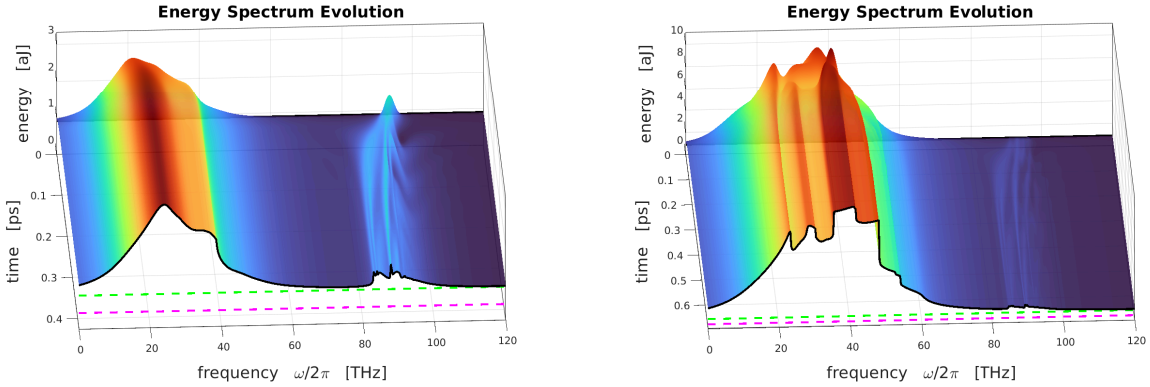

(a) water **(b)** MalL

Figure 5.16: Benzene energy response spectrogram in 3D in comparison to the molecular ZPE (magenta) and thermal equilibrium (green) values.

strong anharmonic behaviour as indicated by the wave instabilities in time, with an amplitude of 1.5 aJ (900 kJ/mol), 0.6 aJ (360 kJ/mol) above thermal equilibrium, that is down-shifted from the oxygen–hydrogen stretching peak of the water DoS. The benzene-MalL simulation (Fig. 5.13b) has a significantly higher peak energy response at 10.7 aJ (6,440 kJ/mol) at 41 THz (1,400 kJ/mol), with a more detailed contour. The high-frequency molecular response of the benzene–MalL simulation has a similar amplitude to the benzene-water simulation (1.50 aJ, 903 kJ/mol) over the same bandwidth (84 to 92 THz, 2,800 to 3,070 cm^{-1}), which implies an lack of specificity of the hydrogen oscillations to stimulus. Of particular interest is the pronounced peak at 28.1 THz (937 cm^{-1}) with an amplitude of 9.10 aJ (5,480 kJ/mol) since it lies within the glycosidic stretch bandwidth. There is a considerable valley on either side of this peak, which hints at selective excitation by MalL.

5.5 Conclusion

In this chapter, I demonstrated the simulation of the QAO EoMs for the response of benzene due to the sudden application of MalL in comparison to a sudden immersion in water. The anharmonic Hamiltonian coefficients were reverse-engineered from the data computed by Gaussian 09 for the simulation of anharmonic spectroscopy. I set the environmental conditions to a biological temperature (34°C), and the initial Lamb shifts were random numbers sampled from a normal distribution. I discussed the selection of the various undetermined parameters for the eVDR and stimulus in lieu of the acquisition of experimental data. I set proxy substrate, benzene, to initially be in a state of thermal equilibrium from which the stimulus (MalL or water) is applied at time zero; the numerical solutions to the QAO EoMs then track the response of the substrate over several hundred femtoseconds while it relaxes into a steady state.

Under the simulation conditions that I have selected for this thesis, the energy response spectra of benzene due to water has a broad peak of 3.3 aJ (1,987 kJ/mol) at frequency 25 THz (834 cm^{-1}); whereas the energy response due to MalL has a more detailed spectra with a pronounced peak of 9.1 aJ (5,480 kJ/mol) at 30 THz (1,000 cm^{-1}), and a maximum of 10.7 aJ (6,440 kJ/mol) at 41 THz (1,400 cm^{-1}). Therefore, the benzene response to MalL exhibits a significant energy peak within the bandwidths associated with glycosidic bond stretching. The

resultant energies of the simulations are larger than the values of typical carbon–oxygen bond energies, implying that it is reasonable that the enzyme does provide larger stimulus that $B_{k,\min}$ for modes pertaining to the glycosidic bond stretch. Therefore, I assert that it is reasonable that there is a phase transition dynamic inherent to the enzyme-catalysed hydrolysis of isomaltose due to MalL, which is not present for isomaltose immersed in water.

Chapter 6

Summary and Future Work

6.1 Summary of New Results

The work performed for this thesis led to the following major achievements:

- A methodology for ascertaining the dominant modes for bond breaking
- A map for the viable anharmonic substrate–enzyme and intramolecular interactions
- The development of the EoMs for a QAO molecule model that experiences dissipation and is stimulated by an enzyme or solvent
- A simplified expression for the QAO enzyme stimulus that is delivered to a substrate
- The derivation for the minimum stimulus required for phase transition behaviour
- The construction of an automated MATLAB package that extracts data and simulates the QAO response of a substrate to an enzyme or solvent
- The comparison of simulations of benzene–water and benzene–MalL complexes demonstrated that MalL supplies a sufficient stimulus to push the bond-stretching modes into a phase transition, which is unlikely to occur in an aqueous environment

6.2 Approximations and their Limitations

In this section, I will itemise the various assumptions made in the model building processes and their limitations to capturing real-world catalytic behaviour. Here I list the set of assumptions and approximations that lead to the enzyme stimulus being treated as a consistent 'phonon laser':

- The interaction Hamiltonian uses the rotating wave approximation which assumes a weak coupling condition such that fast, high-order oscillations quickly average to zero and can be neglected
- Each anharmonic exchange process (absorption, emission, scattering) occur distinctly from each other and are treated separately
- The smeared resonance condition allows for a bandwidth of viable interactions, whose size is taken to be a phenomenological parameter
- The enzyme operators are reduced to classical fields via a semi-classical approximation. This removes the explicit time dependence of the operator, and replace it with a classical field whose complex amplitude evolves according to a harmonic unitary time translation, $\hat{b}_j \mapsto \sqrt{n_j^{\text{enz}}}\, e^{-i\omega_j t}$. This assumption fixes the enzyme phonon number operator to be constant scalar, $\hat{b}_j^\dagger \hat{b}_j \mapsto n_j^{\text{enz}}$

- A corollary of the previous assumptions means that the back-reaction of the substrate phonons into the enzyme are ignored
- The continuum approximation for the distribution of modes is used in order to define the classical field amplitudes (n_j^{enz}) from the DoS
- The DoS is smeared into the summation of Lorentzian resonance distributions, and therefore there are overlaps in the enzyme modes that are able to exchange phonons with molecular mode k
- All modes of the enzyme are taken to be at thermal equilibrium
- The magnitude of the classical field amplitude is taken to be the product of the DoS, smearing frequency and the squareroot of $\bar{n}_k$. Therefore, multiple modes of the enzyme effectively impart a collective influence to the molecule
- The coupling coefficients corresponding to substrate mode k are taken to be equal for all interactions with the enzyme; this is a significant limitation and requires experimentally determined values

These conditions allows for the stimulus superoperator, $\sum_j^{\text{enz}} \Xi_{kj}\hat{b}_j\ \delta(\omega_k - \omega_j)$ to be transformed into $\Xi_{kk}\sqrt{\bar{n}_k}\ (\pi N_{\text{mode}}^{\text{enz}})^{-1} \sum_j^{\text{enz}} \varphi_k^2(\varphi_k^2 + (\omega_k - \omega_j))^{-1}$, which can be computed for each molecular mode by specifying the coupling, smearing, φ_k, and the enzyme modes.

Here I list the approximations and assumptions for the dissipative dynamics of the system (substrate–enzyme system):

- The thermal environment is treated as a continuum of QHOs at thermal equilibrium
- The Markovian approximation for the thermal reservoir eliminates memory effects in the environment, and removes the rapidly evolving free motion of the system
- The QME partitions the system and the thermal environment; a description of the expectation values of a the reduced system is achieved by tracing over reservoir states
- The perturbations of the reduced system due to the environment is expanded only to second-order, and higher-order fluctuations are omitted

Furthermore, the iVDR is taken to be at thermal equilibrium, and does not evolve with the changes in the system phonon number expectation values.

6.3 Future Work

To conclude this thesis, I will describe some of the potential avenues for continuing this work into the future.

6.3.1 Quantum Enzyme–Solvent Interactions

The solvent (for example, the aqueous environment of a living cell) surrounding the enzyme also plays a vital role in catalysis. In many enzyme-catalysed reactions, it is the lysis of small molecules that provides the energy for overcoming the activation energy barrier; in others, energy comes from the thermodynamical fluctuations of the solvent. The fluctuations in the hydration shell surrounding the enzyme are correlated with the internal protein motions, and can be driven by the temperature of the solvent [153]. Thus there is a pathway of energy flow from the solvent,

through the flexible surface loops of the enzyme, throughout the enzyme, to the active site, and into the substrate. A detailed analysis of the hydrogen-bonds vibrational network shows that there are conserved protein residues in species ranging from bacteria to human-scale [8] that facilitate this energy transfer. The rates of the vibrational energy relaxation has been used to probe the behaviour of ligand binding [154, 155], and the structure and dynamics of proteins has been observed to be 'enslaved' with water [156]. In order to capture this behaviour, the catalytic model must be enhanced to treat the enzyme as a dynamical QHO (not a consistent 'phonon laser' as considered in this work) and a QHO interaction of the enzyme and solvent.

6.3.2 Visualisation of the Substrate's Motion Throughout Catalysis

The quantum mechanical model is probabilistic in nature, and therefore the simulation results are not atomic trajectories in the classical sense. However, by taking appropriate approximations, the amplitudes of vibration can be mapped onto the vibrational mode animations of **Chapter 2**, thereby allowing a molecular response to be animated upon superposition of each vibrational mode. The resultant trajectories could be used with conventional MD data to allow for a bridge between the classical and quantum fields of biomolecular study. This data could also be used to produce an attractive multimedia presentation, in a manner similar to the virtual reality framework developed by Glowacki et al [157].

6.3.3 Hearing the Molecule

The energy spectrogram could be mapped into an audio signal, allowing the molecular response to be perceived audibly. One possible approach is using the MATLAB STFT (short-time Fourier transform) magnitude signal reconstruction function, `stftmag2sig`. There is an art form and mastery needed in preparing a good sounding audio from a spectrogram since it is the inverse of the typical mapping of an audio signal to spectrogram via Fourier-related transforms. I believe this would deepen the insight and intuition for the catalytic process by scaling the frequencies and times from quantum molecular (terahertz and picosecond) scale to human hearing (hertz and second) scale.

6.3.4 An Alternative for Smearing the Resonance Condition

The resonance conditions for phonon exchange are described by the Dirac δ-function which requires an exact equality in order for a viable interaction to occur. In this this, I have smeared the δ-function with a Lorentzian resonance distribution (6.1a) since it arises in the steady state analysis of the QHO EoMs, and has been previously applied to proteins [143]. Another option offered by Cupo et al [158] is to use a sinc function, $\mathrm{sinc}(x) = \sin(x)/x$, that has been normalised

$$\delta(x) = \lim_{\varphi_k \to 0} \frac{1}{\pi} \frac{\varphi_k}{\varphi_k^2 + x^2} \tag{6.1a}$$

$$= \lim_{\varphi_k \to 0} \frac{1}{\pi \varphi_k} \mathrm{sinc}\left(\frac{x}{\varphi_k}\right) \tag{6.1b}$$

As can be seen in Fig. 6.1, the Dirac δ is zero-valued everywhere but the point at $x = 0$; the Lorentzian is a symmetric, strictly positive non-oscillatory distribution; however, the sinc

function is oscillatory and has regions that are negative-valued. Cupo et al claim that this represents a state-of-the-art advance in calculating anharmonic phonon properties (frequency shift and lifetime), as well as allowing for a significant reduction in the required simulation time.

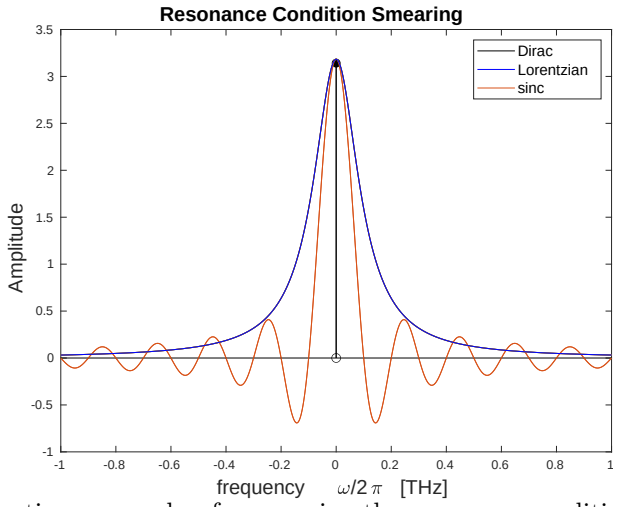

Figure 6.1: Alternative approaches for smearing the resonance conditions. The peak height is π, and the smearing frequency φ_k, is set to 0.1 THz.

6.3.5 Connection with Experiment

Variations of modelling the anharmonic contributions to the dynamics of proteins and enzymes have been probed by experiment. The theory for neutron scattering experiments on anharmonic crystals were performed in the 1960s [71], and more recently neutron scattering experiments have been performed on proteins to determine the changes to their density of states [159]; there are also terahertz spectroscopy experiments with an equivalent aim [160].

There have been recent developments made in the technology for spectroscopy in the range of a few hundreds of gigahertz to several terahertz (10^{11} – 10^{13} Hz), which coincides with the lowest frequency molecular phonons. These techniques have provided insight into many-body quantum kinetics and controlling individual transitions, allowing for experimental probes on the nanostructure of semiconductors [161], the anisotropy of water [162], as well as amino acids [163, 164], and the hydrogen bonding network of proteins [165]. The integration of terahertz spectroscopy at frequencies up to 100 THz with the quantum theory could provide a determination of the vibrational lifetimes required to perform an accurate simulation of catalytic behaviour, and to selectively excite the enzyme vibrational modes associated with catalysis.

A promising direction for experimentally validating the theories presented in this thesis would be via enzyme mutations. Upon further refinement, a prediction can be made for a mutation of the enzyme's active site that would significantly alter the vibrational stimulus, and thus affect the rate of completing a catalytic reaction, which can be tested in a lab setting.

6.3.6 Anharmonic Treatment of the Enzyme

As I have described in **Chapter 4**, the calculation of anharmonic coupling tensor and iVDR are possible if the higher spatial derivatives of the potential are known. Fujisaki et al have obtained a value for the iVDR of one selected carbon–deuterium bond-stretching mode of cytochrome C

into the rest of the protein [144]. To achieve this, they approximated the third-order potential energy coefficient by replacing one of the derivatives with a finite difference

$$\frac{\partial^3 V}{\partial q_k \, \partial q_l \, \partial q_m} \approx \sum_{ij} L_{ik} \, L_{jl} \, \frac{D_{ij}(+\Delta q_k) - D_{ij}(-\Delta q_k)}{2 \, \Delta q_k} \tag{6.2}$$

where they have adopted 'normal mode' coordinates, q_k, D_{ij} is the Christoffel dynamical matrix at eqm, L_{ij} is an element of its eigenvector matrix, and $D_{ij}(\pm\Delta q_k)$ represents that dynamical matrix that has been calculated for a perturbed structure in the direction the k^{th} vibrational mode.

For a quantum anharmonic model of catalysis, the substrate molecule must be able to exchange phonons with an enzyme. Whereas the harmonic model is capable of only a one-for-one exchange, the first-order anharmonics allow for a two–for–one exchange, with higher orders involving more phonons with each exchange. This mechanism allows for a mid-range frequency substrate mode to exchange with a high and a low frequency enzyme mode, or for a high frequency mode to exchange with two lower frequency enzyme modes. Therefore, there is a larger set of viable resonant interactions when accounting for higher-order anharmonics. During the development of quantum anharmonic theory, the molecule was treated anharmonically, and the source of phonons was from the electromagnetic field [79, 166], or from a constant thermal environment [167]. Most material parameters have been obtained by molecular dynamics simulations [99, 168], however the main undetermined parameters required for the computational model are the vibrational dissipation rate and the interaction coupling strength between the substrate–enzyme complex, and the substrate–solvent complex.

6.3.7 Vibrational Dissipation Rate

The specification of the coupling strengths of the molecule–enzyme interactions is extremely important. In many cases of catalytic reactions, the substrate molecule is embedded within the enzyme and does not directly couple to the solvent, so the molecular stimulus is wholly governed by the enzyme.

Essentially, the Christoffel dynamical (mass-weighted hessian) matrix at equilibrium, D_{ij}, is eigendecomposed to obtain the eigenvector matrix (representing atomic polarisations due to each vibrational mode), and then the Christoffel dynamical matrix is computed again for a shifted structure that has been perturbed along the direction of a particular mode for both the positive and negative polarisations. In the study of a CD stretching mode of cytochrome C, Fujisaki, Bu, and Straub smeared out the precise resonance condition (δ-function) in the Maradudin-Fein formula with a Lorentzian curve. They specified the linewidth to be 0.1 THz (3 cm^{-1}), which gave a vibrational lifetime of 0.1 picoseconds (VDR of 1 THz) that is in good agreement with the sub-picosecond time scale for relaxation predicted using the quantum correction method, with lower frequency vibrational modes having a longer lifetime (smaller VER). The Maradudin-Fein formula for dissipation rate is temperature dependent, and at low temperatures the rate becomes flat with a value due to fluctuations associated with zero point energy, and behaves linearly for higher temperature. It is this temperature dependence that is significant in connecting the quantum theory to the MMRT.

The determination of scattering amplitudes (also known as the scattering cross section) is a fundamental quantity of interest in many experiments that aim to probe quantum mechanical behaviour and string theory [169]. In the literature on biological molecules, the concept of vibrational lifetimes is called vibrational energy relaxation [74,75,167], and there exist methodologies to extract these rates [78, 170, 171], and vary from methods used for the computation of the vibrational lifetimes of simple crystals [140, 141]. A useful first approximation for phonon lifetime is the single mode relaxation rate [56], and the Maradudin–Fein formula is a fully quantum description but takes all vibrational modes to be at thermal equilibrium. A better treatment would update the phonon numbers and coupling strength in time. By taking the operator trace to be updated in EoM, $\langle \hat{a}_\alpha^\dagger \hat{a}_\beta \rangle = \langle \hat{n}_\alpha(t) \rangle \ \delta_{\alpha\beta}$, allows for the number operator to be excited above the thermal equilibrium (Planck spectrum), $\langle \hat{n}_\alpha \rangle > \bar{n}_\alpha$. However, this would necessitate that the iVDR is computed for each loop in the EoM numerical solution, which would greatly increase the computational load.

6.3.8 Enzyme Activation and Anharmonic Heat Capacity

A model for the phonon thermodynamics of the enzyme is required in order to bridge the quantum theory presented in this thesis with the MMRT experimental data of enzyme catalytic rates. The activation enthalpy, entropy and heat capacity describe the difference in these quantities for the substrate–enzyme complex and the enzyme-transition state complex. Therefore, a quantum treatment of the enzyme must be simulated, which necessitates that the values for coupling of the enzyme to a solvent are known, as well as the RS and TS QHOSS/QAOSS conformations. These values can perhaps be obtained from computational MD experiments. When taking anharmonics into account, the phonon cannot be assumed to be independent since each mode interacts with all others, and demonstrates a temperature dependence. Therefore, the inclusion of anharmonics introduces additional terms to the description of heat capacity that account for the interactivity of modes across the spectrum.

I consider it likely that there is a phase transition in the enzyme that drives a phase transition in the substrate which results in a spike of energy response in the substrate within the relevant bond stretching bandwidth. The rapid increase in the amplitude of bond stretching vibrations would separate the atoms to such an extent that the interatomic attraction force is weak compared the vibrational energy to the point of cleaving the bond. The evolution of the interatomic distance can be obtained from the QHO/QAO simulations and compared to the bond dissociation curve which would inform the requirement for the attractive forces to become sufficiently diminished.

6.3.9 Substrate Stimulus

The role of anharmonic phonon exchange is crucial in the development of modern semiconductors wherein precise control of individual phonons will allow for novel types of technology, including piezoelectric devices [172, 173], quantum sensors [174], information processing chips [175], and qubits [175]. The strong coupling of nanomechanical oscillators [176] with optical resonant cavities may pave the way for circuits designed with quantum electrodynamics [177]. Recently, a single-phonon ‘microphone’ has been developed for experimentally probing the interaction of

optical phonons with laser [175]. The developments of quantum theory and experimental techniques made for exploring potential technological applications will provide a rich body of work that will help to inform research into biological processes on the quantum scale. The manipulation of enzyme catalysed reactions by lasers is also possible for light-driven enzymes, such as protochlorophyllide reductase which participates in the biosynthetic pathway to chlorophyll in plant cells [178]. A new phonon-based experimental technology involving plasmonic gold nanoparticles coupled to the optical "whispering gallery" modes of a single molecule has been used to perform a study on the temperature dependence of enzyme kinetics, which has validated the notion that MMRT captures the differences in dynamics between states [179].

6.3.10 Controlling Phase Transition

In *'Quantum Phononics'*, Nakamura [58] describes several experiments on the coherent control of optical phonons in crystals such as mode-selective excitation and phase transition control. I will summarise the results here to highlight some of the modern advances in phononics, which could be applied to the study of enzyme catalysis.

The properties of coherent phonons in crystals can be experimentally determined by an initial irradiation of an ultrashort optical pulse, then a measurement is made of its transient optical transmission or reflection via a pump-probe. Recently, coherent phonon oscillations have been detected via X-ray diffraction techniques. Yttrium barium copper oxide is a typical high-temperature superconductor which has two optical phonon modes at harmonic normal mode frequencies 3.4 and 4.3 THz, that have been selectively excited by ultrashort double-pulse excitation of a separation time of above 100 femtoseconds [180]. Optical control of the longitudinal and transverse atomic motions in a single crystal crystal of bismuth has been demonstrated by a pair of chirped femtosecond pulses to excite optical modes of 2 and 3 THz [181]. The longitudinal optical phonons (8.7 THz) as well as the longitudinal optical phonon-plasmon coupled mode oscillations (7.7 THz) in gallium arsenide have been harmonically modulated by pump-probe delay; in addition to the control of the phonon amplitude, the VDR (lifetime) of the phonon-plasmon coupling mode was coherently controlled by adjusting the pump-pulse delay, whereas the optical phonon VDR was unaffected [182].

The coherent control of a phase transition has also been achieved [183]. The chalcogenide, $Ge_2Sb_2Te_5$, has an optically induced phase transition between amorphous and crystalline states. An octahedral $GeTe_6$ phonon mode (3.6 THz) that is only present in the crystalline state has been selectively excited by two pump pulses with a 276 femtosecond delay, which matches the oscillation period of the mode. These pulses coherently controlled the phase transition of the lattice towards the crystalline state.

Appendix A

Quantum Master Equation: The Generator of the Quantum State Equations of Motion

In this appendix, I will describe the derivation for the free and dissipative contributions to the Quantum Master Equation (QME), which is the generator for the equations of motion for the molecular vibrational mode quantum state in **Chapters 3 & 4**. I follow the derivation in [53] for the density operator formalism of quantum damping that Louisell applies to a QHO model of a single atom in a radiation field (QHO reservoir at thermal equilibrium) under the Markoff approximation, which has applications in the study of lasers and quantum optics. Based upon Prof. Moira Steyn-Ross' preliminary work before this thesis, I demonstrate an extension to this method for the vibrational modes of a molecule, and make the replacement of the thermal reservoir with a 'phonon' field. I then recast the QME into an expression that facilitates the evaluation of the harmonic and anharmonic equations of motion.

A.1 Quantum State Density Operator

The physical state of a system in quantum mechanics is represented by state vectors of a Hilbert space, and these quantum state vectors can be represented independently of a coordinate representation via the Dirac bra-ket notation [60, 63]. A ket vector $|\psi\rangle$ is a coordinate-free generalisation of a column vector to accommodate countably infinitely many elements (possible states); thus quantum mechanics uses an extension of linear matrix algebra to accommodate countably infinite vector spaces. The Hermitian conjugate (dagger) transpose returns a row vector analogue called a bra, $\langle\psi| = |\psi\rangle^\dagger$. If $|\psi\rangle$ were to be known exactly, then the probability amplitudes of every quantum state, ψ, of a physical system would be known.

The inner product is computed by the bra-ket product, $\langle\psi|\psi\rangle$, which is a scalar-valued quantity representing the norm or probability amplitude of the system being in state ψ (which is typically normalised to equal unity for pure states); two state vectors are orthogonal if $\langle\phi|\psi\rangle = 0$. Furthermore, the mean or expectation value of an arbitrary operator, $\hat{A}$, is given by, $\langle\hat{A}\rangle = \langle\psi|\hat{A}|\psi\rangle$. The outer product is the ket-bra product, $|\psi\rangle\langle\psi|$, which produces a square matrix (rank-2 tensor). The elements of the outer product matrix represent the probability amplitude for all the possible state combinations available to the quantum system, and is called

the density operator

$$\hat{\rho} \;=\; |\psi\rangle\langle\psi| \tag{A.1}$$

If the time evolution of $\hat{\rho}$ were to be known, then the quantum state of a system for all time would be known; therefore, the EoM for a quantum state is given by (A.1). The time evolution of a pure state ket, $|\psi(t)\rangle$, is given by the Schrödinger equation

$$i\hbar\,\partial_t|\psi\rangle \;=\; \hat{\mathcal{H}}\,|\psi\rangle \tag{A.2}$$

and the evolution of the bra is its conjugate transpose, $-i\hbar\,\partial_t\langle\psi| = \langle\psi|\,\hat{\mathcal{H}}$, since the Hamiltonian is Hermition, $\hat{\mathcal{H}}^\dagger = \hat{\mathcal{H}}$. The equation of motion of the density operator is obtained by taking the temporal derivative of (A.1) then using the chain rule and (A.2)

$$\partial_t\hat{\rho} \;=\; \frac{1}{i\hbar}\,\hat{\mathcal{H}}\,|\psi\rangle\langle\psi| \;-\; \frac{1}{i\hbar}\,|\psi\rangle\langle\psi|\,\hat{\mathcal{H}} \tag{A.3}$$

upon using the definition commutation bracket and $\hat{\rho}$, the von Neumann equation is obtained

$$\partial_t\hat{\rho} \;=\; \frac{1}{i\hbar}\,\Big[\hat{\mathcal{H}}\;,\;\hat{\rho}\Big] \tag{A.4}$$

which states that the density operator evolves according the commutation of itself with the system's Hamiltonian; if $\hat{\mathcal{H}}$ and $\hat{\rho}$ are dynamically distinct, or $\hat{\mathcal{H}}$ is a constant, then the state is static, $\partial_t\hat{\rho} = 0$.

A.2 Time Evolution of Quantum State Expectation Values

The density operator, $\hat{\rho}$, for a molecule immersed in an environment contains all of the quantum states pertaining to the molecule, environment, and their interactions. As it is the evolution and statistical properties of the molecule that is of the most interest, and so a partition is invoked onto $\hat{\rho}$ by assuming that both systems are independent.

For pure states, the expectation value of an observable, $\langle\hat{A}\rangle$, is given by the definition in the previous section, whereas for mixed states (for example, the vibrational modes of a molecule), the density operator is the summation of the outer products of pure states, $|\psi_k\rangle$, each with probability p_k, formally $\hat{\rho} \;=\; \sum_k p_k|\psi_k\rangle\langle\psi_k|$. The expectation value of $\hat{A}$ for mixed states is, $\langle\hat{A}\rangle \;=\; \sum_k p_k\langle\psi_k|\hat{A}|\psi_k\rangle$, which upon algebraic manipulation can be expressed in terms of the trace, $\langle\hat{A}\rangle \;=\; \mathrm{Tr}[\hat{A}\,\hat{\rho}]$, where the partial trace is a generalisation of the trace from linear algebra (sum of diagonal elements) to account for infinite vector spaces and operators.

For the molecule model under investigation in this thesis, the quantum state is the superposition of the molecule and environmental states; however, it is the evolution of the molecule that is of the most interest. Let the partial trace of the density operator over molecular (M) and environmental (E) states be set to unity, $\mathrm{Tr}_{M,E}[\hat{\rho}] = 1$, and let $\hat{\mathcal{M}}$ be a time-dependent operator (observable) that acts only on the molecule. The expectation value of the observable, $\langle\hat{\mathcal{M}}\rangle$, is given by the total trace over M, E which can be decomposed as

$$\langle\hat{\mathcal{M}}(t)\rangle \;=\; \mathrm{Tr}_{M,E}[\,\hat{\mathcal{M}}(t)\;\hat{\rho}(t)\,] \;=\; \mathrm{Tr}_M\Big[\,\hat{\mathcal{M}}(t)\;\;\mathrm{Tr}_E[\,\hat{\rho}(t)\,]\Big] \tag{A.5}$$

The trace of the full density of states, $\hat{\rho}$, over environmental states, E, defines a reduced density operator, $\hat{S}$, from which the expectation value of $\hat{M}$ is,

$$\langle \hat{\mathcal{M}} \rangle \;=\; \mathrm{Tr}_M[\hat{\mathcal{M}}\,\hat{S}] \tag{A.6}$$

The formalism (A.6) means that it is not necessary to have full knowledge of the full density operator for all time. By taking $\hat{\mathcal{H}}$ to be independent of time, then the wavestate at a later time, $t > t_0$ is given by the solution to the first-order ODE Shrödinger equation (A.2)

$$|\psi(t)\rangle \;=\; \exp\left(\frac{1}{i\hbar}\,\hat{\mathcal{H}}\;(t\;-\;t_0)\right)\;|\psi(t_0)\rangle \;=\; \hat{U}(t,t_0)\;|\psi(t_0)\rangle \tag{A.7}$$

where $\hat{U}(t,t_0) \equiv \exp\left(\frac{1}{i\hbar}\,\hat{\mathcal{H}}\;(t\;-\;t_0)\right)$ is the unitary time translation operator. Thus, the density operator, $\hat{\rho}$ can be evolved from an initial state $\hat{\rho}(t_0) = |\psi(t_0)\rangle\langle\psi(t_0)|$ by $\hat{U}$ in the form

$$\hat{\rho}(t) \;=\; \hat{U}(t,t_0)\;\hat{\rho}(t_0)\;\hat{U}^{\dagger}(t,t_0) \tag{A.8}$$

The reduced system density operator can then be evolved in time by the application $\hat{U}\hat{S}\hat{U}^{\dagger}$; this is called the transformation from the time-independent Schrödinger picture into the time-dependent Heisenberg (interaction) picture of quantum mechanics. The time evolution of the expectation value for the molecule observable is then given by

$$\partial_t \langle \hat{\mathcal{M}}(t) \rangle \;=\; \mathrm{Tr}_M\;\left[\hat{\mathcal{M}}\;\partial_t \hat{S}\right] \tag{A.9}$$

The time evolution of $\hat{S}$ is approximated by a perturbative theory

$$\partial_t \hat{S} \;\approx\; \frac{1}{i\hbar}\;\left[\hat{\mathcal{H}}\;,\;\hat{S}\right] \;+\; \frac{\Delta \hat{S}}{\Delta t} \tag{A.10}$$

whose terms, respectively, are the free motion due to the Hamiltonian and a finite difference approximation for the interactions.

A.2.1 Free Contribution

The free behaviour of the quantum state of the non-interacting molecule can be elucidated by the Hamiltonian of the molecule, $\hat{\mathcal{H}}_{\mathrm{mol}}$, which is explicitly independent of time and a function only of M states. The free equation of motion is found by substitution of (A.10) into (A.9), with $\hat{\mathcal{H}}_{\mathrm{mol}}$ and $\Delta \hat{S} = 0$

$$\partial_t \langle \hat{\mathcal{M}}(t) \rangle_{\mathrm{free}} \;=\; \mathrm{Tr}_M\left(\mathcal{M}\;\frac{1}{i\hbar}\;\left[\hat{\mathcal{H}}_{\mathrm{mol}}\;,\;\hat{S}\right] \;+\; 0\right) \tag{A.11a}$$

$$\;=\; \frac{1}{i\hbar}\;\mathrm{Tr}_M\left(\mathcal{M}\;\hat{\mathcal{H}}_{\mathrm{mol}}\;\hat{S} \;-\; \mathcal{M}\;\hat{S}\;\hat{\mathcal{H}}_{\mathrm{mol}}\right) \tag{A.11b}$$

by making use of the cyclic property of the trace for invariance under permutation, $\mathrm{Tr}[abc] = \mathrm{Tr}[bca] = \mathrm{Tr}[cab]$, to move $\hat{S}$ to the right and using (A.6), the free QME is

$$\partial_t \langle \hat{\mathcal{M}}(t) \rangle_{\mathrm{free}} \;=\; \frac{1}{i\hbar} \left\langle \left[\hat{\mathcal{M}} \;,\; \hat{\mathcal{H}}_{\mathrm{mol}} \right] \right\rangle \tag{A.12}$$

which crucially has the commuting operators in a different order than (A.4) due to taking the expectation value. I use the free QME (A.12) in **Chapters 3 & 4** to derive the free behaviour of the molecular vibrational modes.

A.2.2 Dissipative Contribution

The total Hamiltonian for a molecule in an environment (solvent or enzyme) can be partitioned as $\hat{\mathcal{H}} = \hat{\mathcal{H}}_{\mathrm{mol}} + \hat{\mathcal{H}}_{\mathrm{env}} + \hat{\mathcal{H}}_{\mathrm{int}}$. The states of the molecule and environment Hamiltoinians are different, and therefore commute, $[\hat{\mathcal{H}}_{\mathrm{mol}},\, \hat{\mathcal{H}}_{\mathrm{env}}] = 0$; whereas the interaction Hamiltonian contains states from both and hence are dynamically interrelated (non-commutative). Therefore, the total QME is partitioned as

$$\partial_t \langle \hat{\mathcal{M}}(t) \rangle \;=\; \partial_t \langle \hat{\mathcal{M}}(t) \rangle_{\mathrm{free}} \;+\; \partial_t \langle \hat{\mathcal{M}}(t) \rangle_{\mathrm{stim}} \;+\; \partial_t \langle \hat{\mathcal{M}}(t) \rangle_{\mathrm{diss}} \tag{A.13}$$

whose contributions are the free behaviour (M states) (A.12), and additional terms due to $\hat{\mathcal{H}}_{\mathrm{int}}$ (both M and E states) given by (A.10): a stimulated response given by first term,

$$\partial_t \langle \hat{\mathcal{M}}(t) \rangle_{\mathrm{stim}} \;=\; \frac{1}{i\hbar} \Big\langle \big[\hat{\mathcal{M}}, \hat{\mathcal{H}}_{\mathrm{int}} \big] \Big\rangle \tag{A.14}$$

and a perturbation given by the second term, which is more significantly more involved to determine. Let $\hat{s}$ be the reduced density operator in the interaction picture, then its von Neumann equation can be solved by iterative integration by making use of the following property for an arbitrary unitary translation operator. Let $\exp(-i\alpha\hat{G})$ be a unitary translation operator with a real parameter, α, and the Hermition operator $\hat{G}$ is the generator of the transformation, then an arbitary operator, $\hat{A}$, is transformed according to

$$e^{-i\alpha\hat{G}} \hat{A} e^{-i\alpha\hat{G}} \;=\; \hat{A} + (i\alpha)\,[\hat{G},\, \hat{A}] + \frac{1}{2!}\,(i\alpha)^2\,[\hat{G},\, [\hat{G},\, \hat{A}]] + \frac{1}{3!}\,(i\alpha)^3\,[\hat{G},\, [\hat{G},\, [\hat{G},\, \hat{A}]]] + \cdots \tag{A.15}$$

For the transformation into the Heisenberg picture, the interaction Hamiltonian is the generator and the parameter is $\hbar^{-1}(t - t_0)$. After further manipulation, the generalised perturbation of the interactions up to N^{th} order between the molecule and environment is given by a series of multiple time integrals acting on nested commutations,

$$\hat{s}(t) \;=\; \hat{s}(t_0) \;+\; \sum_{n=1}^{N} \left(\frac{1}{i\hbar} \right)^n \;\int_{t_0}^{t} dt_1 \;\cdots\; \int_{t_0}^{t_{n-1}} dt_n \left[\hat{\mathcal{H}}_{\mathrm{int}}(t_1 - t_0) \;,\; \Big[\cdots \Big[\hat{\mathcal{H}}_{\mathrm{int}}(t_n - t_0) \;,\; \hat{s}(t_0) \Big] \Big] \right] \tag{A.16}$$

By iterating up to second-order, and performing the trace over environmental states, the interaction perturbation $\Delta\hat{S} = \hat{S}(t) - \hat{S}(t_0)$ becomes

$$\Delta\hat{S}(t) = \left(\frac{1}{i\hbar}\right) \int_{t_0}^{t} dt_1 \; \mathrm{Tr}_E \left\{ \left[\hat{\mathcal{H}}_{\mathrm{int}}(t_1 - t_0) \; , \; \hat{s}(t_0) \right] \right\} \tag{A.17a}$$

$$+ \left(\frac{1}{i\hbar}\right)^2 \int_{t_0}^{t} dt_1 \int_{t_0}^{t_1} dt_2 \; \mathrm{Tr}_E \left\{ \left[\hat{\mathcal{H}}_{\mathrm{int}}(t_1 - t_0) \; , \; \left[\hat{\mathcal{H}}_{\mathrm{int}}(t_n - t_0) \; , \; \hat{s}(t_0) \right] \right] \right\} \tag{A.17b}$$

The derivation progresses by transforming the interaction Hamiltonian (3.31b) into the interaction picture by use of $\hat{U}$, using the commutative property of the molecule and environment operators.

A.2.3 Markoff Approximation — An Environment with Amnesia

The integrals in (A.17) can be solved upon taking the Markoff approximation. A Markoffian system is one in which its future is determined by the present moment, and retains no memory of its past. Physically, $\Delta\hat{S}(t)$ represents the change in the reduced density operator during the time interval $[t, t_0]$, and the Markoff approximation is applied in order to remove the rapidly varying free motion of the molecule. This condition is sufficient to ensure that the energy which goes into the environment does not return to the molecule; if this condition is not true then *memory* effects will arise. Eventually, (A.17) can be expressed as

$$\Delta\hat{S}(t) = -i \sum_i \left[\hat{Q}_i \; , \; \hat{S}_0 \right] \left\langle \hat{F}_i \right\rangle_R \; I(\omega_i) \tag{A.18a}$$

$$- \sum_{ij} \left(w_{ij}^{+} \left[\hat{Q}_i \; , \; \hat{Q}_j \; \hat{S}_0 \right] - w_{ji}^{-} \left[\hat{Q}_i \; , \; \hat{S}_0 \; \hat{Q}_j \right] \right) I(\omega_i + \omega_j) \tag{A.18b}$$

For the molecular vibrational modes, the summation is over $i, j \in \{1, 2\}$ with the molecule operators defined, $\hat{Q}_1 = \hat{a}_k^{\dagger} = \hat{Q}_2^{\dagger}$ with the associated environment force (with dimensions of $[\text{time}]^{-1}$) is, $\hat{F}_1 = \hat{F}_2^{\dagger}$, which is a function of the environmental operators (E states only). In **Chapter 3**, the force is treated harmonically by a summation of linear operators; in **Chapter 4**, the force is treated anharmonically by taking the summation over operator products.

The $I(\Omega)$ term is a temporal integral of a complex phasor of frequency Ω. By requiring that the period of integration is much larger than the period of oscillation, then they can be replaced by the time-difference and a frequency matching condition, $I(\Omega) = (t - t_0)\, \delta(\Omega)$; if none of the operators evolve with a zero-frequency component, then $I(\omega_i) = 0$, from makes the first-order perturbation in (A.18) vanish. For molecular vibrational modes, this process effectively reduces the set of eigenmodes to the set of normal modes. The quantum environmental forces embedded in (A.18) are in the form of correlation functions $\langle \hat{F}_i(\tau) \hat{F}_k \rangle$ and $\langle \hat{F}_j \hat{F}_i(\tau) \rangle$, with a correlation

time, τ, and are given by spectral density integrals $w_{ij}^{\pm}$, defined by

$$w_{ij}^{+} \equiv \int_0^{\infty} d\tau \; e^{i\omega_i \tau} \langle \hat{F}_i(\tau) \hat{F}_j \rangle \tag{A.19a}$$

$$w_{ij}^{-} \equiv \int_0^{\infty} d\tau \; e^{i\omega_j \tau} \langle \hat{F}_i \hat{F}_j(\tau) \rangle \tag{A.19b}$$

$$w_{ji}^{+} \equiv \int_0^{\infty} d\tau \; e^{i\omega_j \tau} \langle \hat{F}_j(\tau) \hat{F}_i \rangle \tag{A.19c}$$

$$w_{ji}^{-} \equiv \int_0^{\infty} d\tau \; e^{i\omega_i \tau} \langle \hat{F}_j \hat{F}_i(\tau) \rangle \tag{A.19d}$$

with the $\pm$ affecting which environmental force $\hat{F}$ is taken to be variable with τ, and ω_i is the oscillation frequency of $\hat{F}_i$, The frequency matching term is satisfied if, $\omega_i = -\omega_j$, and therefore omits the $i = j$ terms for non-zero frequency. Thus, the dissipative potion of the QME can be approximated by the expression

$$\partial_t \langle \hat{\mathcal{M}}(t) \rangle_{\text{diss}} \approx - \sum_{i,j} \delta(\omega_i + \omega_j) \Big\langle \Big[\hat{\mathcal{M}}, \hat{Q}_i \Big] \hat{Q}_j \; w_{ij}^{+} - \hat{Q}_j \Big[\hat{\mathcal{M}}, \hat{Q}_i \Big] \; w_{ji}^{-} \Big\rangle \tag{A.20}$$

which is generalised for any quantum system, subject to the series of approximations made during the derivation.

A.2.4 Dissipation Superoperator and Lamb Shift

I will now specify (A.20) to be for molecular phonons by setting $\hat{Q}_1 = \hat{a}_k^{\dagger} = \hat{Q}_2^{\dagger}$, where $\hat{a}_k^{\dagger}$ is the creation operator that acts on vibrational mode k. The real and imaginary components of the SDI can be separated on the *an satz* that $w_{ij}^{+} = (w_{ij}^{-})^*$, and so I make the definition $w_{ij}^{\pm} = \Re[w_{ij}] \pm i\,\Im[w_{ij}]$. This relation is established for both the QHO (**Chapter 3**) and QAO (**Chapter 4**) formalisms. Therefore, the dissipative QME for a molecular vibrational mode is given approximately by

$$\begin{aligned} \partial_t \langle \hat{\mathcal{M}}(t) \rangle_{\text{diss}} \approx - \delta(\omega_1 + \omega_2) \Big\langle & \quad \Re[w_{12}] \Big(\Big[\hat{\mathcal{M}}, \hat{a}_k^{\dagger} \Big] \hat{a}_k - \hat{a}_k^{\dagger} \Big[\hat{\mathcal{M}}, \hat{a}_k \Big] \Big) \\ & + \Re[w_{21}] \Big(\Big[\hat{\mathcal{M}}, \hat{a}_k \Big] \hat{a}_k^{\dagger} - \hat{a}_k \Big[\hat{\mathcal{M}}, \hat{a}_k^{\dagger} \Big] \Big) \\ & + i\,\Im[w_{12}] \Big(\Big[\hat{\mathcal{M}}, \hat{a}_k^{\dagger} \Big] \hat{a}_k + \hat{a}_k^{\dagger} \Big[\hat{\mathcal{M}}, \hat{a}_k \Big] \Big) \\ & + i\,\Im[w_{21}] \Big(\Big[\hat{\mathcal{M}}, \hat{a}_k \Big] \hat{a}_k^{\dagger} + \hat{a}_k \Big[\hat{\mathcal{M}}, \hat{a}_k^{\dagger} \Big] \Big) \Big\rangle \end{aligned} \tag{A.21}$$

which upon expanding the commutation brackets and regrouping

$$\begin{aligned}\partial_t\langle\hat{\mathcal{M}}(t)\rangle_{\text{diss}} \;\approx\; -\,\delta(\omega_1+\omega_2)\Big\langle \;& \Re[w_{12}]\Big(\Big\{\hat{\mathcal{M}},\,\hat{a}_k^\dagger\hat{a}_k\Big\}_+ \;-\; 2\,\hat{a}_k^\dagger\hat{\mathcal{M}}\hat{a}_k\Big)\\ &+\; \Re[w_{21}]\Big(\Big\{\hat{\mathcal{M}},\,\hat{a}_k\hat{a}_k^\dagger\Big\}_+ \;-\; 2\,\hat{a}_k\hat{\mathcal{M}}\hat{a}_k^\dagger\Big)\\ &+\; i\,\Im[w_{12}]\,\Big[\hat{\mathcal{M}},\,\hat{a}_k^\dagger\hat{a}_k\Big] \;+\; i\,\Im[w_{21}]\,\Big[\hat{\mathcal{M}},\,\hat{a}_k\hat{a}_k^\dagger\Big]\Big\rangle\end{aligned} \tag{A.22}$$

where $\{a,b\}_+ \equiv ab+ba$, is the Poisson anti-commutation bracket. By using the creation and annihilation grand canonical commutation relation, $\hat{a}_k\hat{a}_k^\dagger = \hat{a}^\dagger\hat{a}_k + 1$, the imaginary terms combine as

$$\Im\Big[\partial_t\langle\hat{\mathcal{M}}(t)\rangle_{\text{diss}}\Big] \;=\; -\,i\;\delta(\omega_1\;+\;\omega_2)\;\Im[w_{12}\;+\;w_{21}]\;\Big\langle\Big[\hat{\mathcal{M}}\;,\;\hat{n}_k\Big]\Big\rangle \tag{A.23}$$

which is an equivalent expression to the free QHO EoM (**Chapter 3**). The physical interpretation of $\delta(\omega_1\;+\;\omega_2)\;\Im[w_{12}\;+\;w_{21}]$ for a molecule is a slight perturbation, called the Lamb shift, to the oscillation frequency of the vibrational modes due to interactions with the environment.

The real component leads to the Lindbladian dissipation superoperator, which was discovered by Lindblad's pioneeering work on dissipative quantum systems [184]. In the modern QME formalisms [54], the Lindbladian dissipation superoperator, $\hat{L}$, for a system density operator $\hat{\rho}$ with jump operator $\hat{A}$ is defined as

$$\hat{L}[\hat{A}](\hat{\rho}) \;\equiv\; \hat{A}\hat{\rho}\hat{A}^\dagger \;-\; \frac{1}{2}\Big\{\hat{A}^\dagger\hat{A}\;,\;\hat{\rho}\Big\}_+ \tag{A.24}$$

I transform this expression for an arbitrary system operator $\hat{\mathcal{M}}$ in the current context by multiplying by $\hat{\mathcal{M}}$ from the left and taking the trace over molecular and environmental states M, E, which gives an expression in terms of the reduced density operator, $\text{Tr}_M\Big\{\hat{\mathcal{M}}\,\hat{L}[\hat{A}](\hat{S})\Big\}$. By using the cyclic property of the trace, I define the dissipation superoperator $\hat{\mathcal{D}}$ for an arbitrary reduced system density operator, $\hat{\mathcal{M}}$, as

$$\hat{\mathcal{D}}[\hat{A}](\hat{\mathcal{M}}) \;\equiv\; \hat{A}^\dagger\hat{\mathcal{M}}\hat{A} \;-\; \frac{1}{2}\Big\{\hat{\mathcal{M}}\;,\;\hat{A}^\dagger\hat{A}\Big\}_+ \tag{A.25}$$

Noting that the order of the anticommuntation bracket does not matter since $\{a,b\}_+ \;=\; \{b,a\}_+$. The modified dissipation superoperator (A.25) differs from the Lindbladian (A.24) by the argument $\hat{S}$ with $\hat{\mathcal{M}}$ and in the ordering of the jump operators, $\hat{A}, \hat{A}^\dagger$, in the first term. The expression for, $\hat{\mathcal{D}}$, is the same can be equivalently expressed as

$$\hat{\mathcal{D}}[\hat{A}](\hat{M}) \;=\; -\,\frac{1}{2}\;\Big(\big[\hat{M},\,\hat{A}^\dagger\big]\;\hat{A} \;-\; \hat{A}^\dagger\;\big[\hat{M},\,\hat{A}\big]\Big) \tag{A.26a}$$

$$\;=\; \hat{A}^\dagger\;\hat{M}\;\hat{A} \;-\; \frac{1}{2}\;\{\hat{M},\,\hat{A}^\dagger\hat{A}\}_+ \tag{A.26b}$$

where $\hat{A}$ is the annihilation or creation operator, and $\{a,b\}_+ = ab + ba$, is the Poisson anti-commutation bracket. The simplest expression for evaluation is obtained by replacing the commutation brackets with operator differentials by the relation

$$\left[f(\hat{a},\hat{a}^\dagger)\ ,\ \hat{a}\ \right] \ = \ -\frac{\partial f}{\partial \hat{a}^\dagger} \tag{A.27a}$$

$$\left[f(\hat{a},\hat{a}^\dagger)\ ,\ \hat{a}^\dagger\right] \ = \ +\frac{\partial f}{\partial \hat{a}} \tag{A.27b}$$

Thus, the dissipation superoperators of the observable, $\hat{\mathcal{M}}$, for the creation and annihilation operators can be expressed in terms of operator derivatives

$$\hat{\mathcal{D}}[\hat{a}\ ](\hat{\mathcal{M}}) \ = \ -\frac{1}{2}\ \left(\left(\frac{\partial \hat{\mathcal{M}}}{\partial \hat{a}} \right) \hat{a} \ + \ \hat{a}^\dagger \left(\frac{\partial \hat{\mathcal{M}}}{\partial \hat{a}^\dagger} \right) \right) \tag{A.28a}$$

$$\hat{\mathcal{D}}[\hat{a}^\dagger](\hat{\mathcal{M}}) \ = \ +\frac{1}{2}\ \left(\left(\frac{\partial \hat{\mathcal{M}}}{\partial \hat{a}^\dagger} \right) \hat{a}^\dagger \ + \ \hat{a} \left(\frac{\partial \hat{\mathcal{M}}}{\partial \hat{a}} \right) \right) \tag{A.28b}$$

The solution structures for $\hat{\mathcal{D}}$ for each quantum state observable, $\hat{\mathcal{M}} \in \{\hat{a}_k,\ \hat{a}_k^\dagger,\ \hat{n}_k\}$ are

$$\hat{\mathcal{D}}[\hat{a}\ ](\hat{a}\ ) \ = \ -\frac{1}{2}\ \hat{a} \tag{A.29a}$$

$$\hat{\mathcal{D}}[\hat{a}\ ](\hat{a}^\dagger) \ = \ -\frac{1}{2}\ \hat{a}^\dagger \tag{A.29b}$$

$$\hat{\mathcal{D}}[\hat{a}\ ](\hat{n}\ ) \ = \ -\hat{n} \tag{A.29c}$$

$$\hat{\mathcal{D}}[\hat{a}^\dagger](\hat{a}\ ) \ = \ +\frac{1}{2}\ \hat{a} \tag{A.29d}$$

$$\hat{\mathcal{D}}[\hat{a}^\dagger](\hat{a}^\dagger) \ = \ +\frac{1}{2}\ \hat{a}^\dagger \tag{A.29e}$$

$$\hat{\mathcal{D}}[\hat{a}^\dagger](\hat{n}\ ) \ = \ \hat{n} \ + \ 1 \tag{A.29f}$$

A.2.5 Dissipative Quantum Master Equation

Finally, an approximate expression for the dissipative portion of the QME is obtained

$$\partial_t \langle \hat{\mathcal{M}} \rangle_{\text{diss}} \ \approx \ \Gamma_{\hat{a}_k} \left\langle \hat{\mathcal{D}}[\hat{a}_k](\hat{\mathcal{M}}) \right\rangle \ + \ \Gamma_{\hat{a}_k^\dagger} \left\langle \hat{\mathcal{D}}[\hat{a}_k^\dagger](\hat{\mathcal{M}}) \right\rangle \ - \ i\,\varphi_k \left\langle \left[\hat{\mathcal{M}}\ ,\ \hat{n}_k \right] \right\rangle \tag{A.30}$$

The real components encapsulate the dissipative behaviour, where the rate of dissipation of the annihilation operator is $\Gamma_{\hat{a}_k} \ = \ 2\ \Re[w_{12}]\ \delta(\omega_1 + \omega_2)$, the VDR of the creation operator has the equivalent expression with w_{21}. The imaginary component is the Lamb shift, $\varphi_k \ = \ \Im[w_{12} \ + \ w_{21}]\ \delta(\omega_1 \ + \ \omega_2)$, whose exact expression is complicated, and therefore I treat it as a phenomenological parameter to smear the resonant frequency (energy conservation) condition in the interaction Hamiltonians [128].

A.3 Total Quantum Master Equation

The total QME for vibrational mode k of an arbitrary molecule is

$$\partial_t \langle \hat{\mathcal{M}} \rangle \approx \frac{1}{i\hbar} \left\langle \left[\hat{\mathcal{M}} \, , \, \hat{\mathcal{H}}_{\text{mol}} + \hat{\mathcal{H}}_{\text{int}} \right] \right\rangle + \Gamma_{\hat{a}_k} \left\langle \hat{\mathcal{D}}[\hat{a}_k](\hat{\mathcal{M}}) \right\rangle + \Gamma_{\hat{a}_k^\dagger} \left\langle \hat{\mathcal{D}}[\hat{a}_k^\dagger](\hat{\mathcal{M}}) \right\rangle - i \, \varphi_k \left\langle \left[\hat{\mathcal{M}} \, , \, \hat{n}_k \right] \right\rangle \tag{A.31}$$

whose terms, respectively, are the free molecule behaviour ($\hat{\mathcal{H}}_{\text{mol}}$), stimulus ($\hat{\mathcal{H}}_{\text{int}}$), dissipation, and oscillation frequency (Lamb) shift. It is this equation that I use to the derive the QHO (**Chapter 3**) and QAO (**Chapter 4**) model EoMs.

Appendix B

Non-Dimensionalised, One-Parameter Quantum Anharmonic Model

In this appendix, I will map the QAO catalytic model equations into expressions that are Non-Dimensionalised with One Parameter (ND1P). The resultant ND1P model equations are mathematically simpler and can be simulated numerically without molecular dynamics data, thus providing an abstraction and insight into the fundamental behaviour of the QAO model.

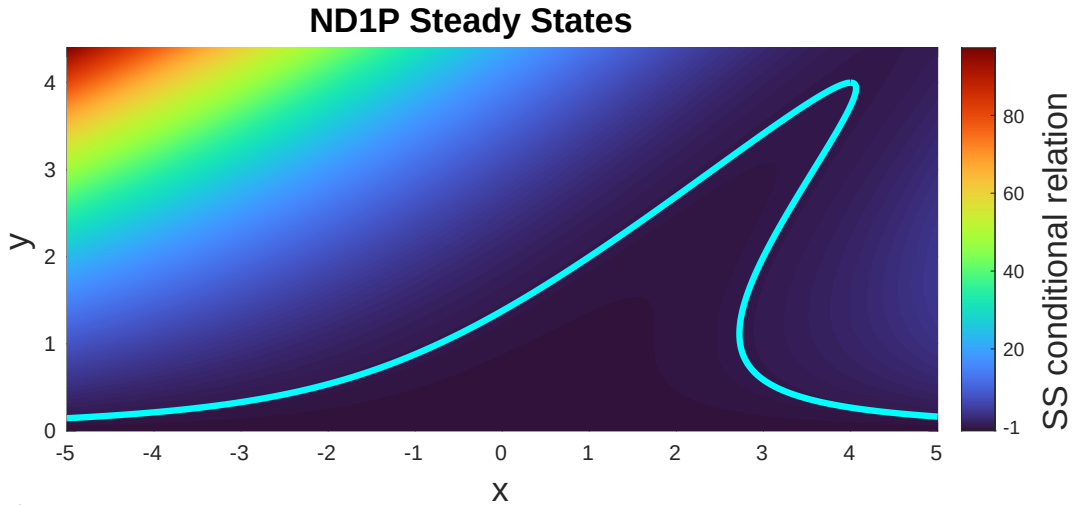

Figure B.1: The ND1P SS distribution, $y(x)$ in the SS3 regime ($\gamma = 0.5$). The background is coloured by the conditional polynomial (B.4), whose zeroes plot the SS distribution (cyan).

B.1 Non-Dimensionalisation of the QAOSS Conditional Relation

The QAO model physical quantities and their dimensions for vibrational mode k are:

- ω_k, natural harmonic (normal mode) oscillation frequency, $[\text{time}]^{-1}$
- ϖ_k, anharmonically adjusted oscillation frequency, $[\text{time}]^{-1}$
- ω, stimulus frequency, $[\text{time}]^{-1}$
- $\langle \hat{n}_k \rangle$, phonon number operator expectation value, [dimensionless]
- $\langle \hat{a}_k^\dagger \rangle, \langle \hat{a}_k \rangle$, creation and annihilation operator expectation values, [dimensionless]
- ξ_{kj} anharmonic Hamiltonian coefficients, $[\text{time}]^{-1}$
- Υ_k, vibrational dissipation rate, $[\text{time}]^{-1}$
- $\bar{n}_k$, thermal equilibrium (Planck) phonon number, [dimensionless]
- B_k, stimulus strength, $[\text{time}]^{-1}$

I will perform the non-dimensionalisation of the QAO model equations via an appropriate substitution of variables for the various physical quantities. In **§ 4.6.2**, the dimensioned QAOSS conditional relation for the stimulated response of vibrational mode k of the dissipative substrate molecule was found to be

$$0 \;=\; \left(\Upsilon_k^2 \;+\; (\omega \;-\; \varpi_k \;-\; 2\xi_{kk}\,N)^2\right)(N \;-\; \bar{n}_k) \;-\; B_k^2 \tag{B.1}$$

where $N = \langle \hat{n}_k \rangle^{\rm ss}$ is the SS phonon number. The QAOSS conditional relation carries physical dimensions of $[\text{time}]^{-2}$, and so non-dimensionalisation is achieved by division of a quantity carrying the same physical dimensions. The best choice is to divide by B_k^2 since the term arising from the enzyme stimulus will be set to unity; this assumes a non-zero stimulus, and therefore the free molecule is not captured by the ND1P. By making use of the non-dissipative barrel (saddle-node bifurcation) point excitation phonon number, ν_k, the enzyme stimulus can be expressed as, $B_k^2 = (4\,\xi_{kk})^2\;\nu_k^3$, and upon division the conditional statement (B.1) can be grouped

$$0 \;=\; \left[\left(\frac{\Upsilon_k}{4\,\xi_{kk}\;\nu_k}\right)^2 \;+\; \frac{1}{4}\left(\frac{\omega \;-\; (\varpi_k \;+\; 2\,\xi_{kk}\,\bar{n}_k)}{2\xi_{kk}\;\nu_k} \;-\; \frac{N \;-\; \bar{n}_k}{\nu_k}\right)^2\right]\;\frac{N \;-\; \bar{n}_k}{\nu_k} \;-\; 1 \tag{B.2}$$

By defining the following dimensionless variables

$$x \;\equiv\; \frac{\omega \;-\; (\varpi_k \;+\; 2\xi_{kk}\,\bar{n}_k)}{2\,\xi_{kk}\;\nu_k} \tag{B.3a}$$

$$y \;\equiv\; \frac{N \;-\; \bar{n}_k}{\nu_k} \tag{B.3b}$$

$$\gamma \;\equiv\; \frac{\Upsilon_k}{4\,\xi_{kk}\;\nu_k} \tag{B.3c}$$

the QAOSS conditional statement is expressed in the ND1P form

$$0 \;=\; \left(\gamma^2 \;+\; \frac{1}{4}\,(x-y)^2\right)\;y \;-\; 1 \tag{B.4}$$

The variables x, y describe the detuning frequency and phonon number, respectively, and the parameter γ is proportional to the vibrational dissipation rate. In the limit of $\gamma \to 0$, an expression equivalent to the dissipationless QAOSS conditional statement ($\Upsilon_k = 0$) is obtained

$$0 \;=\; \frac{1}{4}(x-y)^2\;y \;-\; 1 \tag{B.5}$$

however, the parameter γ encapsulates more than the dissipation. In the dimensioned model, the stimulus B_k characterises the peak height ($\langle \hat{n}_k \rangle^{\rm ss}_{\rm max} = \mu_k = B_k^2/\Upsilon_k^2$), Υ_k is the Half-Width-at-Half-Maximum (HWHM), and ξ_{kk} characterises the skew angle ($\theta = \tan^{-1}(2\,\xi_{kk})$, as measured from the vertical QHOSS distribution). Each of the variables that affect the skew Lorentzian

lineshape are contained within the ND1P parameter

$$\gamma \;=\; \frac{\Upsilon_k}{\sqrt[3]{4\,|\xi_{kk}|\;B_k^2}} \tag{B.6}$$

where the absolute value of the self-interaction ensure that $\gamma \in \mathbb{R}_{\geq 0}$. In the ND1P SS distribution (Fig. B.1), the peak is fixed to a skew angle of 45° ($x = y$), and γ characterises the peak, with $\gamma = \infty$ being a horizontal line at $y = 0$ (representing thermal equilibrium, $N = \bar{n}_k$), and $\gamma = 0$ has a peak at infinity (representing the QAO in the absence of dissipation, $\Upsilon_k = 0$).

The SS distributions can be plotted without use of a root solving algorithm by rearrangement of (B.4) for x in terms of y, giving

$$x_{\pm}^{\text{SS}}(y;\gamma) \;=\; y \;\pm\; 2\,\sqrt{y^{-1} \;-\; \gamma^2} \tag{B.7}$$

and in the $\gamma = 0$ case by

$$x_{\pm}^{\text{SS}}(y;0) \;=\; y \;\pm\; \frac{2}{\sqrt{y}} \tag{B.8}$$

which have been used in the figures throughout this appendix.

B.2 ND1P QAO Equations of Motion

I will now explore the dynamical behaviour of the ND1P model by mapping the QAO catalytic EoMs according to the variable substitutions (B.3). I set the ND1P QAO EoMs by making the following substitutions for the quantum state space operator expectation values

$$A \;=\; \frac{\langle \hat{a}_k \rangle}{\sqrt{\nu_k}} \tag{B.9a}$$

$$A^{\dagger} \;=\; \frac{\langle \hat{a}_k^{\dagger} \rangle}{\sqrt{\nu_k}} \tag{B.9b}$$

$$Y \;=\; \frac{\langle \hat{n}_k \rangle \;-\; \bar{n}_k}{\nu_k} \tag{B.9c}$$

and a dimensionless variable proportional to time

$$\tau \;=\; 4\,\xi_{kk}\;\nu_k\;t \tag{B.10}$$

Upon using these substitutions, the ND1P EoMs are

$$\partial_\tau A \;=\; -\left(\gamma \;-\; \frac{i}{2}\,x\right)\;A \;-\; \frac{i}{2}\,Y\;A \;-\; i \tag{B.11a}$$

$$\partial_\tau A^{\dagger} \;=\; -\left(\gamma \;+\; \frac{i}{2}\,x\right)\;A^{\dagger} \;+\; \frac{i}{2}\,Y\;A^{\dagger} \;+\; i \tag{B.11b}$$

$$\partial_\tau Y \;=\; -\,2\,\gamma\;Y \;-\; i\,\left(A^{\dagger} \;-\; A\right) \tag{B.11c}$$

which can be collected into a matrix equation for the ND1P quantum state, $\mathbf{\Psi} = [A, A^\dagger, Y]^{\mathrm{T}}$

$$\partial_\tau \mathbf{\Psi} \;=\; \begin{bmatrix} -\left(\gamma \;-\; \frac{i}{2}\,x\right) & 0 & 0 \\ 0 & -\left(\gamma \;+\; \frac{i}{2}\,x\right) & 0 \\ +i & -i & -2\,\gamma \end{bmatrix} \mathbf{\Psi} \;+\; \frac{i}{2}\,Y \begin{bmatrix} -1 & 0 & 0 \\ 0 & +1 & 0 \\ 0 & 0 & 0 \end{bmatrix} \mathbf{\Psi} \;+\; \begin{bmatrix} -i \\ +i \\ 0 \end{bmatrix} \tag{B.12}$$

whose terms are the linear, non-linear and inhomogeneous contributions, respectively. The ND1P EoMs can be expressed in purely real terms by the dimensionless position–momentum representation of the quantum state. By applying the map $(A, A^\dagger) \mapsto (q, p)$ according to the transfomations in **§ 3.1.4**, the ND1P position–momentum EoMs are

$$\partial_\tau q \;=\; -\,\gamma\; q \;-\; \frac{1}{2}\,(x \;-\; Y)\; p \tag{B.13a}$$

$$\partial_\tau p \;=\; -\,\gamma\; p \;+\; \frac{1}{2}\,(x \;-\; Y)\; q \tag{B.13b}$$

$$\partial_\tau Y \;=\; -\,2\,\gamma\; Y \;-\; \sqrt{2}\; p \tag{B.13c}$$

B.2.1 Steady States

Now that the EoMs for the ND1P model have been obtained, I will perform a steady state and stability analysis following the same procedure in **§ 4.6.1**. Let the ND1P annihilation operator SS expectation value be, $A^{\mathrm{ss}} = \alpha$, and the phonon number SS expectation value is y, by definition (B.3b), then the SS of (B.11a) gives

$$\alpha(x, y; \gamma) \;=\; \frac{-i}{\gamma \;-\; \frac{i}{2}\,(x \;-\; y)} \tag{B.14}$$

The absolute square is

$$|\alpha|^2 \;=\; \frac{1}{\gamma^2 \;+\; \frac{1}{4}\;(x \;-\; y)^2} \tag{B.15}$$

the real (position) and imaginary (momentum) components are $\Re[\alpha] = \frac{1}{2}(x-y)|\alpha|^2 = \frac{1}{\sqrt{2}}\,q^{\mathrm{ss}}$ and $\Im[\alpha] = -2\gamma\,|\alpha|^2 = \frac{1}{\sqrt{2}}\,p^{\mathrm{ss}}$, respectively. The distribution of α can be plotted on the imaginary plane by the perfect

$$\alpha(\theta; \gamma) \;=\; -\,\frac{i}{2\,\gamma}\;\left(e^{i\theta} \;+\; 1\right) \tag{B.16}$$

for $\theta \in [-\pi, +\pi]$; the angle can be expressed in terms of the ND1P variables by

$$\theta(x, y; \gamma) \;=\; -\,i\;\ln\left[\frac{\gamma \;+\; \frac{i}{2}(x \;-\; y)}{\gamma \;-\; \frac{i}{2}(x \;-\; y)}\right] \tag{B.17}$$

These have been used for the (q, p) state space representation of the simulation trajectories in final section of this appendix. The SS of (B.11c) is

$$\text{at SS:} \quad y \;=\; |\alpha|^2 \tag{B.18}$$

whose rearrangement returns the SS conditional relation (B.4). The SS response distribution, $y(x; \gamma)$, is a skew Lorentzian resonance distribution with a HWHM of γ, and the maximum value

of (B.15) occurs where $x = y$, which has a peak height of γ^{-2}. In the fully dimensioned model, the maximum response in phonon number is $\mu = B_k^2/\Upsilon_k^2$, and can be used in the expression for the maximum ND1P response

$$y_{\max} \;=\; \gamma^{-2} \;=\; \frac{\mu_k}{\nu_k} \tag{B.19}$$

Therefore, the parameter γ is the inverse square of the ratio of the crest-to-barrel (bifurcation) excitation phonon numbers, and defines the peak height in the ND1P model.

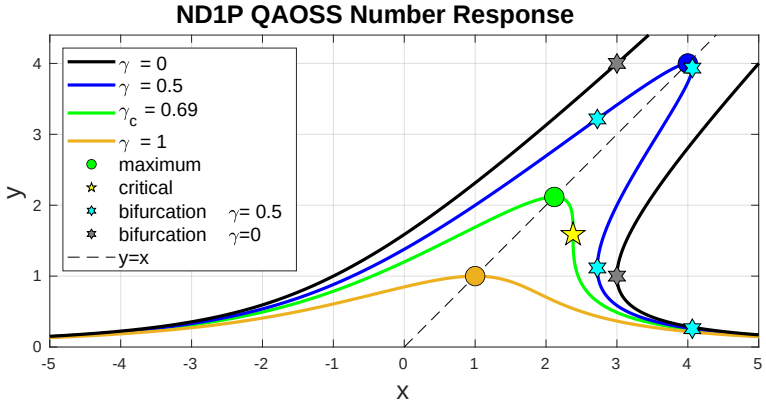

Figure B.2: Steady state distributions, $y(x;\gamma)$, for various parameter values: $\gamma = 0$ corresponds to the non-dissipative behaviour (black), SS3 regime $\gamma = 0.5 < \gamma_c$ (blue), critical $\gamma = \gamma_c$ (green), and SS1 regime $\gamma = 1 > \gamma_c$ (orange). The maximum value (B.19) for each is shown as correspondingly coloured circles, the critical point by the yellow star, and the bifurcation points by hexagrams ($\gamma = 0.5$ in cyan, $\gamma = 0$ in grey). The $x = y$ line (dashed black) coincides with the maximum SS for all values of γ.

B.2.2 ND1P QHO EoM Solutions

The ND1P EoMs (B.11) cannot be solved by standard analytic techniques due to the products, YA and $YA^\dagger$. For the dimensioned model, the form of the QHO EoMs can be recovered from the QAO EoMs by setting the anharmonic coefficients to zero, which allows for an exact solution. By removing the non-linear term in (B.11a), the linear EoM can be solved by

$$A_{\text{lin}}(\tau, x; \gamma) \;=\; \alpha_{\text{lin}} \;+\; e^{-\gamma\,\tau}\; e^{+\frac{i}{2}\,x\,\tau}\; \left(A_0 \;-\; \alpha_{\text{lin}}\right) \tag{B.20}$$

where the SS of A_{lin} is $\alpha_{\text{lin}}(x;\gamma) \;=\; \alpha(x, 0; \gamma)$ (B.14). The behaviour is equivalent to the QHO model in **Chapter 3**; the state evolves as an exponentially decaying phasor from the initial state towards to the SS, with a decay rate γ, rotation period $\tau_p = 4\pi/x$, and rotation direction given by the sign of x ($x > 0$ is counter-clockwise). The ND1P parameter, γ, therefore characterises the lifetime of the response behaviour.

The evolution of Y is found by substituting (B.20) into (B.11c) then solving, which yields

$$\begin{aligned} Y_{\text{lin}}(\tau, x; \gamma) \;=\; Y_0\; e^{-2\,\gamma\,\tau} \;+\; \left|\alpha_{\text{lin}}\right|^2 \Bigg(& 1 \;+\; e^{-2\,\gamma\,\tau} \;-\; 2\,\cos\left(\frac{1}{2}\,x\,\tau\right)\, e^{-\gamma\,\tau} \\ & +\; 2\,e^{-\gamma\,\tau}\, \left[\Re[z_0]\, \left(\cos\left(\frac{1}{2}\,x\,\tau\right) \;-\; e^{-\gamma\,\tau}\right) \;-\; \Im[z_0]\, \sin\left(\frac{1}{2}\,x\,\tau\right)\right] \Bigg) \end{aligned} \tag{B.21}$$

where $z_0 = A_0/\alpha_{\text{lin}} = (A_0^\dagger/\alpha_{\text{lin}}^*)^*$. The evolution of the peak is found by setting $x = 0$ in (B.21), giving

$$Y_{\text{lin}}(\tau, 0; \gamma) \;=\; Y_0\, e^{-2\,\gamma\,\tau} \;+\; \gamma^{-2}\, \left(1 \;-\; e^{-\gamma\,\tau}\right)^2 \tag{B.22}$$

which is non-oscillatory; therefore, relaxation oscillations are present in the linear ND1P only for non-zero detuning frequencies. These results are equivalent to the QHO exact solution in **Chapter 3**, which allowed the phonon number response spectrogram to be plotted without requiring a numerical solution to the EoMs.

B.2.3 Stability Eigenvalues

The linear stability analysis of the SS is determined by the eigenvalues of the Jacobian stability matrix, $\mathbf{J}$, in the same manner as in **Chapter 4**. By differentiating the ND1P EoMs (B.11) with each quantum state observable and setting to SS, the stability matrix is

$$\mathbf{J}(x, y; \gamma) \;=\; \left(\frac{\partial(\partial_\tau \mathbf{\Psi})}{\partial \mathbf{\Psi}}\right)\Bigg|_{\text{ss}} \;=\; \begin{bmatrix} -\gamma + \frac{i}{2}(x-y) & 0 & -\frac{i}{2}\,\alpha \\ 0 & -\gamma - \frac{i}{2}(x-y) & +\frac{i}{2}\,\alpha^* \\ +i & -i & -2\gamma \end{bmatrix} \tag{B.23}$$

Upon following a similar procedure to the dimensioned model in **Chapter 4**, the stability characteristic equation is

$$0 \;=\; -\,(\lambda \;+\; 2\,\gamma)\, \left((\lambda \;+\; \gamma)^2 \;+\; \frac{1}{4}\,(x \;-\; y)(x \;-\; 3y)\right) \tag{B.24}$$

from which the stability eigenvalues are

$$\lambda_0(\gamma) \;=\; -\,2\,\gamma \tag{B.25a}$$

$$\lambda_\pm(x, y; \gamma) \;=\; -\,\gamma \;\pm\; \frac{1}{2}\,\sqrt{-(x \;-\; y)(x \;-\; 3y)} \tag{B.25b}$$

An unstable SS has at least one purely real and positive stability eigenvalue. Since the ND1P parameter is real-valued and strictly positive, $\gamma \in \mathbb{R}_{\geq 0}$, the eigenvalue, λ_0, is always stabilising. The eigenvalue pair, $\lambda_\pm$, is real-valued in the triangular region $y \in [\frac{1}{3}x, x]$, and has a non-zero imaginary component everywhere else. Therefore, the unstable branch of the SS distribution has a boundary that is dependent on the value of γ, which is contained within the aforementioned triangular region. The unstable region of the SS is the mid-branch, which is framed by a two saddle-node bifurcation points (Fig. B.3) that I will term the crest (high y) and the barrel (low y) points for the proceeding discussion.

B.3 Critical Condition for Phase Transition Behaviour

In this section, I will derive the critical condition, (x_c, y_c, γ_c) — the parameter value γ_c whose crest and barrel bifurcation points coincide at (x_c, y_c). The parameter values that neighbour the critical value, γ_c, result in behaviour that is in the SS1 ($\gamma > \gamma_c$) and SS3 ($\gamma \leq \gamma_c$) regime. In the dimensioned model (**Chapter 4**), the critical condition represented the minimum stimulus for

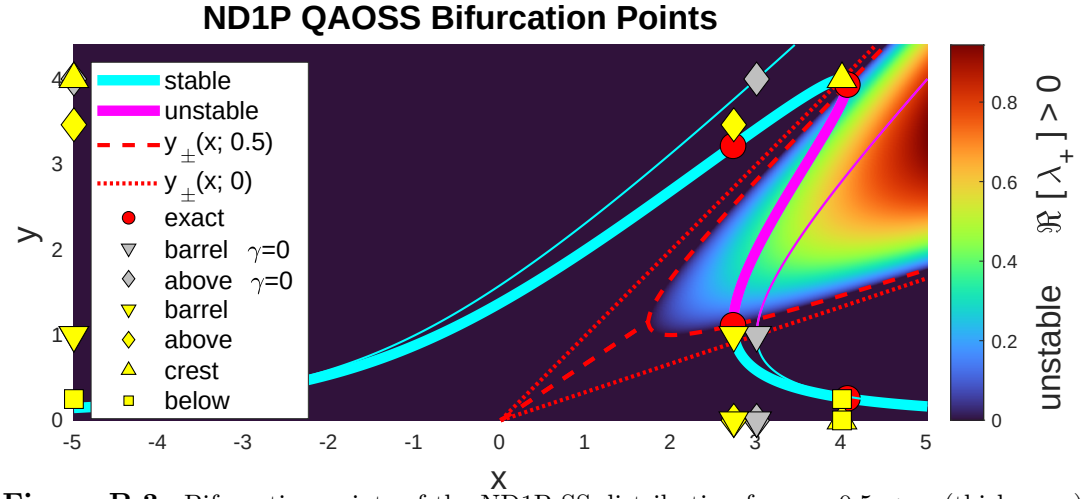

Figure B.3: Bifurcation points of the ND1P SS distribution for $\gamma = 0.5 < \gamma_c$ (thick cyan), and the $\gamma = 0$ case (thin cyan). The background is coloured by the unstable region for the $\gamma = 0.5$ SS distribution (positive real component of λ_+); whose boundary is given by $y_\pm(x; 0.5)$ (B.26) (dashed red), and is contained by the triangular region $y_\pm(x; 0)$ (B.27). For the $\gamma = 0$ case, the bifurcation point is known exactly by (B.31), and the above point by (B.32). In the $\gamma = 0.5$ case, the exact bifurcation point (red circle) are computed numerically by (B.29), along with the approximations for the barrel (B.33a), above-barrel (B.33b), crest (B.33c), and below-crest (B.33d) points.

a phase transition, along with the corresponding detuning frequency and the expectation value for the phonon number response.

B.3.1 Critical Point

The critical point (x_c, y_c) must occur where the stability eigenvalue pairs (B.25b) are equal to zero, since it represents a change in stability condition. For $\gamma > 0$, the eigenvalue pairs are zero-valued along

$$y_\pm(x;\gamma) \;=\; \frac{1}{3}\left(2\,x \;\pm\; \sqrt{x^2 \;-\; 12\,\gamma^2}\right) \tag{B.26}$$

In the case of $\gamma = 0$, the eigenvalue pairs are zero-valued when

$$y_\pm(x;0) \;=\; \left(\frac{2 \;\pm\; 1}{3}\right)\; x \tag{B.27}$$

whose low- and high-branch is $y_-(x;0) = \frac{1}{3}\,x$ and $y_+(x;0) = x$; which is the triangular region identified in the previous section (dotted lines in Fig. B.3). At the critical condition (x_c, y_c), the bifurcation points coincide, and so $y_+(x_c;\gamma) = y_-(x_c;\gamma)$. The value for x that satisfies this condition is elucidated by setting the argument under the squareroot to zero, which gives, $x_c = 2\sqrt{3}\,\gamma$, then upon evaluating $y_\pm(x_c;\gamma) = \frac{4}{\sqrt{3}}\,\gamma$, the critical point is located in terms of the critical parameter value

$$(x_c, y_c) \;=\; \left(2\sqrt{3}\;\gamma_c\;,\quad \frac{4}{\sqrt{3}}\;\gamma_c\right) \tag{B.28}$$

B.3.2 Critical Parameter

The next step is to determine the critical parameter value, γ_c, and is obtained from the SS conditional relation. The extrema values of $x^{\text{ss}}_\pm(y;\gamma)$ (B.7) are found by differentiation with y

then equating to zero, which upon rearrangement leads to a quartic polynomial in y

$$\gamma^2\, y^4 \;-\; y^3 \;+\; 1 \;=\; 0 \tag{B.29}$$

whose real-valued roots locate the bifurcation points of the SS distribution for a given γ (red circles in Fig. B.3). The critical parameter value is obtained by evaluating (B.29) at the non-zero turning point, $y = \frac{3}{4\gamma^2}$, then upon rearrangement, yields $\gamma_c = \frac{\sqrt{3}}{2\sqrt[3]{2}}$. Thus, the ND1P critical condition has been determined precisely

$$(x_c, y_c, \gamma_c) \;=\; \left(\frac{3}{\sqrt[3]{2}}\,,\;\; \sqrt[3]{4}\,,\;\; \frac{\sqrt{3}}{2\sqrt[3]{2}}\right) \;\approx\; (2.381\,,\;\; 1.587\,,\;\; 0.687) \tag{B.30}$$

B.4 Bifurcation Points

For parameter values $\gamma < \frac{\sqrt{3}}{2\sqrt[3]{2}}$, the ND1P model experiences phase transition behaviour. The exact location of the bifurcation points must be computed by a root solving algorithm; however, in this section, I will derive analytic approximations that are in close agreement, and become more accurate as $\gamma \to 0$. The saddle-node bifurcation points occur where the SS conditional relation polynomial has repeated roots in y for a given value of x. I will call the low-y and high-y bifurcation points the barrel and crest points, respectively; I will call the non-repeated root associated with the barrel and crest points the above and below points. These four points marks the boundaries of the phase transition region; their physical interpretation will detailed later in this section.

The $\gamma = 0$ case corresponds to the QAO model with zero dissipation, whose SS distribution has one finite bifurcation point, which I call the free barrel point, $(x, y)^{\gamma=0}_{\text{barrel}}$. Following the same procedure in **§ 4.6.4 & § 4.6.5**, the free barrel point is located by finding the extrema value of $x^{\text{ss}}_{\pm}(y; 0)$ (B.8) with y, and gives $y^{\gamma=0}_{\text{barrel}} = 1$. The x-coordinate of the free barrel point is found by evaluating, $x^{\text{ss}}_{\pm}(y^{\gamma=0}_{\text{barrel}}; 0)$, thus the free barrel point is

$$(x, y)^{\gamma=0}_{\text{barrel}} \;=\; (3\;,\;1) \tag{B.31}$$

and is plotted as the grey down-pointing triangle in Fig. B.3. The point above the barrel is found by making use of the fundamental theorem of algebra which states that any polynomial can be expressed as the product of the difference between its roots and the variable. By setting (B.5) equal to $\frac{1}{4}(y-1)^2(y-y^{\gamma=0}_{\text{above}})$, then equating the coefficients, gives $y^{\gamma=0}_{\text{above}} = 4$, allowing the $\gamma = 0$ above-barrel point to be approximated as

$$(x, y)^{\gamma=0}_{\text{above}} \;=\; (3\;,\;4) \tag{B.32}$$

The high-y bifurcation (crest) point is approximately the maximum SS $x_{\text{crest}} \approx y_{\text{crest}} \approx \gamma^{-2}$. The low-$y$ bifurcation (barrel) point has a y-value that is approximately $y^{\gamma=0}_{\text{barrel}} = 1$, and the x-coordinate is given by evaluating (B.7) at $y = 1$, giving, $x_{\text{barrel}} \approx 1 \pm 2\sqrt{1-\gamma^2}$; this assumes that the y-value is constant for all values is γ, and is the lower limit as $\gamma \to 0$.

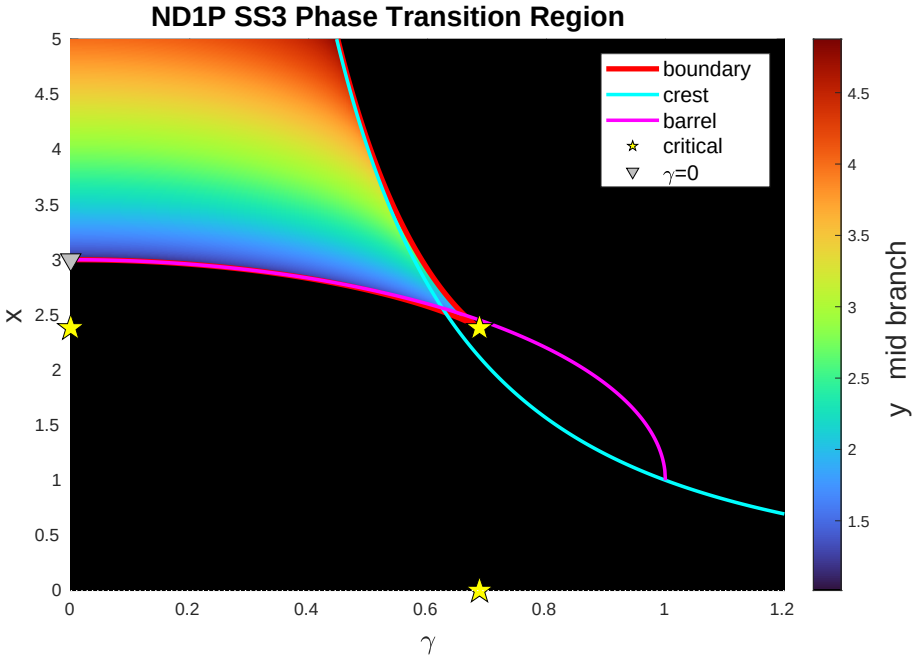

Figure B.4: The SS3 phase transition region for the ND1P model in (x, γ) state space is coloured by the y-value of the mid branch, with its bifurcation boundary in red, and the SS1 region is black. The critical point (x_c, γ_c) (yellow star) (B.30) is the largest value of γ for the SS3 region, and occurs where the bifurcation boundaries coincide in x. The low-y bifurcation (barrel) boundary has an x-value between the critical and free barrel ($\gamma = 0$ bifurcation) point (grey down-triangle). The approximations for the low-y barrel (magenta) (B.33a) and high-y crest (cyan) (B.33c) bifurcation points are in good agreement with the exact values determined by a numeric root solving algorithm.

The above-barrel and below-crest points are approximated by applying the process for finding the non-repeated roots for the $\gamma > 0$ SS conditional relation (B.4) with $\frac{1}{4}(y-y_\mathrm{r})^2(y-y_\mathrm{nr})$, where $y_\mathrm{r}, y_\mathrm{nr}$ are the repeated and non-repeated root y-values, respectively. Equating the quadratic coefficient results in, $y_\mathrm{nr}^{(2)} = 2(x - y_\mathrm{r})$, which is used to approximate the above-barrel point, giving $4\sqrt{1-\gamma^2}$. Equating the zeroth-order coefficient results in, $y_\mathrm{nr}^{(0)} = (2/y_\mathrm{r})^2$, which I use to approximate the below-crest point, giving $4\gamma^4$. Thus, I have found approximate analytic expressions for the bifurcation points and their corresponding non-repeated roots as a function of γ

$$(x, y)_\mathrm{barrel} \approx \left(1 + 2\sqrt{1-\gamma^2}\,,\ \ 1\right) \tag{B.33a}$$

$$(x, y)_\mathrm{above} \approx \left(1 + 2\sqrt{1-\gamma^2}\,,\ \ 4\sqrt{1-\gamma^2}\,\right) \tag{B.33b}$$

$$(x, y)_\mathrm{crest} \approx \left(\gamma^{-2}\,,\ \ \gamma^{-2}\right) \tag{B.33c}$$

$$(x, y)_\mathrm{below} \approx \left(\gamma^{-2}\,,\ \ 4\,\gamma^4\right) \tag{B.33d}$$

The exact values are the non-zero real roots of (B.29), which must be calculated numerically by a root finding algorithm. The approximations are in good agreement with the exact value, as can be seen in Fig. B.4 and Fig. B.5.

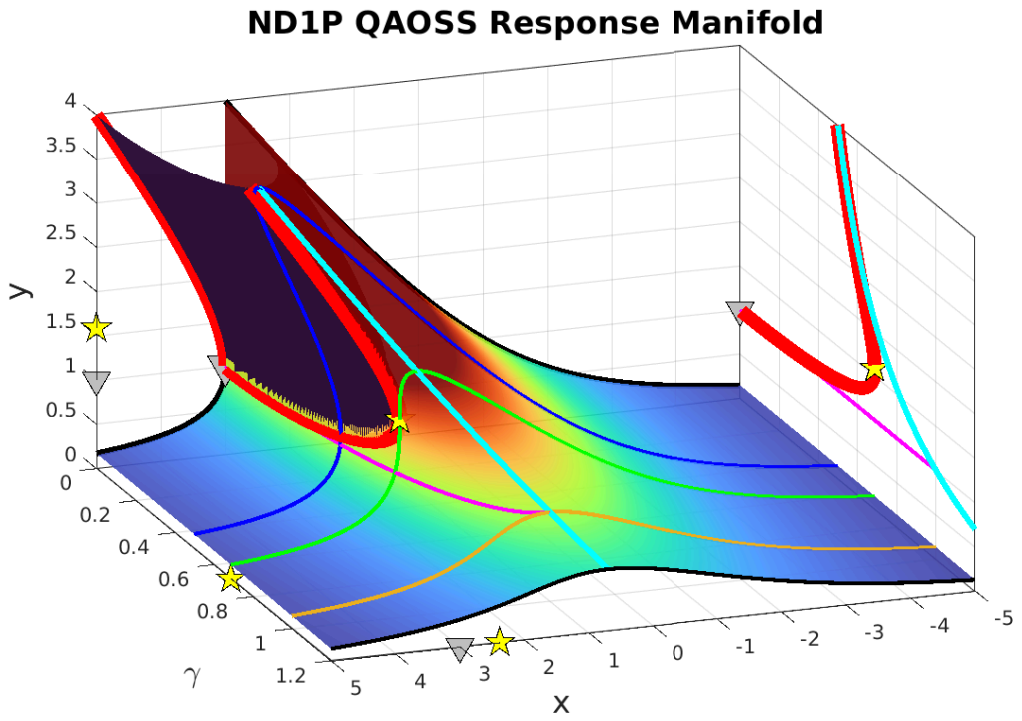

Figure B.5: The ND1P response manifold in (x, y, γ) state space (coloured by y-value), along with the bifurcation boundary (red), SS distributions for varying γ (coloured by Fig. B.2), and the approximations for the barrel (magenta) and crest (cyan) bifurcation points. The critical point (yellow star) and free barrel $\gamma = 0$ bifurcation point are plotted along the axes for each variable. The SS3 boundary in (y, γ) is projected onto the back wall, along with the crest and barrel approximations, which show a good agreement.

B.5 Numerical Solution to the ND1P EoMs

Now that the SS1 and SS3 regimes have been identified, I will perform numerical solutions of the EoMs (B.11). I will detail the establishment of the numerical solution to the QAO EoMs in **Appendix B**, in this section I will provide a brief overview.

I set the simulation duration, τ_{sim}, based upon the approximate time for the exponential behaviour to quiesce. The QHO EoM solutions (§ 3.4.3) show that the vibrational mode relaxation rate is given by Υ_k, with its inverse describing the vibrational lifetime; the excited response dynamics are approximately quiesced after five lifetimes ($e^{-5} \approx 0$), wherein vibrational mode is at its steady state. The lifetime of the linear ND1P response is γ^{-1} (B.20), and therefore, I set the ND1P relaxation time to $\tau_{\text{relax}} = 5\gamma^{-1}$. The non-linearity of the QAO model allows for relatively large persistent dynamics to continue after the QHO relaxation time has elapsed. To capture the non-linear dynamics, I set the simulation duration to $\tau_{\text{sim}} = 2\,\tau_{\text{relax}}$ (10 lifetimes). I performed the numerical solution by using the MATLAB function, `ode45`, over a range of x-values, and then interpolated the results on to the same timeline vector so that the response spectrogram can be plotted.

B.5.1 Initial State

Since the ND1P is an abstraction of the molecular dynamics, I will explore the response behaviour under non-physical initial conditions. By setting the initial ND1P number state, Y_0, to be an arbitrary function in terms of x, the initial states ND1P creation and annihilation states $(A_0, A_0^\dagger)$ are given by (B.14); this state is not a valid SS since $Y_0 \neq A_0^\dagger A_0$. For a given γ, the initial state is

$$\mathbf{\Psi}_0(x;\gamma) \;=\; \begin{bmatrix} \alpha\ (x, Y_0(x);\gamma) \\ \alpha^*(x, Y_0(x);\gamma) \\ Y_0(x) \end{bmatrix} \tag{B.34}$$

In **§ 5.2.9**, I fix the initial molecular state to equilibrium by setting, $\langle \hat{n}_k(0) \rangle = \bar{n}_k$, for each vibrational mode, which is then used to specify the initial creation and annihilation state. In the ND1P model, the thermal equilibrium state corresponds to, $Y_0 = 0$. A simulation from this initial state will be excited to the low-branch of the SS distribution, whose maximum value is the above-barrel point (yellow diamond in Fig. B.6a). In the dimensioned model simulation in **Chapter 5**, the vibrational modes can be excited above this point due to the stimulus from the enzyme or solvent, as well as the other vibrational modes; the ND1P simulation that I am presenting in this section is effectively an isolated vibrational mode that experiences a spectrally flat, constant stimulus of unity.

B.5.2 Comparison of Low- and High-Branch Resting Response Spectra

In this section, I will demonstrate simulations with initial conditions that result in the minimum and maximum resting response spectra. I will term these the low- and high-branch simulations, and are displayed in panels a and b, respectively in Figs. B.6 to B.9. The resting state is the response spectra in the limit of an infinite duration of simulation ND1P time, $\tau_{\text{sim}} \to \infty$; I approximate the resting state to be taken after a ND1P time of ten lifetimes ($\tau_{\text{sim}} = 10/\gamma$) by taking the small amplitude relaxing oscillations to be negligible.

The low-branch simulation has an initial state, $Y_0(x) = y_-(x;0) = \frac{1}{3}\, x\ \Theta(x)$, where $\Theta(x)$ is the Heaviside step function ($\Theta = 0$ for $x < 0$ and $\Theta = 1$ for $x \geq 0$). A simulation for any initial state below the low-y branch $y_-(x;0)$ (B.27) will have a resting state (at τ_{sim}) on the low-branch of the SS, and hence the maximum response value is the above-barrel point (B.33b). The initial state that results in the high-branch resting spectra is given by the high-y branch $Y_0(x) = y_+(x;0) = x\ \Theta(x)$. If the initial state is between the low-y and high-y bifurcation branches, $Y_0(x) \in [y_-(x;0),\, y_+(x;0)]$, then the response will be partially excited up to the high-branch of the SS, and for an initial state that is above the high-y branch, $Y_0(x) > y_+(x;0)$, the tip falls into the low-branch of the SS due to momentum. Therefore, the response is maximised for $Y_0(x) = x\ \Theta(x)$; for all other initial states, the peak of the resting state will be somewhere between the above-barrel point (B.33b) and the crest (B.33c). Therefore the largest resting response spectra for an SS3 simulation ($\gamma < \gamma_c$) from any initial state occurs between $x \in [x_{\text{barrel}},\, x_{\text{crest}}]$ and $y \in [y_{\text{above}},\, y_{\text{crest}}]$, which are approximately given by (B.33).

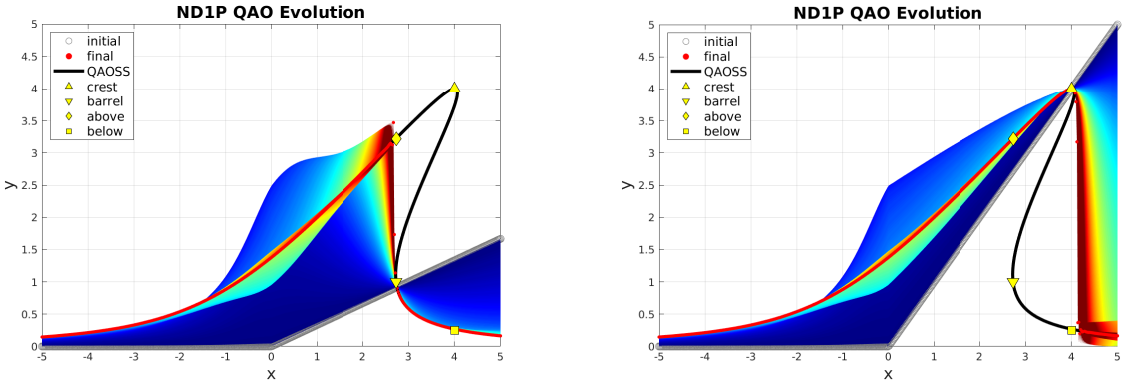

(a) Low branch, $y_0 = \frac{1}{3}\, x\, \Theta(x)$ **(b)** High branch, $y_0 = x\, \Theta(x)$

Figure B.6: Evolution of state for the ND1P model in the SS3 regime ($\gamma = 0.5 < \gamma_c$) under two initial conditions. The initial state (grey) evolves in time from blue to red, before resting on the SS distribution (black); the bifurcation points and their associated non-repeated are plotted using the same symbols as in Fig. B.3.

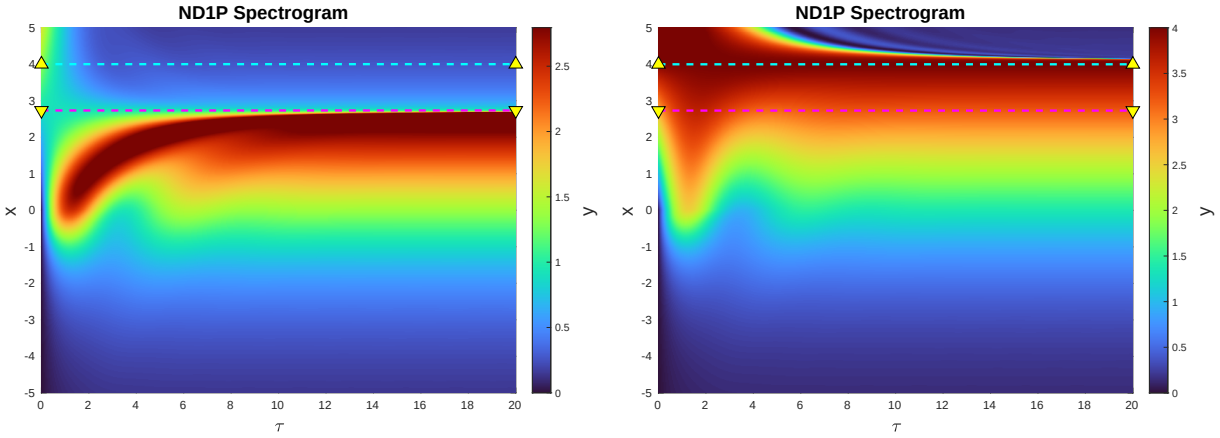

(a) Low branch, $y_0 = \frac{1}{3}\, x\, \Theta(x)$ **(b)** High branch, $y_0 = x\, \Theta(x)$

Figure B.7: ND1P response spectrogram coloured by the y-value. The x-values for the low-y (barrel) and high-y (crest) bifurcation points are shown as the down- and up-triangles, respectively.

The evolution of the response spectra with τ (Fig. B.6) shows the relaxation oscillations from the initial state to resting SS. If the initial state is above (below) the resting state, the state is excited (depressed) towards the SS, which it overshoots, the exhibits relaxation oscillations before coming to rest; this dynamic is most pronounced around $x = 0$. For the low branch simulation (panel a of Fig. B.7), there is no excitation towards the high-y SS branch ($x > x_{\text{barrel}}$, yellow down-triangle), and the state is approximately at rest after $\tau = \tau_{\text{relax}} = 10$. For the high branch simulation (panel b), the spectral region $x < x_{\text{crest}}$ is excited to the high-y SS branch, and for $x > x_{\text{crest}}$, the response has persisting relaxation oscillations for the simulation duration; in the dimensioned model, this spectral region contains the motions of the hydrogen network.

The ND1P evolution in the (q, p) state space and (q, p, τ) state spacetime are shown in Fig. B.8 and Fig. B.9, respectively. The portions of the SS circle that corresponds to the various features of the SS response spectra, $y(x; \gamma)$ (Fig. B.2) can be located by $\alpha(\theta; \gamma)$ (B.16). The crest point approximation (B.33c) has $x = y$, from which the angle is $\theta = 0$, and $\alpha_{\text{crest}}(\gamma) = -i\, \gamma^{-1}$

(down-triangle). The angle of the barrel point is dependent on γ according to

$$\theta_{\text{barrel}}(\gamma) \;=\; -\,i\,\ln\left[2\gamma^2 \;-\; 1 \;+\; i2\gamma\sqrt{1-\gamma^2}\,\right] \tag{B.35}$$

which monotonically decreases from π for $\gamma = 0$, to zero for $\gamma \geq 1$. The unstable region is the arc drawn by the angles $\theta \in [\theta_{\text{crest}}, \theta_{\text{barrel}}]$, which has zero size for the SS1 regime ($\gamma > \gamma_c$), and extends along the SS circle in the positive real quadrants, $\Re[\alpha] > 0$ towards the origin for decreasing γ; in the limit of $\gamma \to 0$, the $\Re[\alpha] > 0$ portion is unstable, which corresponds to the crest bifurcation point at infinity. Therefore, the $\Re[\alpha] > 0$ quadrants are covered by x_+^{ss} (B.7) which spans the unstable and low branches of the SS distribution in $y(x)$, while the $\Re[\alpha] < 0$ quadrants are covered by the high-branch and $x < 0$. In (q, p) state space (Fig. B.8), the high-branch in the SS3 region is of particular interest since it will contain the maximum response, and can be seen to lie within the arc in the $q < 0$ quadrant spanning between the crest (up-triangle) and above-barrel (diamond) points

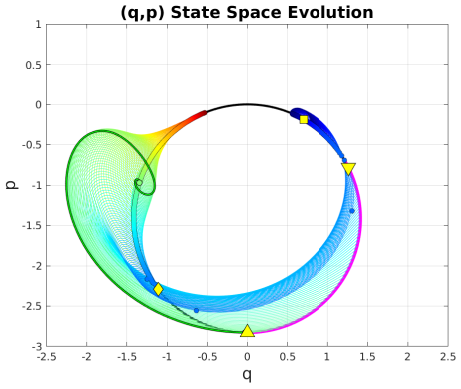

(a) Low branch, $y_0 = \frac{1}{3}\,x\;\Theta(x)$

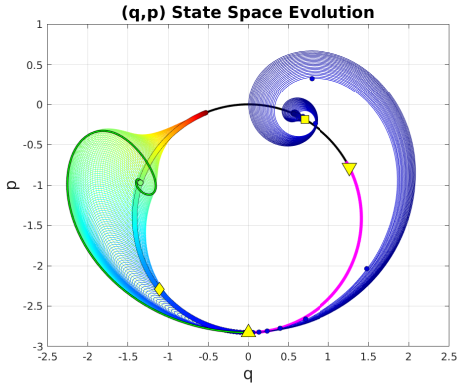

(b) High branch, $y_0 = x\;\Theta(x)$

Figure B.8: ND1P (q, p) state space evolution for a range of x-values from -5 (red) to $+5$ (blue); the trajectory for $x = 0$ is plotted in black. The unstable mid branch (magenta) covers an arc whose angle is dependent on γ, (B.35) which for $\gamma = 0.5$, $\theta_b = 2\pi/3 = 120°$, and so occupies one third of the SS distribution in $\mathbb{C}$. The high-branch of the SS3 region is the arc in the lower portion of the SS (up-triangle to diamond), and the low-branch is arc in the upper region (square to down-triangle).

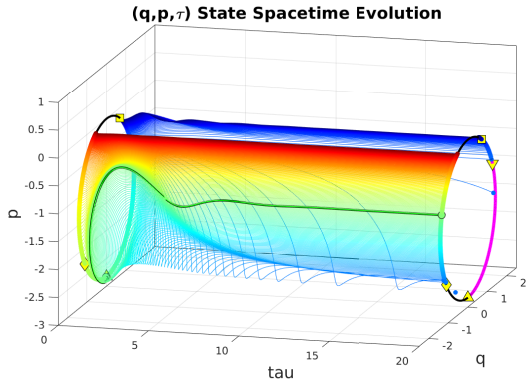

(a) Low branch, $y_0 = \frac{1}{3}\,x\;\Theta(x)$

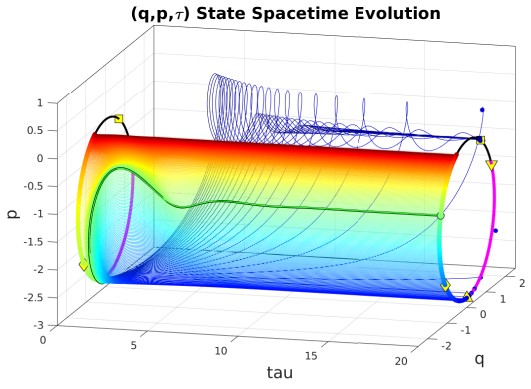

(b) High branch, $y_0 = x\;\Theta(x)$

Figure B.9: ND1P (q, p, τ) state spacetime evolution, a rotation of Fig. B.8 in ND1P time. The difference in the response of the higher x portion (blue) is clearly seen.

The simulations presented in this section are at $\gamma = 0.5$, for which the crest SS can be expressed by $\alpha_{\text{crest}} = -i2 = 2\,e^{-i\pi/2}$, the barrel point angle is $\theta_{\text{barrel}}(0.5) = -i\,\ln\left[\frac{1}{2}(-1+i\sqrt{3})\right] = \frac{2\pi}{3}$ corresponding to a SS at $\alpha_{\text{barrel}}(0.5) = \frac{1}{2}(\sqrt{3}-i) = e^{-i\pi/6}$. These values can be mapped into the ND1P position–momentum state space, thus the crest point is located at $(q,p)^{\gamma=0.5}_{\text{crest}} \approx (0,\,-2\sqrt{2})$ (up-triangle in Fig. B.8), and the barrel point at $(q,p)^{\gamma=0.5}_{\text{barrel}} = \left(\sqrt{\frac{3}{2}},\,\frac{-1}{\sqrt{2}}\right)$ (down-triangle in Fig. B.8). The above-barrel and below

The impact of non-linearity across the spectral region can be identified by the non-circular elliptical paths, since the linear (QHO) trajectories are exponentially decaying circular spiral orbits. The trajectories for $x < x_{\text{barrel}}$ (red to green) are approximately equal for both initial conditions, however the high x-values (corresponding to higher frequencies in the dimensioned QAO model) are attracted to different regions of the SS circle.

B.6 Summary

This appendix represents an abstraction and distillation of the core theoretical results of the main thesis to the simplest mathematical expressions. The methodologies and results are parallel to those that I have demonstrated in **Chapter 3** to **5**. The identification for a dimensionless parameter that characterises the QAO model response is a significant discovery that I made frequent use of throughout the development of the theoretical work to elucidate and explore the fundamental behaviour, as well as during the establishment of the numerical simulation of the catalytic model to ensure that I am capturing phase transition (SS3) behaviour.

The ND1P parameter is used in the approximate algebraic expressions for the crest and barrel bifurcation points of the dimensioned QAO model at the end of **Chapter 4**. The ND1P parameter value for the QAO EoM simulation conditions of **Chapter 5** are shown in Fig. B.10, for the benzene in water (a), and benzene in MalL (b). This offers an equivalent method for determining which vibrational modes are in the SS3 phase transition region (stars), and which are in the SS1 regime (circles).

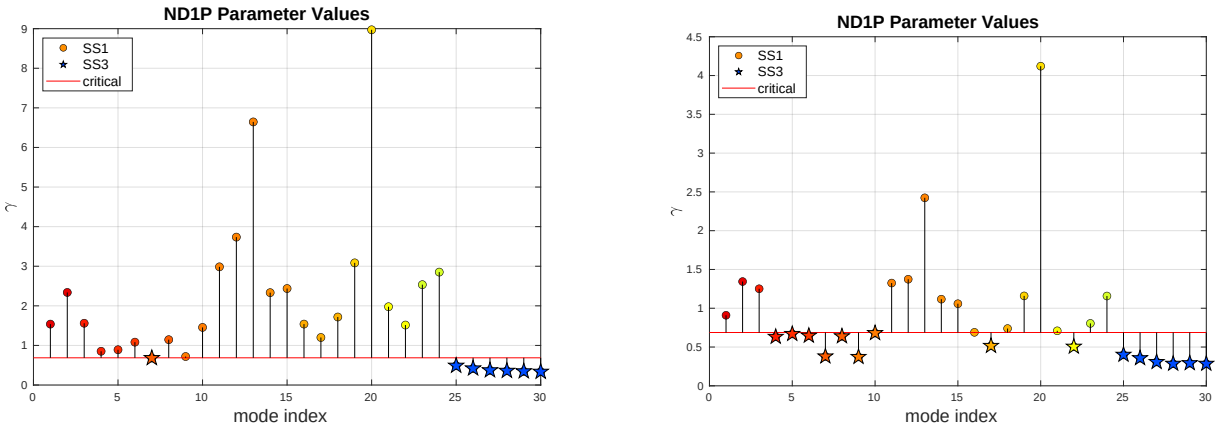

(a) water **(b)** Mall

Figure B.10: The corresponding ND1P parameter values, γ, for each vibrational mode in the QAO EoM simulations of **Chapter 5**. The benzene–water simulation (panel a) has larger values for γ and therefore shows that most modes are in the SS1 regime (circles), whereas for the benzene–MalL simulation (panel b), more parameter values are under the critical γ_c, and hence the molecule has more modes in the SS3 phase transition regime (stars).

Appendix C

Full Catalytic QAO EoM Numerical Solution

The QAO EoMs for all vibrational modes are solved using the internal function `ode45` in MATLAB, which performs numerical integration on a system of non-stiff differential equations. Thus the numerical solution to the QAO EoMs is implemented by

```
[t,X] = ode45( @(t,X) ode_EoM(t,X,P_EoM), t_window, X0_obs, ode_options )
```
(C.1)

where the output variables `X` is the array of the time series solutions for the quantum states of all vibrational modes, and `t` is the associated time vector whose elements are the sample times that the EoMs are computed at. The number of sampled time states (number of elements in the 1D array `t`) is determined by MATLAB and can be on the order of 10^5 to ensure that the high-frequency motions are accurately captured. The following sections detail the parameters that are used in the `ode45` function call to solve the full enzymatic EoMs, and the solutions capture the evolution dynamics of a molecule in response to an enzyme.

C.1 Constructing the Superset Array of Molecular Quantum States

All of the ODE numerical integration functions in MATLAB solve equations of the form

$$\partial_t \, \mathbf{X}(t) \;=\; \mathbf{f}(t, \, \mathbf{X}(t)) \tag{C.2}$$

and the result is the time series solution of an array, $\mathbf{X}(t)$, due to the forcing function array $\mathbf{f}$, which can be time- and state-dependent. The catalytic QAO EoM array is the superset of the annihilation, creation, and number expectation values *for each* vibrational mode, thus the total number of elements in $\mathbf{X}$ is triple the number of vibrational modes. By letting `ann` be the column vector of $\langle \hat{a}_k \rangle$ for all modes k, and similarly `cre`, `num` for $\langle \hat{a}_k^\dagger \rangle$ and $\langle \hat{n}_k \rangle$, respectively, I then choose to construct the superset array by

$$\texttt{X} = \begin{bmatrix} \texttt{ann} \\ \texttt{cre} \\ \texttt{num} \end{bmatrix} \tag{C.3}$$

If `m` is the total number of modes, then the k^{th} vibrational mode quantum states are the elements

$$\langle \hat{a}_k \rangle \;==\; \texttt{X(k)} \tag{C.4a}$$
$$\langle \hat{a}_k^\dagger \rangle \;==\; \texttt{X(k+m)} \tag{C.4b}$$
$$\langle \hat{n}_k \rangle \;==\; \texttt{X(k+2*m)} \tag{C.4c}$$

Thus the array $\mathbf{X}$ for use in (C.2) has been defined, and once the EoMs are codified in terms of $\mathbf{X}$, a solution can be found by numerical integration over a period of time.

C.2 Sweeping over Observed Stimulus Frequencies

Since each quantum state has a spectral distribution (each is a function of forcing frequency ω), scalar elements cannot capture the full dynamics. To resolve this, the EoMs are solved via (C.1) independently over a range of sampled forcing frequencies and collected together later. Letting i be the index for the i^{th} observation state with corresponding frequency, ω_i, then the codified elements of the `ode45` output are related to the mathematical objects by

$$\langle \hat{a}_k \rangle(\omega_i) \;==\; \texttt{X(k, i)} \tag{C.5a}$$
$$\langle \hat{a}_k^\dagger \rangle(\omega_i) \;==\; \texttt{X(k+m, i)} \tag{C.5b}$$
$$\langle \hat{n}_k \rangle(\omega_i) \;==\; \texttt{X(k+2*m, i)} \tag{C.5c}$$

where `X` is a matrix whose rows are the quantum states and whose columns are the sampled frequencies. The choice of how many frequencies to sample, `N_w_EoM`, is a major decision for the trade-off in accuracy and computational resources. Using the computational power available to me for this work, I have been able to run simulations at a maximum of 400 linearly spaced frequencies between 0 and 120 THz.

C.3 EoM Input Parameter Cell

The first entry in the `ode45` braces, `ode_EoM`, is the system of forcing functions (RHS of (C.2)) which represents the QAO EoMs. To begin codifying the QAO EoMs to be used in `ode45`, the EoMs must be cast in terms of the function handles for time and superset state, `(t,X)`, however, the molecular parameters must be passed to the function that constructs `ode_EoM`. The EoM parameters are: natural mode frequencies, ω_k; anharmonic Hamiltonian coefficient array, ξ_{kj}; total VDR, Υ_k; thermal background phonon number, $\bar{n}_k$; and the enzyme stimulus, B_k. Each of these is prepackaged into an initially empty cell and populated by a loop over observation

frequencies

```
P_EoM.w = w_vib
P_EoM.xi = xi
P_EoM.Y = Y_vib
P_EoM.n = n_pl_vib
P_EoM.B = B_vib
```
(C.6)

The initial state array and detuning frequency are of course dependent on observation frequency, and so the parameter cell must be updated in the loop by, `P_EoM.w_obs=w_EoM(i)`, and `X0_obs=X0(:,i)`. If the enzyme stimulus, or any other quantity, were to be a spectral distribution, $B_k(\omega)$, then the parameter cell must also be updated in the `i` loop.

C.4 Codified QAO EoMs

The MATLAB ODE solver `ode45` is used to solve the EoMs by an external function call `Xdot =ode_EoM(t,X,P)` by a loop over all molecular vibrational modes, `for k=1:m`, where `m` is the count of normal modes. The analytic element-wise expressions of the EoM forcing function array, $\mathbf{f}$, are then

$$\partial_t\langle\hat{a}_k(t)\rangle = [\mathbf{f}]_k = -iB_k - (\Upsilon_k - i\phi_k)\, X_k - 2i\,\xi_{kk}\, X_{k+2m}\, X_k \tag{C.7a}$$

$$\partial_t\langle\hat{a}_k^\dagger(t)\rangle = [\mathbf{f}]_{k+m} = +iB_k - (\Upsilon_k + i\phi_k)\, X_{k+m} + 2i\,\xi_{kk}\, X_{k+2m}\, X_{k+m} \tag{C.7b}$$

$$\partial_t\langle\hat{n}_k(t)\rangle = [\mathbf{f}]_{k+2m} = -2\Upsilon_k\,(X_{k+2m} - \bar{n}_k) - iB_k\,(X_{k+m} - X_k) \tag{C.7c}$$

for vibrational mode index is $k \in [1,\, m]$. These are then codified into the MATLAB environment, and then used to solve the EoMs in a nested `for` loop over vibrational modes and observation frequencies using the function call `ode_EoM`. The codified quantum state EoMs are then

```
Xdot(k)   =  - 1i *P.B(k)  -  ( P.Y(k) - 1i *phi ) *X(k)
             - 2i *P.xi(k,k) *X(k+2m) *X(k)

Xdot(k+m) =  + 1i *P.B(k)  -  ( P.Y(k) + 1i *phi ) *X(k+m)
             + 2i *P.xi(k,k) *X(k+2m) *X(k+m)

Xdot(k+2*m) =  - 2 *P.Y(k) * ( X(k+2m) - P.n(k) )
               - 1i *P.B(k) * ( X(k+m) - X(k) )
```
(C.8)

where $\phi_k \equiv$ `phi`. Once the algorithm has completed the loop over all modes, `k = 1:m`, the output structure `Xdot` fulfils the function call of the MATLAB ODE solver.

C.5 Jacobian Sparsity Pattern

An option for running `ode45` is to specify the Jacobian sparsity pattern, `JPattern`, by a sparse matrix whose elements are one where there might be nonzero entries in the Jacobian matrix, or else zero and are not computed. The ODE solver uses the sparse matrix to improve computation time by omitting some trivial calculation. The sparse matrix is implemented by specifying `ode_options = odeset('JPattern',jpattern(m))`, where `jpattern` is a function call that generates the sparsity pattern of size `m`, the number of modes, `JP = jpattern(m)`. The Jacobian, $\mathbf{J}$, is a matrix whose elements are the state derivatives of the EoM forcing function array

$$\mathbf{J} \;=\; \frac{\partial(\partial_t \mathbf{X})}{\partial \mathbf{X}} \;=\; \frac{\partial \mathbf{f}(\mathbf{X})}{\partial \mathbf{X}} \tag{C.9}$$

whose elements are, $[\mathbf{J}]_{ij} = \frac{\partial f_i}{\partial X_j}$. The Jacobian sparsity pattern matrix, `JP`, is such that all of the elements are either zero if $[\mathbf{J}]_{ij} = 0$, or one if $[\mathbf{J}]_{ij} \neq 0$. For the number of modes, m, the indices $i, j \in [1,\, m]$ are reserved for the annihilation operator, $i, j \in [m+1,\, 2m]$ for the creation operator, and $i, j \in [2m+1,\, 3m]$ for the phonon number operator. The sparsity pattern is constructed by partitioning into block matrices

$$\texttt{JP} \;=\; \begin{bmatrix} \texttt{J\_aa} & \texttt{J\_ac} & \texttt{J\_an} \\ \texttt{J\_ca} & \texttt{J\_cc} & \texttt{J\_cn} \\ \texttt{J\_na} & \texttt{J\_nc} & \texttt{J\_nn} \end{bmatrix} \tag{C.10}$$

where the `a,c,n` subscripts denote the annihilation, creation and number states, respectively; for example, `J_an` contains the derivatives of the annihilation forcing functions with all phonon numbers, and produces a square matrix of size `m`. The elements of `JP` are computed using the EoMs in terms of $\mathbf{X}$ (C.7). Using vibrational mode indices $k, l \in [1,\, m]$, the `J_aa` block is populated by

$$\frac{\partial f_k}{\partial X_l} \;=\; \Big((-\Upsilon_k + i\phi_k) \;-\; 2i\;\xi_{kk}\;X_{k+2m} \Big)\;\delta_{kl} \;-\; 2i\;X_k\;\frac{\partial X_{k+2m}}{\partial X_l} \tag{C.11}$$

Since the annihilation, creation and number states are dynamically distinct variables,

$$\frac{\partial \langle \hat{a}_k \rangle}{\partial \langle \hat{a}_l^\dagger \rangle} \;=\; \frac{\partial \langle \hat{a}_k \rangle}{\partial \langle \hat{n}_l \rangle} \;=\; \frac{\partial \langle \hat{a}_k^\dagger \rangle}{\partial \langle \hat{n}_l \rangle} \;=\; 0 \tag{C.12}$$

for any indexed quantity, $\frac{\partial X_k}{\partial X_l} = \delta_{kl}$, and there is no possible $j \in [1, m]$ such that $X_j = X_{k+2m}$, therefore, $\frac{\partial X_{k+2m}}{\partial X_l} = 0$. The elements of the annihilation–annihilation Jacobian sparsity matrix block are, $[\texttt{J\_aa}]_{k,l} = \delta_{kl}$, and so `J_aa` is the identity matrix of size `m`. The top middle block `J_ac` represents the derivatives of the annihilation forcing function, f_k, with the creation operator, however since f_k is not explicitly dependent on the creation state, all of the derivatives are zero, $\frac{\partial f_k}{\partial X_{l+m}} = 0$, hence, the `J_ac` block is populated entirely by zeroes, $[\texttt{J\_ac}]_{k,l} = 0$, and no EoM states need to be computed. The annihilation–number block, `J_an`, is populated by

$$\frac{\partial f_k}{\partial X_{l+2m}} \;=\; i\left(\frac{\partial \phi_k}{\partial X_{l+2m}}\right) X_k \;-\; 2i\;\xi_{kk}\;\delta_{kl}\;X_k \tag{C.13}$$

The detuning frequency ϕ_k contains the intramolecular anharmonic frequency shift, η_k, (4.13) which has contributions from all molecular phonon modes. The derivative of η_k with any other phonon number $\langle \hat{n}_l \rangle$, is

$$\frac{\partial \eta_k}{\partial \langle \hat{n}_l \rangle} \;=\; \sum_{j>k}^{m} \xi_{kj}\; \delta_{jl} \;=\; \xi_{kl}\; (1 - \delta_{kl}) \tag{C.14}$$

where $(1 - \delta_{kl})$ omits the $j = k$ term, thus, $\frac{\partial \eta_k}{\partial \langle \hat{n}_k \rangle} = 0$. The derivative of the observed detuning ϕ_k with any vibrational mode phonon number is

$$\frac{\partial \phi_k}{\partial X_{l+2m}} \;=\; -\; \frac{\partial \eta_k}{\partial X_{l+2m}} \;=\; -\,\xi_{kl}\; (1 - \delta_{kl}) \tag{C.15}$$

Substituting this result into the f_k derivative gives

$$\frac{\partial f_k}{\partial X_{l+2m}} \;=\; -\,i\,\Big(\xi_{kl} \;+\; \xi_{kk}\; \delta_{kl}\Big)\; X_k \tag{C.16}$$

since the derivatives of f_k with X_{l+2m} are able to be non-zero for all elements, the Jacobian sparsity pattern is a block of ones, $[\texttt{J\_aa}]_{k,l} = 1$, and there are no computational savings. The second row of block matrices pertaining to the derivatives of the creation forcing functions, f_{k+m}, can be populated using the annihilation blocks by symmetry and similar arguments: $[\texttt{J\_ca}]_{k,l} = [\texttt{J\_ac}]_{k,l}$, $[\texttt{J\_cc}]_{k,l} = [\texttt{J\_aa}]_{k,l}$, and $[\texttt{J\_cn}]_{k,l} = [\texttt{J\_an}]_{k,l}$. The phonon number forcing function derivatives are

$$\frac{\partial f_{k+2m}}{\partial X_j} \;=\; +\,iB_k\; \delta_{kj} \tag{C.17a}$$

$$\frac{\partial f_{k+2m}}{\partial X_{j+m}} \;=\; -\,iB_k\; \delta_{kj} \tag{C.17b}$$

$$\frac{\partial f_{k+2m}}{\partial X_{j+2m}} \;=\; -\,2\Upsilon_k\; \delta_{kj} \tag{C.17c}$$

whose sparsity matrices are all the identity matrix, $[\texttt{J\_an}]_{k,l} = [\texttt{J\_cn}]_{k,l} = [\texttt{J\_nn}]_{k,l} = \delta_{kj}$. With the forcing function array derivatives computed, the Jacobian sparsity matrix is thus determined, and the `jpattern(m)` function call is solved using the block matrices for each quantum state operator: annihilation `J_aa=eye(m)`, `J_ac=zeros(m)`, `J_an=ones(m)`; creation `J_ca=J_ac`, `J_cc=J_aa`, `J_cn=J_an`; and number `J_na=eye(m)`, `J_nc=eye(m)`, `J_nn=eye(m)`. Here, `eye(m)` is the identity matrix of size `m`$\times$`m`, and `ones(m)` and `zeros(m)` are square matrices of the same size containing all 1 or 0, respectively. The Jacobian sparsity matrix is finally composed using (C.10), and passed out of the function to be used by the ODE solver. The Jacobian sparsity matrix of size `m` $\times$ `m` is

$$\texttt{JP(m)} \;=\; \begin{bmatrix} \texttt{eye(m)} & \texttt{zeros(m)} & \texttt{ones(m)} \\ \texttt{zeros(m)} & \texttt{eye(m)} & \texttt{ones(m)} \\ \texttt{eye(m)} & \texttt{eye(m)} & \texttt{eye(m)} \end{bmatrix} \tag{C.18}$$

C.6 Computational Savings

An estimate of the computation savings of using the sparsity matrix can be made by comparing the total number of elements in `JP` to the number of non-zero elements. The matrix `JP` is a square matrix of size (`3m` $\times$ `3m`) and therefore has $(3m)^2$ elements. The number of non-zero elements in the identity matrix, `eye(m)`, is `m`; the matrix of ones has m^2 non-zero elements; and the zero matrix has no non-zero elements. The total number of non-zero elements is the sum of two matrices of ones and five identity matrices, $2m^2 + 5m$. By expressing the computational load, CL, as a ratio of the count of computed elements to the total count

$$\mathrm{CL}(m) \;=\; \frac{2m^2 + 5m}{(3m)^2} \;=\; \frac{2m + 5}{9m} \tag{C.19}$$

shows that in the limit of large molecules, $\mathrm{CS}(\infty) = \frac{2}{9}$, the computational load when using the sparsity matrix is 22.2% that of the task run without. For benzene, $\mathrm{CL}(30) = 0.241$, which is 92% of the asymptotic value.

C.7 Extracting Results from the Quantum State Superset Array

In order to keep high accuracy for the fast oscillations in state, `ode45` will dynamically adjust the time step at which each `X` states that are sampled. This procedure results in time series solutions with a varying number of elements. To resolve this, the outputs `[t,X]` of `ode45` at each `i` are collected into cell arrays for time, `TIME_c{i}=t`, and state, `X_c{i}=X`, then `[t,X]` are cleared from memory, and the loop progresses through to the next observation frequency state. If using `N_w_EoM` many frequency samples, the resultant collection cell array `X_c` contains `N_w_EoM` cells, and each cell is an array whose columns are the quantum states and whose rows are the time series solutions. All of the data containing the evolutions of the molecule over time in response to an enzyme and its environment have thus been computed, and are stored in the superset collection cell array, `Xc`, and its associated cell array for time, `TIME_c`, where the cells represent observation frequencies of the molecular response dynamics. The next task is to unpack and put all trajectories on the same time line.

The number of time samples that the ODE solver uses to approximate a continuous integration is a major consideration in establishing an appropriate solution. I have chosen to allow `ode45` to use as many time points as necessary in order to accurately capture the high-frequency and rapidly evolving dynamics of each vibrational mode, and then to interpolate after the ODE solving computation is complete. The number of time samples that the ODE solver used for each vibrational mode, `c_raw_EoM`, can be found by performing a `for` loop over the cells in `Xc` and calling `c_raw_EoM(i) = size(Xc{i},1)`. There may be dozens of thousands of time points used to capture the large-amplitude initial dynamics and the low-amplitude persisting oscillations. Thus there is a careful decision to be made about choosing how many time interpolation points to store as it will result in a very large data file. I have placed the option for setting the maximum number of time points at the top of the script such that it can be adjusted for quality and data size.

The user specifies `N_t_EoM` to be the maximum number of time points to store. The EoM timeline (1D vector of time samples) is then defined by a linearly spaced array with `N_t_int` points between zero and the simulation duration. Before unpacking `Xc`, there are preallocation arrays defined for the annihilation (`ANN`), creation (`CRE`), and number (`NUM`) states `zeros( N_modes, N_w_EoM, N_t_int )`, the solution states are rank-3 tensors whose indices represent vibrational mode index, sampled frequencies, and sampled times, respectively. The solution arrays are populated in a nested `for` loop over vibrational mode k, and observation frequency index i, where at each pass a spline interpolation is performed and entered

```
ANN(k,i,:)  = interp1( TIME_c{i}, Xc{i}(:,k),     t_EoM, 'spline' )    (C.20a)
CRE(k,i,:)  = interp1( TIME_c{i}, Xc{i}(:,k+m),   t_EoM, 'spline' )    (C.20b)
NUM(k,i,:)  = interp1( TIME_c{i}, Xc{i}(:,k+2*m), t_EoM, 'spline' )    (C.20c)
```

The collection cell arrays `Xc, TIME_c` can then safely be cleared to minimise workspace storage requirements. The evolutions of the quantum state are collected into rank-3 tensors of equal sizes,

$$\langle \hat{a}_k(t_j, \omega_i) \rangle \;==\; \texttt{ANN(k,} \quad \texttt{i, j)} \tag{C.21a}$$

$$\langle \hat{a}_k^\dagger(t_j, \omega_i) \rangle \;==\; \texttt{CRE(k+m,} \quad \texttt{i, j)} \tag{C.21b}$$

$$\langle \hat{n}_k(t_j, \omega_i) \rangle \;==\; \texttt{NUM(k+2*m,} \; \texttt{i, j)} \tag{C.21c}$$

whose tensor indices are: the vibrational mode index, k, the forcing frequency index, ω_i, and the interpolated timeline index, t_j. The position (`POS`) and momentum (`MOM`) evolutions of state are computed using the mapping from the creation and annihilation representation stored in the `GEN` substructure

```
POS = P.GEN.UC.creann2pos( CRE, ANN )    (C.22a)
MOM = P.GEN.UC.creann2mom( CRE, ANN )    (C.22b)
```

This concludes the solution of the EoMs, the output data is then added to the parameter cell, `P.EoM.ANN = ANN`, and similarly for `CRE, NUM, POS, MOM`. The full solutions to the EoMs are now all packaged in `P` for plotting and saving.

C.8 Building the Molecular Energy Spectrogram

The final step is to build the energy response spectrogram from the number operator expectation values of all vibrational modes. The expectation value for energy is given by the trace average of the total Hamiltonian operator, $E = \langle \hat{\mathcal{H}} \rangle$. The physical interpretation of $E(t, \omega)$, is the expected value of molecular energy for a given forcing frequency at a particular time. Therefore, the molecular energy response spectrogram is constructed upon substitution of (C.21c) into the QAO Hamiltonian. The energy response spectra at the end of the simulation approximates the resting quantum state of the molecule due to the stimulus from its environment, if the simulation duration is sufficiently large enough for all relaxation oscillations to dissipate.

References

[1] Alistair Steyn-Ross and Moira Steyn-Ross. *Modeling phase transitions in the brain*, volume 509. Springer, 2010.

[2] Moira L Steyn-Ross. Laser excitation of vibrational modes of molecules. Master's thesis, University of Waikato, 1979.

[3] Alan D McNaught, Andrew Wilkinson, et al. *Compendium of chemical terminology*, volume 1669. Blackwell Science Oxford, 1997.

[4] Donald G Truhlar, Bruce C Garrett, and Stephen J Klippenstein. Current status of transition-state theory. *The Journal of physical chemistry*, 100(31):12771–12800, 1996.

[5] Sam Hay and Nigel S Scrutton. Good vibrations in enzyme-catalysed reactions. *Nature chemistry*, 4(3):161–168, 2012.

[6] Mireia Garcia-Viloca, Jiali Gao, Martin Karplus, and Donald G Truhlar. How enzymes work: analysis by modern rate theory and computer simulations. *Science*, 303(5655):186–195, 2004.

[7] Hans Frauenfelder, Guo Chen, Joel Berendzen, Paul W Fenimore, Helén Jansson, Benjamin H McMahon, Izabela R Stroe, Jan Swenson, and Robert D Young. A unified model of protein dynamics. *Proceedings of the National Academy of Sciences*, 106(13):5129–5134, 2009.

[8] Pratul K Agarwal. Enzymes: An integrated view of structure, dynamics and function. *Microbial cell factories*, 5:1–12, 2006.

[9] Pratul K Agarwal. Role of protein dynamics in reaction rate enhancement by enzymes. *Journal of the American Chemical Society*, 127(43):15248–15256, 2005.

[10] Svante Arrhenius. Über die dissociationswärme und den einfluss der temperatur auf den dissociationsgrad der elektrolyte. *Zeitschrift für physikalische Chemie*, 4(1):96–116, 1889.

[11] Henry Eyring. The activated complex in chemical reactions. *The Journal of Chemical Physics*, 3(2):107–115, 1935.

[12] Vickery L Arcus, Erica J Prentice, Joanne K Hobbs, Adrian J Mulholland, Marc W Van der Kamp, Christopher R Pudney, Emily J Parker, and Louis A Schipper. On the temperature dependence of enzyme-catalyzed rates. *Biochemistry*, 55(12):1681–1688, 2016.

[13] Vickery L Arcus and Adrian J Mulholland. Temperature, dynamics, and enzyme-catalyzed reaction rates. *Annual review of biophysics*, 49:163–180, 2020.

[14] Michael J Seewald, Kumar Pichumani, Cheri Stowell, Benjamin V Tibbals, Lynne Regan, and Martin J Stone. The role of backbone conformational heat capacity in protein stability:

temperature dependent dynamics of the B1 domain of streptococcal protein G. *Protein Science*, 9(6):1177–1193, 2000.

[15] Javier Gomez, Vincent J Hilser, Dong Xie, and Ernesto Freire. The heat capacity of proteins. *Proteins: Structure, Function, and Bioinformatics*, 22(4):404–412, 1995.

[16] Vickery L Arcus and Christopher R Pudney. Change in heat capacity accurately predicts vibrational coupling in enzyme catalyzed reactions. *FEBS letters*, 589(17):2200–2206, 2015.

[17] Louis A Schipper, Joanne K Hobbs, Susanna Rutledge, and Vickery L Arcus. Thermodynamic theory explains the temperature optima of soil microbial processes and high Q10 values at low temperatures. *Global change biology*, 20(11):3578–3586, 2014.

[18] John F Brandts. The thermodynamics of protein denaturation. i. the denaturation of chymotrypsinogen. *Journal of the American Chemical Society*, 86(20):4291–4301, 1964.

[19] Simon A Hawley. Reversible pressure-temperature denaturation of chymotrypsinogen. *Biochemistry*, 10(13):2436–2442, 1971.

[20] Yee-Joo Tan, Mikael Oliveberg, and Alan R Fersht. Titration properties and thermodynamics of the transition state for folding: comparison of two-state and multi-state folding pathways. *Journal of molecular biology*, 264(2):377–389, 1996.

[21] Joanne K Hobbs, Wanting Jiao, Ashley D Easter, Emily J Parker, Louis A Schipper, and Vickery L Arcus. Change in heat capacity for enzyme catalysis determines temperature dependence of enzyme catalyzed rates. *ACS chemical biology*, 8(11):2388–2393, 2013.

[22] Alexandre Cipolla, François Delbrassine, Jean-Luc Da Lage, and Georges Feller. Temperature adaptations in psychrophilic, mesophilic and thermophilic chloride-dependent alpha-amylases. *Biochimie*, 94(9):1943–1950, 2012.

[23] Salvino D'Amico, Jean-Claude Marx, Charles Gerday, and Georges Feller. Activity-stability relationships in extremophilic enzymes. *Journal of Biological Chemistry*, 278(10):7891–7896, 2003.

[24] JE Lennard and I Jones. On the determination of molecular fields.—i. from the variation of the viscosity of a gas with temperature. *Proceedings of the Royal Society of London. Series A, containing papers of a mathematical and physical character*, 106(738):441–462, 1924.

[25] Xipeng Wang, Simón Ramírez-Hinestrosa, Jure Dobnikar, and Daan Frenkel. The Lennard-Jones potential: when (not) to use it. *Physical Chemistry Chemical Physics*, 22(19):10624–10633, 2020.

[26] Xi Xu and Yang Yang. Full-quantum descriptions of molecular systems from constrained nuclear–electronic orbital density functional theory. *The Journal of Chemical Physics*, 153(7), 2020.

[27] Fabijan Pavošević, Tanner Culpitt, and Sharon Hammes-Schiffer. Multicomponent quantum chemistry: Integrating electronic and nuclear quantum effects via the nuclear–electronic orbital method. *Chemical Reviews*, 120(9):4222–4253, 2020.

[28] Xi Xu and Yang Yang. Constrained nuclear-electronic orbital density functional theory: Energy surfaces with nuclear quantum effects. *The Journal of Chemical Physics*, 152(8), 2020.

[29] Ivet Bahar, Timothy R Lezon, Ahmet Bakan, and Indira H Shrivastava. Normal mode analysis of biomolecular structures: functional mechanisms of membrane proteins. *Chemical reviews*, 110(3):1463–1497, 2010.

[30] Fedor I Fedorov. *Theory of elastic waves in crystals*. Springer Science & Business Media, 2013.

[31] Jan W Jaeken and Stefaan Cottenier. Solving the christoffel equation: Phase and group velocities. *Computer Physics Communications*, 207:445–451, 2016.

[32] Thomas Vasileiadis, Jeena Varghese, Visnja Babacic, Jordi Gomis-Bresco, Daniel Navarro Urrios, and Bartlomiej Graczykowski. Progress and perspectives on phononic crystals. *Journal of Applied Physics*, 129(16), 2021.

[33] Abdelkrim Khelif and Ali Adibi. Phononic crystals. *Berlin, Germany, Springer*, 10:978–1, 2015.

[34] James Deane Patterson and Bernard C Bailey. *Solid-state physics: introduction to the theory*. Springer Science & Business Media, 2007.

[35] Alan K Cooper, Frederick J Davey, and JC Behrendt. Seismic stratigraphy and structure of the Victoria Land basin, western Ross Sea, Antarctica. 1987.

[36] Bjarne SG Almqvist and David Mainprice. Seismic properties and anisotropy of the continental crust: Predictions based on mineral texture and rock microstructure. *Reviews of Geophysics*, 55(2):367–433, 2017.

[37] Valeria La Saponara. 1.19 an overview of wave propagation techniques in fiber-reinforced polymer composite plates. In Peter W.R. Beaumont and Carl H. Zweben, editors, *Comprehensive Composite Materials II*, pages 490–501. Elsevier, Oxford, 2018.

[38] H.L. Alberts. Ultrasonic wave velocities in solids: Elastic properties, temperature, and pressure dependence. In K.H. Jürgen Buschow, Robert W. Cahn, Merton C. Flemings, Bernhard Ilschner, Edward J. Kramer, Subhash Mahajan, and Patrick Veyssière, editors, *Encyclopedia of Materials: Science and Technology*, pages 1–5. Elsevier, Oxford, 2002.

[39] HJ McSkimin. Ultrasonic measurement techniques applicable to small solid specimens. *The Journal of the Acoustical Society of America*, 22(4):413–418, 1950.

[40] Léon Brillouin. Tensors in mechanics and elasticity. 1964.

[41] Victor Giurgiutiu. *Stress, Vibration, and Wave Analysis in Aerospace Composites: SHM and NDE Applications*. Academic Press, 2022.

[42] Vladislav Babuska and Michel Cara. *Seismic anisotropy in the Earth*, volume 10. Springer Science & Business Media, 1991.

[43] James P Wolfe. *Imaging phonons*. 1998.

[44] H.J. Pain. The physics of vibrations and waves. 2005.

[45] Pierre A Deymier. *Acoustic metamaterials and phononic crystals*, volume 173. Springer Science & Business Media, 2013.

[46] Steven Hayward and Bert L De Groot. Normal modes and essential dynamics. *Molecular Modeling of Proteins*, pages 89–106, 2008.

[47] H.J. Pain. The physics of vibrations and waves. 2005.

[48] Peter A Rinck. *Magnetic resonance in medicine: a critical introduction*. BoD–Books on Demand, 2019.

[49] Paul T Callaghan. *Principles of nuclear magnetic resonance microscopy*. Clarendon press, 1993.

[50] Ivana Kovacic and Michael J Brennan. *The Duffing equation: nonlinear oscillators and their behaviour*. John Wiley & Sons, 2011.

[51] Ivana Kovacic, Livija Cveticanin, Miodrag Zukovic, and Zvonko Rakaric. Jacobi elliptic functions: A review of nonlinear oscillatory application problems. *Journal of Sound and Vibration*, 380:1–36, 2016.

[52] B Van der Pol. A theory of the amplitude of free and forced triode vibrations, radio rev. 1 (1920) 701-710, 754-762. *Selected scientific papers*, 1, 1960.

[53] William Henry Louisell. Quantum statistical properties of radiation. 1973.

[54] Daniel Manzano. A short introduction to the Lindblad master equation. *AIP Advances*, 10(2):025106, 2020.

[55] Andy Chia, Leong Chuan Kwek, and C Noh. Relaxation oscillations and frequency entrainment in quantum mechanics. *Physical Review E*, 102(4):042213, 2020.

[56] Gyaneshwar P Srivastava. *The physics of phonons*. Routledge, 2019.

[57] Charles Kittel and Ching-yao Fong. *Quantum theory of solids*. Wiley, 1987.

[58] Kazutaka Nakamura. *Quantum Phononics*. Springer, 2019.

[59] Erwin Schrödinger. An undulatory theory of the mechanics of atoms and molecules. *Physical review*, 28(6):1049, 1926.

[60] Nouredine Zettili. Quantum mechanics: concepts and applications. 2009.

[61] Kenneth S Krane. *Modern physics*. John Wiley & Sons, 2019.

[62] Simon Eidelman, KG Hayes, KA ea Olive, M Aguilar-Benitez, C Amsler, D Asner, KS Babu, RM Barnett, J Beringer, PR Burchat, et al. Review of particle physics. *Physics letters B*, 592(1-4):1–5, 2004.

[63] Roger Penrose. *The road to reality: A complete guide to the laws of the universe*. Random house, 2005.

[64] Werner Heisenberg. Über den anschaulichen inhalt der quantentheoretischen kinematik und mechanik. *Zeitschrift für Physik*, 43(3-4):172–198, 1927.

[65] Brent Fultz. Vibrational thermodynamics of materials. *Progress in Materials Science*, 55(4):247–352, 2010.

[66] Tianli Feng and Xiulin Ruan. Quantum mechanical prediction of four-phonon scattering rates and reduced thermal conductivity of solids. *Physical Review B*, 93(4):045202, 2016.

[67] E Gruneissen. Zur theorie der spezifischen waerme. *Ann. Phys.(Leipzig)*, 39(4):789, 1912.

[68] Nicola Manini. *Introduction to the physics of matter: basic atomic, molecular, and solid-state physics*. Springer Nature, 2020.

[69] Dima Bolmatov, VV Brazhkin, and Kostya Trachenko. The phonon theory of liquid thermodynamics. *Scientific reports*, 2(1):421, 2012.

[70] Mikito Toda, Tamiki Komatsuzaki, Tetsuro Konishi, R Stephen Berry, and Stuart A Rice. *Geometric Structures of Phase Space in Multi-Dimensional Chaos: Applications to Chemical Reaction Dynamics in Complex Systems, Part A*, volume 130. John Wiley and Sons, 2005.

[71] AA Maradudin and AE Fein. Scattering of neutrons by an anharmonic crystal. *Physical Review*, 128(6):2589, 1962.

[72] JL Skinner and Kisam Park. Calculating vibrational energy relaxation rates from classical molecular dynamics simulations: Quantum correction factors for processes involving vibration- vibration energy transfer. *The Journal of Physical Chemistry B*, 105(28):6716–6721, 2001.

[73] Chihiro Hamaguchi and C Hamaguchi. *Basic semiconductor physics*, volume 9. Springer, 2010.

[74] Lintao Bu and John E Straub. Vibrational frequency shifts and relaxation rates for a selected vibrational mode in cytochrome C. *Biophysical journal*, 85(3):1429–1439, 2003.

[75] Hiroshi Fujisaki, Yong Zhang, and John E Straub. Time-dependent perturbation theory for vibrational energy relaxation and dephasing in peptides and proteins. *The Journal of chemical physics*, 124(14), 2006.

[76] Paul Adrien Maurice Dirac. The quantum theory of the emission and absorption of radiation. *Proceedings of the Royal Society of London. Series A, Containing Papers of a Mathematical and Physical Character*, 114(767):243–265, 1927.

[77] Paul Adrien Maurice Dirac. The quantum theory of dispersion. *Proceedings of the Royal Society of London. Series A, Containing Papers of a Mathematical and Physical Character*, 114(769):710–728, 1927.

[78] Hiroshi Fujisaki and John E Straub. Vibrational energy relaxation of isotopically labeled amide i modes in cytochrome c: Theoretical investigation of vibrational energy relaxation rates and pathways. *The Journal of Physical Chemistry B*, 111(41):12017–12023, 2007.

[79] LM Narducci, SS Mitra, RA Shatas, and CA Coulter. Selective multiple-photon absorption by an anharmonic molecule. *Physical Review A*, 16(1):247, 1977.

[80] The MathWorks Inc. Matlab version: 9.13.0 (r2022b), 2022.

[81] MJ ea Frisch, GW Trucks, HB Schlegel, GE Scuseria, MA Robb, JR Cheeseman, G Scalmani, VPGA Barone, GA Petersson, HJRA Nakatsuji, et al. Gaussian 16, revision c. 01, 2016.

[82] Mark James Abraham, Teemu Murtola, Roland Schulz, Szilárd Páll, Jeremy C Smith, Berk Hess, and Erik Lindahl. Gromacs: High performance molecular simulations through multi-level parallelism from laptops to supercomputers. *SoftwareX*, 1:19–25, 2015.

[83] RDII Dennington, Todd A Keith, John M Millam, et al. Gaussview, version 6.0. 16. *Semichem Inc Shawnee Mission KS*, 2016.

[84] Marcus D Hanwell, Donald E Curtis, David C Lonie, Tim Vandermeersch, Eva Zurek, and Geoffrey R Hutchison. Avogadro: an advanced semantic chemical editor, visualization, and analysis platform. *Journal of cheminformatics*, 4:1–17, 2012.

[85] Emma J Walker, Carlin J Hamill, Rory Crean, Michael S Connolly, Annmaree K Warrender, Kirsty L Kraakman, Erica J Prentice, Alistair Steyn-Ross, Moira Steyn-Ross, Christopher R Pudney, et al. Cooperative conformational transitions underpin the activation heat capacity in the temperature dependence of enzyme catalysis. *ACS catalysis*, 14(7):4379–4394, 2024.

[86] Hiroshi Fujisaki, Lintao Bu, and John E Straub. Vibrational energy relaxation (VER) of a CD stretching mode in cytochrome C. *Geometric Structures of Phase Space in Multidimensional Chaos: Applications to Chemical Reaction Dynamics in Complex Systems*, 130:179–203, 2005.

[87] Eric C Dykeman and Otto F Sankey. Normal mode analysis and applications in biological physics. *Journal of Physics: Condensed Matter*, 22(42):423202, 2010.

[88] Nobuhiro Go, Tosiyuki Noguti, and Testuo Nishikawa. Dynamics of a small globular protein in terms of low-frequency vibrational modes. *Proceedings of the National Academy of Sciences*, 80(12):3696–3700, 1983.

[89] Bernard Brooks and Martin Karplus. Harmonic dynamics of proteins: normal modes and fluctuations in bovine pancreatic trypsin inhibitor. *Proceedings of the National Academy of Sciences*, 80(21):6571–6575, 1983.

[90] Michael Levitt, Christian Sander, and Peter S Stern. The normal modes of a protein: Native bovine pancreatic trypsin inhibitor. *International Journal of Quantum Chemistry*, 24(S10):181–199, 1983.

[91] Ivet Bahar and AJ Rader. Coarse-grained normal mode analysis in structural biology. *Current opinion in structural biology*, 15(5):586–592, 2005.

[92] José Emilio Jimenez-Roldan, RB Freedman, Rudolf A Römer, and Stephen A Wells. Rapid simulation of protein motion: merging flexibility, rigidity and normal mode analyses. *Physical Biology*, 9(1):016008, 2012.

[93] Daniel C Harris and Michael D Bertolucci. *Symmetry and spectroscopy: an introduction to vibrational and electronic spectroscopy*. Courier Corporation, 1989.

[94] Steven Hayward et al. Normal mode analysis of biological molecules. *Computational biochemistry and biophysics*, pages 153–168, 2001.

[95] Rv H Austin, KW Beeson, L Eisenstein, H Frauenfelder, and IC Gunsalus. Dynamics of ligand binding to myoglobin. *Biochemistry*, 14(24):5355–5373, 1975.

[96] R Elber and Martin Karplus. Multiple conformational states of proteins: a molecular dynamics analysis of myoglobin. *Science*, 235(4786):318–321, 1987.

[97] Wenjun Zheng. Anharmonic normal mode analysis of elastic network model improves the modeling of atomic fluctuations in protein crystal structures. *Biophysical journal*, 98(12):3025–3034, 2010.

[98] M. J. Frisch, G. W. Trucks, H. B. Schlegel, G. E. Scuseria, M. A. Robb, J. R. Cheeseman, G. Scalmani, V. Barone, G. A. Petersson, H. Nakatsuji, X. Li, M. Caricato, A. V. Marenich, J. Bloino, B. G. Janesko, R. Gomperts, B. Mennucci, H. P. Hratchian, J. V. Ortiz, A. F. Izmaylov, J. L. Sonnenberg, D. Williams-Young, F. Ding, F. Lipparini, F. Egidi, J. Goings, B. Peng, A. Petrone, T. Henderson, D. Ranasinghe, V. G. Zakrzewski, J. Gao, N. Rega, G. Zheng, W. Liang, M. Hada, M. Ehara, K. Toyota, R. Fukuda, J. Hasegawa, M. Ishida, T. Nakajima, Y. Honda, O. Kitao, H. Nakai, T. Vreven, K. Throssell, J. A. Montgomery, Jr., J. E. Peralta, F. Ogliaro, M. J. Bearpark, J. J. Heyd, E. N. Brothers, K. N. Kudin, V. N. Staroverov, T. A. Keith, R. Kobayashi, J. Normand, K. Raghavachari, A. P. Rendell, J. C. Burant, S. S. Iyengar, J. Tomasi, M. Cossi, J. M. Millam, M. Klene, C. Adamo,

R. Cammi, J. W. Ochterski, R. L. Martin, K. Morokuma, O. Farkas, J. B. Foresman, and D. J. Fox. Gaussian 09 Revision A.02, 2016. Gaussian Inc. Wallingford CT.

[99] Joseph W Ochterski. Vibrational analysis in gaussian. *help@ gaussian. com*, 1999.

[100] Cathrine Bergh Christian Blau Eliane Briand Mahesh Doijade Stefan Fleischmann Vytas Gapsys Gaurav Garg Sergey Gorelov Gilles Gouaillardet Alan Gray M. Eric Irrgang Farzaneh Jalalypour Joe Jordan Christoph Junghans Prashanth Kanduri Sebastian Keller Carsten Kutzner Justin A. Lemkul Magnus Lundborg Pascal Merz Vedran Miletic Dmitry Morozov Szilard Pall Roland Schulz Michael Shirts Alexey Shvetsov Balint Soproni David van der Spoel Philip Turner Carsten Uphoff Alessandra Villa Sebastian Wingbermuehle Artem Zhmurov Mark Abraham, Andrey Alekseenko. Gromacs 2023.3, 2023.

[101] Peter W Atkins and Ronald S Friedman. *Molecular quantum mechanics*. Oxford university press, 2011.

[102] Paul K Weiner and Peter A Kollman. Amber: Assisted model building with energy refinement. a general program for modeling molecules and their interactions. *Journal of Computational Chemistry*, 2(3):287–303, 1981.

[103] Bernard R Brooks, Robert E Bruccoleri, Barry D Olafson, David J States, S a Swaminathan, and Martin Karplus. Charmm: a program for macromolecular energy, minimization, and dynamics calculations. *Journal of computational chemistry*, 4(2):187–217, 1983.

[104] Charlotte Froese Fischer. General hartree-fock program. *Computer physics communications*, 43(3):355–365, 1987.

[105] John C Slater. Atomic shielding constants. *Physical review*, 36(1):57, 1930.

[106] Peter MW Gill. Molecular integrals over gaussian basis functions. In *Advances in quantum chemistry*, volume 25, pages 141–205. Elsevier, 1994.

[107] Jeng-Da Chai and Martin Head-Gordon. Long-range corrected hybrid density functionals with damped atom–atom dispersion corrections. *Physical Chemistry Chemical Physics*, 10(44):6615–6620, 2008.

[108] RHWJ Ditchfield, Warren J Hehre, and John A Pople. Self-consistent molecular-orbital methods. ix. an extended gaussian-type basis for molecular-orbital studies of organic molecules. *The Journal of Chemical Physics*, 54(2):724–728, 1971.

[109] Max Born and W Heisenberg. Zur quantentheorie der molekeln. *Original Scientific Papers Wissenschaftliche Originalarbeiten*, pages 216–246, 1985.

[110] Valdis Blūms, Marcin Piotrowski, Mahmood I Hussain, Benjamin G Norton, Steven C Connell, Stephen Gensemer, Mirko Lobino, and Erik W Streed. A single-atom 3D sub-attonewton force sensor. *Science advances*, 4(3):eaao4453, 2018.

[111] Sydney Schreppler, Nicolas Spethmann, Nathan Brahms, Thierry Botter, Maryrose Barrios, and Dan M Stamper-Kurn. Optically measuring force near the standard quantum limit. *Science*, 344(6191):1486–1489, 2014.

[112] Julien Bloino, Malgorzata Biczysko, and Vincenzo Barone. Anharmonic effects on vibrational spectra intensities: infrared, raman, vibrational circular dichroism, and raman optical activity. *The Journal of Physical Chemistry A*, 119(49):11862–11874, 2015.

[113] Matthias Schmitz and Paul Tavan. Vibrational spectra from atomic fluctuations in dynamics simulations. i. theory, limitations, and a sample application. *The Journal of chemical physics*, 121(24):12233–12246, 2004.

[114] Silvia E Braslavsky. Glossary of terms used in photochemistry, (iupac recommendations 2006). *Pure and Applied Chemistry*, 79(3):293–465, 2007.

[115] Nataliya A Nikonenko, Dmitrii K Buslov, Nataliya I Sushko, and Rostislav G Zhbankov. Investigation of stretching vibrations of glycosidic linkages in disaccharides and polysaccarides with use of ir spectra deconvolution. *Biopolymers: Original Research on Biomolecules*, 57(4):257–262, 2000.

[116] Marc W Van Der Kamp, Erica J Prentice, Kirsty L Kraakman, Michael Connolly, Adrian J Mulholland, and Vickery L Arcus. Dynamical origins of heat capacity changes in enzyme-catalysed reactions. *Nature communications*, 9(1):1177, 2018.

[117] Daniel-Albert Schipper. Finding the good vibes of life, man: Identifying catalytic vibrations in enzyme catalysis. Master's thesis, The University of Waikato, 2020.

[118] Hung Dien, Charlotte M Deane, and Bernhard Knapp. Gro2mat: A package to efficiently read gromacs output in matlab, 2014.

[119] Michael Holmbe. Atom: a Matlab package for manipulation of molecular systems, 2019. "Clays and Clay Minerals".

[120] Hyuntae Na, Guang Song, and Daniel Ben-Avraham. Universality of vibrational spectra of globular proteins. *Biophysical Journal*, 110(3):53a, 2016.

[121] Erwin Schrödinger. Quantisierung als eigenwertproblem. *Annalen der physik*, 385(13):437–490, 1926.

[122] Richard P Feynman, Robert B Leighton, and Matthew Sands. The feynman lectures on physics; vol. i. *American Journal of Physics*, 33(9):750–752, 1965.

[123] Ying Wu and Xiaoxue Yang. Strong-coupling theory of periodically driven two-level systems. *Physical review letters*, 98(1):013601, 2007.

[124] Xin Yu and David M Leitner. Vibrational energy transfer and heat conduction in a protein. *The Journal of Physical Chemistry B*, 107(7):1698–1707, 2003.

[125] Xin Yu and David M Leitner. Heat flow in proteins: computation of thermal transport coefficients. *The Journal of chemical physics*, 122(5), 2005.

[126] David M Leitner. Energy flow in proteins. *Annu. Rev. Phys. Chem.*, 59:233–259, 2008.

[127] Aleksandr Sergeevich Davydov. The theory of molecular excitons. *Soviet Physics Uspekhi*, 7(2):145, 1964.

[128] Carlos M Bustamante, Tchavdar N Todorov, Cristián G Sánchez, Andrew Horsfield, and Damian A Scherlis. A simple approximation to the electron–phonon interaction in population dynamics. *The Journal of Chemical Physics*, 153(23), 2020.

[129] Simon Gelin, Alexandre Champagne-Ruel, and Normand Mousseau. Enthalpy-entropy compensation of atomic diffusion originates from softening of low frequency phonons. *Nature communications*, 11(1):3977, 2020.

[130] Vincenzo Barone. Anharmonic vibrational properties by a fully automated second-order perturbative approach. *The Journal of chemical physics*, 122(1):014108, 2005.

[131] Eizi Hirota. Anharmonic potential function and equilibrium structure of methane. *Journal of Molecular Spectroscopy*, 77(2):213–221, 1979.

[132] William H Miller, Rigoberto Hernandez, Nicholas C Handy, Dylan Jayatilaka, and Andrew Willetts. Ab initio calculation of anharmonic constants for a transition state, with application to semiclassical transition state tunneling probabilities. *Chemical physics letters*, 172(1):62–68, 1990.

[133] Friedrich Siebert and Peter Hildebrandt. *Vibrational spectroscopy in life science*. John Wiley & Sons, 2008.

[134] Albert F Lawrence, James C McDaniel, David B Chang, Brian M Pierce, and Robert R Birge. Dynamics of the Davydov model in alpha-helical proteins: Effects of the coupling parameter and temperature. *Physical Review A*, 33(2):1188, 1986.

[135] Gene H Golub and Charles F Van Loan. *Matrix computations*. JHU press, 2013.

[136] KB Petersen and MS Pedersen. The matrix cookbook, version 20121115. *Technical Univ. Denmark, Kongens Lyngby, Denmark, Tech. Rep*, 3274, 2012.

[137] Lorenzo Paulatto, Ion Errea, Matteo Calandra, and Francesco Mauri. First-principles calculations of phonon frequencies, lifetimes, and spectral functions from weak to strong anharmonicity: The example of palladium hydrides. *Physical Review B*, 91(5):054304, 2015.

[138] Roberto Marquardt and Martin Quack. Infrared-multiphoton excitation and wave packet motion of the harmonic and anharmonic oscillators: Exact solutions and quasiresonant approximation. *The Journal of Chemical Physics*, 90(11):6320–6327, 1989.

[139] Steven Hepplestone and Gyaneshwar P Srivastava. Anharmonic lifetime of phonons in nanophononic semiconductors. *MRS Online Proceedings Library (OPL)*, 1172:1172–T03, 2009.

[140] Gernot Deinzer, Gerd Birner, and Dieter Strauch. Ab initio calculation of the linewidth of various phonon modes in germanium and silicon. *Physical Review B*, 67(14):144304, 2003.

[141] Atsushi Togo, Laurent Chaput, and Isao Tanaka. Distributions of phonon lifetimes in brillouin zones. *Physical review B*, 91(9):094306, 2015.

[142] Shaul Mukamel and ROCHESTER UNIV NY DEPT OF CHEMISTRY. Intermolecular and intramolecular vibrational relaxation and energy transfer. *Final Report*, 1988.

[143] AA Maradudin. On the lifetime of phonons in one-dimensional crystals. *Physics Letters*, 2(6):298–300, 1962.

[144] Hiroshi Fujisaki and John E Straub. Vibrational energy relaxation in proteins. *Proceedings of the National Academy of Sciences*, 102(19):6726–6731, 2005.

[145] Robert M Whitnell, Kent R Wilson, and James T Hynes. Vibrational relaxation of a dipolar molecule in water. *The Journal of chemical physics*, 96(7):5354–5369, 1992.

[146] Jun Young Yoon, Minkyun Noh, and David L. Trumper. Duffing oscillation and jump resonance: Spectral hysteresis and input-dependent resonance shift. *Precision Engineering*, 70:63–69, 2021.

[147] Dominic Jordan and Peter Smith. *Nonlinear ordinary differential equations: an introduction for scientists and engineers*. OUP Oxford, 2007.

[148] Farid Tajaddodianfar, Mohammad Reza Hairi Yazdi, and Hossein Nejat Pishkenari. Nonlinear dynamics of MEMS/NEMS resonators: analytical solution by the homotopy analysis method. *Microsystem Technologies*, 23:1913–1926, 2017.

[149] Fábio Javaroni, Aurélio BB Ferreira, and Clarissa O da Silva. The (α-1, 6) glycosidic bond of isomaltose: a tricky system for theoretical conformational studies. *Carbohydrate research*, 344(10):1235–1247, 2009.

[150] Brina Brauer, Madeleine Pincu, Victoria Buch, Ilana Bar, John P Simons, and R Benny Gerber. Vibrational spectra of α-glucose, β-glucose, and sucrose: anharmonic calculations and experiment. *The Journal of Physical Chemistry A*, 115(23):5859–5872, 2011.

[151] Riccardo Dettori, Michele Ceriotti, Johannes Hunger, Claudio Melis, Luciano Colombo, and Davide Donadio. Simulating energy relaxation in pump–probe vibrational spectroscopy of hydrogen-bonded liquids. *Journal of chemical theory and computation*, 13(3):1284–1292, 2017.

[152] Tom Leadbetter Cottrell. The strengths of chemical bonds. *(No Title)*, 1954.

[153] Alexander L Tournier, Jiancong Xu, and Jeremy C Smith. Translational hydration water dynamics drives the protein glass transition. *Biophysical Journal*, 85(3):1871–1875, 2003.

[154] Kei Moritsugu, Brigitte M Njunda, and Jeremy C Smith. Theory and normal-mode analysis of change in protein vibrational dynamics on ligand binding. *The Journal of Physical Chemistry B*, 114(3):1479–1485, 2010.

[155] Erika Balog, David Perahia, Jeremy C Smith, and Franci Merzel. Vibrational softening of a protein on ligand binding. *The Journal of Physical Chemistry B*, 115(21):6811–6817, 2011.

[156] Marie-Claire Bellissent-Funel, Ali Hassanali, Martina Havenith, Richard Henchman, Peter Pohl, Fabio Sterpone, David Van Der Spoel, Yao Xu, and Angel E Garcia. Water determines the structure and dynamics of proteins. *Chemical reviews*, 116(13):7673–7697, 2016.

[157] Michael O'Connor, Helen M Deeks, Edward Dawn, Oussama Metatla, Anne Roudaut, Matthew Sutton, Lisa May Thomas, Becca Rose Glowacki, Rebecca Sage, Philip Tew, et al. Sampling molecular conformations and dynamics in a multiuser virtual reality framework. *Science advances*, 4(6):eaat2731, 2018.

[158] Andrew Cupo, Damien Tristant, Kyle Rego, and Vincent Meunier. Theoretical analysis of spectral lineshapes from molecular dynamics. *npj Computational Materials*, 5(1):82, 2019.

[159] Erika Balog, Torsten Becker, Martin Oettl, Ruep Lechner, Roy Daniel, John Finney, and Jeremy C Smith. Direct determination of vibrational density of states change on ligand binding to a protein. *Physical review letters*, 93(2):028103, 2004.

[160] Katherine A Niessen, Mengyang Xu, and AG Markelz. Terahertz optical measurements of correlated motions with possible allosteric function. *Biophysical reviews*, 7:201–216, 2015.

[161] Ronald Ulbricht, Euan Hendry, Jie Shan, Tony F Heinz, and Mischa Bonn. Carrier dynamics in semiconductors studied with time-resolved terahertz spectroscopy. *Reviews of Modern Physics*, 83(2):543, 2011.

[162] Fabio Novelli, Luis Ruiz Pestana, Kochise C Bennett, Federico Sebastiani, Ellen M Adams, Nikolas Stavrias, Thorsten Ockelmann, Alejandro Colchero, Claudius Hoberg, Gerhard

Schwaab, et al. Strong anisotropy in liquid water upon librational excitation using terahertz laser fields. *The Journal of Physical Chemistry B*, 124(24):4989–5001, 2020.

[163] Feng Zhang, Houng-Wei Wang, Keisuke Tominaga, and Michitoshi Hayashi. Mixing of intermolecular and intramolecular vibrations in optical phonon modes: terahertz spectroscopy and solid-state density functional theory. *Wiley Interdisciplinary Reviews: Computational Molecular Science*, 6(4):386–409, 2016.

[164] Feng Zhang, Keisuke Tominaga, Michitoshi Hayashi, and Houng-Wei Wang. Low-frequency vibration study of amino acids using terahertz spectroscopy and solid-state density functional theory. In *Infrared, Millimeter-Wave, and Terahertz Technologies III*, volume 9275, pages 44–52. SPIE, 2014.

[165] Hossam Elgabarty, Tobias Kampfrath, Douwe Jan Bonthuis, Vasileios Balos, Naveen Kumar Kaliannan, Philip Loche, Roland R Netz, Martin Wolf, Thomas D Kühne, and Mohsen Sajadi. Energy transfer within the hydrogen bonding network of water following resonant terahertz excitation. *Science Advances*, 6(17):eaay7074, 2020.

[166] CH Raymond Ooi and KJ Cedric Chia. Unified master equation for molecules in phonon and radiation baths. *Scientific reports*, 12(1):20015, 2022.

[167] Yuqing Deng and Richard M Stratt. Vibrational energy relaxation of polyatomic molecules in liquids: The solvent's perspective. *The Journal of chemical physics*, 117(4):1735–1749, 2002.

[168] Shaoqing Wang. Efficiently calculating anharmonic frequencies of molecular vibration by molecular dynamics trajectory analysis. *ACS omega*, 4(5):9271–9283, 2019.

[169] Wieland Staessens and Bert Vercnocke. Lectures on scattering amplitudes in string theory. *arXiv preprint arXiv:1011.0456*, 2010.

[170] Diane E Sagnella and John E Straub. A study of vibrational relaxation of B-state carbon monoxide in the heme pocket of photolyzed carboxymyoglobin. *Biophysical journal*, 77(1):70–84, 1999.

[171] Jens Poulsen, Søren R Keiding, and Peter J Rossky. Extracting rates of vibrational energy relaxation from centroid molecular dynamics. *Chemical physics letters*, 336(5-6):488–494, 2001.

[172] Walter Heywang, Karl Lubitz, and Wolfram Wersing. *Piezoelectricity: evolution and future of a technology*, volume 114. Springer Science & Business Media, 2008.

[173] Syed T Haider, Muhammad A Shah, Duck-Gyu Lee, and Shin Hur. A review of the recent applications of aluminum nitride-based piezoelectric devices. *IEEE Access*, 2023.

[174] Junqiu Liu, Hao Tian, Erwan Lucas, Arslan S Raja, Grigory Lihachev, Rui Ning Wang, Jijun He, Tianyi Liu, Miles H Anderson, Wenle Weng, et al. Monolithic piezoelectric control of soliton microcombs. *Nature*, 583(7816):385–390, 2020.

[175] Patricio Arrangoiz-Arriola, E Alex Wollack, Zhaoyou Wang, Marek Pechal, Wentao Jiang, Timothy P McKenna, Jeremy D Witmer, Raphaël Van Laer, and Amir H Safavi-Naeini. Resolving the energy levels of a nanomechanical oscillator. *Nature*, 571(7766):537–540, 2019.

[176] Ewold Verhagen, Samuel Deléglise, Stefan Weis, Albert Schliesser, and Tobias J Kippenberg. Quantum-coherent coupling of a mechanical oscillator to an optical cavity mode. *Nature*, 482(7383):63–67, 2012.

[177] Thomas Niemczyk, F Deppe, H Huebl, EP Menzel, F Hocke, MJ Schwarz, JJ Garcia-Ripoll, D Zueco, T Hümmer, E Solano, et al. Circuit quantum electrodynamics in the ultrastrong-coupling regime. *Nature Physics*, 6(10):772–776, 2010.

[178] Derren J Heyes, C Neil Hunter, Ivo HM van Stokkum, Rienk Van Grondelle, and Marie Louise Groot. Ultrafast enzymatic reaction dynamics in protochlorophyllide oxidoreductase. *Nature Structural & Molecular Biology*, 10(6):491–492, 2003.

[179] Sivaraman Subramanian, Hannah BL Jones, Simona Frustaci, Samuel Winter, Marc W van der Kamp, Vickery L Arcus, Christopher R Pudney, and Frank Vollmer. Sensing enzyme activation heat capacity at the single-molecule level using gold-nanorod-based optical whispering gallery modes. *ACS Applied Nano Materials*, 4(5):4576–4583, 2021.

[180] Hiroshi Takahashi, Keiko Kato, Hidetoshi Nakano, Masahiro Kitajima, Kenji Ohmori, and Kazutaka G Nakamura. Optical control and mode selective excitation of coherent phonons in YBa2Cu3O7- δ. *Solid state communications*, 149(43-44):1955–1957, 2009.

[181] H Katsuki, JC Delagnes, K Hosaka, K Ishioka, H Chiba, ES Zijlstra, ME Garcia, H Takahashi, K Watanabe, M Kitajima, et al. All-optical control and visualization of ultrafast two-dimensional atomic motions in a single crystal of bismuth. *Nature communications*, 4(1):2801, 2013.

[182] Jianbo Hu, Oleg V Misochko, Arihiro Goto, and Kazutaka G Nakamura. Delayed formation of coherent lo phonon-plasmon coupled modes in n-and p-type gaas measured using a femtosecond coherent control technique. *Physical Review B*, 86(23):235145, 2012.

[183] Kotaro Makino, Junji Tominaga, and Muneaki Hase. Ultrafast optical manipulation of atomic arrangements in chalcogenide alloy memory materials. *Optics express*, 19(2):1260–1270, 2011.

[184] Goran Lindblad. On the generators of quantum dynamical semigroups. *Communications in Mathematical Physics*, 48(2):119–130, 1976.